N° d'ordre NNT : 2026ISAL0017

THESE de DOCTORAT DE L'INSA LYON, membre de l'Université de Lyon

Ecole Doctorale N° 160

EEA de Lyon

Spécialité/ discipline de doctorat : Automatique

Soutenue publiquement le 19/03/2026, par :

Zaman Yazbeck

Efficient hydrogen production for decarbonization: Modeling, implementation, and validation of prognostic and health management solutions for solid oxide electrolysis.

Devant le jury composé de :

PÉRA, Marie-Cécile	Professeur des Universités	FCLAB / FEMTO-ST, Université Marie et Louis Pasteur	Présidente
POINOT, Thierry	Professeur des Universités	LIAS, Université de Poitiers	Rapporteur
JURIČIĆ, Đani	Professeur des Universités	Jožef Stefan Institute, University of Nova Gorica	Rapporteur
MOREL, Bertrand	Ingénieur de Recherche	LITEN, CEA Grenoble	Examinateur
PHAM, Minh Tu	Professeur des Universités	Laboratoire Ampère, INSA Lyon	Directeur de thèse
BRIBIESCA ARGOMEDO, Federico	Maître de Conférences	Laboratoire Ampère, INSA Lyon	Co-encadrant de thèse
DIMITRIOU, Vincent	Digital Technologies Manager	GENVIA	Invité
KERGUS, Pauline	Chargée de Recherche	LAPLACE, CNRS	Invitée

Thèse accessible à l'adresse : https://theses.insa-lyon.fr/publication/2026ISAL0017/these.pdf © [Z. Yazbeck], [2026], INSA Lyon, tous droits réservés

Thèse accessible à l'adresse : https://theses.insa-lyon.fr/publication/2026ISAL0017/these.pdf © [Z. Yazbeck], [2026], INSA Lyon, tous droits réservés

Département FEDORA – INSA Lyon - Ecoles Doctorales

SIGLE	ECOLE DOCTORALE	NOM ET COORDONNEES DU RESPONSABLE
ED 206 CHIMIE	**CHIMIE DE LYON** https://www.edchimie-lyon.fr Sec. : Renée EL MELHEM Bât. Blaise PASCAL, 3e étage secretariat@edchimie-lyon.fr	**M. Stéphane DANIELE** C2P2-CPE LYON-UMR 5265 Bâtiment F308, BP 2077 43 Boulevard du 11 novembre 1918 69616 Villeurbanne directeur@edchimie-lyon.fr
ED 341 E2M2	**ÉVOLUTION, ÉCOSYSTÈME, MICROBIOLOGIE, MODÉLISATION** http://e2m2.universite-lyon.fr Sec. : Bénédicte LANZA Bât. Atrium, UCB Lyon 1 Tél : 04.72.44.83.62 secretariat.e2m2@univ-lyon1.fr	**Mme Sandrine CHARLES** Université Claude Bernard Lyon 1 UFR Biosciences, Bâtiment Mendel 43, boulevard du 11 Novembre 1918 69622 Villeurbanne CEDEX e2m2.codir@listes.univ-lyon1.fr
ED 205 EDISS	**INTERDISCIPLINAIRE SCIENCES-SANTÉ** http://ediss.universite-lyon.fr Sec. : Bénédicte LANZA Bât. Atrium, UCB Lyon 1 Tél : 04.72.44.83.62 secretariat.ediss@univ-lyon1.fr	**Mme Sylvie RICARD-BLUM** Laboratoire ICBMS - UMR 5246 CNRS - Université Lyon 1 Bâtiment Raulin - 2ème étage Nord 43 Boulevard du 11 novembre 1918 69622 Villeurbanne Cedex Tél : +33(0)4 72 44 82 32 sylvie.ricard-blum@univ-lyon1.fr
ED 34 EDML	**MATÉRIAUX DE LYON** http://ed34.universite-lyon.fr Sec. : Yann DE ORDENANA Tél : 04.72.18.62.44 yann.de-ordenana@ec-lyon.fr	**M. Stéphane BENAYOUN** Ecole Centrale de Lyon Laboratoire LTDS 36 avenue Guy de Collongue 69134 Ecully CEDEX Tél : 04.72.18.64.37 stephane.benayoun@ec-lyon.fr
ED 160 EEA	**ÉLECTRONIQUE, ÉLECTROTECHNIQUE, AUTOMATIQUE** https://edeea.universite-lyon.fr Sec. : Philomène TRECOURT Bâtiment Direction INSA Lyon Tél : 04.72.43.71.70 secretariat.edeea@insa-lyon.fr	**M. Philippe DELACHARTRE** INSA LYON Laboratoire CREATIS Bâtiment Blaise Pascal, 7 avenue Jean Capelle 69621 Villeurbanne CEDEX Tél : 04.72.43.88.63 philippe.delachartre@insa-lyon.fr
ED 512 INFOMATHS	**INFORMATIQUE ET MATHÉMATIQUES** http://edinfomaths.universite-lyon.fr Sec. : Renée EL MELHEM Bât. Blaise PASCAL, 3e étage Tél : 04.72.43.80.46 infomaths@univ-lyon1.fr	**M. Hamamache KHEDDOUCI** Université Claude Bernard Lyon 1 Bât. Nautibus 43, Boulevard du 11 novembre 1918 69 622 Villeurbanne Cedex France Tél : 04.72.44.83.69 direction.infomaths@listes.univ-lyon1.fr
ED 162 MEGA	**MÉCANIQUE, ÉNERGÉTIQUE, GÉNIE CIVIL, ACOUSTIQUE** http://edmega.universite-lyon.fr Sec. : Philomène TRECOURT Tél : 04.72.43.71.70 Bâtiment Direction INSA Lyon mega@insa-lyon.fr	**M. Etienne PARIZET** INSA Lyon Laboratoire LVA Bâtiment St. Exupéry 25 bis av. Jean Capelle 69621 Villeurbanne CEDEX etienne.parizet@insa-lyon.fr
ED 483 ScSo	**ScSo**[1] https://edsciencessociales.universite-lyon.fr Sec. : Mélina FAVETON Tél : 04.78.69.77.79 melina.faveton@univ-lyon2.fr	**M. Bruno MILLY** (INSA : J.Y. TOUSSAINT) Univ. Lyon 2 Campus Berges du Rhône 18, quai Claude Bernard 69365 LYON CEDEX 07 Bureau BEL 319 bruno.milly@univ-lyon2.fr

[1] ScSo : Histoire, Géographie, Aménagement, Urbanisme, Archéologie, Science politique, Sociologie, Anthropologie

Thèse accessible à l'adresse : https://theses.insa-lyon.fr/publication/2026ISAL0017/these.pdf © [Z. Yazbeck], [2026], INSA Lyon, tous droits réservés

Thèse accessible à l'adresse : https://theses.insa-lyon.fr/publication/2026ISAL0017/these.pdf © [Z. Yazbeck], [2026], INSA Lyon, tous droits réservés

Acknowledgements

This work was carried out within the framework of a CIFRE PhD in partnership with GENVIA. Two years of this thesis were spent at CEA Grenoble, whose support and collaboration are gratefully acknowledged. For this reason, I would like to thank Patrice Tochon, Vincent Dimitriou, and Federico Monaco from GENVIA for the many discussions we had throughout the project, and for their valuable insights and feedback. I would also like to thank Mathias Gérard and Cyril Bourasseau from CEA for their support and for the constructive exchanges that contributed to this work.

I would also like to express my sincere gratitude to my thesis supervisors, Minh Tu, Federico, and Bertrand, for their guidance, support, and constructive feedback throughout this work. I feel privileged to have benefited from their expertise and am truly grateful for the opportunity to learn from them.

I also thank all my colleagues at CEA Grenoble for their support and for the warm working environment. The constructive discussions and everyday moments shared during this thesis made this experience easier and enjoyable.

I am deeply thankful to my friends Aya, Zakia, Ghida, Yara, and Sara for their constant encouragement, their presence, and the many conversations and moments that helped me throughout this journey. Your support has meant a great deal to me.

Finally, I would like to thank my family and my partner, Mostafa, for their unconditional love, patience, and support throughout these years. I am profoundly grateful for all that you have done for me.

Thèse accessible à l'adresse : https://theses.insa-lyon.fr/publication/2026ISAL0017/these.pdf © [Z. Yazbeck], [2026], INSA Lyon, tous droits réservés

Contents

List of Figures ix

List of Tables xiii

Nomenclature xiv

1 Introduction 1
- 1.1 Motivation . . . 1
- 1.2 Hydrogen as energy storage . . . 4
- 1.3 Electrolysis Technologies: General Background . . . 5
- 1.4 Prognosis and Health management strategy . . . 9
  - 1.4.1 PHM and the Maintenance Strategy Framework . . . 10
  - 1.4.2 PHM approaches . . . 12
- 1.5 Why PHM for SOEC systems? . . . 14
- 1.6 Degradations of SOEC systems . . . 14
  - 1.6.1 Intrinsic degradation . . . 15
  - 1.6.2 Degradation related to system operation . . . 17
- 1.7 Objectives of the PhD . . . 19
- 1.8 Publications and communications . . . 20
- 1.9 Manuscript outline . . . 21

2 SOEC technology 24
- 2.1 Solid Oxide cells . . . 24
  - 2.1.1 Electrochemical reactions: SOEC . . . 25
  - 2.1.2 Materials for SOC components . . . 26
  - 2.1.3 Cell Design . . . 26
  - 2.1.4 Cell thermal regimes . . . 29
- 2.2 Modeling of SOECs . . . 31
  - 2.2.1 Fundamentals of SOEC modeling . . . 31
  - 2.2.2 State of the art of SOEC modeling . . . 33
  - 2.2.3 Positioning of the present work: . . . 35

Thèse accessible à l'adresse : https://theses.insa-lyon.fr/publication/2026ISAL0017/these.pdf © [Z. Yazbeck], [2026], INSA Lyon, tous droits réservés

2.3 Mathematical model . . . 36
2.3.1 Mass transport and conservation . . . 36
2.3.2 Electrochemical Model . . . 40
2.3.3 Thermal Balance model . . . 44
2.4 Model summary . . . 45
2.5 Time integration . . . 46

3 Parameter estimation 48
3.1 Motivation and Background . . . 49
3.1.1 Problem description . . . 49
3.1.2 State of the art . . . 51
3.2 State-space formulation . . . 54
3.3 Sensitivity analysis . . . 56
3.3.1 Sensitivity differential equations . . . 58
3.3.2 Sensitivity equations as a tool for parameter identifiability . . . 59
3.3.3 Parameter identification using grouping-based approach . . . 60
3.3.4 Does temperature provide additional information for parameter estimation? 63
3.4 Sensitivity function-based parameter identification . . . 64
3.4.1 Truncated Levenberg-Marquardt method . . . 64
3.4.2 Estimation results for synthetic data . . . 66
3.5 Monte-Carlo Simulation . . . 70
3.6 Confidence interval . . . 78
3.7 Parameter estimation with experimental data . . . 79
3.8 Design of optimal experimental data . . . 81
3.9 Sequential OED . . . 86
3.10 OED based on a predefined library . . . 89
3.11 Conclusion . . . 94

4 Fault detection 98
4.1 Introduction . . . 99
4.2 Fault description . . . 100
4.3 State of the art . . . 100
4.4 Fault detection methodology . . . 104
4.4.1 Square-Root Unscented Kalman Filter . . . 106
4.4.2 Adaptive Threshold for Fault Detection . . . 110
4.4.3 Experimental Studies . . . 111
4.5 Aging-aware monitoring . . . 117
4.5.1 Proposed Approach . . . 118
4.5.2 Application to experimental data . . . 120

Thèse accessible à l'adresse : https://theses.insa-lyon.fr/publication/2026ISAL0017/these.pdf © [Z. Yazbeck], [2026], INSA Lyon, tous droits réservés

4.5.3 Results . . . 122
4.6 Conclusion . . . 123

Conclusion and perspectives **126**

Bibliography **131**

A Résumé étendu en Français **150**
A.1 Motivation et contexte . . . 151
A.2 Dégradations des SOEC et diagnostic des défauts basé sur un modèle . . . 153
A.3 Technologie SOEC . . . 154
A.3.1 Cellule d'électrolyse à oxyde solide et mécanismes de réaction . . . 154
A.3.2 Régimes thermiques et fonctionnement thermoneutre . . . 155
A.3.3 Niveaux de modélisation . . . 155
A.3.4 Courbe de performance électrochimique et de polarisation . . . 155
A.3.5 Structure globale du modèle . . . 157
A.3.6 Intégration temporelle . . . 157
A.4 Estimation des paramètres . . . 157
A.4.1 Représentation d'état . . . 158
A.4.2 Modèle d'espace d'état et fonctions de sensibilité . . . 158
A.4.3 Méthode de Levenberg-Marquardt tronqué . . . 159
A.4.4 Estimation à partir de données simulées . . . 160
A.4.5 Intervalle de confiance . . . 161
A.4.6 Estimation à partir de données experimentaux . . . 162
A.4.7 Planification optimale d'expériences (OED) . . . 163
A.4.8 Stratégies alternatives de planification expérimentale optimale . . . 164
A.5 Détection des défauts . . . 166
A.5.1 Application aux données expérimentales . . . 170
A.5.2 Résultats . . . 170
A.6 Conclusion et perspectives . . . 172

Thèse accessible à l'adresse : https://theses.insa-lyon.fr/publication/2026ISAL0017/these.pdf © [Z. Yazbeck], [2026], INSA Lyon, tous droits réservés

List of Figures

1.1 Global primary energy consumption by source 2
1.2 Relationship between CO_2 concentration in the atmosphere and global temperature anomaly 3
1.3 Hydrogen production capacity by production process in Europe in 2023 4
1.4 Comparison of energy storage time and capacity 5
1.5 Energy demand for water electrolysis as a function of temperature 8
1.6 Pyramid of maintenance strategies 10
1.7 PHM Architecture 11
1.8 Classification of PHM approaches 12
1.9 Schematic description of the model-based fault diagnosis scheme 13
1.10 Different degradation phenomena that can occur at the cell and stack level. . . . 16

2.1 SOEC individual electrodes and complete cell 25
2.2 Schematics of (a) planar, (b) tubular designs of SOC. 26
2.3 Planar SOEC stack 27
2.4 SOEL200 Genvia pilot project (300 kW, 200 kg H_2/day), an industrial-scale SOEC demonstrator 27
2.5 Various types of SOEC configurations 28
2.6 Operating regimes of SOECs 29
2.7 Thermoneutral voltage in a function of temperature 30
2.8 General model categories 32
2.9 2D model summary and architecture 34
2.10 Triple Phase Boundary 37
2.11 Decomposition of a typical polarization curve. 41
2.12 Schematic of Solid Oxide Electrolysis Stack (SOES) modeling. 45

3.1 Input trajectory used for the sensitivity analysis. 56
3.2 Voltage impact of 20-30% parameter perturbations around the nominal parameter vector λ^*. 57
3.3 Normalized sensitivity magnitudes calculated using sensitivity differential equations with the true parameter vector λ^*. 59

Thèse accessible à l'adresse : https://theses.insa-lyon.fr/publication/2026ISAL0017/these.pdf © [Z. Yazbeck], [2026], INSA Lyon, tous droits réservés

3.4 Sensitivity collinearity and QR-based orthogonalization. 61
3.5 Relative error. 62
3.6 QR-based orthogonalized and sorted temperature-sensitivity magnitudes obtained using the input trajectory in Figure 3.1 and the initial parameter vector λ_0. . . . 63
3.7 Orthogonalized sensitivity magnitudes with true parameter vector (λ^*) and an initial guess λ_0 64
3.8 Evolution of the squared error versus iterations for different optimizers under noise-free measurements (left) and noisy measurements (right). 69
3.9 Number of parameters updated in each iteration with TLM algorithm under noise-free measurements (N_0) 69
3.10 Evolution of β_k in TLM algorithm under noise-free measurements (N_0) 70
3.11 Absolute voltage error between simulated and noise-free observed output for different optimizers 70
3.12 Parameter estimation using TLM starting from IG1. 73
3.13 Parameter estimation using TLM starting from IG2 73
3.14 Parameter estimation using TLM starting from IG3 74
3.15 Parameter estimation using TLM starting from IG4 74
3.16 Parameter estimation using TLM starting from IG5 75
3.17 Parameter estimation using TLM starting from IG6 75
3.18 Parameter estimation using TLM starting from IG7 76
3.19 Parameter estimation using TLM starting from IG8 76
3.20 Parameter estimation using TLM starting from IG9 77
3.21 Parameter estimation using TLM starting from IG10 77
3.22 Solid Oxide electrolyzer stack test bench with auxiliary components 79
3.23 Experimental input trajectory. 79
3.24 Absolute voltage error between experimental and output model for different optimizers 81
3.25 Cross-validation on experimental data 81
3.26 Geometric interpretation of optimality criterion in the (λ_1, λ_2) parameter plane [127]. 83
3.27 Single Shooting vs Multiple Shooting 84
3.28 OED data 85
3.29 Orthogonalized sensitivity magnitudes for the input profile in Figure 3.1 and for the profile generated from OED using the initial guess λ_0. 86
3.30 Sequential OED scheme. 87
3.31 Input profile generated using sequential OED. 88
3.32 Evolution of the normalized parameter estimates in sequential OED 88
3.33 Effect of initially constraining Genetic Algorithm (GA) population within duration and test number constraints. 92

Thèse accessible à l'adresse : https://theses.insa-lyon.fr/publication/2026ISAL0017/these.pdf © [Z. Yazbeck], [2026], INSA Lyon, tous droits réservés

3.34 Genetic Algorithm (GA) optimization result for constraints of 3600 seconds, and maximum 12 tests. . . . 93
3.35 Parameter estimates and 95% confidence intervals obtained using a standard input profile and an input profile generated from OED. . . . 94

4.1 Fault diagnosis approach proposed in [163]. . . . 102
4.2 Fault diagnosis approach proposed in [159]. . . . 103
4.3 Validation of the model outputs against measured data from the experimental test bench. . . . 105
4.4 Starvation detection scheme. . . . 106
4.5 Example of the Unscented Transform (UT) for mean and covariance propagation. a) actual, b) first-order linearization used by EKF, c) Unscented Transform (UT) 107
4.6 Operating conditions showing both estimated and nominal inlet total flow rates during the steam starvation scenario for comparison. The colored regions indicate the time windows where the fault is injected. . . . 112
4.7 Outputs in steam starvation case. . . . 113
4.8 Outputs in hydrogen starvation case. . . . 113
4.9 Operating conditions showing both estimated and nominal inlet total flow rates during the Hydrogen Starvation scenario for comparison. The colored regions indicate the time windows where the fault is injected. . . . 114
4.10 States estimation in steam starvation scenario and fault detection thresholds ($Th_{min/max}$) for each variable. . . . 115
4.11 States estimation in hydrogen starvation scenario and fault detection thresholds ($Th_{min/max}$) for each variable. . . . 116
4.12 Total resistance behavior in steam and hydrogen starvation scenarios, respectively. 116
4.13 Aging-aware monitoring approach scheme . . . 118
4.14 Bathtub curve . . . 120
4.15 Operating condition window . . . 121
4.16 SoH estimation for whole measurement data. . . . 122

A.1 Besoins énergétiques pour l'électrolyse de l'eau en fonction de la température . . 152
A.2 Description schématique du schéma de diagnostic de panne basé sur un modèle . 153
A.3 Électrodes individuelles SOEC et cellule complète . . . 154
A.4 Décomposition d'une courbe de polarisation typique. . . . 156
A.5 Schéma de modélisation d'une pile d'électrolyse à oxyde solide (SOES). . . . 157
A.6 Trajectoire d'entrée expérimentale. . . . 162
A.7 Validation croisée sur des données expérimentales . . . 163
A.8 Trajectoire d'entrée générée à partir de l'OED et conversion de vapeur correspondante. . . . 165

Thèse accessible à l'adresse : https://theses.insa-lyon.fr/publication/2026ISAL0017/these.pdf © [Z. Yazbeck], [2026], INSA Lyon, tous droits réservés

A.9 Schéma de détection de la famine. 167
A.10 Les conditions de fonctionnement, illustrées par les débits totaux d'entrée estimés et nominaux lors du scénario de starvation de vapeur, sont comparées. Les zones colorées indiquent les intervalles de temps durant lesquels le défaut est injecté. . 168
A.11 Estimation des états dans un scénario de starvation de vapeur et seuils de détection des défauts ($Th_{min/max}$) pour chaque variable. 169
A.12 Aging-aware monitoring scheme 170
A.13 Estimation de l'état de santé (SoH) pour l'ensemble des données de mesure. . . 171

Thèse accessible à l'adresse : https://theses.insa-lyon.fr/publication/2026ISAL0017/these.pdf © [Z. Yazbeck], [2026], INSA Lyon, tous droits réservés

List of Tables

1.1 Comparison of the AWE, PEMWE, SOEC, and AEMWE technologies 7

3.1 Physical parameters and their units 55
3.2 Parameter groups 61
3.3 Parameters estimates with sequential estimation 62
3.4 Estimation on noise-free output (N_0) 67
3.5 Estimation under noisy output (6%) (N_1) 67
3.6 Computation time in minutes for N_0 and N_1 cases 68
3.7 Normalized initial guesses used in the Monte Carlo simulation. 71
3.8 Estimation with experimental data 80
3.9 Normalized OED parameter estimates and confidence intervals. 85
3.10 Normalized sequential OED parameter estimates ($\hat{\lambda}_{seq,OED}$) and confidence intervals. 89
3.11 Normalized parameter estimates and 95% confidence intervals for the library-based OED input. 94

4.1 PRBS bandwidth, excitation duration, and associated acquisition sampling time. 120

A.1 Estimation de la sortie sans bruit(N_0) 160
A.2 Estimation avec bruit de sortie (6%) (N_1) 161
A.3 Estimation with experimental data 164

Thèse accessible à l'adresse : https://theses.insa-lyon.fr/publication/2026ISAL0017/these.pdf © [Z. Yazbeck], [2026], INSA Lyon, tous droits réservés

Nomenclature

Symbols

ΔH_f	Enthalpy of formation
ΔH	Reaction enthalpy
δ	Electrode Thickness
$\dot{n}$	Molar flow rate
η	Overpotential
y	Through-plane coordinate (through-cell thickness direction)
σ	Electrical conductivity
σ_{SB}	Stefan-Boltzmann constant
τ	Tortuosity
ε	Porosity
A_{stack}	Surface area of the stack
C_{p_s}	Average Stack heat Capacity
D_i^{eff}	Effective diffusion coefficient, $i \in \{H_2, H_2O, O_2, N_2\}$
E_{act}	Activation energy
F	Faraday constant
h_i	Enthalpy
I	Current density
m_s	Stack mass
N_i	Molar flux

Thèse accessible à l'adresse : https://theses.insa-lyon.fr/publication/2026ISAL0017/these.pdf © [Z. Yazbeck], [2026], INSA Lyon, tous droits réservés

P	Pressure
p_i	Partial pressure
R	Universal gas constant
r_p	Mean pore radius
T	Stack temperature
$T_{furnace}$	Furnace temperature
U_{cell}	Cell voltage
U_{rev}	Reversible voltage
V_s	Stack voltage
V_{ch}	Volume of the channel
y_i^{in}	Inlet molar fraction
y_i^{TPB}	Molar fraction at the TPBs
M_i	Molar mass
V_i	Fuller diffusion volume

Acronyms

EIS	Electrochemical Impedance Spectroscopy
EKF	Extended Kalman Filter
FIM	Fisher Information Matrix
GN	Gauss-Newton
LM	Levenberg-Marquardt
OED	Optimal Experiment Design
PRBS	Pseudo-Random Binary Sequence
SOC	Solid Oxide Cell
SOEC	Solid Oxide Electrolyzer Cell
SOES	Solid Oxide Electrolyzer Stack

Thèse accessible à l'adresse : https://theses.insa-lyon.fr/publication/2026ISAL0017/these.pdf © [Z. Yazbeck], [2026], INSA Lyon, tous droits réservés

SOFC Solid Oxide Fuel Cell

SR-UKF Square-Root Unscented Kalman Filter

SRU Single Repeating Unit

TGN Truncated Gauss-Newton

TLM Truncated Levenberg-Marquardt

TPB Triple Phase Boundary

UKF Unscented Kalman Filter

Functions and Operators

$E\{\cdot\}$ Expected value

$chol$ Cholesky factorization

$cholupdate$ Rank 1 update to Cholesky factorization

qr QR factorization

Thèse accessible à l'adresse : https://theses.insa-lyon.fr/publication/2026ISAL0017/these.pdf © [Z. Yazbeck], [2026], INSA Lyon, tous droits réservés

Thèse accessible à l'adresse : https://theses.insa-lyon.fr/publication/2026ISAL0017/these.pdf © [Z. Yazbeck], [2026], INSA Lyon, tous droits réservés

Thèse accessible à l'adresse : https://theses.insa-lyon.fr/publication/2026ISAL0017/these.pdf © [Z. Yazbeck], [2026], INSA Lyon, tous droits réservés

Chapter 1

Introduction

Contents

1.1 Motivation 1
1.2 Hydrogen as energy storage 4
1.3 Electrolysis Technologies: General Background 5
1.4 Prognosis and Health management strategy 9
1.4.1 PHM and the Maintenance Strategy Framework 10
1.4.2 PHM approaches 12
1.5 Why PHM for SOEC systems? 14
1.6 Degradations of SOEC systems 14
1.6.1 Intrinsic degradation 15
1.6.2 Degradation related to system operation 17
1.7 Objectives of the PhD 19
1.8 Publications and communications 20
1.9 Manuscript outline 21

1.1 Motivation

The world population is expected to continue increasing over the next five to six decades, reaching a peak of approximately 10.3 billion by the mid-2080s, up from 8.2 billion in 2024 [1]. This demographic growth, along with economic growth, particularly in developing countries [2], and rapid urbanization is placing unprecedented demands on global energy systems [3, 4, 5, 6]. This trend is illustrated in Figure 1.1, which shows the evolution of global primary energy consumption.

This surge in consumption is closely related to the historical reliance on fossil fuels, a trend

Thèse accessible à l'adresse : https://theses.insa-lyon.fr/publication/2026ISAL0017/these.pdf © [Z. Yazbeck], [2026], INSA Lyon, tous droits réservés

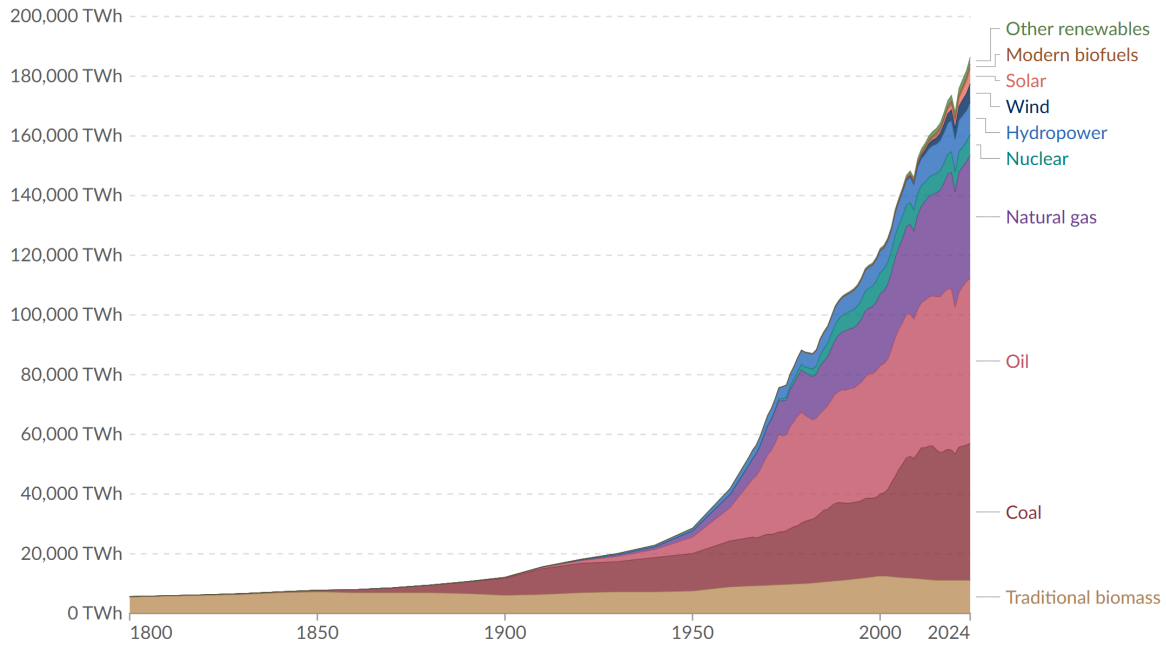

Figure 1.1: Global primary energy consumption by source [7].

that began with the Industrial Revolution and intensified during its second phase around 1870, marked by large-scale technological progress [8]. Fossil fuels, namely coal, natural gas, and oil, have since become the dominant sources of energy [9], as shown in Figure 1.1. These fuels are formed over geological timescales, over millions of years, through complex natural processes [10], yet their current consumption rates exceed natural regeneration by several orders of magnitude. This imbalance between formation and consumption raises serious questions about the long-term sustainability of fossil fuel use [11].

Despite their finite nature and known environmental drawbacks, fossil fuels remain the primary source of modern energy systems, largely due to challenges associated with the transition to sustainable energy, such as high costs and limited infrastructure [12, 13]. However, the environmental consequences are severe. The combustion of fossil fuels releases large volumes of waste gases into the atmosphere, most notably carbon dioxide, whose concentration began to increase significantly with the expansion of industrial activities [14], and which in recent years has exceeded 35 billion tonnes emitted annually [15]. Carbon dioxide (CO_2) acts as a greenhouse gas by absorbing infrared radiation, thereby trapping heat and contributing to global warming, a phenomenon that has led to profound disruptions in the climate system [16].

This warming is not minor; the ongoing rise in global temperatures is clearly observable. As shown in Figure 1.2, the global surface temperature has followed a consistent upward trajectory over the past century, particularly accelerating in recent decades with the increase of the CO_2 concentration in the atmosphere.

Therefore, the 2015 Paris agreement was established to limit this increase in the average temper-

Thèse accessible à l'adresse : https://theses.insa-lyon.fr/publication/2026ISAL0017/these.pdf © [Z. Yazbeck], [2026], INSA Lyon, tous droits réservés

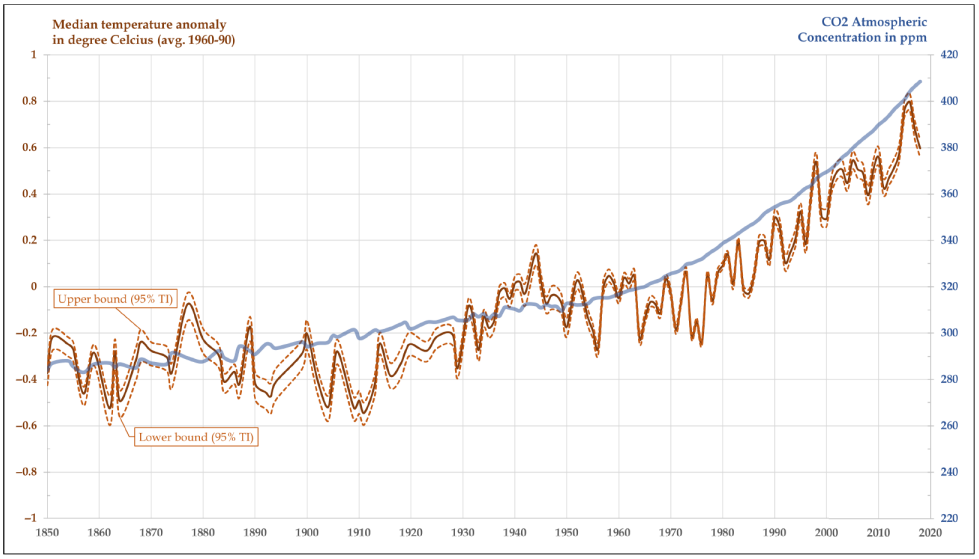

Figure 1.2: Relationship between CO_2 concentration in the atmosphere and global temperature anomaly [17].

ature to below 2°C compared with the pre-industrial global average. To achieve the targets stated by the Paris agreement and support sustainable development, it is crucial to not only reduce CO_2 emissions but also remove CO_2 from the atmosphere. Thus, to achieve net zero carbon emissions, complementary cooperation is needed at the social, economic, environmental, and technological levels [18].

In this context, hydrogen has the potential to be a key player in the global energy mix because of its clean combustion nature, high energy content, and versatility. It can be used in different applications, including fuel for transportation, heating, and electricity generation. In transportation, it can serve as a green fuel to power vehicles, producing only water and heat as by-products. For electricity generation, it can be used in fuel cells, which convert the chemical energy of hydrogen into electricity by reacting with oxygen [17].

However, producing hydrogen from fossil fuels negates many of its environmental benefits. This is evident from the fact that steam methane reforming (SMR) is the dominant method for hydrogen production, accounting for approximately 89.9% of total hydrogen production capacity in 2023, as shown in Figure 1.3, due to its low cost and high efficiency. This process, however, does not produce pure hydrogen, it also emits harmful greenhouse gases. To fully exploit the environmental advantages of hydrogen, it must be produced from renewable and sustainable energy sources. Currently, these sources contribute only a small percentage of total production. For instance, hydrogen produced as a by-product of industrial chemical manufacturing, such as ethylene, styrene, chlorine, and sodium chlorate, represents a relatively small share, about 9.2% of production capacity. Low-carbon hydrogen can also be produced via reforming coupled with

Thèse accessible à l'adresse : https://theses.insa-lyon.fr/publication/2026ISAL0017/these.pdf © [Z. Yazbeck], [2026], INSA Lyon, tous droits réservés

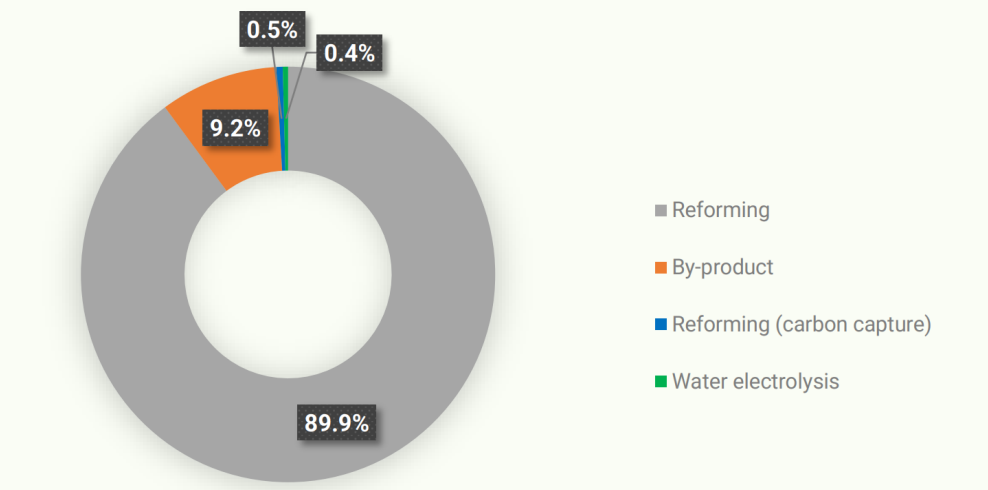

Figure 1.3: Hydrogen production capacity by production process in Europe in 2023 [19].

carbon capture and storage, which is known as blue hydrogen. Meanwhile, green hydrogen, produced by electrolysis of water powered by renewable electricity, represents a very limited share, less than 1% of total hydrogen production capacity in Europe [19].

1.2 Hydrogen as energy storage

Hydrogen (H_2) has the highest specific energy content among all conventional fuels, with a lower heating value (LHV) of approximately 120 MJ/kg, which is around 2.75 times higher than that of typical hydrocarbon fuels. A relatively small amount of hydrogen is needed to store significant amounts of energy [20]. However, despite its high gravimetric energy, hydrogen has a low volumetric energy density ($\sim$ 0.0108 MJ/L at standard conditions); therefore, it is typically compressed ($\sim$ 5.6 MJ/L at 700 bar) or liquefied ($\sim$ 8-9 MJ/L). Solid-state phase also is an option, but it is less convenient due to the added mass, heat management, and system complexity [21].

The integration of renewable energy sources into the global energy mix is a necessary step to reduce dependence on fossil fuels. However, renewable energy systems are characterized by intermittent and fluctuating outputs that complicate their direct integration into the electrical grid. For instance, nuclear energy, which is considered as a low carbon energy source, delivers a nearly constant power output that cannot be easily modulated to match variable demand. To balance these fluctuations, excess electricity must be stored using different technologies, as illustrated in Figure 1.4. Conventional storage systems such as batteries, flywheels, or pumped storage hydropower offer limited discharge durations ranging from seconds to a few days. In contrast, hydrogen-based energy storage enables both large-capacity and long-term storage, making it a promising solution for stabilizing future low-carbon energy systems.

Thèse accessible à l'adresse : https://theses.insa-lyon.fr/publication/2026ISAL0017/these.pdf © [Z. Yazbeck], [2026], INSA Lyon, tous droits réservés

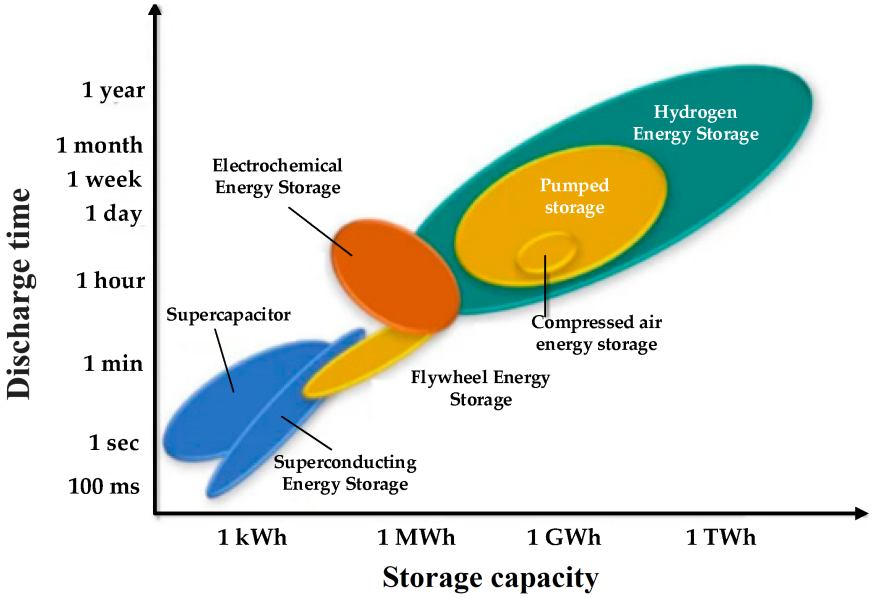

Figure 1.4: Comparison of energy storage time and capacity [22].

1.3 Electrolysis Technologies: General Background

Environmentally sustainable energy strategies are actively pursued to replace the currently dominant SMR method for hydrogen production, thus supporting the transition to a more sustainable energy system [19]. Among these, water electrolysis is considered a promising method, enabling the production of high-purity, eco-friendly hydrogen with oxygen production generated as a by-product through an electrochemical reaction driven by electrical and thermal energy, as shown in the following equation:

$$H_2O \xrightarrow{\textit{Electricity + Heat}} H_2 + \frac{1}{2}O_2 \tag{1.1}$$

Electrolyzers play a pivotal role in Power-to-Gas systems, converting renewable electricity into storable gases such as hydrogen and methane [23]. Fuel cells, in turn, provide a cleaner alternative to combustion-based power generation by directly converting chemical energy into electricity, thereby avoiding combustion-related emissions. These technologies are increasingly being integrated into multi-energy systems, such as fossil-renewable power plants [24], electric propulsion units [25], and renewable-based multigeneration systems [26, 27], making them central to the energy transition.

There are different types of electrolyzer technology. Although all of them operate under the same physical principle, the use of different electrolytes results in different electrochemical reactions and technical characteristics. The main electrolyzer types are:

Thèse accessible à l'adresse : https://theses.insa-lyon.fr/publication/2026ISAL0017/these.pdf © [Z. Yazbeck], [2026], INSA Lyon, tous droits réservés

- Alkaline Water Electrolysis (AWE).
- Proton-exchange membrane electrolysis water electrolysis (PEMWE).
- Anion exchange membrane water electrolysis (AEMWE).
- Solid oxide electrolysis (SOEC).

In Table 1.1, the main characteristics of different electrolyzer technologies are presented, highlighting their respective advantages and disadvantages. These technologies vary significantly in their operating conditions, maturity levels, and associated challenges. Alkaline Water Electrolysis (AWE) and Proton Exchange Membrane Water Electrolysis (PEMWE) are well-established and commercially available, while Anion Exchange Membrane Water Electrolysis (AEMWE), considered a promising technology for low-cost hydrogen production, remains in the early stages of development.

Among these technologies, the Solid Oxide Electrolysis Cell (SOEC) is notable for its potential high efficiency, which is the focus of this work. Therefore, only this type of electrolyzer is described in detail.

The history of solid oxide cells (SOC) begins with the discovery of the high ionic conductivity of the yttria-doped zirconia at elevated temperatures (between 600-1000°C) [35]. The first application appeared in the 1930s, when two Swiss scientists, Baur and Preis [36], generated electric power in fuel cell mode from gaseous fuels; then the development accelerated in the 1970s [37]. The concept of a solid oxide electrolysis cell, which is the reverse operation of the fuel cell mode, was reported for the first time in the late 1960s [38]. Later in the 1980s, SOEC stacks were developed within the HOT Elly project, sponsored by the German Federal Ministry of Research and Technology [37, 39]. Today, the option of operating the same device alternately in the fuel cell mode and electrolysis mode is a unique and distinctive feature of high-temperature fuel cells and is currently the most mature in SOC systems [37].

In addition to steam electrolysis for hydrogen production, SOECs can also operate with different fuels, like CO_2 or H_2O-CO_2 mixtures as feedstocks, enabling the co-electrolysis process for the production of carbon monoxide, and facilitating direct integration with carbon capture. Operating at high temperatures (600-1000°C), SOECs utilize both electricity and thermal energy (e.g., industrial waste heat), thereby reducing electrical energy demand and improving overall efficiency [40]. These operating temperatures enable operation without expensive catalysts: nickel is mostly used at high temperature (14.9 $/kg) compared to, for instance, platinum (43661.3 $/kg) [41]. This advantage arises from the thermodynamics of the water electrolysis reaction:

$$\Delta H = \Delta G + T\Delta S \tag{1.2}$$

With ΔH denoting the total energy demand, ΔG the change in Gibbs free energy or electrical

Thèse accessible à l'adresse : https://theses.insa-lyon.fr/publication/2026ISAL0017/these.pdf © [Z. Yazbeck], [2026], INSA Lyon, tous droits réservés

Table 1.1: Comparison of the AWE, PEMWE, SOEC, and AEMWE technologies. Adapted from [28]

Characteristics	AWE [28, 29]	PEMWE [28, 29, 30]	SOEC [28, 31, 32, 33]	AEMWE [28, 30, 34]
Electrolyte	20–30% KOH	Pure water	Solid oxide (stabilized YSZ)	Alkali solution, pure water
Charge carrier	OH^-	H^+	O^{2-}	OH^-
Operating temperature range (°C)	60–90	50–90	600–1000	40–90
Operating pressure range (bar)	10–30	20–50	1–15	1–30
Discharge H_2 pressure (bar)	25–30	30–80	1–3	30
Cathode reaction	$2H_2O + 2e^- \rightarrow H_2 + 2OH^-$	$4\ H^+ + 4e^- \rightarrow 2H_2$	$H_2O + 2e^- \rightarrow H_2 + O^{2-}$	$2H_2O + 2e^- \rightarrow H_2 + 2OH^-$
Anode reaction	$2OH^- \rightarrow H_2O + 1/2\ O_2 + 2e^-$	$2H_2O \rightarrow O_2 + 4H^+ + 4e^-$	$O^{2-} \rightarrow 1/2O_2 + 2e^-$	$2\ OH^- \rightarrow H_2O + 1/2O_2 + 2e^-$
Current density (mA/cm^2)	$\sim$500	1000–2000	1000–2000	1000–2000
Current efficiency (%)	50–70.8	48.5–65.5	80–95	39.7
Hydrogen purity (vol%)	99.3–99.9	99.9999	99.999	99.99
Investigated durability (kh)	$\sim$100	$\sim$10	$\sim$10	$\sim$2
Rated production (Nm^3/h)	1–760	0.265–30	>100 for large-scale system	0.25–1
Rated power (kW)	2.8–3534	1.8–174	>100 for large-scale system	1.3–4.8
Energy consumption (kWh/Nm^3)	4.5–7.5	5.8–7.3	3–5	4.8–5.2
H_2 production cost ($/kg)	2.36–6.98	2.5–6.8	2.99–7.02	3.0–7.0
System cost ($/kW)	800–1300	1200–2000	$\sim$2000 $/kW^{-1}	–
Advantages	Commercialized technology; Non-PGM catalyst; Low cost; Highly stable; Megawatt range	High voltage efficiencies; Good partial load; Higher performance; Compact cell design; rapid system response	High efficiency; High operating temperature; Scalability for large-scale production; Reversible operation; Versatility in feedstock	Non-corrosive electrolyte; Non-noble metal catalyst Low cost; Compact cell design; High operating pressure
Disadvantages	Corrosive liquid electrolyte; low current densities; low operating pressure; Crossover of gas; Low dynamic	Noble metal catalysts; Costly components; Acidic corrosive components; Below megawatt range; Low durability	High initial cost; Limited durability; Slow start-up and shutdown time; Thermal management challenges; Material degradation issues	Low current densities; Membrane degradation; Low durability; Maximum catalysts loading
Technology status	Mature	Commercialized for small-scale	Pilot projects/under development	R & D

Thèse accessible à l'adresse : https://theses.insa-lyon.fr/publication/2026ISAL0017/these.pdf © [Z. Yazbeck], [2026], INSA Lyon, tous droits réservés

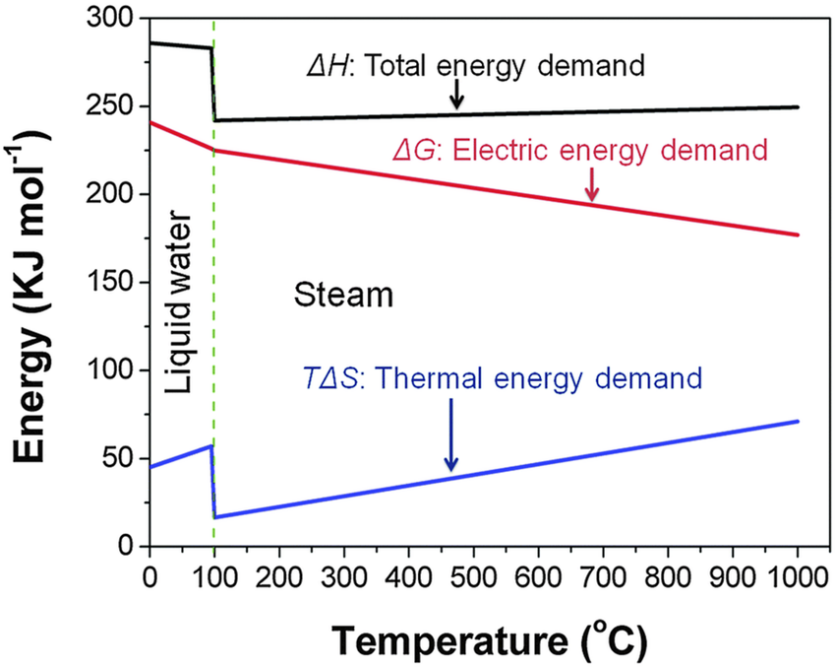

Figure 1.5: Energy demand for water electrolysis as a function of temperature [40].

energy input, T the temperature, and ΔS the change in entropy. Theoretically, ΔH is a thermodynamic property of the water splitting reaction and is primarily dependent on temperature rather than on the technology. However, since AWE, PEMWE, and SOEC operate at different temperature ranges, their corresponding ΔH differ in practice. The actual energy demand often exceeds the theoretical value due to overpotentials, kinetic limitations, mass transport resistances, and thermal losses.

Using water in its gaseous phase for electrolysis reduces the energy demand ΔH required to split water molecules into hydrogen and oxygen, as shown in Figure 1.5. This energy difference corresponds to the latent heat of vaporization of water. As the temperature increases, a part of the electrical energy can be substituted with thermal energy, while the total energy demand remains nearly constant. In addition to the substitution of electrical energy by thermal energy, high temperature electrolysis also offers improved reaction kinetics and reduced electrode reaction losses [42].

Despite their advantages, the widespread deployment of solid Oxide Cells (SOECs) remains limited because of high manufacturing costs and durability concerns. Nevertheless, SOEC technology is considered suitable for industrial deployment, especially in large-scale plants where heat recovery and integration can increase its overall efficiency. However, the national roadmaps planning the scale-up of electrolysis capacity increase the need for reliable operation. For instance, in France, the National Hydrogen Strategy targets 6.5 GW of installed electrolyzer capacity by 2030 [43]. To address these challenges, research efforts have focused on developing alternative cathode, electrolyte, and anode materials to improve long-term stability. Although advances in material properties have improved SOC performance [44], they alone are not sufficient

Thèse accessible à l'adresse : https://theses.insa-lyon.fr/publication/2026ISAL0017/these.pdf © [Z. Yazbeck], [2026], INSA Lyon, tous droits réservés

to ensure long-term reliability. Equally important is the implementation of effective health management strategies, which involve continuous monitoring of internal states, early fault detection and prognostics, to predict the Remaining Useful Life (RUL), and optimal control actions. Such approaches enable the prevention of irreversible degradation, ensuring optimal performance over the system lifetime, and supporting safe and efficient operation under varying conditions.

In this context, the present Ph.D. work has been undertaken with the aim of contributing to the development of advanced health management strategies for SOECs. This research is carried out as part of a collaboration between GENVIA, CEA-Liten in Grenoble, and the Ampère Laboratory in Lyon. This work was financed by the ANRT (Association Nationale de la Recherche et de la Technologie) and GENVIA, a company that develops innovative solutions for low carbon hydrogen production through SOEC technology, addresses large-scale decarbonization challenges. CEA-Liten, which is a major player in the research of new energy technologies, contributes its expertise in the design, modeling, and experimental characterization of advanced electrochemical systems. The Ampère Laboratory brings its knowledge in physical modeling consistent with diagnostics and prognostics of complex systems, parameter and state estimation, and methodological guidance.

1.4 Prognosis and Health management strategy

Solid oxide cells in electrolysis or fuel cell mode operate under rigorous thermal conditions and demanding availability targets. In this context, the maintenance strategy is essential for its availability, useful lifetime, cost, and safety. Classical maintenance approaches are commonly grouped into: (i) corrective maintenance, which repairs damage after failure has occurred, and leads to unplanned downtime, production loss, and high cost due to unexpected outages as shown in Figure 1.6; and (ii) preventive or planned maintenance, which schedules interventions periodically based on fixed time and the frequency of usage [45]. However, these approaches can be insufficient for systems degrading in time and strongly dependent on operating conditions, especially since shutting down the system for maintenance of damaged components is not straightforward and has a non-negligible effect on the degradation of solid oxide cell systems [46]. Thus, condition-based maintenance (CBM) and Predictive maintenance (PdM) address this limitation by using sensors and monitoring data to assess current and future health, by scheduling interventions only when needed. While CBM and PdM overlap, the difference is [47]:

- CBM is provided when fault is detected, or the health state of an asset degrades to a certain threshold using the past and current health condition of the system.

- PdM uses acquired data to track the degradation trend and estimate the remaining useful life (RUL), enabling optimal decision-making according to the past, current and estimated future trend of the system's state of health.

Thèse accessible à l'adresse : https://theses.insa-lyon.fr/publication/2026ISAL0017/these.pdf © [Z. Yazbeck], [2026], INSA Lyon, tous droits réservés

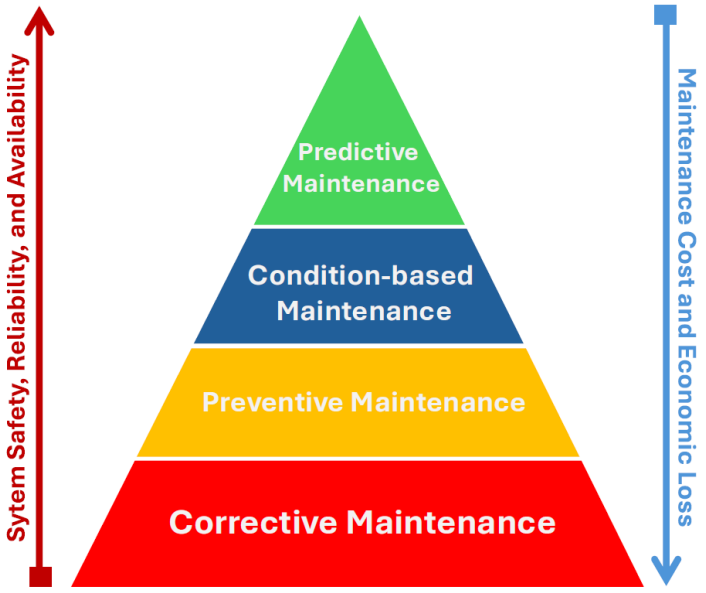

Figure 1.6: Pyramid of maintenance strategies [47].

Thus, CBM and PdM shift the focus from fixed intervals to signal-informed actions that reflect the evolving condition of the system.

1.4.1 PHM and the Maintenance Strategy Framework

The Prognostics and Health Management (PHM) process employs both CBM and PdM for complex systems. It transforms raw measurements from sensors into health indicators, detects and diagnoses faults, forecasts RUL, and further takes the optimal control actions based on the state of the system. PHM is typically organized as a layered workflow using standardized architectures [47], providing traceability from what is measured to what should be done and when. A general PHM architecture is presented in Figure 1.7 with a brief description of each layer.

- Layer 1: Data Acquisition
  It collects data in real-time from sensors.
- Layer 2: Data Manipulation
  It uses the collected data and processes it to extract features or to build health indicators.
- Layer 3: Health Assessment
  It determines the current state-of-health of the system and detects abnormalities in the behavior of the system.

Thèse accessible à l'adresse : https://theses.insa-lyon.fr/publication/2026ISAL0017/these.pdf © [Z. Yazbeck], [2026], INSA Lyon, tous droits réservés

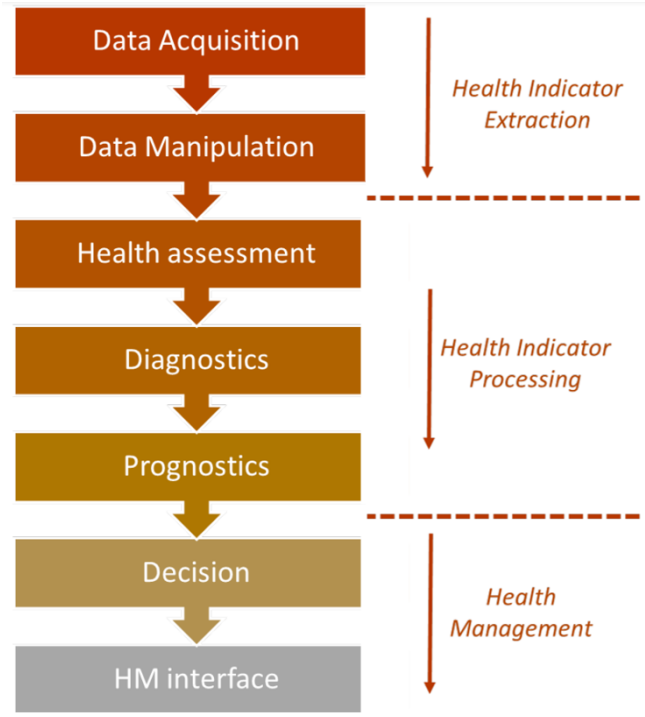

Figure 1.7: PHM Architecture [48, 49].

- Layer 4: Diagnostics
  It determines if the condition of the system has degraded, isolates and identifies the component that has been affected by the fault.

- Layer 5: Prognostics
  It predicts the future behavior of the monitored system by modeling the degradation trend in time.

- Layer 6: Decision
  It provides the recommended maintenance actions based on the state-of-health of the system.

- Layer 7: Human-Machine Interface (HMI)
  After receiving data from all previous modules, it presents diagnostics, prognostics, and recommendations to enable the interaction between the operator and the system to monitor and execute the resulting decisions.

Thus, PHM is a strategy coupling two main algorithms: diagnostics (detection/isolation of faults) and prognostics (RUL estimation and degradation prediction), integrated with decision-making to schedule maintenance and adapt optimal control policies. This strategy has matured across multiple industries and is now commonly used and often required in energy systems to increase the reliability of the system.

Thèse accessible à l'adresse : https://theses.insa-lyon.fr/publication/2026ISAL0017/these.pdf © [Z. Yazbeck], [2026], INSA Lyon, tous droits réservés

1.4.2 PHM approaches

Prognostics and Health Management (PHM) methods are commonly classified into three main categories (see Figure 1.8): data-driven, model-based and hybrid approaches. This classification reflects how prior knowledge about the system and data are used to detect faults, and to predict remaining useful life (RUL). An overview of the different categories is given below [50].

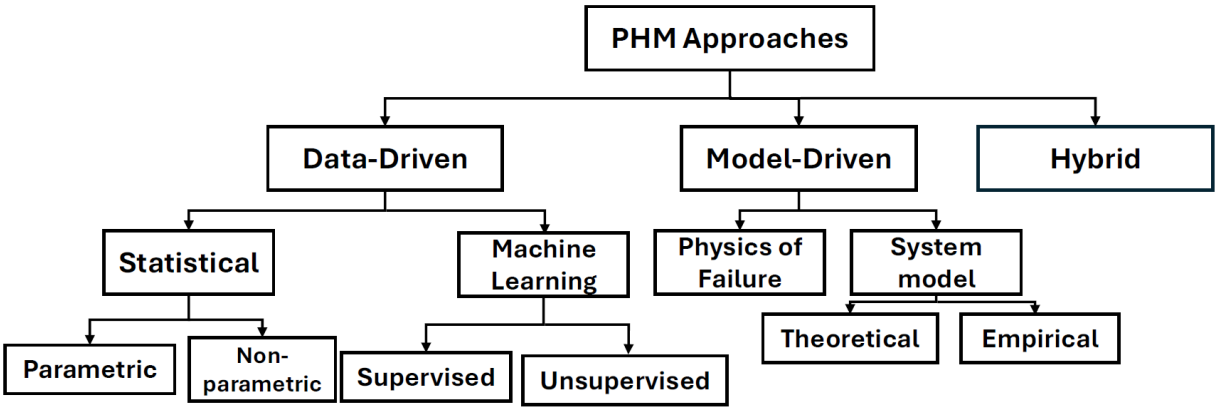

Figure 1.8: Classification of PHM approaches. Adapted from [50].

Data-driven approaches: These methods rely on data and treat the system as a black box where no physical models or domain knowledge is required. Using monitored and historical data, they learn the system behavior, extract health indicators, classify faults, and estimate RUL [50]. Two subcategories dominate:

- Statistical methods (parametric and nonparametric): It attributes statistical properties to the data, such as type of distribution, stationary or non-stationary, etc., to detect when a new observation deviates from the expected properties, declaring an abnormality. Parametric approach assumes a specific underlying distribution (e.g., normal, Weibull) and estimates its parameters to detect anomalies or predict RUL. On the other hand, non-parametric method offers more flexibility compared to the parametric approach by not assuming a specific distribution and estimating the density function, making them suitable for real-world data where statistical properties are unknown [50].

- Machine learning (supervised and unsupervised): It learns system behavior from data to predict and forecast its future performance, without requiring a physical model of the system. This approach can be formulated as a supervised learning problem, where data is labeled for a set of input to train models (e.g. neural networks, support vector machines, Gaussian processes, Bayesian networks, or hidden Markov models) to detect and isolate faults, and regress or estimate the RUL for new input data. In contrast, unsupervised learning is not guided by the target labels, rather it uses clustering methods to discover patterns

Thèse accessible à l'adresse : https://theses.insa-lyon.fr/publication/2026ISAL0017/these.pdf © [Z. Yazbeck], [2026], INSA Lyon, tous droits réservés

in data to classify it into different groups [51], like principal component analysis (PCA) or k-means [50].

Model-based approaches: In these approaches a model of the system is needed to explain how inputs, outputs, and degradation mechanisms interact and evolve over time [52].

- Physics of failure models capture specific mechanisms (e.g., Nickel migration modeling in Solid Oxide Cell [53]) via specific mechanistic models, but it requires solid knowledge of the active failure mechanisms. This methodology is usually applied offline, especially in the design stage, to optimize the design to ensure the expected performance of systems or products given certain reliability requirements.

- Phenomenological models (e.g., electrochemical-thermal SOEC/SOFC models using Nernst, Butler-Volmer, and porous-media transport) link inputs and operating conditions to outputs. Aging can be captured by introducing parameters varying in time, or explicit degradation states to model and track the performance of the system evolving in time.

Hybrid approaches: Hybrid PHM incorporates advanced features from both data-driven and model-based approaches to overcome the limitations of each. Different techniques can be used in this framework, such as Bayesian observers (e.g., Kalman filters [54, 55, 56] and particle filters [57]), and physics-informed neural networks [58]. These approaches use a physical model of the system to map the non-linear relationships between inputs and outputs, thereby requiring less data in the training phase. They bridge the gap between experimental measurements and the outputs of the physical model, in the case of physics-informed neural networks, or estimate and update the system states using measured outputs, e.g. in the case of Bayesian observers.

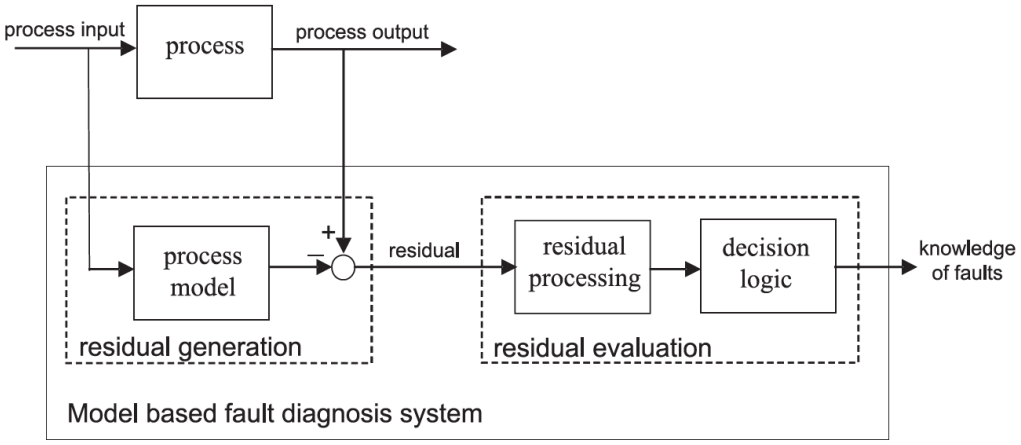

Figure 1.9: Schematic description of the model-based fault diagnosis scheme [59].

Moving from general approaches to practical implementation, model-based methods generally follow the workflow in Figure 1.9, particularly for diagnostics. Measured outputs are compared

Thèse accessible à l'adresse : https://theses.insa-lyon.fr/publication/2026ISAL0017/these.pdf © [Z. Yazbeck], [2026], INSA Lyon, tous droits réservés

with model predictions to generate residuals, these are then processed to extract relevant features, and evaluated using a decision logic (like thresholds, statistical tests, or classification rules) to interpret the residuals and determine the health state via the extracted indicators, and isolate the fault type. This workflow can also be applied to hybrid approaches and is the one adopted in this thesis; it will be developed in the following chapters.

1.5 Why PHM for SOEC systems?

PHM is important for SOCs in the fuel cell and electrolysis mode for many reasons:

- Strong dependence of degradation on the operating condition: Dominant SOEC aging drivers (such as contact resistance growth [60], nickel migration [53], nickel reoxidation [37], seal leakage [60], and temperature gradient [61]) can be accelerated by thermal, electrochemical, and mass transport conditions. Hence, calendar-based maintenance alone is neither sufficient nor aligned with the actual risk. A PHM strategy is therefore essential to extract and continuously track health indicators (e.g., voltage, overpotentials, partial pressures, thermal gradients, impedance measurements), enable early detection of deviations, and estimate the remaining useful life (RUL).

- Multiscale integration and coupled risks: Multiple SOEC/SOFC stacks are connected to form modules and plants with a balance of plant (BoP) components that provide gas handling, heat management, and power conversion. Thus, small anomalies at the cell/stack level can be amplified at the system scale. The layered architecture of PHM is well suited to fuse different measurements (electrical, thermal, flow/composition) and to propagate health assessments across different levels.

- Health-aware control, safety, and cost efficiency: By monitoring health indicators and detecting faults as they occur, irreversible degradation can be avoided or attenuated. PHM supports health-aware and fault-tolerant control, limiting harmful effects through countermeasures that account for the actual degradation trajectory and production costs [62]. This aligns with the CBM and PdM logic widely advocated in the fuel-cell literature and, in this work, is pursued via model-based monitoring using observer-based fault detection and parameter estimation for SOCs in electrolysis mode.

1.6 Degradations of SOEC systems

As mentioned earlier, solid oxide cells (SOCs), operating in either fuel cell mode (SOFC) or electrolysis mode (SOEC), are one of the most promising electrochemical technologies for decarbonization thanks to their high efficiency, fuel flexibility and reversible operation. However,

Thèse accessible à l'adresse : https://theses.insa-lyon.fr/publication/2026ISAL0017/these.pdf © [Z. Yazbeck], [2026], INSA Lyon, tous droits réservés

their widespread deployment depends on achieving application-specific lifetimes at acceptable cost. The practical challenge is to preserve the initial performance as long as possible while minimizing progressive degradation across the stack and the balance of plant components [37]. In practice, SOC degradation arises from the effects of use (electrochemical aging), time (calendar aging), and various permanent and/or accidental stress conditions, such as thermal cycling, load cycling, mechanical wear, imperfect conditioning, or poisoning, acting at different time scales and on different components [63].

The stack is the principal component of an SOC system, and the auxiliary subsystems serve the stack to enable its safe and efficient operation. The performance of the stack typically reflects the overall system health, and observed degradations are influenced by component design, materials, operating conditions, and BoP components interactions. Based on different studies [37, 60, 64], it is convenient to group the degradation drivers into two groups: intrinsic material degradation (driven by aging of the materials with time and usage) and extrinsic degradation (due to malfunctions or system-level faults). A structured view of degradations, presented in the next subsections, is thus essential to build a proper PHM strategy and to enable robust design, by clarifying how to intervene.

Although many degradation phenomena are common to SOFC and SOEC, the literature on SOEC is comparatively less extensive. Generally speaking, degradation phenomena in SOECs are very close to those in SOFCs. Some specific features exist in SOEC, and degradation rates are often higher compared to fuel cell mode [60]. The next subsection provides an overview of degradation mechanisms specific to SOECs, in line with the PHM objectives of this thesis.

1.6.1 Intrinsic degradation

Material degradation at the stack level due to aging typically appears as gradual performance decay rather than sudden failure caused by malfunctions at the system level. It arises from chemical, physico-chemical, electrochemical phenomena that are thermally activated in the electrodes, electrolyte, interconnects, seals, and their interfaces. In addition, mechanical phenomena can happen, such as cracking, or delamination of different components. Figure 1.10 summarizes different degradation phenomena that can be encountered at the cell and stack component levels. Representative issues include:

- **Fuel or hydrogen electrode (Ni-YSZ cermet):** The main source of degradation concerns microstructural changes in the electrode material, because of different phenomena such as nickel migration and coarsening, which are thermally activated and cause a reduction in the active sites where the reactions occur, thereby increasing polarization. Additionally, high steam contents and overpotentials can accelerate these changes [37, 53, 65, 66].

Thèse accessible à l'adresse : https://theses.insa-lyon.fr/publication/2026ISAL0017/these.pdf © [Z. Yazbeck], [2026], INSA Lyon, tous droits réservés

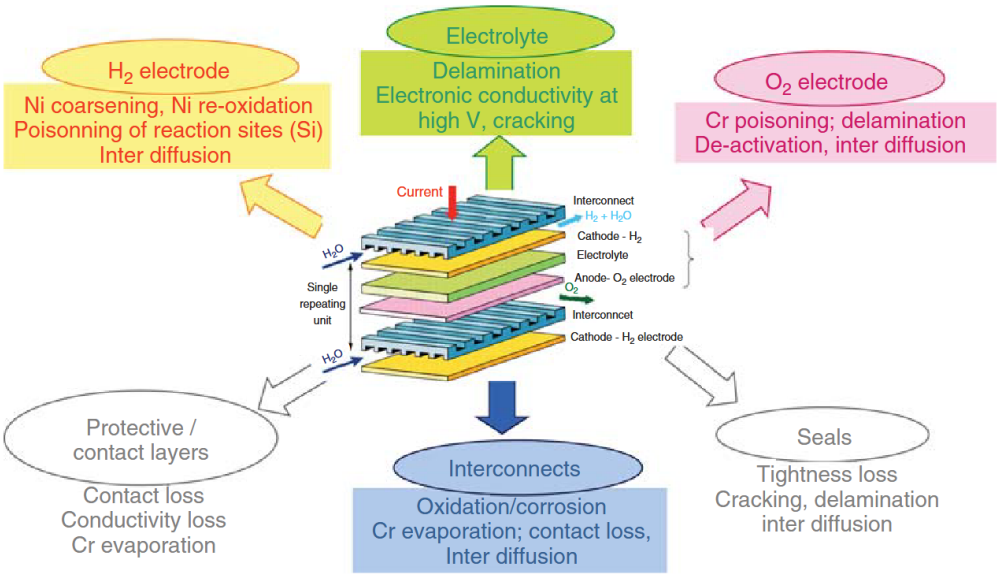

Figure 1.10: Different degradation phenomena that can occur at the cell and stack level [60].

- **Air or oxygen electrode:** In SOEC mode, anode polarization can accelerate surface segregation of oxygen electrode material, interdiffusion with the electrolyte, secondary phase growth, interfacial delamination linked to the formation of oxygen at this electrode, and electrode microcracking. In addition, humidity on the air side can further accelerate these processes [37, 65, 67].

- **Interconnects and contact layers:** These layers are not electrochemically active, but they are crucial for gas separation, mechanical support, and electrical continuity between adjacent cells in SOC stacks. An increase of contact resistance over time due to oxidation and interfacial reactions lead to contact loss, thus contributing to a gradual performance decay. Their degradation mechanisms are commonly grouped into two groups: i) solid-gas reactions with the surrounding atmosphere, and ii) solid-solid reactions at interfaces with the active cell, seals, or contact layers [37, 65, 66].

- **Seals:** Seal materials can change their microstructure over time (crystallize), suffer from thermal-expansion mismatch with other components, or creep leading to micro-cracks and can lead to secondary damage [37, 60].

- **Electrolyte:** The electrolyte may lose ionic conductivity over time due to microstructural changes, thereby increasing ohmic losses and promoting electrode-electrolyte delamination. In addition, interdiffusion occurs with the O_2 electrode, thus, a barrier layer is added between the electrolyte and the electrode [37, 60, 65, 68].

The interfaces between components are often the main areas where instabilities initiate and propagate [60]. These degradations related to aging effect are not recoverable or reversible and lead to a gradual decrease in performance. They are affected by many internal and external factors,

Thèse accessible à l'adresse : https://theses.insa-lyon.fr/publication/2026ISAL0017/these.pdf © [Z. Yazbeck], [2026], INSA Lyon, tous droits réservés

such as cell design and assembly, the quality of materials, operating conditions. Improving material durability can essentially mitigate these degradations. Consequently, extensive research in material science and mechanical engineering concerns understanding and mitigating aging-related degradations.

1.6.2 Degradation related to system operation

Apart from intrinsic SOEC degradation, malfunctions or problems at the system level, balance-of-plant components, control errors, or hardware defects can impose harsh operating conditions. These are extrinsic causes that accelerate overall degradation, if not detected and addressed, such faults can trigger irreversible damage, and cause a shortening in life and reduced efficiency. Some of these common problems are:

- **Internal and external leakage:**
  In SOEC, leakages can occur internally between anode and cathode or externally between the cell and its surrounding. They are typically driven by the difference in pressure and concentration between the cathode and anode sides, which promote the crossover of fuel or air through the electrolyte and affect the local stoichiometry [69]. Mitigation actions are generally ineffective in this case because the problem originates from design and material limitation, often at the sealant level. Leakages can cause cell degradation via multiple pathways; by increasing thermal gradients [70], degrading the material and changing the microstructure of the electrolyte and the oxygen electrodes [60, 71]. Additionally, leaks may induce fuel (steam in case of SOEC) starvation due to increased fuel use.

- **Steam starvation:** In SOEC operation, steam can be electrochemically consumed by the current more rapidly than what is provided, thus limiting the performance of the cell and causing an increase in overpotential. This can lead to high thermal gradient with a related possibility to damage the cell. Steam starvation has been reported to cause a damage in the electrolyte [65, 72]. Steam starvation is typically triggered by system-level problems, like leakage in pipelines, BoP malfunctions (mass flow controller, pumps, humidifiers), manifold maldistribution, or it can be caused by aggressive current transients. For this reason, it is treated as a fault in PHM frameworks. In addition to the immediate performance loss, the associated thermal hotspots accelerate aging of the fuel electrode microstructure [65] and can lead to further degradations if not corrected. In some transient cases, the fault may self-recover once the operating point stabilizes, but early detection and mitigation are essential to avoid irreversible damage [73].

- **Contamination/poisoning:**
  Sulfur, chromium, silica, chlorine and moisture related contaminants originating from fuels, balance-of-plant, or interconnects and seals can have a detrimental impact on the cell

Thèse accessible à l'adresse : https://theses.insa-lyon.fr/publication/2026ISAL0017/these.pdf © [Z. Yazbeck], [2026], INSA Lyon, tous droits réservés

performance, even at very low concentrations. They lead to an increase in polarization by affecting the active sites, and blocking the gas channel, thus reducing the electrode porosity [37, 74]. Mitigation relies on interconnect coatings and material selection, low-volatility sealing glasses, gas cleaning and filtration, and operating conditions that limit contaminant transport and reaction. [37, 60, 74]

- **Thermomechanical stress:** Thermal cycling is another significant source of aging for solid oxide cells, where heating up and cooling down the stack is considered as a weak point and unavoidable during the lifetime of SOEC, not only at the start or the shut down of the system, but also for scheduled maintenance and unexpected problems at the system level. In the literature, degradation resulting from these cycles is less studied compared to steady-state operation [60]. The complex assembly between the different layers of the ceramic cell: anode, cathode, and electrolyte, with the metallic interconnect plates and the glass ceramic sealants, makes the transition from the operating temperature (700-800 °C) to the room temperature critical and can lead to mismatches in thermal expansion coefficients (TECs), even when materials are carefully selected. Consequently, differences in TEC results in thermo-mechanical issues within the cell and at the stack level, particularly at the interface of different layers, and can cause cracks or even thermomechanical failure. Additionally, thermal cycling can affect the cell microstructure, especially at the electrodes, as well as the effective TEC, which can evolve over cycles. Further studies are required to understand the distribution of thermal stresses and their impact on degradation rates, to interpret the mechanisms of mechanical failure and to guide design optimizations, efforts that help in the cell/stack design and broaden potential applications [37, 60, 75, 76]. Poor thermal management also has a non-negligible role and can further increase temperature gradients across the stack, intensifying these stresses and accelerating degradation, therefore, beyond design optimization, robust thermal management and control are also required [77, 78].

- **Electrical loading:**
  Fast current ramps and operation away from the nominal point can increase activation and concentration overpotentials and drive the stack through different thermal regimes (detailed in Chapter 2, Section 2.1.4). This can create local temperature gradients and mechanical stresses that accelerate degradation. Without sufficiently fast system control, these conditions may lead to transient local hot spots. Mitigation is typically implemented at the system level by enforcing ramp-rate limits on stack current, adjusting reactant flow rates, and operating near the thermoneutral region to simplify thermal management and reduce thermal gradients [60, 73].

To conclude, the efforts to minimize performance loss in SOECs target both the understanding of material degradation mechanisms and improvements in stack design and assembly, which is

Thèse accessible à l'adresse : https://theses.insa-lyon.fr/publication/2026ISAL0017/these.pdf © [Z. Yazbeck], [2026], INSA Lyon, tous droits réservés

essential to mitigate cell aging. In addition to these physical advances, the operation of the stack within appropriate operation conditions contributes further to limit the performance decay. Thus, faults related to operating conditions must be detected, isolated and corrected quickly to avoid severe and irreversible damage.

At the system level, stack components and BoP subsystems are strongly coupled, so a single anomaly can escalate. Many operation induced faults are initially recoverable, but without timely intervention they may evolve into irreversible damage (e.g., interfacial cracking, delamination). The PHM strategy aims to design algorithms and models for monitoring and detecting operating faults as well as adapted mitigation strategies [37, 60, 73].

In summary, this degradation overview motivates PHM for SOECs where different health indicators can be used and are sensitive to aging (e.g., polarization resistance, impedance features, partial pressures) and to faulty operating conditions (e.g., starvation) to enable early detection and timely intervention and mitigation before irreversible damage occur [37].

1.7 Objectives of the PhD

The goal of this work is to develop a health management approach for Solid Oxide Electrolysis Cell (SOEC) at the system level, using model-based approaches, enabling internal state monitoring, early fault detection, and aging-aware monitoring. The approach relies on a physical model of the SOEC stack, with its parameters identified from experimental data through dedicated estimation techniques based on sensitivity analysis. Accurate modeling and parameter identification form the foundation for reliable state estimation, fault diagnosis, and prognostics. This methodology aims to enhance the reliability, safety, and performance of electrolyzers under dynamic operating conditions, while considering industrial constraints and large-scale deployment perspectives. The originality of this work lies in its application to SOEC stacks operating under different operating conditions, with a methodology that combines parameter estimation, fault detection, and aging-aware monitoring.
The specific objectives of this work can be defined as follows:

- Design and implementation of a model-based health management framework for SOEC stacks, enabling internal state estimation, early fault detection with aging-aware monitoring. This framework relies on a physical model, parameterized and validated using experimental data.
- Development of reliable parameter estimation procedures for identifying key electrochemical parameters of the SOEC stack from operational data. These procedures must account for dynamic operating conditions and measurement noises.
- Formulation of optimal experimental design (OED) strategies to maximize the information content of experiments, thereby improving practical identifiability of parameters to estimate

Thèse accessible à l'adresse : https://theses.insa-lyon.fr/publication/2026ISAL0017/these.pdf © [Z. Yazbeck], [2026], INSA Lyon, tous droits réservés

and the accuracy of model-based diagnostics.

- Detection and classification of starvation-related faults (hydrogen and steam starvation) through the analysis of estimated internal variables and polarization resistance, using experimental data from real SOEC stacks.

- Development of an integrated, aging-aware diagnostic framework that combines parameter updates of slowly varying state-of-health parameters with fault detection, including adaptive thresholds to separate slow degradation from abrupt faults, thereby improving fault isolation and supporting predictive maintenance decisions

This approach aims to enhance the reliability, efficiency, and safety of SOEC operation under real-world conditions, while addressing the requirements of industrial-scale deployment.

1.8 Publications and communications

The work presented in this Ph.D. thesis has led to the following publications and communications.
Journal paper:

- “System-level monitoring and diagnosis of starvation faults in solid oxide electrolyzers”, *International Journal of Hydrogen Energy*, 198 (2026): 152808 [79].

Conference papers and oral communications:

- “Sensitivity function-based Identification Of Solid Oxide Electrolyzer Parameters”, *2024 IEEE 63rd Conference on Decision and Control (CDC)*, pp. 3278–3284 [80].

- “Analyse de l’identifiabilité locale des paramètres d’un électrolyseur haute température à solide oxide”, SAGIP (Société d’Automatique, de Génie Industriel & de Productique), national French conference.

- Oral presentation at CNAM Paris (CT identif, SAGIP) on the parameter-estimation methodology developed during the thesis.

Patent submitted:

- “Starvation detection – Virtual sensor of inlet flow rate”, French patent application n°2503420, filed 1 April 2025 (GENVIA, CEA, CNRS, Université Claude Bernard Lyon 1, École Centrale de Lyon, INSA Lyon).

Thèse accessible à l'adresse : https://theses.insa-lyon.fr/publication/2026ISAL0017/these.pdf © [Z. Yazbeck], [2026], INSA Lyon, tous droits réservés

1.9 Manuscript outline

- **Chapter 2**
  This chapter gives an overview on SOEC designs at cell and stack levels, with materials used for different components, geometries, and operating regimes and how these choices affect electrochemistry, mass transport, and thermal management. It then sets the modeling framework used throughout the thesis and finish the chapter with a general scheme showing how different sub-models are coupled: electrochemical, mass transport, and thermal models.

- **Chapter 3**
  In this chapter, we first present the nonlinear state-space model that links inputs, states, parameters to estimate, and measured outputs and serves as the basis for sensitivity analysis and estimation. We then assess practical identifiability using sensitivity differential equations to quantify sensitivity and linear dependence between parameters. This analysis shows that some parameters have negligible influence on the measured outputs for the considered inputs. Based on this, we implement an estimation procedure combining gradient-based optimization with sensitivity assessment, and truncating the sensitivity matrix using singular value decomposition (SVD) to keep dominant singular directions, mitigating collinearity. The MATLAB function `fmincon` (using interior-point algorithm), the classical Levenberg-Marquardt algorithm (LM), the truncated Levenberg-Marquardt version (TLM), and the truncated Gauss-Newton method (TGN) are used and compared in simulation on synthetic cases where the parameters are known. The robustness is tested against different initial guesses and additive output noise to validate the methodology. The different methods are then applied to experimental data, where confidence intervals are computed to quantify the uncertainty of the estimated parameters. We also address optimal experimental design via nonlinear programming to generate informative inputs, introduce a sequential OED strategy based on a succession of short experiments in which the excitation is updated iteratively using the current parameter estimate, and propose an alternative OED method based on a predefined library with a genetic selection strategy that accounts for time-window and test-count constraints at lower computational cost.

- **Chapter 4**
  After model calibration in Chapter 3 using a systematic parameter-estimation approach and after defining the faults of interest, we design a Square-Root Unscented Kalman Filter to reconstruct and monitor internal partial pressures and stack temperature from limited measurements. Using stack voltage, outlet air temperature, and outlet hydrogen flow rate as measurements, adaptive thresholds are used to detect fuel-side starvation and to discriminate steam versus hydrogen starvation of solid oxide cells in electrolysis mode. It was also shown that this steam starvation fault (a decrease in the total fuel flow rate compared to

Thèse accessible à l'adresse : https://theses.insa-lyon.fr/publication/2026ISAL0017/these.pdf © [Z. Yazbeck], [2026], INSA Lyon, tous droits réservés

the nominal setpoint, leading to high steam conversion) causes a marked change in polarization resistance and a noticeable voltage variation. Whereas hydrogen starvation (a decrease in inlet hydrogen composition) has almost no effect on the total resistance, but internal partial pressure of reactants can be effectively reconstructed. The approach is validated under intended fault scenarios, demonstrating early, detection and accurate monitoring suitable for online deployment. The approach is then extended toward aging-aware monitoring by coupling the fast dynamic state estimation with slowly varying parameters due to aging considered as the state of health (SoH) parameters. These SoH parameters are updated using Pseudo-Random Binary Sequence (PRBS) current density excitation at different frequencies, with voltage used as measurement. This time-scale separation approach makes the monitoring framework more robust over long operating periods and is applied to 650 hours of experimental data under a fault-free assumption as a first validation case. The resulting evolution of the SoH estimates shows a small drift in the expected direction, while the effect on the model output and on the estimated states remains negligible, since the considered window is not long enough for significant degradation to develop.

- **Conclusion**
  It synthesizes results across the thesis, discusses limitations, and outlines perspectives related to the methodology developed in this thesis, and to additional work that can be done to have a more effective health management strategy.

Thèse accessible à l'adresse : https://theses.insa-lyon.fr/publication/2026ISAL0017/these.pdf © [Z. Yazbeck], [2026], INSA Lyon, tous droits réservés

Thèse accessible à l'adresse : https://theses.insa-lyon.fr/publication/2026ISAL0017/these.pdf © [Z. Yazbeck], [2026], INSA Lyon, tous droits réservés

Chapter 2

SOEC technology

Contents

2.1 Solid Oxide cells 24
2.1.1 Electrochemical reactions: SOEC 25
2.1.2 Materials for SOC components 26
2.1.3 Cell Design 26
2.1.4 Cell thermal regimes 29
2.2 Modeling of SOECs 31
2.2.1 Fundamentals of SOEC modeling 31
2.2.2 State of the art of SOEC modeling 33
2.2.3 Positioning of the present work: 35
2.3 Mathematical model 36
2.3.1 Mass transport and conservation 36
2.3.2 Electrochemical Model 40
2.3.3 Thermal Balance model 44
2.4 Model summary 45
2.5 Time integration 46

2.1 Solid Oxide cells

Solid oxide cells (SOCs) are high-temperature electrochemical energy-conversion devices. A cell consists of a dense ceramic electrolyte sandwiched between two porous electrodes. When operating at high temperatures between 600 and 1000 $^{\circ}C$, the ceramic electrolyte becomes conductive to oxygen ions with very low electronic conductivity [81, 82]. This operating temperature

Thèse accessible à l'adresse : https://theses.insa-lyon.fr/publication/2026ISAL0017/these.pdf © [Z. Yazbeck], [2026], INSA Lyon, tous droits réservés

provides also several advantages: (i) high efficiency, (ii) reversibility, allowing the cell to function in both electrolysis and fuel cell modes, (iii) fuel flexibility, (iv) the use of inexpensive catalysts, and (v) the possibility to recover useful heat which can be reused in cogeneration or hybrid energy systems [60, 83, 84]. Figure 2.1 illustrates the structure of the SOC in steam electrolysis mode, showing the individual electrodes with their respective half-reactions, as well as the complete single cell.

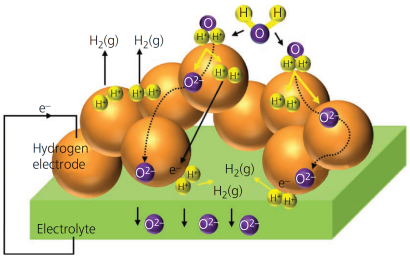

(a) Hydrogen electrode (cathode).

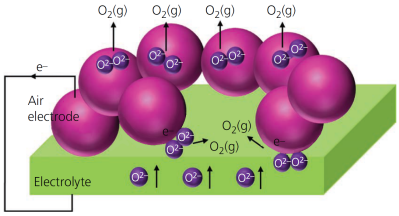

(b) Air electrode (anode).

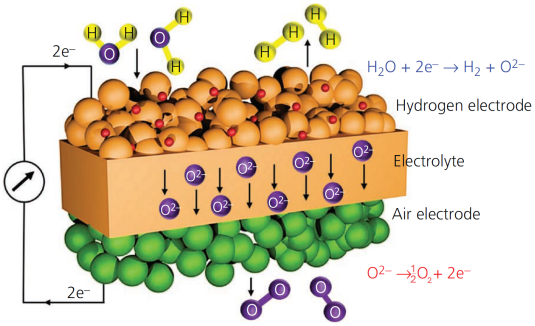

(c) SOEC single cell and its compartments.

Figure 2.1: SOEC individual electrodes and complete cell [85].

2.1.1 Electrochemical reactions: SOEC

In solid oxide electrolysis, the electrochemical reaction is driven by superheated steam flowing over the cathode with a sufficient potential difference applied across the electrodes to force the reaction forward. At the cathode, water molecules in gaseous phase are reduced at the interface between the cathode and the electrolyte, producing hydrogen gas and oxygen ions (Figure 2.1). The oxygen ions migrate through the dense electrolyte and are oxidized at the interface between the anode and electrolyte to form oxygen gas. Meanwhile, the hydrogen produced at the cathode remains mixed with the residual steam [60, 86]. The corresponding half-cell and overall reactions are expressed as follows:

$$\text{Cathode:} \quad H_2O_{(g)} + 2e^- \rightarrow H_{2(g)} + O^{2-} \tag{2.1a}$$

$$\text{Anode:} \quad O^{2-} \rightarrow \frac{1}{2}\,O_{2(g)} + 2e^- \tag{2.1b}$$

$$\text{Overall:} \quad H_2O_{(g)} \rightarrow \frac{1}{2}\,O_{2(g)} + H_{2(g)} \tag{2.1c}$$

Thèse accessible à l'adresse : https://theses.insa-lyon.fr/publication/2026ISAL0017/these.pdf © [Z. Yazbeck], [2026], INSA Lyon, tous droits réservés

2.1.2 Materials for SOC components

The operation of SOC depends on key performance requirements at the cell level. The porous electrodes must provide (i) high electronic conductivity and adequate catalytic activity to sustain the electrochemical half-reactions, (ii) sufficient porosity to support mass transport of steam and gaseous products with limited pressure drop, and (iii) chemical and mechanical stability [60, 81]. Furthermore, the electrolyte must exhibit high oxygen ion conductivity with negligible electronic leakage within the 600-1000°C, ensure gas-tightness to avoid cross-over, and remain stable under operating conditions [82, 87]. Ultimately, matched thermal expansion and mechanical integrity are required between the different layers of the SRU, in order to limit the thermo-mechanical stresses during operation [81, 84].

Accordingly, some materials have become standard in planar SOCs. For fuel electrodes, nickel (Ni) ceramic cermets (e.g., Ni-YSZ or Ni-GDC) combine the electronic conduction and H_2/H_2O electrocatalysis of Ni with an ion-conducting ceramic phase, maximizing reaction sites at the electrode-electrolyte interface. On the air side, perovskite oxides are prevalent: LSM-based composites with YSZ are widely used at higher temperatures, whereas mixed-conducting LSCF-GDC composites help reduce polarization losses toward intermediate temperatures. Finally, the most common electrolyte is 8 mol% yttria-stabilized zirconia (8YSZ), thanks to its O^{2-} conductivity and thermochemical stability at high temperatures [60, 65, 81, 84, 87].

2.1.3 Cell Design

Different designs of solid oxide cells exist, with the planar and tubular configurations being the most commonly employed today [88] (see Figure 2.2).

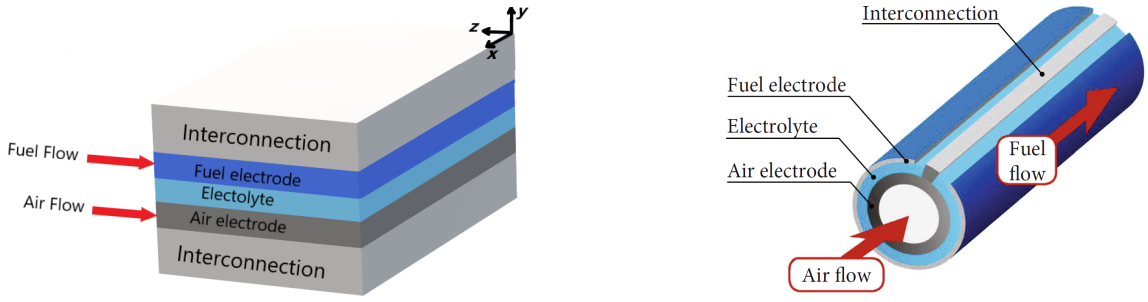

(a) Planar Configuration.

(b) Tubular Configuration [89].

Figure 2.2: Schematics of (a) planar and (b) tubular designs of SOC.

The tubular design of solid oxide cells provides high mechanical strength and simple sealing process, but offer lower power densities compared to the planar cell [88]. In contrast, the planar configuration shows better performance, with advantages such as simpler fabrication and reduced ohmic resistance at intermediate operating temperatures (500-800 °C). However, the

Thèse accessible à l'adresse : https://theses.insa-lyon.fr/publication/2026ISAL0017/these.pdf © [Z. Yazbeck], [2026], INSA Lyon, tous droits réservés

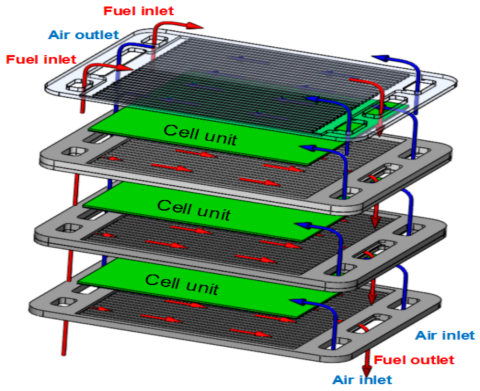

Figure 2.3: Schematic of a planar SOEC stack. Adapted from [90].

complexity lies in the sealing process required to ensure reliable gas tightness [88]. In the planar configuration, the cells are assembled with metallic interconnects to increase power capacity, and are sealed to prevent gas leakage. The interconnects enable the distribution of gases to the electrodes in various flow configurations (such as co-flow in Figure 2.2, counter-flow in Figure 2.3, or cross-flow), ensure sealing, and connect the current collectors of the electrode to the external electric circuit. The assembly of the cell with its interconnects forms the single repeating unit (SRU). To scale up to higher power capacities, several SRUs (on the order of a few tens of watts each) are connected in series to form a stack (up to a few tens of kW). Multiple stacks assembled together form a SOC module, in the hundred-kilowatt range. At this stage, a balance of plant (BoP) is required to manage gas and current flows, as shown in Figure 2.4. Ultimately, a set of modules, together with the BoP, constitutes a megawatt-scale system. Examples of such MW-scale SOC installations are either under construction or in planning [91, 92].

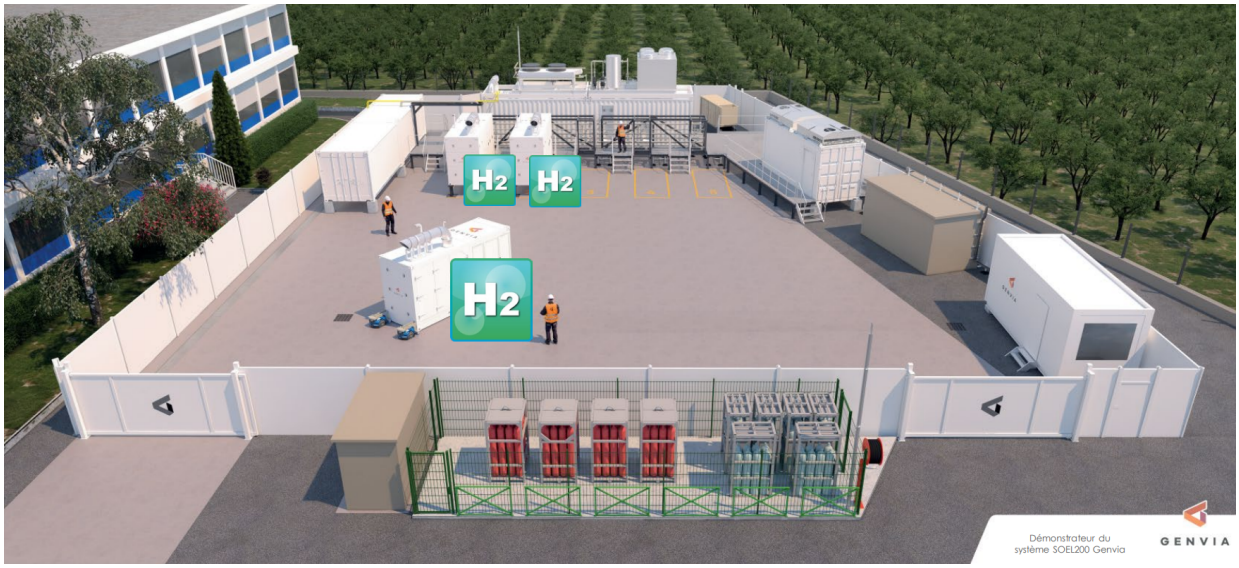

Figure 2.4: SOEL200 Genvia pilot project (300 kW, 200 kg H_2/day), an industrial-scale SOEC demonstrator [93].

Thèse accessible à l'adresse : https://theses.insa-lyon.fr/publication/2026ISAL0017/these.pdf © [Z. Yazbeck], [2026], INSA Lyon, tous droits réservés

As mentioned before, one of the most important advantages of planar cell configuration is the mechanical robustness; this is ensured by a supporting layer. Thus, according to the supporting layer, SOECs can be classified into different architectures [60, 88], as shown in Figure 2.5:

1. Electrolyte supported Cell (ESC): The electrolyte serves as the mechanical support and electrodes are deposited onto it on both sides as thin films. The high electrolyte thickness increases the ohmic resistance, hence higher temperatures need to be used to achieve good performance [81]. Higher temperatures also demand special materials for the interconnects such as $LaCrO_3$ and Cr-based alloys [60]. These materials are expensive and difficult to manufacture. Nevertheless, the ESC architecture is under development to improve performance and durability.

2. Cathode supported cells (CSC): The issue of electrolyte resistance was overcome by decreasing its thickness and making the hydrogen electrode the support layer, which increases the concentration and activation overpotential due to the increase in fuel diffusion resistance. As a result of the thinner electrolyte, lower operating temperatures are required, higher current densities can be obtained, and a larger choice of materials for interconnects exists. However, the main drawback of the electrode supported cell architecture is the difficulty for the reactants to reach the active sites due to the longer path through the thicker electrode [81].

3. Metal supported cells (MSC): An externally supported cell, electrochemically inactive metal serves as the mechanical support onto which the ceramic components of the cell are deposited as thin layers. It provides structural robustness, high tolerance to rapid thermal cycling, and good electrical and thermal conductivity, but it also suffers from oxidation at high temperatures, generally moderate electrochemical performance, thermal-expansion mismatch between cell parts, and a high fabrication cost [81].

Today, the most commonly used architectures are the hydrogen electrode and the electrolyte supported configurations [94, 95].

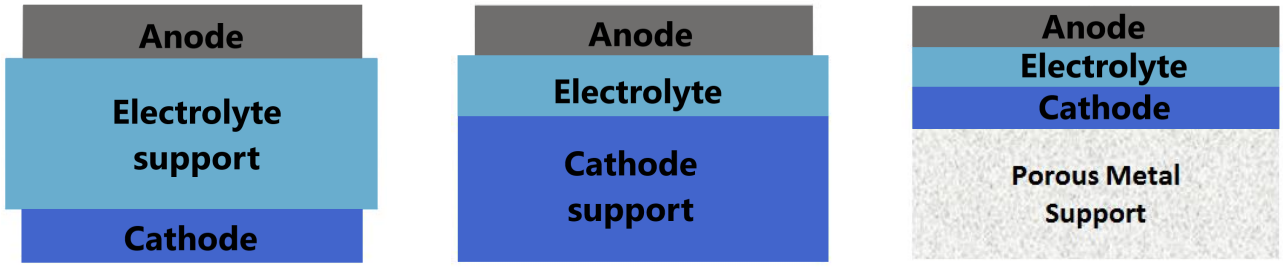

(a) ESC (b) CSC (c) MSC

Figure 2.5: Various types of SOEC configurations [88].

Thèse accessible à l'adresse : https://theses.insa-lyon.fr/publication/2026ISAL0017/these.pdf © [Z. Yazbeck], [2026], INSA Lyon, tous droits réservés

2.1.4 Cell thermal regimes

In electrolysis mode, the energy consumed by the cell to drive the electrochemical reactions is provided by electrical (ΔG) and thermal ($T\Delta S$) energy, as presented in Equation (1.2). Thus, depending on the balance between these two contributions, three thermal regimes can be distinguished for high-temperature electrolyzers: endothermal, thermoneutral, and exothermal, as presented in the Figure 2.6.

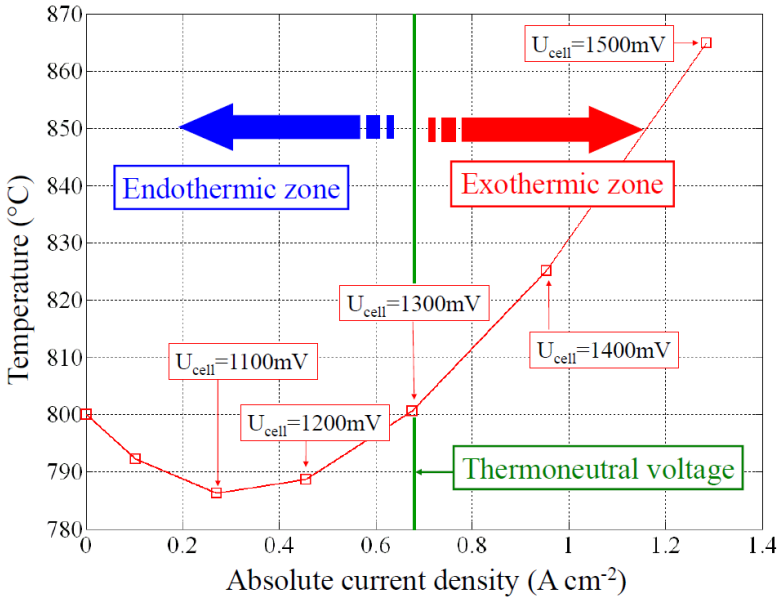

Figure 2.6: Operating regimes of solid oxide electrolysis: endothermal, thermoneutral, and exothermal. Adapted from [87].

The electrolysis process changes the system entropy ΔS, and the heat balance can be written as:

$$\Delta Q = T\Delta S = -\left(\frac{I}{2F}\Delta H(T) - UI\right) \tag{2.2}$$

where $\Delta H(T)$ is the change in enthalpy of the electrolysis reaction at temperature T, F is the Faraday constant, I the current density, and U is the cell voltage.
The reaction enthalpy is expressed in terms of the enthalpies of formation ΔH_f of the species involved:

$$\Delta H(T) = \sum \Delta H_f^{\circ}(\text{products}) - \sum \Delta H_f^{\circ}(\text{reactants}), \tag{2.3}$$

which for the water splitting reaction in the gaseous phase is:

$$\Delta H(T) = \Delta H_f^{\circ}(\mathrm{H_2}) + \frac{1}{2}\Delta H_f^{\circ}(\mathrm{O_2}) - \Delta H_f^{\circ}(\mathrm{H_2O}). \tag{2.4}$$

Thèse accessible à l'adresse : https://theses.insa-lyon.fr/publication/2026ISAL0017/these.pdf © [Z. Yazbeck], [2026], INSA Lyon, tous droits réservés

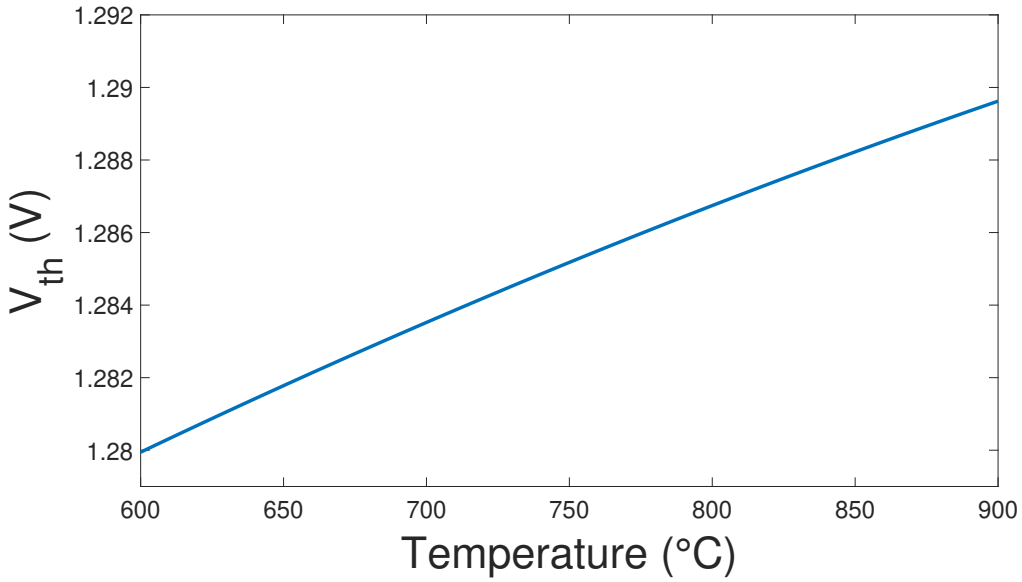

Figure 2.7: Thermoneutral voltage in a function of temperature.

In *thermoneutral mode*, the cell operates at the thermoneutral voltage V_{Th}, where it remains thermally stable ($\Delta Q = 0$). In this case, the heat generated by internal irreversibilities is used to supply the energy required for water splitting. In other words, the enthalpy of reaction ΔH is entirely provided by the electrical work ΔG, and the contribution of entropy is negligible. Consequently, the cell operates at thermal equilibrium with an electrical-to-hydrogen conversion efficiency of 100% $\left(\eta = \Delta H/\Delta G = 1\right)$.
The corresponding thermoneutral voltage V_{Th} is given by:

$$V_{Th}(T) = \frac{\Delta H(T)}{2F}, \tag{2.5}$$

At typical SOEC operating temperatures (e.g., between 600-900°C), the thermoneutral potential is between 1.28 V and 1.29 V as shown in Figure 2.7, as the enthalpy change of the reaction remains nearly constant. This operating mode is particularly important for SOECs, as it avoids the need for external heat sources or heat exchangers.

In the *exothermal mode* ($\Delta Q > 0$, and $V > V_{Th}$), the electrical energy input exceeds the enthalpy of reaction. This results in an electrical efficiency below 100%, and excess heat is generated inside the cell. This heat can be recovered and reused within the system, for instance to preheat inlet gases. Exothermal operation also enables higher current densities as shown in Figure 2.6, thereby reducing the required cell area and overall system size. However, the continuous release of excess heat can accelerate degradation and shorten the lifetime of the system [60].

Conversely, in the *endothermal mode* ($\Delta Q < 0$, and $V < V_{Th}$), the electrical energy input is

Thèse accessible à l'adresse : https://theses.insa-lyon.fr/publication/2026ISAL0017/these.pdf © [Z. Yazbeck], [2026], INSA Lyon, tous droits réservés

lower than the enthalpy of reaction. The deficit must be supplied as external heat to maintain the system temperature. In this regime, the electrical-to-hydrogen conversion efficiency exceeds 100%, since part of the reaction enthalpy is provided by heat. Endothermal operation also minimizes long-term degradation due to operation at lower power densities as shown in Figure 2.6, and requires efficient external heat management [60].

2.2 Modeling of SOECs

2.2.1 Fundamentals of SOEC modeling

There are different models of SOEC available in the literature, but the choice of model depends on the purpose and objectives of the study. There are multiple ways to classify the approaches used for modeling, with common categorizations based on type, state, and scale or dimension, as illustrated in Figure 2.8. Regarding the type, a fundamental distinction is made between empirical (black-box) or semi-empirical models and phenomenological models [96, 97]. Black-box models do not require full understanding of the underlying physical phenomenon and relationships between the inputs and outputs. This method has gained popularity in recent years with the availability of more computational resources. However, calibration of these models requires large amounts of experimental data over a wide range of conditions, and it is often specific to the studied system. By contrast, phenomenological models are based on physicochemical laws and first principles governing the process, in order to develop relationships between the inputs, outputs, and parameters [98]. Another common distinction can be made between dynamic models and steady-state or stationary models. Dynamic models provide information about temporal evolution of states, with the transient behavior essential for real-time operation, safety considerations, control strategies, etc. Whereas, stationary models are used to predict the system efficiency, performance, and to optimize the operating and design parameters of an SOEC [97].

Additionally, based on modeling level, SOEC models can be classified into microscale and macroscale models. At the microscale level, modeling focuses on the electrodes to study the effects of the microstructural parameters of porous electrodes, such as layer thickness, porosity, mean particle diameter, and ionic or electronic phase composition. This type of models is essential for microstructural optimization by analyzing the reaction and transport processes in porous electrodes [98]. On the other hand, macroscale models can be divided into cell-level, stack-level, and system-level models, which includes SOEC stacks and the balance of plant (BoP) components such as pumps and heat exchangers [96, 97, 98]. These models are used in general to improve efficiency, enable control design, enhance safety by supporting fault detection algorithms, and to optimize system architecture and operating conditions.

In cell-level modeling, the main objective is to model the transfer of mass, heat and charge transfer, with electrochemical reactions in the SOEC. Such models help to analyze the perfor-

Thèse accessible à l'adresse : https://theses.insa-lyon.fr/publication/2026ISAL0017/these.pdf © [Z. Yazbeck], [2026], INSA Lyon, tous droits réservés

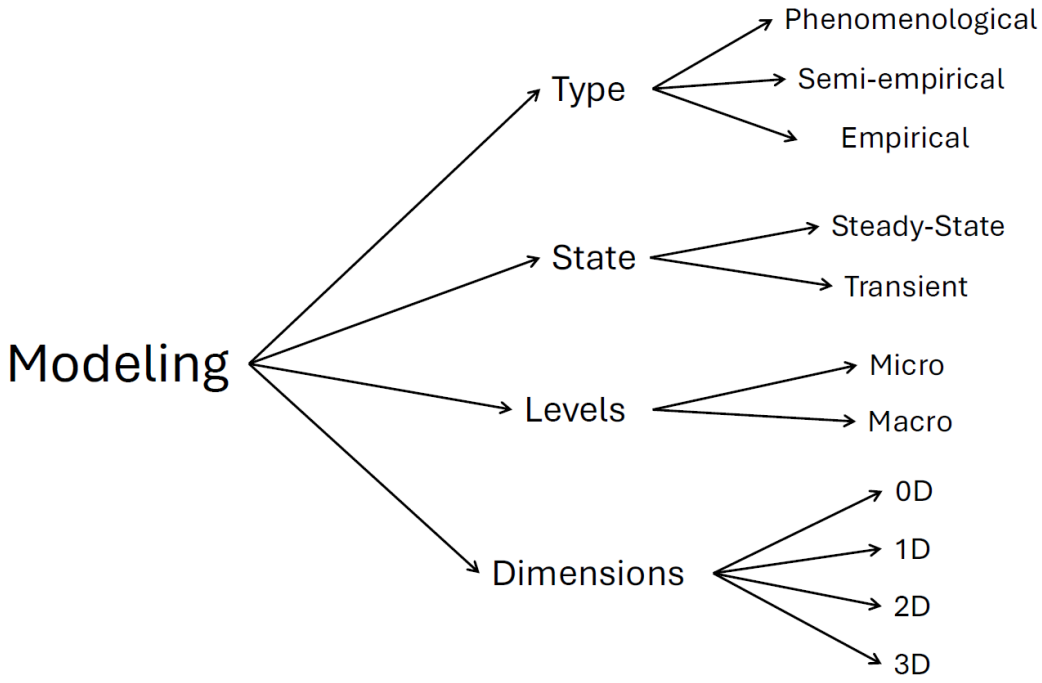

Figure 2.8: General model categories [97].

mance of the cell under various operating conditions and to quantify the sensitivity of certain cell-level parameters on loss mechanisms, thereby helping to optimize cell design and operating conditions [84, 87]. Depending on the geometry of the model, the distribution of species concentrations, current density, overpotentials and other parameters can be resolved along one or more directions of the cell. On the other hand, stack-level models often adopt simplifying assumptions in the geometry that sacrifice some details at the cell level. These models can simulate the behavior of the SOEC stack, which consists of multiple cells connected in series together, and can provide valuable information to refine the design to homogenize the temperature, current density and species distributions in order to maximize stack efficiency and limit aging [99]. This is typically done by integrating the cell-level model with the other components of a single repeating unit (SRU) and modeling its thermal, mass transport, and electrochemical behavior; once established at the SRU level, the SOEC stack can be simulated with multiple SRUs [100]. Finally, the system-level model neglects details on the stack behavior and focuses on the interaction between the output of the stack-level model and BoP [54, 101, 102].

In addition to the categories above, models are also classified by geometric dimensionality: zero-dimensional (0D, lumped) [54, 103, 104], one-dimensional (1D; through-plane or along-channel) [99, 105, 106], two-dimensional (2D) [87], and three-dimensional (3D/CFD) [107]. The increase in dimensionality resolves spatial gradients in temperature, composition, and current density, but it has a higher computational cost. Conversely, reduced-order 0D/1D models are well suited to parametric studies, control-oriented development, real-time application and system-level integration [54, 103, 104].

Thèse accessible à l'adresse : https://theses.insa-lyon.fr/publication/2026ISAL0017/these.pdf © [Z. Yazbeck], [2026], INSA Lyon, tous droits réservés

2.2.2 State of the art of SOEC modeling

In this section, we review the modeling approaches for SOECs/SOFCs with clarification on different formulations used at the cell, stack and system levels. The literature ranges from detailed spatial descriptions to more simplified models and data-driven-based models designed for fast computation.

High-fidelity models based on distributed-parameter models describe thermo-electrochemical behavior at cell and stack levels. One and two-dimensional formulations resolve mass, charge, and heat transport along channels and through porous layers to compute local current density, species distributions, and temperature fields. Three-dimensional CFD-electrochemical stack models further resolve manifolds and cells, capturing coupled flow, temperature, and electrochemistry, as in [108] for a 60 SOEC cells and [107] for a 4 SOFC cells with external manifolds. These studies show the importance of the manifold and channel design to ensure a uniform gas distribution and current density. In these works, the electrochemical model at the macro level is employed, and when used as representative for a specific test bench, such models require calibration with experimental data. However, their complexity and computational cost limit direct deployment for real-time and control/diagnostic applications.

To go beyond macro-level modeling while maintaining the single-repeat-unit (SRU) description, a multiscale framework was developed in [109] to inform the macro model with microscale information. The objective of this work is to link the electrode microstructure and local reaction mechanisms to the SRU model. The approach combines synthetic or tomographic 3D microstructures, microscale electrode models with elementary kinetics and transport, and a 2D macro-scale SRU model developed by Laurencin et al. in [87]. The Electrode-scale model is solved in COMSOL, and the SRU macroscopic model is implemented in Matlab or COMSOL depending on the geometry. Apparent macro parameters (which are the exchange current densities, pressure exponents, activation energies) are identified so that the macro-scale activation losses at the SRU model reproduce those obtained from micro-scale electrode-level simulations, and adjusted with polarization and impedance measured data. Thus, even at this level of detail, effective parameter identification and calibration remain necessary.

The mentioned macro-level 2D thermo-electrochemical SRU of [87] is often adopted as a modeling basis. The solution strategy is presented in Figure 2.9 and follows a coupled scheme with two loops. First, in the electrochemical loop, the SRU is discretized along the channel, local mass balance equations propagate gas flows, and the local current densities are iterated until the voltage constraints (equipotentiality across voltage meshes) are met and the current densities and compositions are stable. The resulting compositions then feed the thermal loop with distributed thermal sources to update the 2D temperature field. Both loops are repeated until global convergence. This model has been used in later studies with some minor adaptations.

In the dissertation [110] for instance, a variant of this 2D thermo-electrochemical model is used to represent the stack model at the system level. It models a stack comprising 2500

Thèse accessible à l'adresse : https://theses.insa-lyon.fr/publication/2026ISAL0017/these.pdf © [Z. Yazbeck], [2026], INSA Lyon, tous droits réservés

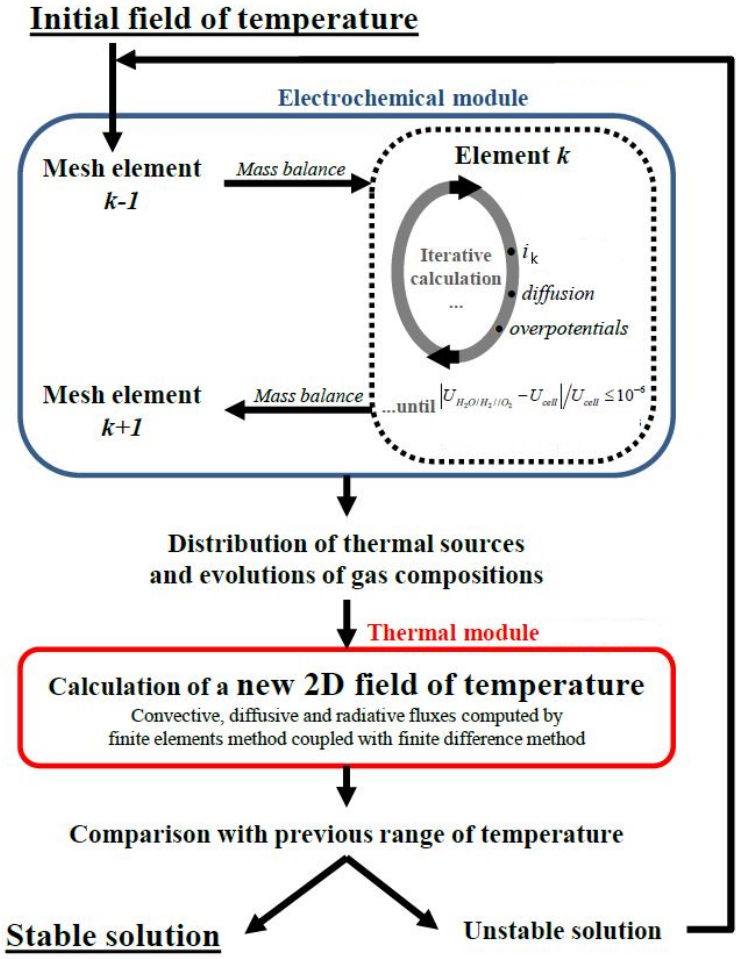

Figure 2.9: 2D model summary and architecture. Adapted from [84].

cathode-supported, cross-flow planar cells, creating a 300 kW electrolyzer stack module, where a single SRU is assumed representative of all cells. The model is similar to [87], with one main difference that it solves along the channel mass and energy balances dynamically, whereas [87] reports steady-state equations. Then the model is calibrated and validated on a 6-cell short stack in both electrolysis and fuel-cell modes and shows a good agreement for steady-state and time-varying profiles. In a similar work but with different scope, the author in [105] developed a 1D dynamic reversible SOC stack with 130 cells, experimentally calibrated and validated to analyze and study thermal safety during mode switching.

Other simplified formulations are also used at stack level. Murshed et al. in [111] presents two 0D SOFC stack models that do not take into account the spatial resolution. The first model uses a single lumped thermal state and a simple voltage law with fitted exchange current density and a constant limiting current density for concentration losses. The second model refines the thermal part by assigning separate lumped temperatures to the solid, interconnect, fuel stream, and air stream, forming four thermal states, while keeping the same 0D electrochemistry model.

A hierarchical modeling approach is presented in [112] by Sorrentino et al., where a 1D

Thèse accessible à l'adresse : https://theses.insa-lyon.fr/publication/2026ISAL0017/these.pdf © [Z. Yazbeck], [2026], INSA Lyon, tous droits réservés

steady-state SRU model (along-channel) is used as a high-fidelity layer, where the thermal submodel contains three thermal equations (solid, air, fuel). Electrochemical parameters are identified and validated with experimental data and literature benchmarks. A lumped dynamic stack model is further used as a the control-oriented model with a single thermal state and a voltage relation fitted to a transient dataset generated by the 1D model due to a lack of experimental transient data.

A 0D model with a single thermal state and a voltage law that aggregates overpotentials into a temperature-dependent total resistance, is presented by Dolenc et al. in [54]. This model is used for prognosis, where the total resistance is modeled with a linear drift to capture gradual degradation, and estimated online with a two-stage Kalman filtering, enabling remaining-useful-life prediction on experimental data from a 10 kW SOFC stack. The results in [102] adopt a similar 0D model and couple it with features extracted from impedance measurements, like ohmic and polarization resistance using an equivalent circuit model, to update degradation in real time, supporting diagnosis of fuel starvation and improving aging tracking on a 6-cell short stack in fuel cell mode.

On the data-driven side, in Chapter 4 of the dissertation [113], a steady-state feed-forward neural network is trained on IV curves and long-term data for a 5-cell stack. Additionally, dynamic recurrent neural networks are developed for two stacks using an input vector composed of current density, flows, temperatures, and output feedback to reproduce transients with low error on independent tests. These models can track aging trends when time or health indicators are included, but they require representative datasets and have limited extrapolation capability.

2.2.3 Positioning of the present work:

The objective of this work in this thesis is to develop a model-based system health management strategies, with emphasis on fault detection and prognosis, in a form suitable for real-time execution. To this end, a 0D stack model is therefore adopted with dynamic mass and thermal balances. The selected electrochemical model preserves sufficient detail to capture fuel utilization (steam conversion in SOEC mode), and diffusion effects through effective transport and mass-balance dynamics. However, the thermal model is limited to a single dynamic energy equation because detailed geometric information (such as convective areas, hydraulic diameters) is not available. This modeling approach yields a set of identifiable states and parameters that are well suited for online monitoring and diagnostic purposes, while maintaining the computational efficiency necessary for real-time implementation.

Thèse accessible à l'adresse : https://theses.insa-lyon.fr/publication/2026ISAL0017/these.pdf © [Z. Yazbeck], [2026], INSA Lyon, tous droits réservés

2.3 Mathematical model

A 0D dynamic model was developed in MATLAB, where the spatial distribution of concentrations and temperatures is not taken into account. This 0D model can be extended to a 1D or 2D model to get the distribution of the current densities and the flows in the channels using the equipotential property along the cell as in Figure 2.9 [87]. The model is general and applies to both fuel cell and electrolysis modes. In fuel cell mode, a positive current density is used, while in electrolysis mode, the current density is negative to reflect the reverse electrochemical reaction.
The model while simplified, is based on material and thermal balances and includes several assumptions. Therefore, its formulation follows the standard assumptions used in SOEC/SOFC modeling:

1. The pressure drop along the gas channels has been assumed to be negligible: atmospheric pressure has been considered [87].
2. Ideal gas behavior is assumed due to the high operating temperature and atmospheric pressure [100].
3. The stack is modeled as a single repeating unit (SRU), assuming uniform behavior across all cells for scalability, so the stack voltage is equal to the number of cells multiplied by the cell voltage.
4. The outlet air temperature is considered to be representative of the overall stack temperature, consolidating the anode and cathode temperatures into a single value, denoted T.

2.3.1 Mass transport and conservation

Gas Transport in SOEC Electrode: Dusty-Gas Model

Assumption: The mass transfer in an SOEC porous electrode (i.e. in the y direction which is through the electrode thickness, as shown in Figure 2.2a) can be adequately represented by the Dusty-gas model [60, 114], which is widely employed in SOEC models [84, 87, 115]. It combines the Knudsen transport as well as the molecular diffusion for a mixture of several gas species [60, 114]. Based on this transport model, the concentration profile through the porous electrode, expressed along the through-electrode direction (the y-axis for the planar cell configuration presented in Figure 2.2a), is given by:

$$\frac{N_i}{D_{i,k}^{eff}} + \sum_{j=1,\, j\neq i}^{n} \frac{y_j\, N_i - y_i\, N_j}{D_{i,j}^{eff}} = -\frac{P}{RT}\,\frac{dy_i}{dy}, \tag{2.6}$$

where y_i and N_i are the molar fraction and molar flux, respectively, of species $i \in \{H_2O, H_2, O_2, N_2\}$, and P the total pressure ($= 1\,\text{atm}$). $D_{i,j}^{\text{eff}}$ and $D_{i,k}^{\text{eff}}$ are the effective Knudsen coefficient and binary diffusion coefficient, respectively, according to the electrode microstructure parameters, *i.e.*,

Thèse accessible à l'adresse : https://theses.insa-lyon.fr/publication/2026ISAL0017/these.pdf © [Z. Yazbeck], [2026], INSA Lyon, tous droits réservés

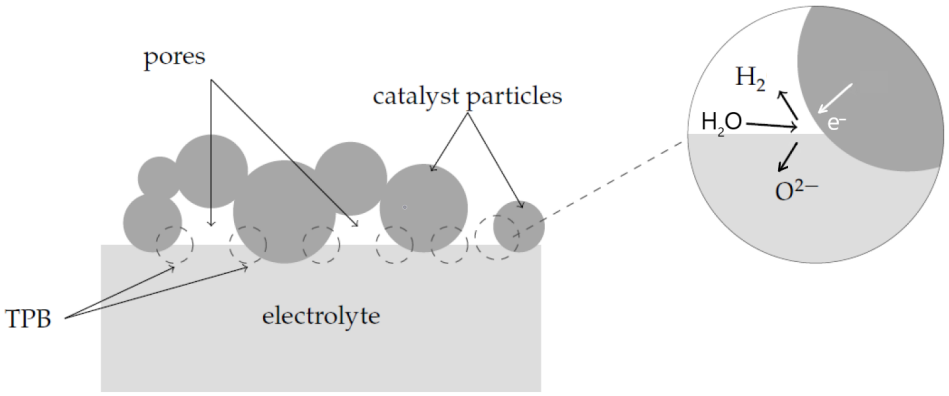

Figure 2.10: Triple Phase Boundary (TPB), the region where pores, electrolyte, and catalyst particles converge. Adapted from [116] and modified accordingly.

mean pore radius r_p, tortuosity factor τ, and porosity ε. To calculate the molar fractions at the interface between the electrodes and the electrolyte, *i.e.*, the triple-phase boundaries (TPBs) as shown in Figure 2.10 for the hydrogen electrode, the system of Equation (2.6) must be solved analytically or numerically and will be detailed later.

Effective diffusion coefficients.

The effective Knudsen and binary diffusion coefficients ($D_{i,K}^{\text{eff}}$ and $D_{i,j}^{\text{eff}}$, respectively, in $\mathrm{m^2\,s^{-1}}$) account for the electrode microstructure through the porosity ε, tortuosity τ, and mean pore radius r_p. Two electrode-specific microstructural correction factors are introduced:

$$\psi_{\text{fuel}} = \frac{\varepsilon_{\text{fuel}}}{\tau_{\text{fuel}}}, \qquad \psi_{\text{air}} = \frac{\varepsilon_{\text{air}}}{\tau_{\text{air}}}. \tag{2.7}$$

Since the porosity and tortuosity of each electrode are not known independently with sufficient accuracy, ψ_{fuel} and ψ_{air} are treated as lumped parameters to be estimated. The factor ψ_{fuel} is used for species diffusion through the fuel electrode, whereas ψ_{air} is used for species diffusion through the air electrode.

The effective diffusion coefficients are given by

$$D_{i,K}^{\text{eff}} = \psi\, D_{i,K}, \quad \text{with} \quad D_{i,K} = \frac{2}{3}\, r_p \sqrt{\frac{8000RT}{\pi M_i}}, \tag{2.8}$$

$$D_{i,j}^{\text{eff}} = \psi\, D_{i,j}, \quad \text{with} \quad D_{i,j} = \frac{0.00143\, T^{1.75}}{P\left(V_i^{1/3} + V_j^{1/3}\right)^2 M_{i,j}^{0.5}} \times 10^{-4}, \tag{2.9}$$

Thèse accessible à l'adresse : https://theses.insa-lyon.fr/publication/2026ISAL0017/these.pdf © [Z. Yazbeck], [2026], INSA Lyon, tous droits réservés

where $\psi = \psi_{\text{fuel}}$ for the fuel electrode and $\psi = \psi_{\text{air}}$ for the air electrode, and

$$M_{i,j} = \frac{2}{\frac{1}{M_i} + \frac{1}{M_j}}. \tag{2.10}$$

Here, M_i is the molar mass of species i, and V_i is its Fuller diffusion volume, whose values can be found in [117].

Finally, the overall effective diffusion coefficient of species i, accounting for both Knudsen and binary diffusion, is calculated as follows:

$$\frac{1}{D_i^{\text{eff}}} = \frac{1}{D_{i,j}^{\text{eff}}} + \frac{1}{D_{i,K}^{\text{eff}}}. \tag{2.11}$$

Effective partial pressures at reaction interface

Electrochemical reactions occur at the electrode electrolyte interfaces, known as the triple-phase boundaries (TPBs). The porous anode and cathode introduce mass-transfer resistance, so the effective partial pressures at the reaction interfaces differ from those in the adjacent gas channels. We derive the effective interface partial pressures for H_2O, H_2, and O_2 from Equation (2.6).

Anode (Air) side: The one-dimensional (1D) concentration profile of oxygen in the anode electrode based on the diffusion model is given by:

$$\frac{dy_{O_2}}{dy} = \frac{RT}{P_a^{ch}} \left(\frac{y_{O_2} N_{N_2} - y_{N_2} N_{O_2}}{D_{O_2}^{eff}} \right), \tag{2.12}$$

where P_a^{ch} is the pressure of the anode channel.
The diffusion process occurs inside the porous anode, but the local gas temperature is assumed to be identical, in the zero-dimensional model, to the lumped temperature (T) on the SOEC anode-electrolyte-cathode assembly. Since nitrogen does not take part in the chemical reaction, the net nitrogen N_2 molar flux normal to the anode surface can be set to zero, and the molar flux of O_2 can be determined using Faraday's law:

$$N_{O_2} = -\frac{I}{4F}, \qquad y_{O_2} + y_{N_2} = 1, \tag{2.13}$$

Integrating Equation (2.12) across the anode thickness δ_{an} (from electrolyte/anode interface, where $y = 0$ to channel/anode interface, where $y = \delta_{an}$) gives the interface (TPB) partial pressure:

$$p_{O_2}^{TPB} = P_a^{ch} + \left(p_{O_2}^{ch} - P_a^{ch} \right) \exp\left(\frac{RT\,\delta_{an}}{4F\,P_a^{ch}\,D_{O_2}^{eff}}\, I \right) \tag{2.14}$$

Thèse accessible à l'adresse : https://theses.insa-lyon.fr/publication/2026ISAL0017/these.pdf © [Z. Yazbeck], [2026], INSA Lyon, tous droits réservés

Cathode (Steam + Hydrogen) side: The one-dimensional (1D) concentration of steam in the cathode electrode is given by:

$$\frac{dy_{H_2O}}{dy} = \frac{RT}{P_c^{ch}} \left(\frac{y_{H_2O} N_{H_2} - y_{H_2} N_{H_2O}}{D_{H_2O}^{eff}} \right), \tag{2.15}$$

where P_c^{ch} is the pressure in the cathode channel, and $D_{H_2O}^{\text{eff}}$ is the effective diffusion coefficient in the porous cathode, and the molar flux of H_2O and H_2 is determined using Faraday's law:

$$N_{H_2} = -N_{H_2O} = \frac{-I}{2F} \tag{2.16}$$

Note that the molar flux is assumed constant along the cathode in the 0D model, as well as P_c^{ch}, so the following relationship is satisfied at the cathode:

$$y_{H_2O} + y_{H_2} = 1 \tag{2.17}$$

Then Equation (2.15) can be rewritten as:

$$\frac{dp_{H_2O}}{dy} = \frac{RT}{D_{H_2O}^{\text{eff}}} \frac{I}{2F} \tag{2.18}$$

And analogously, we obtain for the H_2 species:

$$\frac{dp_{H_2}}{dy} = -\frac{RT}{D_{H_2}^{\text{eff}}} \frac{I}{2F} \tag{2.19}$$

Integrating Equations (2.18) and (2.19) with respect to y from the cathode/electrolyte interface (TPB), where $y = 0$ to the channel/cathode interface, where $y = \delta_{cath}$, we obtain the following expression for the partial pressure of H_2O and H_2 species at the reaction interface:

$$p_{H_2O}^{\text{TPB}} = p_{H_2O}^{ch} + \frac{RT\delta_{cath}}{D_{H_2O}^{\text{eff}}} \frac{I}{2F} \tag{2.20}$$

$$p_{H_2}^{\text{TPB}} = p_{H_2}^{ch} - \frac{RT\delta_{cath}}{D_{H_2}^{\text{eff}}} \frac{I}{2F} \tag{2.21}$$

Mass conservation

Under the ideal gas assumption, justified by the high temperature and near atmospheric pressure, the partial pressure dynamics are given by [118]:

In the cathode channel:

$$\frac{V_c}{RT} \frac{dp_{H_2O}^{ch}}{dt} = \dot{n}_{H_2O}^{in} - \dot{n}_{H_2O}^{out} + N_{H_2O} \tag{2.22}$$

Thèse accessible à l'adresse : https://theses.insa-lyon.fr/publication/2026ISAL0017/these.pdf © [Z. Yazbeck], [2026], INSA Lyon, tous droits réservés

$$\frac{V_c}{RT}\frac{dp_{H_2}^{ch}}{dt} = \dot{n}_{H_2}^{in} - \dot{n}_{H_2}^{out} + N_{H_2} \tag{2.23}$$

In the anode channel:

$$\frac{V_a}{RT}\frac{dp_{O_2}^{ch}}{dt} = \dot{n}_{O_2}^{in} - \dot{n}_{O_2}^{out} + N_{O_2} \tag{2.24}$$

Where V_a and V_c are the volume of the anode and cathode channels, and T, the lumped temperature.

The molar flow rates of gas species at the channel inlet and outlet can be given by:

$$\begin{cases} \dot{n}_{H_2O}^{in} = \dot{n}_{fuel}^{in} y_{H_2O}^{in} = \dot{n}_{fuel}^{in} \dfrac{p_{H_2O}^{in}}{P_c^{ch}} \\ \dot{n}_{H_2}^{in} = \dot{n}_{fuel}^{in} y_{H_2}^{in} = \dot{n}_{fuel}^{in} \dfrac{p_{H_2}^{in}}{P_c^{ch}} \\ \dot{n}_{O_2}^{in} = \dot{n}_{air}^{in} y_{O_2}^{in} = \dot{n}_{air}^{in} \dfrac{p_{O_2}^{in}}{P_a^{ch}} \end{cases} \qquad \begin{cases} \dot{n}_{H_2O}^{out} = \dot{n}_{fuel}^{out} y_{H_2O}^{out} = \dot{n}_{fuel} \dfrac{p_{H_2O}^{out}}{P_c^{ch}} \\ \dot{n}_{H_2}^{out} = \dot{n}_{fuel}^{out} y_{H_2}^{out} = \dot{n}_{fuel} \dfrac{p_{H_2}^{out}}{P_c^{ch}} \\ \dot{n}_{O_2}^{out} = \dot{n}_{air}^{out} y_{O_2}^{out} = \dot{n}_{air}^{out} \dfrac{p_{O_2}^{out}}{P_a^{ch}} \end{cases}$$

And the outlet flow rate is:

$$n_j^{out} = n_j^{in} + N_i \tag{2.25}$$

where $j \in \{fuel, air\}$ and $i \in \{H_2, H_2O, O_2, N_2\}$. Therefore, Equations (2.22)-(2.24) can be rewritten as:

$$\frac{dp_{H_2O}^{ch}}{dt} = \frac{\dot{n}_{fuel}RT}{V_c P_c^{ch}} p_{H_2O}^{in} - \frac{\dot{n}_{fuel}RT}{V_c P_c^{ch}} p_{H_2O}^{ch} + \frac{RT}{2FV_c} I \tag{2.26}$$

$$\frac{dp_{H_2}^{ch}}{dt} = \frac{\dot{n}_{fuel}RT}{V_c P_c^{ch}} p_{H_2}^{in} - \frac{\dot{n}_{fuel}RT}{V_c P_c^{ch}} p_{H_2}^{ch} - \frac{RT}{2FV_c} I \tag{2.27}$$

$$\frac{dp_{O_2}^{ch}}{dt} = \frac{\dot{n}_{air}RT}{V_a P_a^{ch}} p_{O_2}^{in} - \frac{\dot{n}_{air}RT}{V_a P_a^{ch}} p_{O_2}^{ch} - \frac{RT}{4FV_a} I \tag{2.28}$$

2.3.2 Electrochemical Model

SOEC electrochemical performance is characterized by the polarization curve, *i.e.,* Current-Voltage (IV) curve, which shows the evolution of cell voltage in function of current density as presented in Figure 2.11.

Thèse accessible à l'adresse : https://theses.insa-lyon.fr/publication/2026ISAL0017/these.pdf © [Z. Yazbeck], [2026], INSA Lyon, tous droits réservés

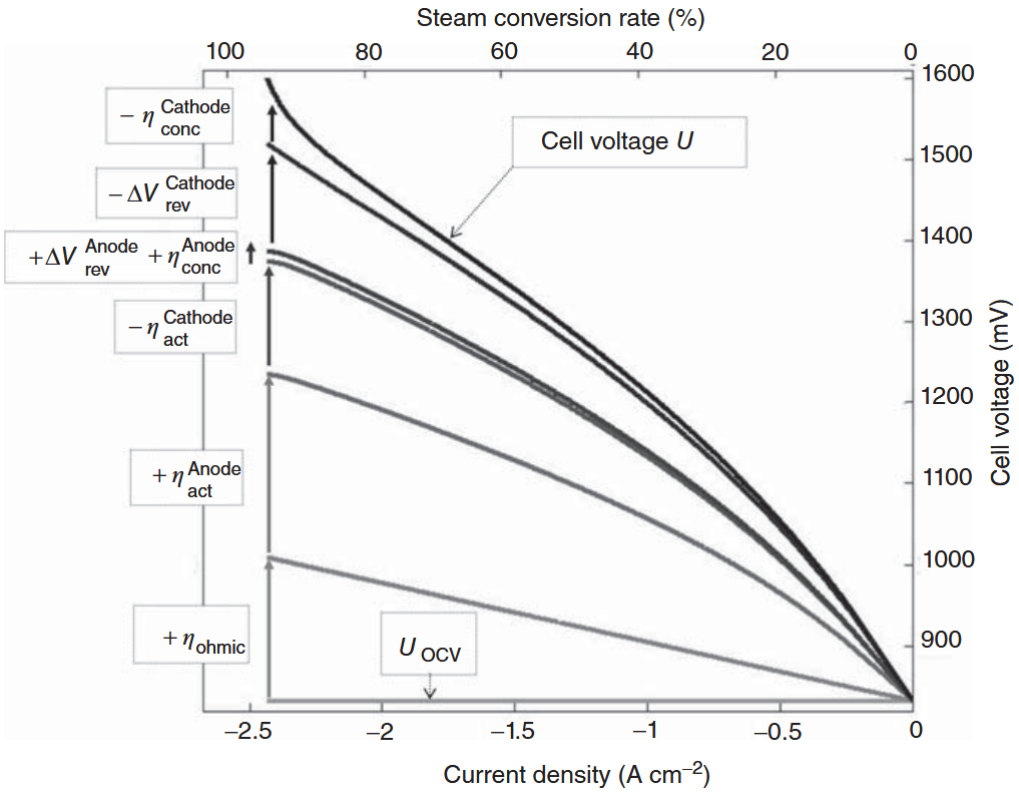

Figure 2.11: Decomposition of a typical polarization curve. Adapted from [60].

It consists of two main contributions: the reversible voltage, U_{rev}, representing the minimum thermodynamic potential required to drive the electrolysis reaction, and the cell polarization that arises under current with the overpotentials, which increases the voltage in SOEC as shown in Figure 2.11 according to:

$$U_{cell} = U_{rev} - \eta \tag{2.29}$$

The term η can be decomposed into different contributions, with each term attributed to a specific process that limits the cell efficiency and thus the hydrogen production rate.
According to assumption 3, the stack voltage V_s is given by the cell voltage, U_{cell}, multiplied by the number of cells in the stack, N_{cell}, as follows:

$$V_s = N_{cell}U_{cell} = N_{cell}\left(U_{rev} - \eta_{ohmic} - (\eta_{act}^{cathode} - \eta_{act}^{anode}) - (\eta_{conc}^{cathode} - \eta_{conc}^{anode})\right) \tag{2.30}$$

Reversible or thermodynamic voltage

The reversible voltage can be expressed according to the Nernst Equation as a function of temperature, and the activities of gas species [119], are equal to their partial pressures, as stated in

Thèse accessible à l'adresse : https://theses.insa-lyon.fr/publication/2026ISAL0017/these.pdf © [Z. Yazbeck], [2026], INSA Lyon, tous droits réservés

Assumption 1. Therefore, the reversible or Nernst voltage is expressed as follows:

$$\begin{aligned} V_{\text{Nernst}} &= E^{\circ}(T) + \frac{RT}{2F}\ln\left(\frac{p_{H_2}^{ch}\, p_{O_2}^{ch\,1/2}}{p_{H_2O}^{ch}}\right) \\ &= \underbrace{E^{\circ}(T) + \frac{RT}{2F}\ln\left(\frac{y_{H_2}^{in}\, y_{O_2}^{in\,1/2}}{y_{H_2O}^{in}}\right)}_{U_{OCV}} + \underbrace{\frac{RT}{2F}\ln\left(\frac{p_{O_2}^{ch}}{y_{O_2}^{in}}\right)^{1/2}}_{\Delta V_{rev}^{Anode}} - \underbrace{\frac{RT}{2F}\ln\left(\frac{y_{H_2}^{in}\, p_{H_2O}^{ch}}{y_{H_2O}^{in}\, p_{H_2}^{ch}}\right)}_{\Delta V_{rev}^{Cathode}} \end{aligned} \tag{2.31}$$

Where $E^0 = -\dfrac{\Delta G}{2F} = -\dfrac{\Delta H - T\Delta S}{2F}$ is the standard potential as a function of the Gibbs free-energy change ΔG of the reaction, where the enthalpies and entropies of gas species are calculated using the empirical formulas from [120].
The reversible voltage in Equation (2.31) consists of two components, the Open Circuit Voltage (OCV) (i.e. $I = 0$) and the electrode polarization under current (i.e. $I \neq 0$) denoted as ΔV_{rev}^{Anode}, and $\Delta V_{rev}^{Cathode}$.

Ohmic loss

It includes the ionic resistance of the electrolyte, the electronic resistances of both electrodes, which are very low in planar configurations compared to the electrolyte resistance [87], and the global contact resistances between the electrodes and the interconnects [60]. Thus, the internal ohmic resistance R_s, encompassing all these contributions at temperature T_0, is expressed in function of the operating temperature using an Arrhenius law and is taken as:

$$\eta_{ohm} = IR_s \times exp\left(\frac{E_{act}^{ohm}}{R}\left(\frac{1}{T} - \frac{1}{T_0}\right)\right) \tag{2.32}$$

Generalized Butler-Volmer equation

In addition to the reversible contribution, the potential at the electrode is influenced by several irreversible processes occurring at the electrode. These irreversibilities modify the potential through the so-called activation and concentration overpotentials, denoted as η_{act} and η_{conc}, respectively. η_{act} and η_{conc} are related to the mechanisms that limit the kinetics of the overall electrochemical reaction. Specifically, the concentration overpotential η_{conc} rises at high steam conversion due mass transport limitations through the porous electrode, while the activation overpotential η_{act} arises from the intrinsic kinetics of the electrode reaction. The global overpotential η can be expressed from the known generalized Butler-Volmer equation that describes how the current densities through an electrode depends on the electrode potential [119]:

$$I = I_0^{\text{Anode}}\left\{\left(\frac{p_{O_2}^{\text{TPBs}}}{p_{O_2}^{\text{ch}}}\right)^{1/2}\exp\left(\frac{-(1-\alpha^{\text{Anode}})2F\eta^{\text{Anode}}}{RT}\right) - \exp\left(\frac{\alpha^{\text{Anode}}2F\eta^{\text{Anode}}}{RT}\right)\right\} \tag{2.33}$$

Thèse accessible à l'adresse : https://theses.insa-lyon.fr/publication/2026ISAL0017/these.pdf © [Z. Yazbeck], [2026], INSA Lyon, tous droits réservés

$$I = I_0^{\text{Cathode}} \left\{ \left(\frac{p_{H_2}^{\text{TPBs}}}{p_{H_2}^{\text{ch}}} \right) \exp\left(\frac{(1-\alpha^{\text{Cathode}})2F\eta^{\text{Cathode}}}{RT} \right) - \left(\frac{p_{H_2O}^{\text{TPBs}}}{p_{H_2O}^{\text{ch}}} \right) \exp\left(\frac{-\alpha^{\text{Cathode}}2F\eta^{\text{Cathode}}}{RT} \right) \right\} \tag{2.34}$$

$$\text{with } \eta^{\text{Anode}} = \eta_{\text{conc}}^{\text{Anode}} + \eta_{\text{act}}^{\text{Anode}}, \quad \eta^{\text{Anode}} > 0$$
$$\text{and } \eta^{\text{Cathode}} = \eta_{\text{conc}}^{\text{Cathode}} + \eta_{\text{act}}^{\text{Cathode}}, \quad \eta^{\text{Cathode}} < 0$$

α^{Anode} and α^{Cathode} are the anodic and cathodic charge-transfer coefficients, respectively, and are assumed here to be symmetric, with a value of 0.5. I_0^{anode} and I_0^{cathode} represent the anode and cathode exchange current densities, respectively.

Activation Overpotential

At low current density, the cell polarization is dominated by the activation overpotential as result of the charge transfer to and from the electrode surface to drive electrochemical reactions as the activation barrier must be overcome. Thus, when the current density $|I|$ is close to zero, $\eta \to \eta_{act}$ and $p_i^{ch} \approx p_i^{TPB}$, so from the generalized Butler-Volmer relation in Equations (2.33), (2.34) with α, the symmetrical factor, taken as 0.5 for both electrodes, the activation overpotential is presented as follows [60]:

$$\eta_{act} = \frac{RT}{F} \left[\sinh^{-1}\left(\frac{I}{2I_0^{an}} \right) + \sinh^{-1}\left(\frac{I}{2I_0^{cath}} \right) \right] \tag{2.35}$$

Where the anodic and cathodic exchange current densities, I_0^{an} and I_0^{cath}, respectively follow the Arrhenius's law [87]:

$$I_0^{cath} = \gamma_{cath} \left(p_{H_2}^{ch} \right)^{\zeta} \left(p_{H_2O}^{ch} \right)^{\theta} \exp\left(-\frac{E_{act}^{cath}}{RT} \right) \tag{2.36}$$

$$I_0^{an} = \gamma_{an} \left(p_{O_2}^{ch} \right)^{\kappa} \exp\left(-\frac{E_{act}^{an}}{RT} \right) \tag{2.37}$$

where γ_{an} and γ_{cath} are the pre-exponential factors of the exchange current densities, E_{act}^{an} and E_{act}^{cath} are the activation energies of the anode and cathode reactions, respectively; ζ, θ, κ are constant exponents to account for the pressure effect on exchange current density, which are fixed to be equal to 0.066, 0.81, and 0.15 respectively according to [121], while the others are identified from experimental data.

Concentration Overpotential

Also denoted as the diffusion overpotential, it models the resistance due to the gas transfer from the channel to the electrochemical active sites (TPBs). This induce partial pressure gradient, which is strongly dependent on the microstructural properties of porous electrodes, as shown in

Thèse accessible à l'adresse : https://theses.insa-lyon.fr/publication/2026ISAL0017/these.pdf © [Z. Yazbeck], [2026], INSA Lyon, tous droits réservés

Equations (2.8), (2.9), (**??**), (2.12), (2.18),(2.19).
Concentration overpotentials become significant when operating at high current densities, as this operating condition impose high gas fluxes through the electrodes. Thus, for high current densities, the cell polarization is dominated by the concentration overpotential. Considering also that electrode kinetics are accelerated at high temperature, the exchange current density I_0 is typically much higher than the operating current density I (so that $|I|/I_0 \to 0$). Thus, the concentration overpotential can be derived from Equations (2.33) (2.34) as follows [60]:

$$\eta_{conc} = \frac{RT}{2F} \ln \left(\frac{p_{H_2}^{TPB} p_{H_2O}}{p_{H_2} p_{H_2O}^{TPB}} \right) + \frac{RT}{4F} \ln \left(\frac{p_{O_2}^{TPB}}{p_{O_2}} \right) \tag{2.38}$$

2.3.3 Thermal Balance model

The thermal balance equation describing the temperature dynamics of the stack is expressed as follows [112]:

$$m_s C_{p_s} \frac{dT}{dt} = \dot{E}^{in} - \dot{E}^{out} - IV_s + N_{cell} N_{H_2O} \Delta H + Q^{rad} \tag{2.39}$$

where V_s is the stack voltage presented in Equation (2.30), $\dot{E}^{in/out}$ denote the inlet and outlet energy flows of the stack respectively, further decomposed as:

$$\dot{E}^{\alpha} = \dot{n}_j^{\alpha} \sum_i y_i^{\alpha} h_i(T_j^{\alpha}), \tag{2.40}$$

where $i \in \{H_2, H_2O, O_2, N_2\}$, $j \in \{fuel, air\}$, $\alpha \in \{in, out\}$. The molar enthalpy of species i is computed using the empirical formula provided by the NIST WebBook [120]:

$$h_i = A_i \left(\frac{T_j^{\alpha}}{1000} \right) + \frac{B_i}{2} \left(\frac{T_j^{\alpha}}{1000} \right)^2 + \frac{C_i}{3} \left(\frac{T_j^{\alpha}}{1000} \right)^3 + \frac{D_i}{4} \left(\frac{T_j^{\alpha}}{1000} \right)^4 - \frac{E_i}{\left(\frac{T_j^{\alpha}}{1000} \right)} + F_i,$$

where $A_i, B_i, C_i, D_i, E_i, F_i$ are empirical coefficients that depend on the chemical species i and on the temperature range for which the polynomial is fitted. These coefficients are taken from the tabulated values provided in the NIST WebBook [120]. The enthalpy h_i given by this expression is in kJ/mol and is converted to J/mol in the model. The term Q^{rad} represents the radiative heat exchange between the stack and the furnace and is given by [122]:

$$Q^{rad} = A_{stack} \sigma_{SB} \left(T_{furnace}^4 - T^4 \right) \tag{2.41}$$

where σ_{SB} is the Stefan-Boltzmann constant, A_{stack} is the area of the stack exposed to radiation, and $T_{furnace}$ is the furnace temperature.
The reaction enthalpy $\Delta H(T)$ appearing in Equation (2.39) corresponds to the enthalpy change of the global steam electrolysis reaction: $H_2O_{(g)} \to H_{2_{(g)}} + \frac{1}{2} O_{2_{(g)}}$, and is defined as previously

Thèse accessible à l'adresse : https://theses.insa-lyon.fr/publication/2026ISAL0017/these.pdf © [Z. Yazbeck], [2026], INSA Lyon, tous droits réservés

introduced in Equation (2.4). It is evaluated using the species molar enthalpies computed from the NIST polynomial expression given above [120]. Nitrogen does not appear in this expression because it is considered as an inert species and does not participate in the electrochemical reaction.

2.4 Model summary

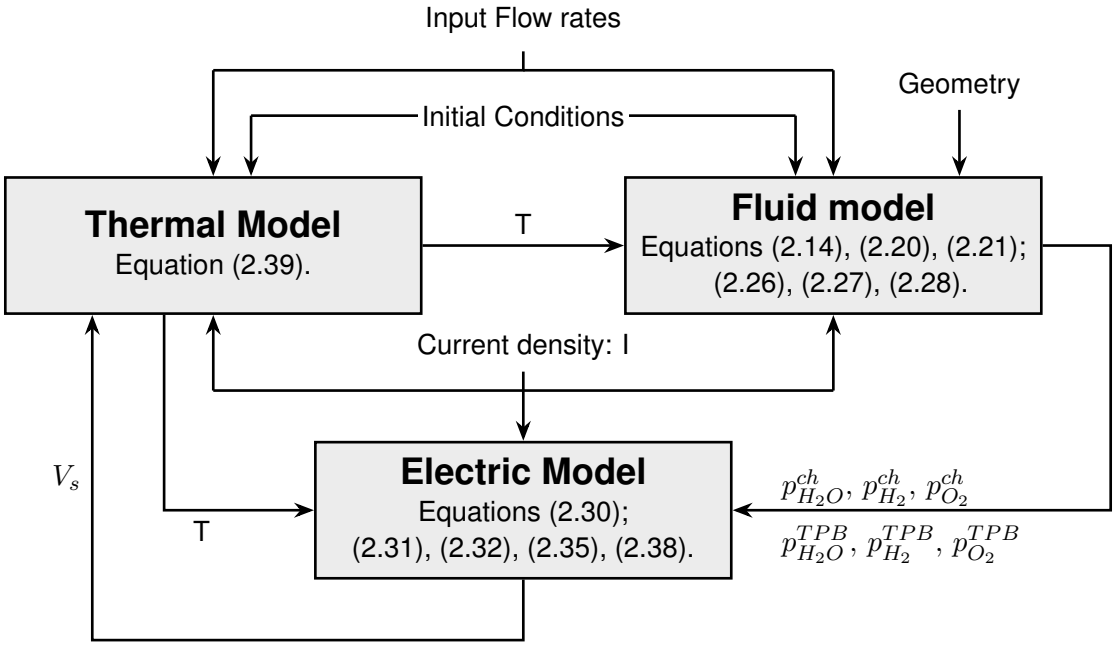

Figure 2.12: Schematic of Solid Oxide Electrolysis Stack (SOES) modeling.

To clarify how the three sub-models (thermal, fluid and electrochemical) are coupled, the overall structure of the model, together with the corresponding governing equations, is summarized and illustrated in Figure 2.12.

The thermal sub-model computes the stack temperature T from the global energy balance equation in Equations (2.39), which accounts for the reaction enthalpy, Joule heating, energy flows of the inlet and outlet gas streams, and radiative exchange between the stack and the furnace. This model provides the uniform stack temperature used by both the fluid and electrochemical sub-models.

The fluid sub-model referring the mass transport and conservation sub-models describes the gas flows in the channels and its diffusion through porous electrodes. For a given geometry, inlet flow rates and stack temperature, it solves species mass balances coupled with a mass transport based on the Dusty-Gas model. It yields the channel compositions and the effective partial pressures at the electrochemically active triple reaction sites (TPBs), namely p_{H_2}, p_{H_2O}, p_{O_2}, and $p^{TPB}_{H_2}$, $p^{TPB}_{H_2O}$, $p^{TPB}_{O_2}$.

Thèse accessible à l'adresse : https://theses.insa-lyon.fr/publication/2026ISAL0017/these.pdf © [Z. Yazbeck], [2026], INSA Lyon, tous droits réservés

Using the stack temperature and the interfacial partial pressures, the electrochemical sub-model determines the reversible cell voltage and the different overpotential contributions. For a specific current density I, the model returns the stack voltage as well as the heat sources associated with electrochemical reactions and ohmic dissipation.

As indicated in Figure 2.12, the coupling between sub-models is through T, I, and the partial pressures. The main inputs to the overall model are the stack geometry and materials, the initial conditions and the inlet flow rates, together with the imposed current profile.

2.5 Time integration

The coupled thermal-fluid-electrochemical equations form a stiff system of ordinary and differential and algebraic equations. Thus the time integration is performed with an implicit scheme, which provides good stability properties for the fast electrochemical transients and allows the use of big time steps compatible with long scenario simulations. This choice is also well suited for the intended control-oriented applications, state estimation and optimal input design.

Thèse accessible à l'adresse : https://theses.insa-lyon.fr/publication/2026ISAL0017/these.pdf © [Z. Yazbeck], [2026], INSA Lyon, tous droits réservés

Thèse accessible à l'adresse : https://theses.insa-lyon.fr/publication/2026ISAL0017/these.pdf © [Z. Yazbeck], [2026], INSA Lyon, tous droits réservés

Chapter 3

Parameter estimation

Contents

3.1 Motivation and Background 49
3.1.1 Problem description 49
3.1.2 State of the art 51
3.2 State-space formulation 54
3.3 Sensitivity analysis 56
3.3.1 Sensitivity differential equations 58
3.3.2 Sensitivity equations as a tool for parameter identifiability 59
3.3.3 Parameter identification using grouping-based approach 60
3.3.4 Does temperature provide additional information for parameter estimation? 63
3.4 Sensitivity function-based parameter identification 64
3.4.1 Truncated Levenberg-Marquardt method 64
3.4.2 Estimation results for synthetic data 66
3.5 Monte-Carlo Simulation 70
3.6 Confidence interval 78
3.7 Parameter estimation with experimental data 79
3.8 Design of optimal experimental data 81
3.9 Sequential OED 86
3.10 OED based on a predefined library 89
3.11 Conclusion 94

Thèse accessible à l'adresse : https://theses.insa-lyon.fr/publication/2026ISAL0017/these.pdf © [Z. Yazbeck], [2026], INSA Lyon, tous droits réservés

3.1 Motivation and Background

3.1.1 Problem description

As discussed in Section 2.2.2, physics-based or phenomenological SOEC models represent the fundamental phenomena occurring in the system. These include mass transport, thermodynamics, and electrochemical processes in SOEC/SOFC, using conservation laws to describe the behavior of the system. Compared with data-driven models, they typically require significantly less experimental data for calibration because nonlinear input-output relationships are already described by the governing equations [98]. However, depending on the level of detail of the model (see Chapter 2, Subsection 2.2.1), these models introduce parameters that must be calibrated to fit experimental data and to represent a specific setup. Consequently, the associated model calibration task is nontrivial, and its complexity rises with the complexity of the mathematical formulation and the number of parameters to estimate.

In practice, physics-based models depend on parameters that are rarely directly measurable, especially in electrochemical systems. Consequently, the reliability of the model depends on the parameter selection and estimation from the experimental data. Moreover, electrochemical systems commonly degrade over time, thus, from a modeling point of view, this can be represented by parameters varying in time at the macro-level when one does not explicitly model the physics of failure. Therefore, accurate estimation of these time-varying parameters is crucial to track performance degradation [54]. Thus, the parameter estimation problem is central to achieve accurate, reliable models and, in turn, to enable robust diagnostic and prognostic methods in SOEC systems, which is the core of this thesis. The main technical issues associated to parameter identification in these systems include:

1. **Over-parameterization and dependence between parameters:** Many parameters have to be estimated even when using reduced or simplified SOEC cell or stack models (e.g., pre-exponential factors of the exchange current densities and activation energies at both electrodes, etc.). Several of these parameters can be locally linearly dependent and not be practically identifiable from standard operating data [123, 124, 125]. Thus, this is a practical parameters identifiability problem.

2. **Non-convex optimization problem:** Electrochemical models are nonlinear, thus, the resulting optimization problem is non-convex with the possibility of flat directions in the parametric sensitivity of the outputs. In addition, the quality of the estimates and the practical identifiability of the parameters depend on the informativeness of the experiments, that must respect safety and operability constraints [123, 126].

3. **Validation of estimates quality and its dynamic variation:** Reliability of estimated parameters cannot be directly verified without additional specific tests like electrochemical

Thèse accessible à l'adresse : https://theses.insa-lyon.fr/publication/2026ISAL0017/these.pdf © [Z. Yazbeck], [2026], INSA Lyon, tous droits réservés

impedance measurements for instance. In addition, some parameters evolve because of aging, so assuming static parameters is not necessarily valid over long time horizons [54].

Accordingly, there is a need for a systematic approach for parameter calibration, which is a typical challenge in electrochemical systems. To address these gaps, a practice methodology is adopted that couples the estimation method with informative experimentation, explicitly takes into account the dependence between the parameters to be estimated.

A truncated Levenberg-Marquardt algorithm, which combines Gauss-Newton and gradient descent methods, is used for the calibration methodology in order to damp ill-conditioned directions in the correction steps while updating the most informative directions. This approach is first assessed on synthetic datasets with known ground-truth parameters, using different initial guesses with noise addition, and is then applied to experimental dataset.

To enhance the quality of the parameter estimates, an optimal experimental design of the input trajectory is also required, with the objective of obtaining weakly collinear (ideally near-orthogonal) output sensitivity directions with respect to the parameters. In order to achieve this, one needs to generate an excitation profile in which each parameter has a distinct and independent influence on the measured output. With this goal, an optimization problem is formulated in order to maximize the information of the input trajectory taking into account the physical constraints on the input signals. Classical criteria like D, A or E-optimality of the discrete Fisher information matrix are examples of such optimization problems [127, 128]. However, solving the resulting non-convex optimization problem can be numerically and computationally challenging since its complexity increases rapidly with the number of parameters and the dimension of the system. Consequently, an alternative strategy inspired by [123] is presented, based on a library-design approach rather than direct optimization.

This alternative method is based on a bank of admissible excitation signals, including frequency sweeps, pseudo-random binary sequences (PRBS) or multisine segments, ramps and steps, all satisfying the applicable safety and operability constraints (such as temperature gradients, conversion rate, oxygen partial pressure and total experimental duration). Short test sequences are then selected from this library, optionally through a multi-objective optimization that trades off parameter-variance reduction against experiment duration.

Throughout this chapter, identifiability is addressed in a practical and local sense for a given operating trajectory constrained by safety, physical constraints and noisy measurement. Even when the discrete sensitivity matrix of the output with respect to the parameter vector has full column rank along a given experiment (so that the parameters are locally identifiable in principle [129]), the estimation problem may remain ill-conditioned. A large condition number of the sensitivity matrix reveals correlations between sensitivity directions and leads to large variances in the estimates [130], and then amplification in poorly informed directions due to measurement noise.

Accordingly, the methods developed in this chapter are therefore aimed at improving practical identifiability and robustness to noise by combining sensitivity-based analysis, truncation

Thèse accessible à l'adresse : https://theses.insa-lyon.fr/publication/2026ISAL0017/these.pdf © [Z. Yazbeck], [2026], INSA Lyon, tous droits réservés

of the sensitivity matrix within the estimation algorithm, and the design of informative excitation trajectories using different methods.

A preliminary version of this work was presented in our CDC 2024 paper, “Sensitivity function-based Identification Of Solid Oxide Electrolyzer Parameters” [80], where parameter estimation relied on a Gauss-Newton scheme. In the present manuscript, this approach is extended by using Levenberg-Marquardt, adding a regularization term to Gauss-Newton method, which improves numerical robustness and convergence when the initial parameter guess is far from the optimum, thereby reducing sensitivity to poor initialization while preserving the fast local convergence of Gauss-Newton [131].

3.1.2 State of the art

Calibrating physical models is essential to represent a specific setup. However, focusing on reducing the error between measured outputs and the model is not sufficient. It is important to study the reliability of the estimates, especially for electrochemical systems like SOEC/SOFC, where the proliferation of parameters to be fitted is common. Thus, it is important to investigate the practical identifiability of the parameters. However, little work on SOEC/SOFC models addresses this question, as many studies fit all parameters to be estimated without studying or checking whether the data used are sufficiently rich to estimate them all. In [132] and [133], the authors used an “all-in-one” strategy to fit more than ten parameters for solid oxide cell models in reversible and electrolysis modes, respectively, using nonlinear curve-fitting and a genetic algorithm, respectively. Leonide et al. in [115], estimated the parameters of an SOFC electrochemical model using a wide set of experiments and the distribution of relaxation times method (DRT).

Lam et al. [129] highlight in their review the issues of practical identifiability that can be caused by noise, weak persistent excitation, and pointed out that the richness of the data is essential to reliably estimate parameters, which is not often addressed in the literature. Thus, practical identifiability can be lost even when a model is structurally identifiable because different parameter combinations can compensate each other and produce nearly indistinguishable output trajectories. In addition to the distinction between structural and practical identifiability, the review also highlighted the importance of the sensitivity matrix, the excitation profile, and the experimental protocol.

In other applications, sensitivity analysis has been conducted for batteries, fuel cell systems, and power plant calibration to quantify the impact of parameter variations on model outputs, enabling collinearity assessment and parameter screening. In battery modeling, for instance, Park et al. [123] assessed the sensitivity across a large library of different input profiles and showed that the output sensitivity to many parameters are linearly dependent. Consequently, in the identification procedure, parameters were clustered into groups after orthogonalizing the sensitivities to reduce collinearity. Levenberg-Marquardt iterations were then used to estimate the parameter groups sequentially, starting with the most sensitive ones while keeping the remaining

Thèse accessible à l'adresse : https://theses.insa-lyon.fr/publication/2026ISAL0017/these.pdf © [Z. Yazbeck], [2026], INSA Lyon, tous droits réservés

groups fixed at their nominal values, and proceeding accordingly.

Another closely related work is done by Goshtasbi et al. [125] for PEM fuel cell models. Their methodology consists of extending local sensitivity analysis by sampling several points in the parameter space in order to obtain a global picture of the influence of parameters. The results show strong collinearity among parameters, indicating limitations in the practical identifiability of some parameters. Consequently, a parameter subset-selection procedure is used to determine which parameters can be meaningfully identified, based on collinearity indices and sensitivity directions.

Other works have used sensitivity information to improve parameter estimation. Dangwal et al. [134] incorporate the sensitivity information in the particle swarm optimization algorithm to improve the convergence and robustness of the algorithm to estimate parameters in a lithium-ion battery model. Gima et al. [135] calculate the parameter sensitivities for a reduced-order model of lithium-ion battery (Single Particle Model with Electrolyte and Thermal Dynamics, SP-MeT) to decrease computational cost while retaining the dominant sensitivity directions of the full-order system, and showed that the calculated approximates the sensitivity of the full-order model (Doyle-Fuller-Newman Model, DFN) with high accuracy. In fuel cell systems, Radaideh et al. [136] conducted a sensitivity analysis with uncertainty quantification for a solid oxide fuel cell model. For local sensitivity analysis, the finite difference method is used, and for global sensitivity, several methods were used, Morris screening, regression-based sensitivities, and Sobol indices were used, to evaluate twenty-one uncertain design parameters. For uncertainty quantification, both deterministic propagation and Monte-Carlo sampling were used to compare the consistency of the different approaches. Acilan et al. [124] used trajectory sensitivities with cosine similarity measures to identify collinear parameters and remove them from the estimation set. Jayasankar et al. [137] showed that even structurally identifiable SOFC models may become practically non-identifiable under specific, poorly informative excitation profiles. These results confirm that identifiability depends not only on the model equations but also on the informativeness of the experimental protocol and the data.

Inspired by these results, we introduce a different approach for parameter estimation that uses sensitivity differential equations and, instead of relying on manual clustering and ad hoc parameter choices for the identification process, applies a variation of the Levenberg-Marquardt algorithm with a truncated singular-value decomposition (SVD) to automate the parameter-update directions followed at each step. This automated process allows the optimization algorithm to update the most influential directions, thereby enhancing efficiency, while limiting the condition number of the linear system solved at each iteration. The truncation is designed to reduce the effects of measurement noise and prevent the algorithm from taking large steps in directions where the sensitivity is particularly low. This helps avoid non-physical parameter values and decreases estimated parameter variability in the presence of measurement noise.

As previously mentioned, sensitivity analysis consistently indicates that practical identifiability of parameters depends strongly on the richness of the excitation. This naturally motivates the use

Thèse accessible à l'adresse : https://theses.insa-lyon.fr/publication/2026ISAL0017/these.pdf © [Z. Yazbeck], [2026], INSA Lyon, tous droits réservés

of optimal experimental design (OED) frameworks, in which the Fisher Information Matrix (FIM) is employed to construct input trajectories that maximize parameter informativeness.

In battery systems, Park et al. [123] formulate the OED problem as an optimization problem to select a set of input profiles having the maximum information about the parameters to estimate from a predefined library. The selection in the original problem is based on a binary variable indicating whether that profile is used or not. Due to difficulty to solve this integer programming problem, the author relaxed this optimization problem to allow the coefficients to take real values between 0 and 1, so that each coefficient represents how strongly a given profile contributes to the overall excitation, thus, rendering the problem convex and efficient in terms of computation using standard convex optimization tools. Pozzi et al. [126] used A-optimality criterion which is equal to the trace of FIM, obtained from sensitivity matrix computed using finite differences, as the objective function to minimize it in the OED framework for single particle lithium-ion battery model, yielding a better practical identifiability when compared with standard current profiles

Two review articles discuss the broader conceptual framework for model-based optimal experimental design (MBDoE). Franceschini and Macchietto [127] introduce MBDoE in their review as a systematic procedure linking the structure of the model, sensitivity analysis, reliability of estimates, and experiment design. They present the confidence intervals of estimates based on the FIM, compare different optimality criteria (A, D, and E-optimality), and address practical challenges in nonlinear dynamic systems, including the computation of sensitivity matrix and its conditioning affected directly by the excitation, and the optimization of excitation profiles under operational constraints.

Another recent review paper by Geremia et al. [128] discusses different methodological advances in model-based optimal experimental design. It reports the increasing use of Bayesian approaches where the aim is to maximize expected information gain between the parameters and the future measurements. In this approach, a prior probability distribution describes the uncertainty about the parameters, and candidate designs are evaluated according to how much they are expected to reduce this uncertainty. Thus, the “utility” of a design can be defined as its expected information gain, which means experiments are chosen so that, after collecting data and updating the prior to a posterior, the posterior distribution is as concentrated and informative as possible about the true parameter values. However, these methods suffer from high computational complexity because the required integrals often need Monte-Carlo simulations and depend strongly on the choice of prior distributions. This work also presents other methods, like the sigma-point method, which is more computationally efficient and is based on deterministic sampling and propagation of uncertainty of parameters to avoid the high cost of full Bayesian integration and is particularly effective when the parameter dimension is not too large. This work discusses also the extended FIM formulation as an alternative of classical FIM which can be problematic for highly nonlinear models, by adding a deviation term to take into account model mismatch. Finally, the paper highlights the important role of optimal-control formulations to design excitation trajectories that enable to handle time varying inputs and constraints to maintain

Thèse accessible à l'adresse : https://theses.insa-lyon.fr/publication/2026ISAL0017/these.pdf © [Z. Yazbeck], [2026], INSA Lyon, tous droits réservés

feasibility.

In the OED part of this chapter, we adopt a classical FIM-based formulation, in which input trajectories are generated by solving an optimization problem to maximize parameter informativeness under operational constraints, using alphabetic optimality criteria (e.g., A- or D-optimality) within a nonlinear programming (NLP) framework. We also present a sequential OED method in which input profiles are generated iteratively using the current parameter estimates, and an alternative strategy inspired by the literature, where a predefined library of candidate input profiles is generated and a genetic algorithm is used to select an informative subset subject to additional requirements such as total test duration and a maximum number of tests.

3.2 State-space formulation

All the equations introduced in the modeling part (Subsection 2.3 of Chapter 2) are expressed in state-space form as follows:

- The state vector $x = [p^{ch}_{H_2}\ p^{ch}_{H_2O}\ p^{ch}_{O_2}\ T]^\top$:

$$\begin{cases} \dot{p}^{ch}_{H_2} &= \dfrac{RT}{P^{ch}_c V_c}\left(\dot{n}^{in}_{fuel}p^{in}_{H_2} - \dot{n}^{out}_{fuel}p^{ch}_{H_2} - \dfrac{I}{2F}\right), \\ \dot{p}^{ch}_{H_2O} &= \dfrac{RT}{P^{ch}_c V_c}\left(\dot{n}^{in}_{fuel}p^{in}_{H_2O} - \dot{n}^{out}_{fuel}p^{ch}_{H_2O} + \dfrac{I}{2F}\right) \\ \dot{p}^{ch}_{O_2} &= \dfrac{RT}{P^{ch}_a V_a}\left(\dot{n}^{in}_{air}p^{in}_{O_2} + \dot{n}^{out}_{air}p^{ch}_{O_2} - \dfrac{I}{4F}\right) \\ \dot{T} &= \big[(p^{in}_{H_2}h_{H_2}(T^{in}_{fuel}) + p^{in}_{H_2O}h_{H_2O}(T^{in}_{fuel}))\dot{n}^{in}_{fuel} \\ &\quad + \left(p^{in}_{O_2}h_{O_2}(T^{in}_{air}) + p^{in}_{N_2}h_{N_2}(T^{in}_{air})\right)\dot{n}^{in}_{air} \\ &\quad - \left(p^{ch}_{H_2}h_{H_2}(T) + p^{ch}_{H_2O}h_{H_2O}(T)\right)\dot{n}^{out}_{fuel} \\ &\quad - \left(p^{ch}_{O_2}h_{O_2}(T) + p^{ch}_{N_2}h_{N_2}(T)\right)\dot{n}^{out}_{air} \\ &\quad - IV_s + N_{cell}N_{H_2O}\Delta H(T) + Q^{rad}(T, T_{furnace})\big]/(m_s C_{p_s}) \end{cases} \tag{3.1}$$

where $n^{out}_{fuel} = n^{in}_{fuel}$, $n^{out}_{air} = n^{out}_{air} + N_{O_2}$, $p^{in}_i = y^{in}_i$ (for $i \in \{H_2,\ H_2O,\ O_2,\ N_2\}$) due to atmospheric pressure.

To perform a time integration of the differential equations, the initial state must be specified. In this work, the initial partial pressures in the gas channels are determined from the first experimental operating point. More specifically, they are initialized using the outlet partial pressures corresponding to the initial flow rates, gas compositions, pressure, temperature, and current density. This choice provides an initial gas-channel composition consistent with the operating conditions at the beginning of the experiment.

Thèse accessible à l'adresse : https://theses.insa-lyon.fr/publication/2026ISAL0017/these.pdf © [Z. Yazbeck], [2026], INSA Lyon, tous droits réservés

The stack temperature is initialized using the furnace temperature measured at the beginning of the experiment. Since the differential equations governing the gas-channel dynamics are stable, the model converges toward the operating conditions imposed by the inputs, making this initialization a practical and physically consistent starting point for the dynamic model.

- The control inputs are:

$$u = [I\ \dot{n}^{in}_{fuel}\ \dot{n}^{in}_{air}\ y^{in}_{H_2O}\ T_{furnace}\ T^{in}_{fuel}\ T^{in}_{air}]^T \tag{3.2}$$

where $y^{in}_{H_2} = 1 - y^{in}_{H_2O}$.

- The measured output Y:

$$Y = V_s(x, u, \lambda) \tag{3.3}$$

Where V_s is defined in Equation (2.30), and λ is the vector of unknown electrochemical parameters whose elements and units are listed in Table 3.1, and which has to be fitted in order to calibrate the electrochemical model.

Parameters	R_s	E^{ohm}_{act}	E^{an}_{act}	E^{cath}_{act}	γ_{an}	γ_{cath}	ψ_{fuel}	ψ_{air}
Units	$\Omega \cdot cm^2$	J/mol	J/mol	J/mol	A/cm^2	A/cm^2	-	-

Table 3.1: Physical parameters and their units

Even though we consider here eight electrochemical parameters to estimate, other models may include even more parameters. For instance [132, 133], has a model requiring 13 parameters. In this work, we fixed the extra parameters from the literature to slightly reduce the complexity of the parameter identification, such as the exchange density exponent in Equations (2.36), (2.37), and the charge transfer coefficients in the Butler-Volmer Equations (2.33), (2.34) [65, 87].

From the nonlinear state-space in Equation (3.1), it can be seen that the identification problem is nonlinear. Additionally, the challenge is compounded by the presence of a large number of physical parameters requiring identification and a reduced number of available measurements. To address this issue, constrained nonlinear identification techniques offer a potential solution. However, employing such methodologies may result in solutions where some identified parameters saturate at the predefined physical boundaries set by the user. This raises the question of whether these parameters are practically identifiable along the considered excitation trajectory and whether prioritizing their selection over direct identification efforts is advisable. Thus, before presenting the parameter estimation method used, a sensitivity analysis is conducted to assess the sensitivity of the output to local perturbations of the parameters.

Thèse accessible à l'adresse : https://theses.insa-lyon.fr/publication/2026ISAL0017/these.pdf © [Z. Yazbeck], [2026], INSA Lyon, tous droits réservés

3.3 Sensitivity analysis

Sensitivity analysis is used to analyze how changes in the parameters of a model affect its output. Local sensitivity analysis, in particular, examines the impact of small or local variations in parameter values around their nominal values.

Due to the nonlinearity of the model, it is difficult to establish global identifiability, and the analysis therefore focuses on local practical identifiability. In [138], the author clarifies the relation between the sensitivity, which measures the effect of the perturbation of parameters on the output, and the practical identifiability of parameters. Therefore, sensitivity analysis is carried out in order to verify if the output is sufficiently sensitive to the parameters for the input trajectory used. This provides insight into the feasibility of reliably estimating parameters under a particular excitation profile.

In this work, we focus on the local sensitivities of the measured stack voltage with respect to the physical parameters, evaluated along representative operating trajectories and later integrated in the parameter estimation algorithm.

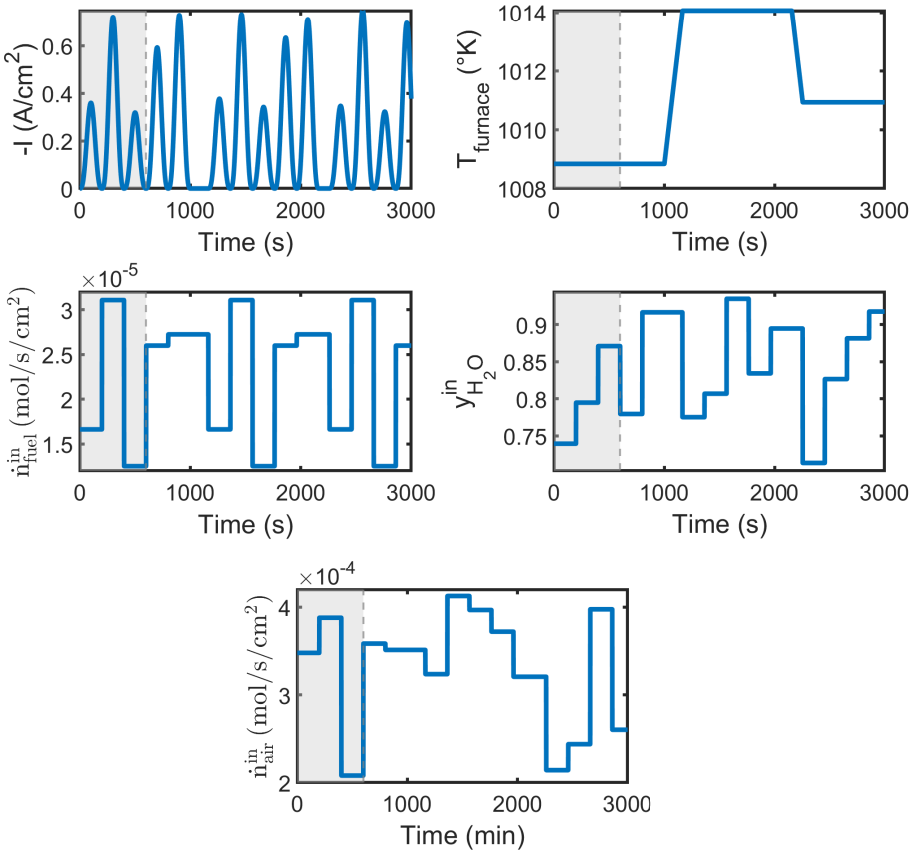

Figure 3.1: Input trajectory for the sensitivity analysis.

A synthetic data set is generated using the model presented in the previous chapter with known parameters (λ^*) to validate the parameter estimation methodology that will be presented

Thèse accessible à l'adresse : https://theses.insa-lyon.fr/publication/2026ISAL0017/these.pdf © [Z. Yazbeck], [2026], INSA Lyon, tous droits réservés

in the next section. The dataset presented in Figure 3.1 consists of multiple current-voltage (IV) polarization curves, which is a standard characterization technique in electrochemical systems such as SOECs [87, 121], simulated across a range of operating temperatures, ramp-rate limitations, inlet fuel flow rates with varying steam molar compositions (e.g., 75-95% H_2O in the inlet fuel flow), and varying air flow rates to emulate experimental conditions and capture parameter sensitivities under different scenarios. A sampling time of t_s = 1 s is used, and the total duration of the profile window is 3000 seconds. To perform sensitivity analysis, each parameter λ_i can be perturbed alone by 20% and 30% around the true parameter value λ_i^*, while the other parameters are kept fixed, and the model is re-simulated with the same experimental input for each perturbation. To clarify the visualization, we only show the sensitivities in the colored region corresponding to the first 500 seconds.

The result of this "one-at-a-time perturbation" analysis is reported in Figure 3.2, where the effect of these perturbations of selected parameters on the voltage profile is illustrated. Thus, intuitively, parameters that have a significant effect on the voltage are considered influential and have high local sensitivity, while other parameters in which the output is almost unaffected are considered to be weakly sensitive to the operating conditions.

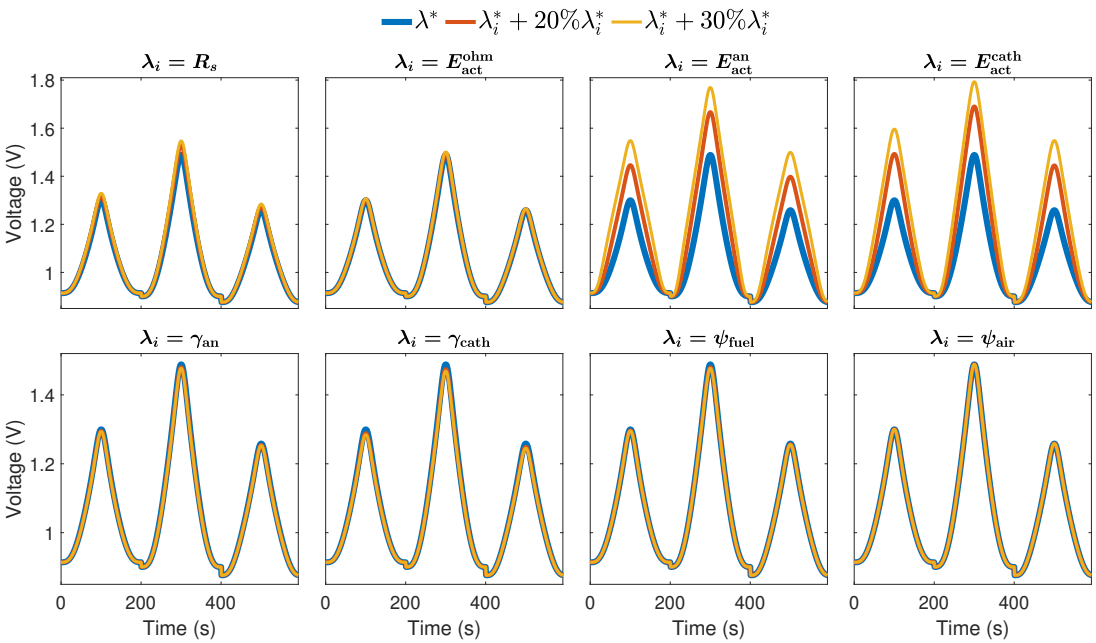

Figure 3.2: Voltage impact of 20-30% parameter perturbations around the nominal parameter vector λ^*.

However, calculating the local sensitivity of the output $\left(\frac{\partial Y}{\partial \lambda}\right)$ using a finite-difference approach can present several drawbacks, because the numerical derivative depends on the chosen perturbation step. If small steps are taken, numerical errors may dominate, and if it is too large, the derivative no longer reflects a local sensitivity. For this reason, an alternative approach based on sensitivity differential equations is considered in the sequel. This approach allows to compute

Thèse accessible à l'adresse : https://theses.insa-lyon.fr/publication/2026ISAL0017/these.pdf © [Z. Yazbeck], [2026], INSA Lyon, tous droits réservés

local sensitivities along a trajectory by augmenting the original state-space model with additional differential equations.

3.3.1 Sensitivity differential equations

The nonlinear state-space model can be presented as an ordinary differential system of equations (ODEs) of the form:

$$\begin{cases} \dot{x} = f(x, \lambda, u) \\ Y = h(x, \lambda, u) \end{cases} \tag{3.4}$$

Denote $x \in R^{n_x}$ is the state vector, $Y \in R^{n_Y}$ is the measured output Equation (3.3), $u \in R^{n_u}$ is the control input Equation (3.2), and $\lambda \in R^{n_\lambda}$ is the vector of parameters to be estimated, where $n_x = 4$, $n_Y = 1$, $n_u = 5$, and $n_\lambda = 8$.

In the context of continuous dynamical systems, local sensitivities can be represented by the first-order partial derivatives of the output of the system with respect to its parameters. Differentiating the state-space equations Equation (3.4) in both sides by λ with the use of the chain rule gives:

$$\begin{aligned} \frac{\partial}{\partial \lambda}\left(\frac{dx}{dt}\right) = \frac{\partial f}{\partial x}\frac{\partial x}{\partial \lambda} + \frac{\partial f}{\partial \lambda}, \quad \Leftrightarrow \quad \frac{d}{dt}\left(\frac{\partial x}{\partial \lambda}\right) &= \frac{\partial f}{\partial x}\frac{\partial x}{\partial \lambda} + \frac{\partial f}{\partial \lambda} \\ \frac{\partial}{\partial \lambda}(Y) = \frac{\partial h}{\partial x}\frac{\partial x}{\partial \lambda} + \frac{\partial h}{\partial \lambda} & \end{aligned} \tag{3.5}$$

Therefore, the total number of equations to integrate is augmented, and the sensitivity differential equations can be written as [139]:

$$\begin{cases} \dot{S}_x = \dfrac{\partial f}{\partial x} S_x + \dfrac{\partial f}{\partial \lambda} \\ S_y = \dfrac{\partial h}{\partial x} S_x + \dfrac{\partial h}{\partial \lambda} \end{cases} \tag{3.6}$$

Where $S_x(\lambda, t) = \dfrac{\partial x}{\partial \lambda}(\lambda, t) \in R^{n_x \times n_\lambda}$, and $S_y(\lambda, t) = \dfrac{\partial Y}{\partial \lambda}(\lambda, t) \in R^{n_Y \times n_\lambda}$ are the sensitivity matrices, defined for each time t.

The Jacobians $\left(\frac{\partial f}{\partial \lambda}\right)$ and $\left(\frac{\partial f}{\partial x}\right)$ in Equation (3.6) are obtained analytically using a symbolic framework, instead of being derived by hand from the model in Equation (3.1). In this work, we used CasADi [140] to build the model symbolically and to generate exact derivatives via algorithmic differentiation, which enables efficient and reliable Jacobian and sensitivity evaluations for the subsequent optimization. The system dynamics are integrated using the IDAS integrator provided by SUNDIALS [141].

Thèse accessible à l'adresse : https://theses.insa-lyon.fr/publication/2026ISAL0017/these.pdf © [Z. Yazbeck], [2026], INSA Lyon, tous droits réservés

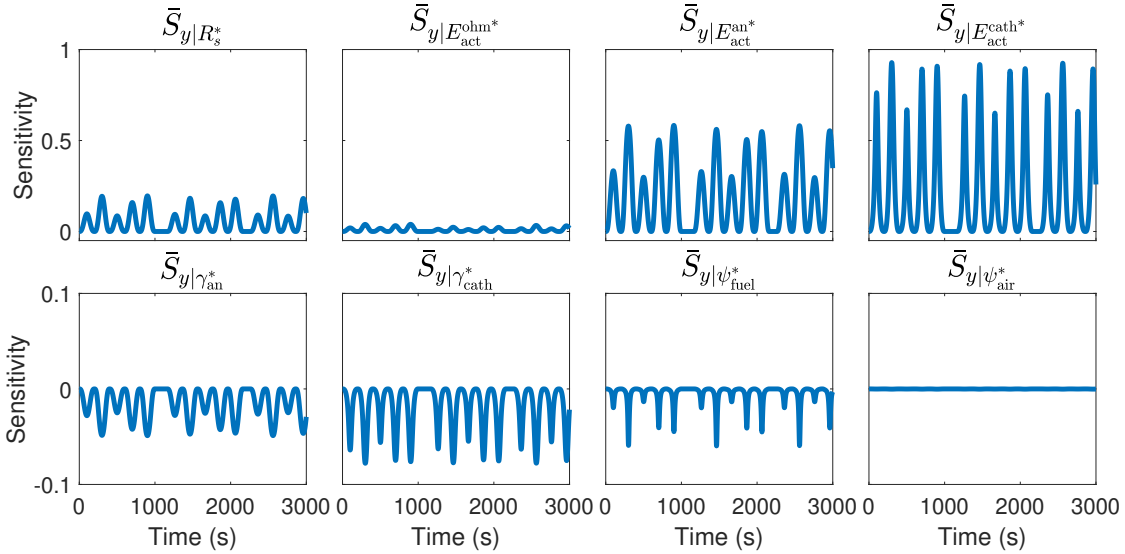

Figure 3.3: Normalized sensitivity magnitudes calculated using sensitivity differential equations with the true parameter vector λ^*.

Thus, normalized local sensitivities computed using Equation (3.6) for the input trajectory in Figure 3.1 are reported in Figure 3.3, and are consistent with those observed in Figure 3.2. The highest normalized sensitivities are associated with E_{act}^{cath} and E_{act}^{an}, whereas R_s, E_{act}^{ohm}, γ_{an}, γ_{cath} and ψ_{fuel} show smaller sensitivities, and ψ_{air} has a sensitivity magnitude close to zero.

3.3.2 Sensitivity equations as a tool for parameter identifiability

As mentioned previously, practical local identifiability of a parameter can be assessed to their sensitivity on the output that can be quantified locally by the sensitivity differential Equations (3.6). These equations describe how the states and thus the output are affected when perturbing the parameter vector λ.

A matrix $S(\lambda, t)$ can be constructed by concatenating the output sensitivities over the whole input trajectory as in Equation (3.7). Then the discrete sensitivity matrix is:

$$S(\lambda,t) = \begin{bmatrix} S_{y,t_1}(\lambda,t_1) \\ \vdots \\ S_{y,t_N}(\lambda,t_N) \end{bmatrix} \in R^{Nn_Y \times n_p}, \tag{3.7}$$

Where $S_{y,t_k} = \frac{\partial Y}{\partial \lambda}(\lambda, t_k)$, for $k = 1, \ldots, N$, where t_k are the sampling instants.

However, practical identifiability of parameters is not governed solely by the individual sensitivity magnitude, but also by the collinearity with other parameter sensitivities, when it exists. For instance, if collinearity exists between the sensitivities of two parameters, a variation in one parameter can be compensated by an opposite variation in the other, which is reflected in the corresponding columns of $S(\lambda, t)$ and leads to an ill-conditioned estimation problem. Thus, in the

Thèse accessible à l'adresse : https://theses.insa-lyon.fr/publication/2026ISAL0017/these.pdf © [Z. Yazbeck], [2026], INSA Lyon, tous droits réservés

following sections, the sensitivity matrix is normalized to take into account the different orders of magnitude of the parameters, and its column vectors are orthogonalized to rank the most informative directions in the parameter space. This information is then integrated in the parameter estimation algorithm to update directions that are well-informed while mitigating the variation of poorly identifiable or highly correlated sensitivity directions.

3.3.3 Parameter identification using grouping-based approach

Before introducing the proposed estimation framework, we briefly present a method from the literature used when sensitivities are highly correlated. This method is based on clustering the parameters manually into groups according to their orthogonalized sensitivity magnitudes, and either do a sequential estimation of the groups [123, 135] or reduce the parameter space to just estimate the highly sensitive parameters [142].

After computing the sensitivity matrix along the input trajectory starting from an initial guess λ_0 chosen within literature ranges [87, 115, 121, 143], $S(t, \lambda_0)$ in Equation (3.7) is normalized to take into account the different order of magnitudes of parameters, so that each column becomes comparable in terms of sensitivity. Thus:

$$S_{y,nrm}(t, \lambda_0) = S(t, \lambda_0)\Gamma, \tag{3.8}$$

where

$$\Gamma = diag\left(\frac{\lambda_0(1)}{\|Y\|}, \ldots, \frac{\lambda_0(n_p)}{\|Y\|}\right), \tag{3.9}$$

The value of λ_0 normalized with respect to λ^* is listed in the second column of Table 3.3, and the true parameter vector is:

$$\lambda^* = [0.22, 120e3, 100e3, 100e3, 1e5, 2.25e5, 0.18, 0.205]^\top$$

The normalized matrix is then orthogonalized to analyze the linear dependence between the sensitivity profiles. A QR factorization with column pivoting can be used to determine an orthogonal matrix Q, an upper triangular matrix R with a decreasing magnitude of the orthogonalized sensitivity magnitudes in its diagonal elements, and a permutation matrix P which determines a new order of sensitivity columns so that the most sensitive parameters appear in the first entries of the parameter vector λ, so that:

$$S_{y,nrm}\, P = QR, \tag{3.10}$$

For the current studied input trajectory, the order of parameters ranking from the most sensitive

Thèse accessible à l'adresse : https://theses.insa-lyon.fr/publication/2026ISAL0017/these.pdf © [Z. Yazbeck], [2026], INSA Lyon, tous droits réservés

to the least is given by:

$$[R_s\ E_{act}^{ohm}\ E_{act}^{an}\ E_{act}^{cath}\ \gamma_{an}\ \gamma_{cath}\ \psi_{fuel}\ \psi_{air}]^\top P = [\ E_{act}^{an}\ R_s\ E_{act}^{cath}\ E_{act}^{ohm}\ \psi_{fuel}\ \gamma_{an}\ \psi_{air}\ \gamma_{cath}]^\top \quad (3.11)$$

Thus, based on the orthogonalized magnitudes $|\mathrm{diag}(R)|$ obtained from the QR-based orthogonalization in Figure 3.4, the parameters can be clustered into different groups according to their influence. Table 3.2 lists the three groups, where the first group contains the most informative parameters, the second group contains moderately sensitive and linearly dependent parameters, whereas the third group contains weakly sensitive or strongly dependent parameters.

The estimation is then performed sequentially, starting with the first group while the remaining groups are kept fixed, then the second group is estimated after, and finally the third. Proceeding in this way limits compensation between parameters identified as highly collinear in the sensitivity analysis and reduces the dimensionality of each optimization stage.

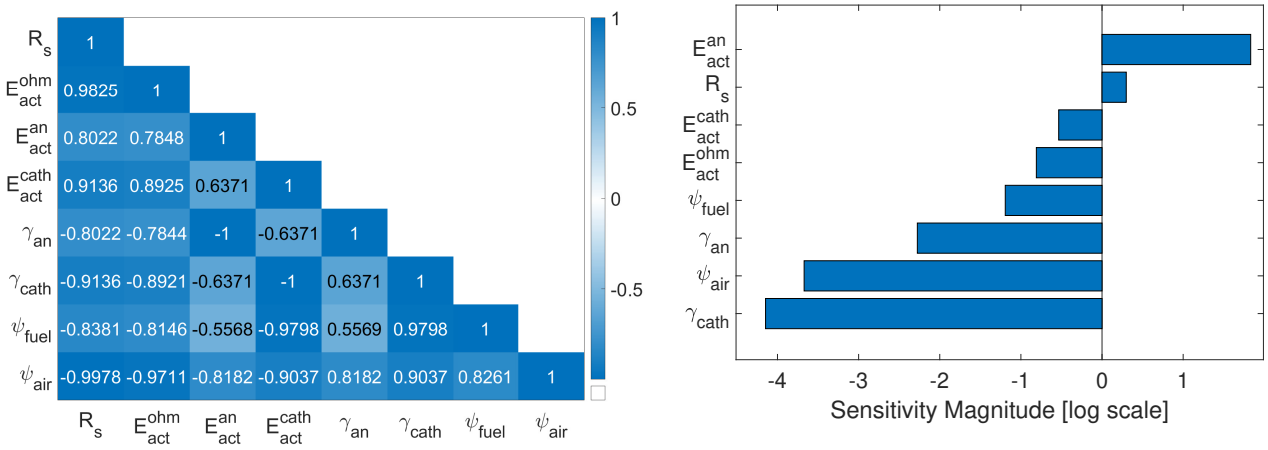

a) Sensitivity collinearity matrix

b) QR-based orthogonalized sorted voltage sensitivity magnitude

Figure 3.4: Sensitivity collinearity and QR-based orthogonalization.

Group 1	Group 2	Group 3
E_{act}^{an}	E_{act}^{cath}	γ_{an}
R_s	E_{act}^{ohm}	ψ_{air}
	ψ_{fuel}	γ_{cath}

Table 3.2: Parameter groups

Table 3.3 presents the normalized estimates using the sequential estimation of the parameter groups in Table 3.2. The optimizer used is the built-in nonlinear least-squares solver `lsqnonlin` in MATLAB with Levenberg-Marquardt algorithm and the initial guess λ_0. It can be seen that

Thèse accessible à l'adresse : https://theses.insa-lyon.fr/publication/2026ISAL0017/these.pdf © [Z. Yazbeck], [2026], INSA Lyon, tous droits réservés

λ	λ_0/λ^*	$\hat{\lambda}/\lambda^*$
R_s	0.7	1.53
E_{act}^{ohm}	1.5	1.5
E_{act}^{an}	1.4	0.908
E_{act}^{cath}	0.75	0.75
γ_{an}	1.25	$6.92e5$
γ_{cath}	1.5	0.38
ψ_{fuel}	1.2	0.71
ψ_{air}	0.75	$2.99e7$

Table 3.3: Parameters estimates with sequential estimation

the estimation of the parameters in the first group is not perfect, but it is still better than for other groups. Some others remain at their initial guesses, while others, particularly γ_{an} and ψ_{air}, which belong to the weakest sensitive group, take values that are not physically meaningful. Although the most of parameters are not well estimated, Figure 3.5 shows a good fit between the voltage model with the estimated parameters and the reference voltage generated using the true parameter vector λ^*, with a root mean square error (RMSE) of 0.0094.

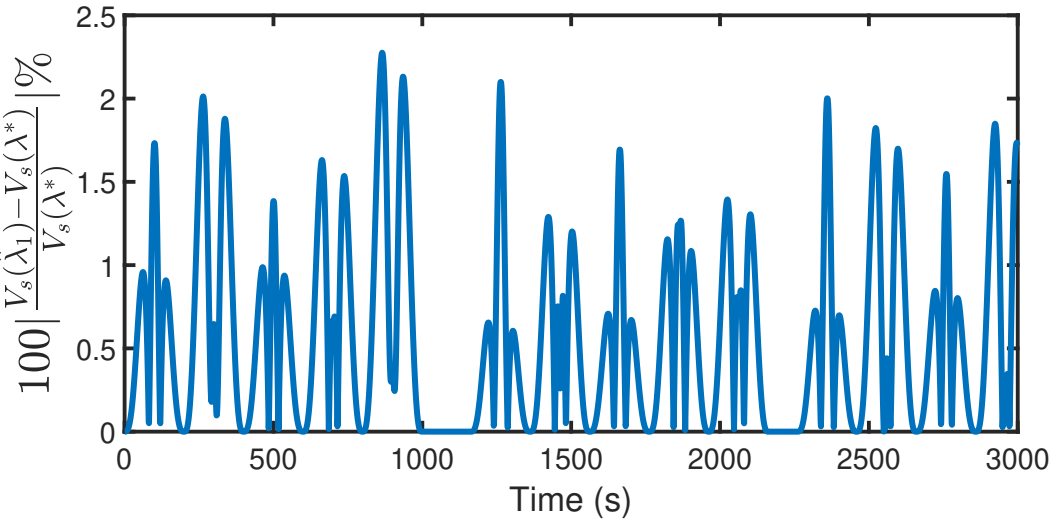

Figure 3.5: Relative error.

However, this estimation method depends on the sensitivity structure evaluated at a single parameter vector, which evolves during the optimization process. This limitation motivates the proposed truncated Levenberg-Marquardt method, which embeds sensitivity evaluation within the optimization loop and uses singular value decomposition (SVD) at each iteration to select the most informative update directions.

Thèse accessible à l'adresse : https://theses.insa-lyon.fr/publication/2026ISAL0017/these.pdf © [Z. Yazbeck], [2026], INSA Lyon, tous droits réservés

3.3.4 Does temperature provide additional information for parameter estimation?

Although both stack voltage and temperature are experimentally available, their information content with respect to the parameters to be estimated is not equivalent. To evaluate whether the temperature measurement could provide additional information for parameter identification, the normalized sensitivities of the stack temperature with respect to the estimated parameters were computed using the same input trajectory, initial parameter vector λ_0, and normalization procedure as those used for the voltage sensitivities presented in Figure 3.4.

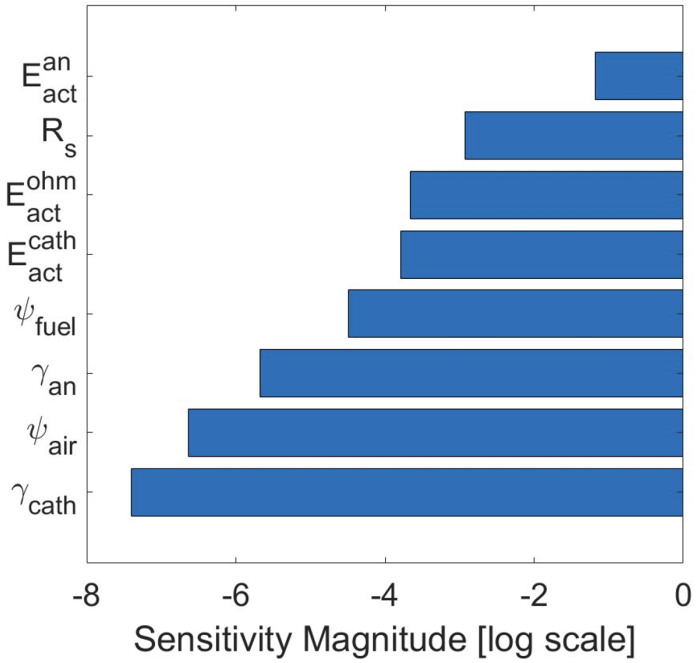

Figure 3.6: QR-based orthogonalized and sorted temperature-sensitivity magnitudes obtained using the input trajectory in Figure 3.1 and the initial parameter vector λ_0.

Compared with the voltage-sensitivity magnitudes presented in Figure 3.4(b), Figure 3.6 shows that the stack temperature is less sensitive to most of the parameters considered for estimation under the investigated operating trajectory. Consequently, including temperature in the parameter-estimation cost function is expected to provide only limited additional information under these conditions. The stack voltage is therefore retained as the measured output for the parameter-identification procedure developed in the following sections.
This choice is specific to the parameter-identification objective and does not imply that temperature is uninformative for monitoring. In Chapter 4, temperature is included among the measurements used by the Square-Root Unscented Kalman Filter (SR-UKF), since it provides direct information about the thermal state of the stack and contributes to state reconstruction and fault detection.

Thèse accessible à l'adresse : https://theses.insa-lyon.fr/publication/2026ISAL0017/these.pdf © [Z. Yazbeck], [2026], INSA Lyon, tous droits réservés

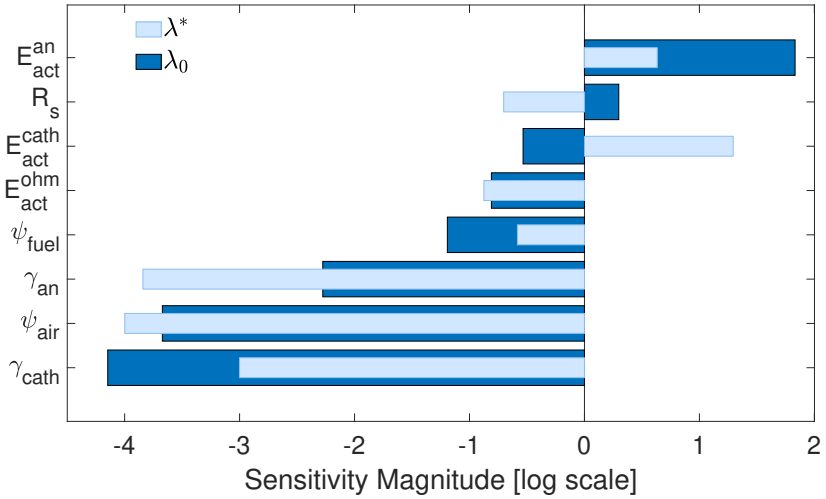

Figure 3.7: Orthogonalized sensitivity magnitudes with true parameter vector (λ^*) and an initial guess λ_0 .

3.4 Sensitivity function-based parameter identification

The proposed parameter identification methodology is based on the Levenberg-Marquardt (LM) method, which combines the rapid convergence of Gauss-Newton when initial conditions are close to the optimum, with the stability of gradient descent in poorly initialized or ill-conditioned problems [131]. Truncating the sensitivity matrix in LM based on a Singular Value Decomposition (SVD) automates the selection of update directions, prioritizing orthogonal, high-sensitivity directions while taking safe small steps for low-sensitivity or noise dominated parameters. This not only prevents non-physical parameter values and divergence, but also significantly reduces sensitivity to measurement noise. The methodology is validated using simulations with known parameters, testing it with different initial guesses (within the acceptable range) and with output with added Gaussian noise, complemented by confidence-interval calculations, and applied to experimental data.

3.4.1 Truncated Levenberg-Marquardt method

It is crucial to note that parameter sensitivities are local and depend on the input trajectory used and the parameter vector λ. This is highlighted in Figure 3.7, where orthogonalized sensitivities are computed with λ^*, the true parameter vector, and λ_0, the initial guess for the parameter estimation algorithm, showing a variation in sensitivity magnitudes.

In nonlinear systems like the SOES model, the sensitivity matrix $S(\lambda, t)$ evolves as λ moves through the parameter space during optimization. A parameter that appears weakly identifiable at the initial guess may become more sensitive near the solution. Therefore, sensitivity must be re-evaluated at each iteration in optimization to prevent excluding parameters that may later become

Thèse accessible à l'adresse : https://theses.insa-lyon.fr/publication/2026ISAL0017/these.pdf © [Z. Yazbeck], [2026], INSA Lyon, tous droits réservés

informative and to avoid rank deficiency of $S^\top S$. This dynamic reassessment is integrated into the truncated Levenberg-Marquardt (TLM) algorithm, which combines Gauss-Newton with gradient descent through an adaptive damping parameter β_k.

To present the methodology, we first formulate the parameter estimation problem as a nonlinear least-squares problem:

$$\min_{\lambda} ||\epsilon(\lambda)||_2^2, \qquad \text{where } \epsilon_k(\lambda) = V_s(\lambda, t_k) - V_s^{exp}(t_k),), \quad k = 1, \ldots, N_t. \tag{3.12}$$

Where k indexes the time steps, $V_s^{exp}(t_k)$ is the experimentally measured voltage, $V_s(\lambda, t_k)$ is the prediction of the voltage model at time step k, and N is the number of sampling times. Thus $\dfrac{\partial \epsilon(\lambda)}{\partial \lambda} = S(\lambda, t)$.
Levenberg-Marquardt (LM) augments the Gauss-Newton method by adding an identity matrix as regularization term:

$$\begin{aligned} \lambda_{k+1} &= \lambda_k - \left(\frac{\partial \epsilon(\lambda_k)}{\partial \lambda}^\top \frac{\partial \epsilon(\lambda_k)}{\partial \lambda} + \beta_k I\right)^{-1} \frac{\partial \epsilon(\lambda_k)}{\partial \lambda}^\top \epsilon(\lambda_k) \\ &= \lambda_k - \left(S(\lambda_k, t)^\top S(\lambda_k, t) + \beta_k I\right)^{-1} S(\lambda_k, t)^\top \epsilon(\lambda_k) \end{aligned} \tag{3.13}$$

The damping parameter β_k is adjusted to reduce the cost, using the delayed gratification strategy for a systematic update of β_k [144].
The proposed parameter estimation methodology consists of two steps:

1. Normalization: Because parameters have different scales, we normalize the columns of $S(\lambda, t)$ by multiplying it by the current absolute parameter magnitude (λ_k), since the order of magnitude of the voltage is 1. Thus

$$S_{nrm} = S\Gamma, \quad \text{where } \Gamma = diag\left(\frac{|\lambda_k|}{||y||}\right), \tag{3.14}$$

2. Truncation: At each iteration, we compute the SVD of the normalized sensitivity, thus:

$$S_{nrm} = U\,\Sigma\,V^\top, \text{ where } \Sigma = diag(\sigma_1, \ldots, \sigma_{n_p}), \tag{3.15}$$

and truncate directions to exclude negligible informative directions using the relative and absolute tolerances:

$$\sigma_{thr} = \max\{\sigma_1 \times TOL_{rel},\ TOL_{abs}\}, \tag{3.16}$$

with $TOL_{rel} = 10^{-3}$ and $TOL_{abs} = 10^{-1}$. Thus, the truncated sensitivity matrix is as follow:

$$S_{nrm}^{trc} = U_{(:,\mathcal{I})}\, diag(\sigma_{\mathcal{I}})\, V_{(:,\mathcal{I})}^\top, \quad \mathcal{I} = \{i : \sigma_i \geq \sigma_{thr}\}, \tag{3.17}$$

Thèse accessible à l'adresse : https://theses.insa-lyon.fr/publication/2026ISAL0017/these.pdf © [Z. Yazbeck], [2026], INSA Lyon, tous droits réservés

This truncation suppresses ill-conditioned, noise-amplifying directions while prioritizing well conditioned, informative and independent directions, which is re-assessed at each iteration, instead of using fixed *a priori* knowledge of linear dependence between the output sensitivity to different parameters as in [123], because sensitivities evolve along the solution path.

Thus, truncated Levenberg-Marquardt (TLM) methodology addresses highly correlated sensitivity directions without permanently removing parameters, and previously truncated directions can re-enter the solution subspace when their sensitivity grows. Thus the Truncated Levenberg-Marquardt (TLM) iteration is:

$$\lambda_{k+1} = \lambda_k - \Gamma\Big({S_{nrm}^{trc}}^{\top} S_{nrm}^{trc} + \beta_k I\Big)^{-1} {S_{nrm}^{trc}}^{\top} \epsilon \tag{3.18}$$

TLM and LM are compared subsequently with `fmincon`, an optimizer that by default uses the interior-point algorithm, and with truncated Gauss-Newton (TGN), defined as:

$$\lambda_{k+1} = \lambda_k - \mu_k \Gamma\Big({S_{nrm}^{trc}}^{\top} S_{nrm}^{trc}\Big)^{-1} {S_{nrm}^{trc}}^{\top} \epsilon \tag{3.19}$$

Where μ_k is updated using a line search algorithm [145].

3.4.2 Estimation results for synthetic data

Different parameter estimation algorithms are presented in this subsection to estimate the parameter vector λ for the input excitation in Figure 3.1, generated with the same λ^* and initialized from the same initial guess λ_0 chosen in the previous section where sequential parameter estimation was performed.

For the noise-free output voltage (we will refer to this as case N_0), the normalized estimates from different optimizers are listed in Table 3.4, where bold values indicate poor estimates. Using `fmincon`, which is a constrained optimization with only positivity constraint used here, the estimates of ψ_{air} and ψ_{fuel} blow up to values that do not have physical meaning. The output is weakly sensitive along these sensitivity directions, so the optimizer can assign widely different parameter values with little effect on the voltage. The truncated Gauss-Newton (TGN) scheme shows poor estimation of parameters, especially for R_s, E_{act}^{cath}, which are known from Figure 3.7 to have large impacts on the output, the divergence is consistent with an initialization relatively far from λ^*. In contrast, LM and TLM recover R_s, E_{act}^{ohm}, E_{act}^{an}, and E_{act}^{cath} well, but the remaining parameters remain very close to their initial guesses, indicating limited sensitivity during optimization. This can be highlighted in Figure 3.9, where the rank of S in each iteration shows the dimension of the updated subspace of parameters.

Gaussian noise is added to the output, so the observed data is:

$$y_{obs}(t) = h(x, \lambda^*, u) + v(t) \tag{3.20}$$

Thèse accessible à l'adresse : https://theses.insa-lyon.fr/publication/2026ISAL0017/these.pdf © [Z. Yazbeck], [2026], INSA Lyon, tous droits réservés

Table 3.4: Estimation on noise-free output (N_0)

λ^*	$\frac{\lambda_0}{\lambda^*}$	$\frac{\hat{\lambda}_{fmincon}}{\lambda^*}$	$\frac{\hat{\lambda}_{TGN}}{\lambda^*}$	$\frac{\hat{\lambda}_{LM}}{\lambda^*}$	$\frac{\hat{\lambda}_{TLM}}{\lambda^*}$
R_s^*	0.7	1.28	**0.048**	0.95	1.08
E_{act}^{ohm*}	1.5	1.5	1.16	0.97	1.15
E_{act}^{an*}	1.4	1.06	1.16	1.02	0.96
E_{act}^{cath*}	0.75	0.74	**0.61**	1.03	1.04
${\gamma_{an}}^*$	1.25	1.27	1.2	1.25	1.26
${\gamma_{cath}}^*$	1.5	1.5	1.52	1.4	1.49
${\psi_{fuel}}^*$	1.2	**8.04e4**	**0.375**	0.94	1.19
${\psi_{air}}^*$	0.75	**8.03e5**	0.75	0.75	0.76

Table 3.5: Estimation under noisy output (6%) (N_1)

λ^*	$\frac{\lambda_0}{\lambda^*}$	$\frac{\hat{\lambda}_{fmincon}}{\lambda^*}$	$\frac{\hat{\lambda}_{TGN}}{\lambda^*}$	$\frac{\hat{\lambda}_{LM}}{\lambda^*}$	$\frac{\hat{\lambda}_{TLM}}{\lambda^*}$
R_s^*	0.7	1.56	**0.01**	1.32	1.10
E_{act}^{ohm*}	1.5	1.5	1.14	0.87	1.16
E_{act}^{an*}	1.4	0.93	1.22	**0.33**	0.95
E_{act}^{cath*}	0.75	0.74	**0.61**	1.04	1.03
${\gamma_{an}}^*$	1.25	1.28	1.19	1.27	1.26
${\gamma_{cath}}^*$	1.5	1.50	1.51	1.82	1.49
${\psi_{fuel}}^*$	1.2	**1.09e5**	**0.018**	0.86	1.19
${\psi_{air}}^*$	0.75	**1.09e5**	0.74	0.75	0.75

Thèse accessible à l'adresse : https://theses.insa-lyon.fr/publication/2026ISAL0017/these.pdf © [Z. Yazbeck], [2026], INSA Lyon, tous droits réservés

where $v(t) \sim N(0, \sigma_y^2)$. In this example, a noise level of 6% (standard deviation) is used, and we refer to this as case N_1.
The estimation results are listed in Table 3.5. In this case, TLM remains nearly unaffected by noise, and the steps taken by the damping factor β_k are illustrated in Figure 3.10 under noise-free measurements (N_0). In contrast, LM degrades noticeably for some parameters, specifically E_{act}^{an} and γ_{cath} under noisy measurement. The general trends for `fmincon` and TGN remain the same: estimates are affected by noise, `fmincon` returns very large values for ψ_{fuel} and ψ_{air}, and TGN yields poor estimation, especially for R_s, E_{act}^{cath} and ψ_{fuel}, as in N_0.

Figure 3.11 shows the absolute voltage error for the input trajectory used by the different algorithms in the N_0 and N_1 cases. LM and TLM achieve the smallest output errors in both cases less than 0.9% (RMSE: LM-N_0 0.0039, N_1 0.0044; TLM-N_0 0.0040, N_1 0.0042). Whereas `fmincon` shows larger errors, up to about 5% (RMSE: N_0 0.0169; N_1 0.0170), and TGN show large absolute errors, up to 20% (RMSE: N_0 0.0383; N_1 0.0973). The evolution of the cost function defined in Equation (3.12) for different algorithms at each iteration is presented in Figure 3.8, where it can be seen that LM and TLM are the fastest algorithms to converge. This figure also confirms that a good output fit does not necessarily imply accurate or identifiable parameter estimates. The computation times of different optimizers in the N_0 and N_1 cases are reported in Table 3.6. In case N_0, LM and TLM require the same number of iterations as shown in Figure 3.8, however, TLM is slower because it includes SVD decomposition as an additional step. All computations were performed on a PC with an Intel 11th Gen Core i7-11850H CPU at 2.50 GHz and 32 GB of RAM.

Table 3.6: Computation time in minutes for N_0 and N_1 cases

Algorithm	N_0	N_1
LM	4.2 mins	6.03 mins
TLM	4.418 mins	4.69 mins
`fmincon`	64.4 mins	91.8 mins
TGN	4.53 mins	15.12 mins

Thèse accessible à l'adresse : https://theses.insa-lyon.fr/publication/2026ISAL0017/these.pdf © [Z. Yazbeck], [2026], INSA Lyon, tous droits réservés

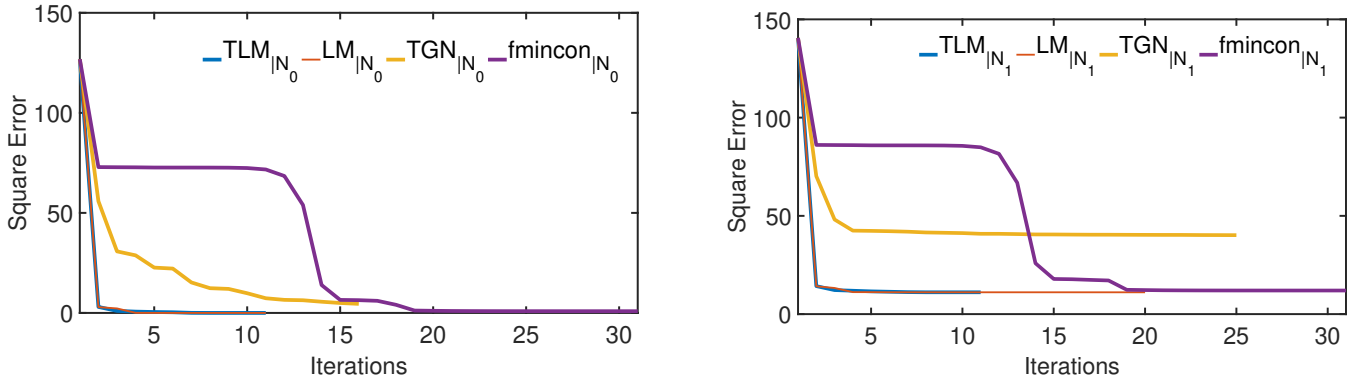

Figure 3.8: Evolution of the squared error versus iterations for different optimizers under noise-free measurements (left) and noisy measurements (right).

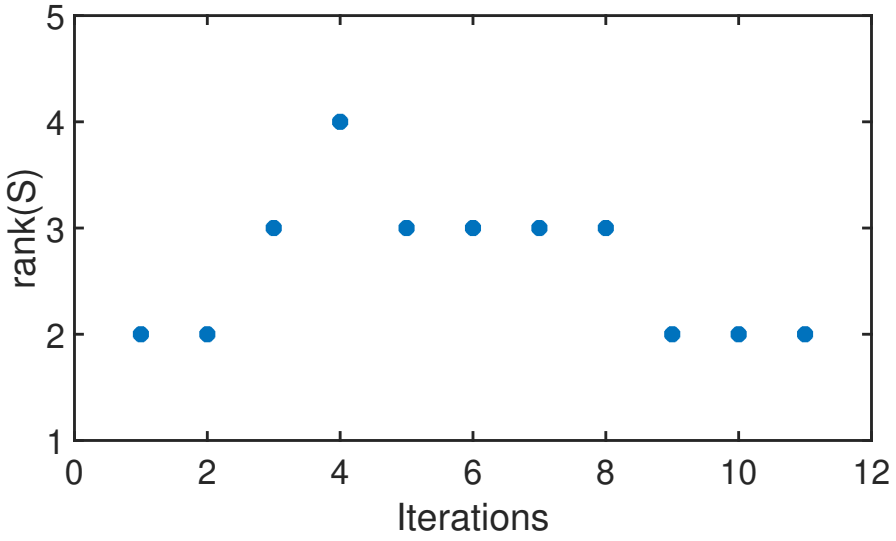

Figure 3.9: Number of parameters updated in each iteration with TLM algorithm under noise-free measurements (N_0)

Thèse accessible à l'adresse : https://theses.insa-lyon.fr/publication/2026ISAL0017/these.pdf © [Z. Yazbeck], [2026], INSA Lyon, tous droits réservés

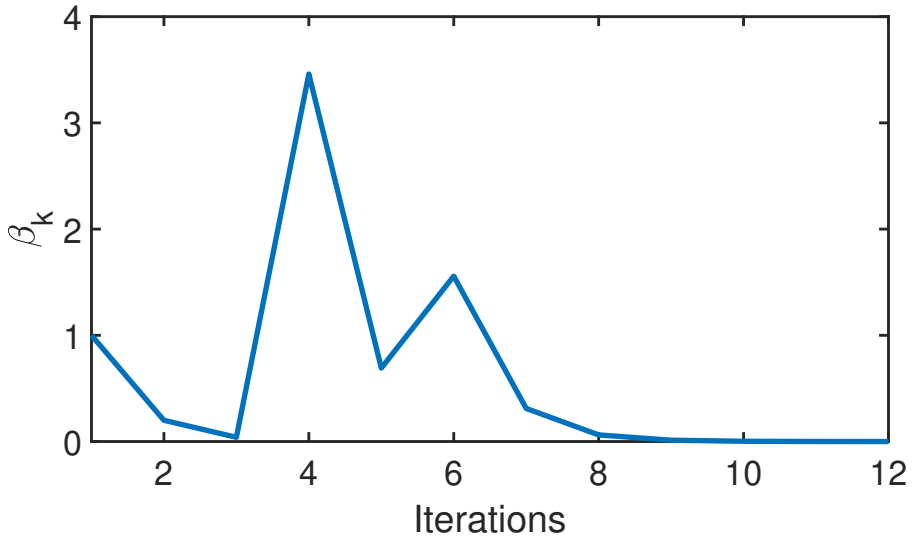

Figure 3.10: Evolution of β_k in TLM algorithm under noise-free measurements (N_0)

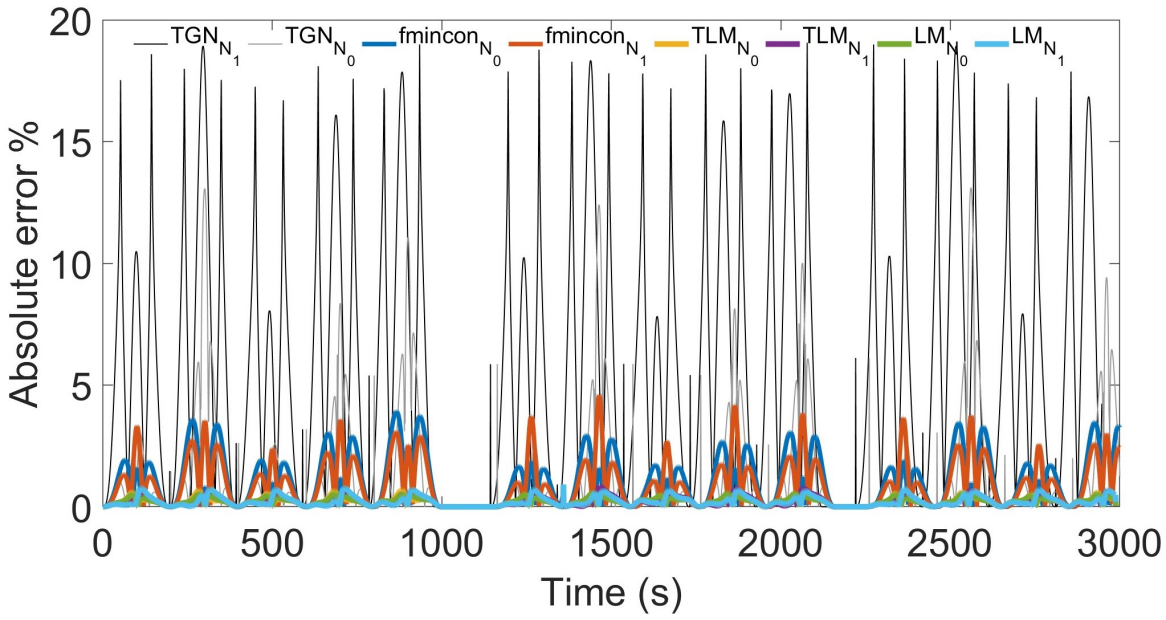

Figure 3.11: Absolute voltage error between simulated and noise-free observed output for different optimizers

3.5 Monte-Carlo Simulation

To further study the influence of both initialization and measurement noise on the estimates using the truncated Levenberg-Marquardt method, a Monte Carlo study was carried out. 50 scenarios of current-voltage (IV) profiles were first generated by varying the the operating conditions

Thèse accessible à l'adresse : https://theses.insa-lyon.fr/publication/2026ISAL0017/these.pdf © [Z. Yazbeck], [2026], INSA Lyon, tous droits réservés

($T_{furnace}, \dot{n}^{in}_{air}, \dot{n}^{in}_{fuel}, y^{in}_{H_2O}$,and I), respecting the physical constraints, thus:

$$968 \leq T_{furnace} \leq 1022\ (^{\circ}K) \tag{3.21}$$

$$9e-6 \leq \dot{n}^{in}_{fuel} \leq 4.2e-5\ (mol/s/cm^2) \tag{3.22}$$

$$1.2e-4 \leq \dot{n}^{in}_{air} \leq 4.2e-4\ (mol/s/cm^2) \tag{3.23}$$

$$0.7\ \leq y^{in}_{H_2O} \leq 0.95, \qquad y^{in}_{H_2} = 1 - y^{in}_{H_2O} \tag{3.24}$$

$$\begin{aligned} 0\ &\leq I \leq I_{90\%\,S.C.}, \\ \text{where } S.C. &= \frac{I}{2F y^{in}_{H_2O} \dot{n}^{in}_{fuel}} \Rightarrow I_{90\%\,S.C.} = 0.9 \times 2F y^{in}_{H_2O} \dot{n}^{in}_{fuel} \end{aligned} \tag{3.25}$$

$$|T_{furnace}(t_{k+1}) - T_{furnace}(t_k)| \leq 0.033^{\circ}K/s \tag{3.26}$$

In addition to the minimum and maximum bounds taken for each variable in Equations (3.21)-(3.24) and the ramp rate of the furnace temperature variation in Equations (3.26), an upper limit on the maximum current density is considered in Equation (3.25) to ensure that the steam conversion (S.C.) does not exceed 90%, thus ensuring safe operating conditions. For each scenario with a duration of 3000 s and a sampling time of 1 s, the synthetic stack voltage was simulated using the parameter vector λ^* with the nonlinear Solid Oxide electrolysis Stack (SOES) model and used as a reference for parameter estimation using different initial guesses and two noise levels.

Table 3.7: Normalized initial guesses used in the Monte Carlo simulation.

λ	$\frac{IG_1}{\lambda^*}$	$\frac{IG_2}{\lambda^*}$	$\frac{IG_3}{\lambda^*}$	$\frac{IG_4}{\lambda^*}$	$\frac{IG_5}{\lambda^*}$	$\frac{IG_6}{\lambda^*}$	$\frac{IG_7}{\lambda^*}$	$\frac{IG_8}{\lambda^*}$	$\frac{IG_9}{\lambda^*}$	$\frac{IG_{10}}{\lambda^*}$
R_s	0.5	1.5	0.4	0.8	0.75	0.3	0.6	0.7	0.9	2.3
$E^{\text{ohm}}_{\text{act}}$	0.8	0.7	1.3	0.8	1.4	1.6	1.8	1.5	1.8	1.2
$E^{\text{an}}_{\text{act}}$	1.2	1.5	1.3	1.3	1.75	1.5	1.2	1.4	1.35	1.25
$E^{\text{cath}}_{\text{act}}$	1.5	0.7	1.5	0.8	0.75	1.35	1.6	0.75	0.65	1.45
γ_{an}	0.6	1.3	1.6	0.8	0.75	0.85	0.95	1.25	1.8	1.6
γ_{cath}	1.3	0.7	0.8	1.2	1.4	0.7	0.75	1.5	1.4	1.5
ψ_{fuel}	1.3	0.8	1.5	1.2	1.4	1.8	1.45	1.2	0.9	1.3
ψ_{air}	0.9	1.3	0.8	1.5	2	2	1.3	0.75	0.9	1.7

Ten initial guesses, listed in Table 3.7, are used to estimate the scenarios 50 with the TLM algorithm. The resulting estimates are presented in normalized form and summarized in Figures 3.12-3.21, where each subplot shows the distribution of the estimated parameters for a given initial guess and the three noise cases N_0, N_1 and N_2. Here, N_0 denotes noise-free voltage, while N_1 and N_2 correspond to Gaussian noise levels (standard deviations of 3% and 6%, respectively)

Thèse accessible à l'adresse : https://theses.insa-lyon.fr/publication/2026ISAL0017/these.pdf © [Z. Yazbeck], [2026], INSA Lyon, tous droits réservés

added independently to each sample of the synthetic output.

For nonlinear least-squares problems, the estimates exhibit some dependence on the initial guess as the optimization is local, and this is confirmed by the estimates obtained for the different initial guesses used across the 50 scenarios, and is more noticeable for parameters to which the output is weakly sensitive (γ_{an}, γ_{cath} and ψ_{air}). However, even when starting from relatively poor initial guess, the estimates for the parameters identified as most informative in the sensitivity analysis (R_s, E_{act}^{ohm}, E_{act}^{an} and E_{act}^{cath}), converge close to the true values for almost all scenarios and initial guesses. Nonetheless, their accuracy is affected by the richness of the scenario inputs, since some scenarios combine the operating conditions in a way that excites the system more than others. The average bias introduced by the different initial guesses used is relatively limited for the well-informed directions, confirming the effectiveness of the truncation strategy in guiding the search of the solution along sensitive directions. Regarding the least sensitive parameters (γ_{an}, γ_{cath} and ψ_{air} which belong to Group 3 in the estimation Table 3.2), their estimates remain around their initial guesses regardless of the IV scenario or the noise level. Therefore, these estimates cannot be trusted, even though the output voltage fit is acceptable.

The impact of measurement noise can be assessed by comparing N_0, N_1 and N_2 in Figures 3.12-3.21. The dispersion of the estimated parameters increases slightly, when adding 3% and 6% Gaussian noise to the output voltage, but the effect on the estimates remains moderate particularly for the informative parameters, due to the truncation of the small singular values in the normalized sensitivity matrix, which prevents the noise-amplifying directions from dominating the update and limits the propagation of measurement noise into the parameter estimates. However, the effect of the noise on the weakly sensitive parameters (γ_{an}, γ_{cath} and ψ_{air}) is much less important than the effect of the initial guess.

Overall, these simulations under a wide range of scenarios and realistic initialization shows that the TLM yields good estimates for the most sensitive electrochemical parameters and moderate noise conditions, while the microstructural and pre-exponential factors of the exchange current densities parameters in Group 3 remain practically unidentifiable with the standard IV-type experiments. This motivates, in the next section, the design of optimal experimental design to generate more informative input trajectories.

Thèse accessible à l'adresse : https://theses.insa-lyon.fr/publication/2026ISAL0017/these.pdf © [Z. Yazbeck], [2026], INSA Lyon, tous droits réservés

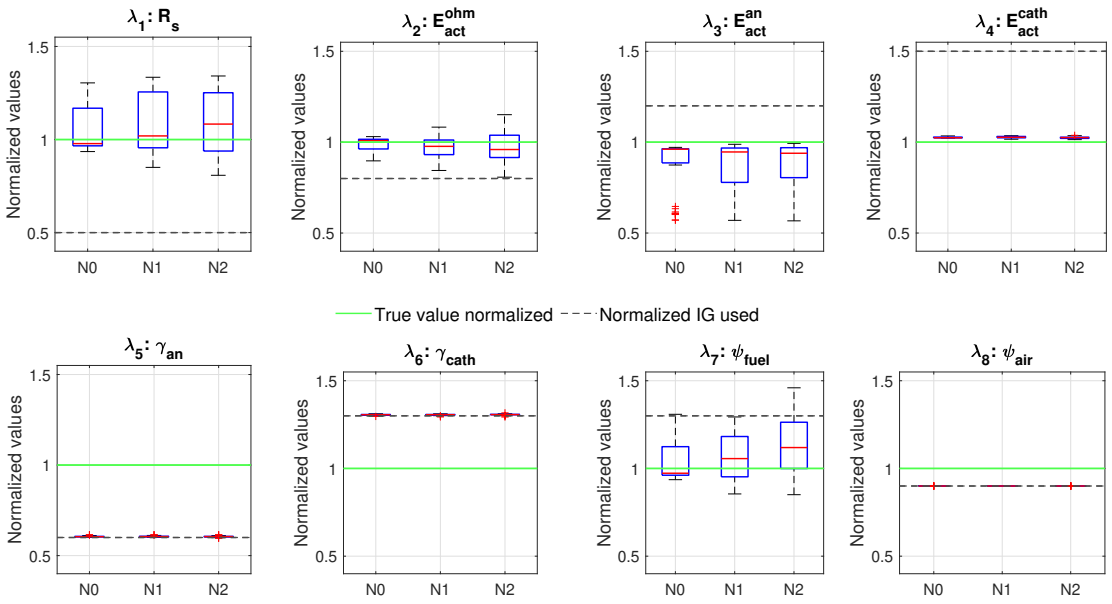

Figure 3.12: Parameter estimation using TLM starting from IG1.

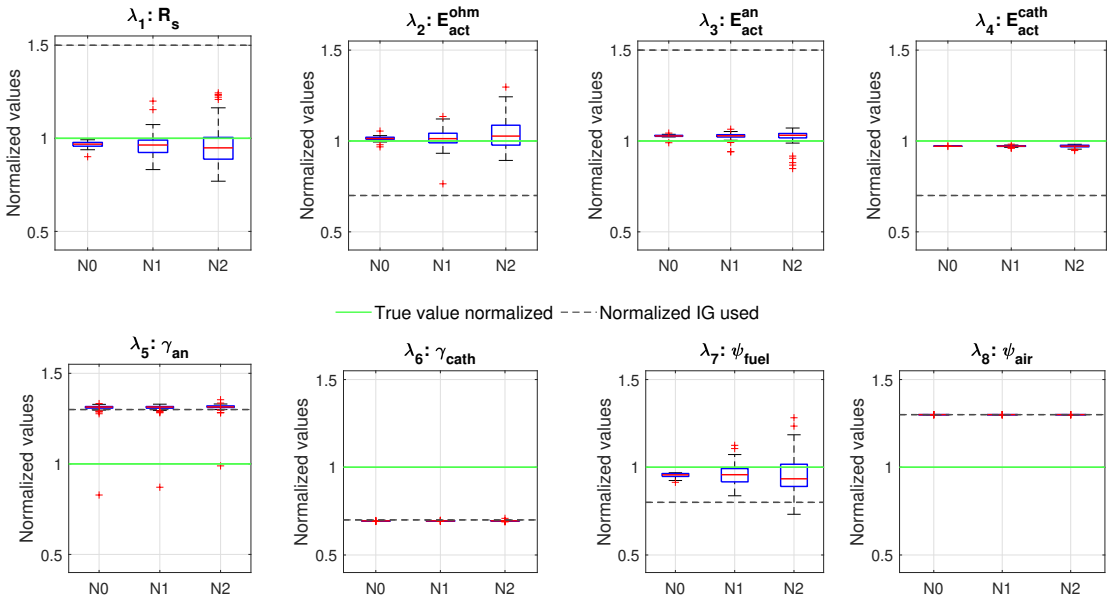

Figure 3.13: Parameter estimation using TLM starting from IG2

Thèse accessible à l'adresse : https://theses.insa-lyon.fr/publication/2026ISAL0017/these.pdf © [Z. Yazbeck], [2026], INSA Lyon, tous droits réservés

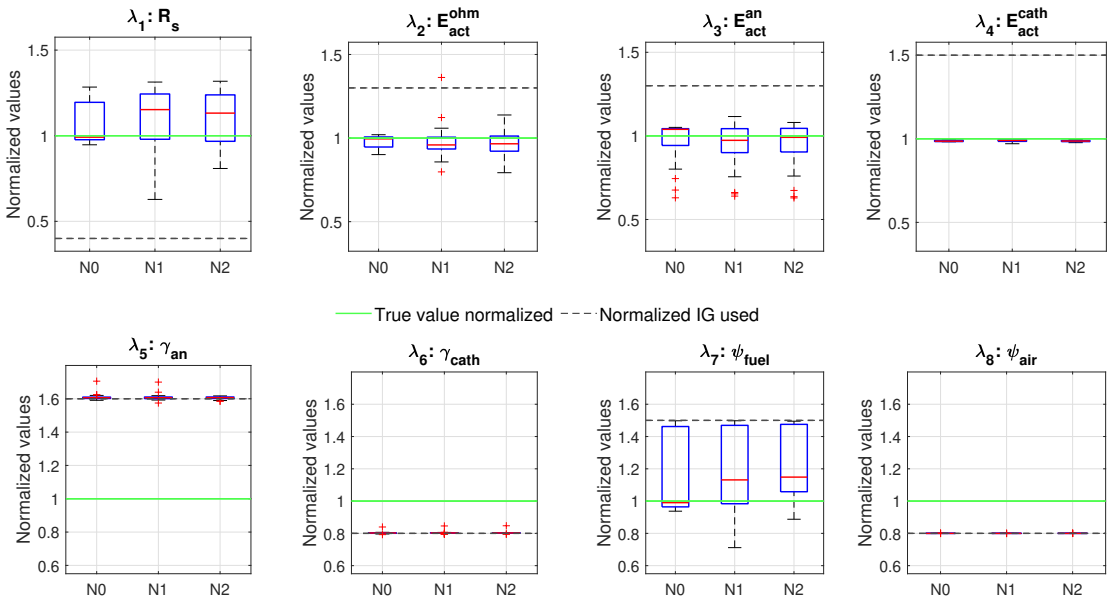

Figure 3.14: Parameter estimation using TLM starting from IG3

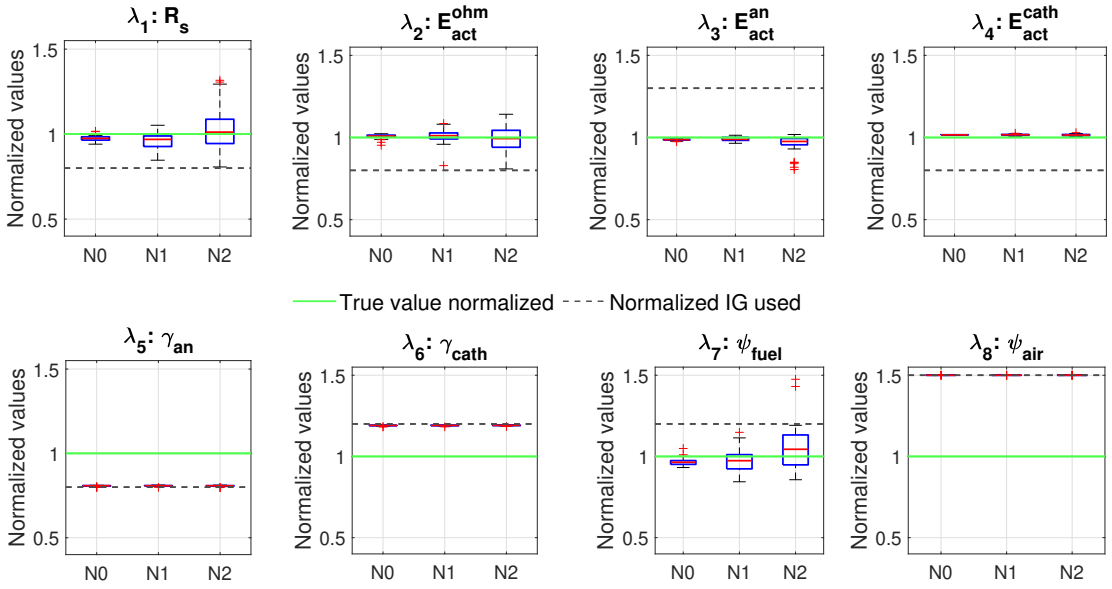

Figure 3.15: Parameter estimation using TLM starting from IG4

Thèse accessible à l'adresse : https://theses.insa-lyon.fr/publication/2026ISAL0017/these.pdf © [Z. Yazbeck], [2026], INSA Lyon, tous droits réservés

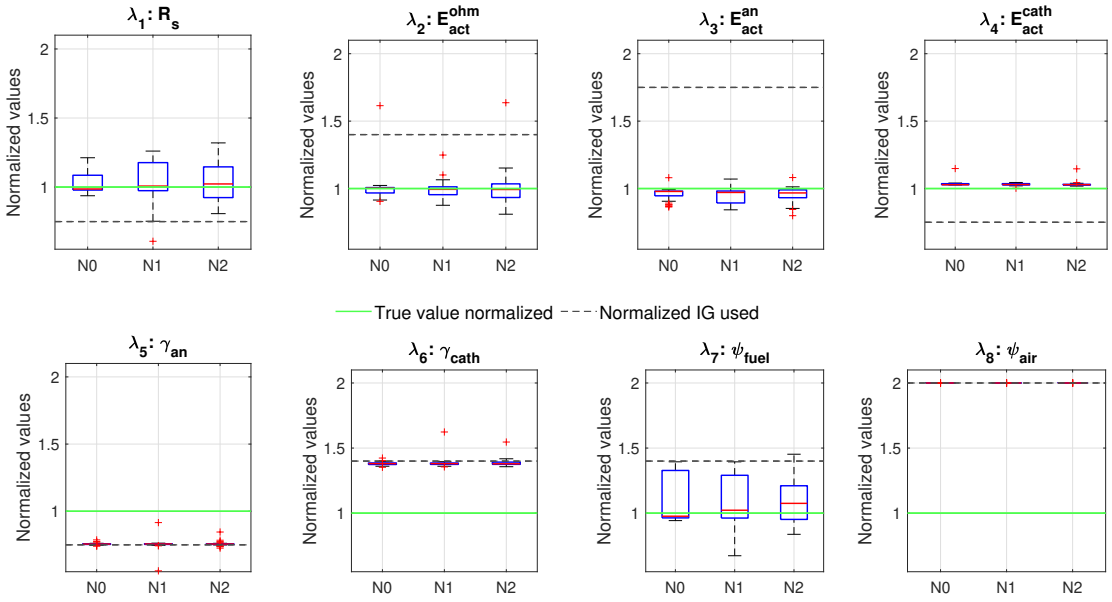

Figure 3.16: Parameter estimation using TLM starting from IG5

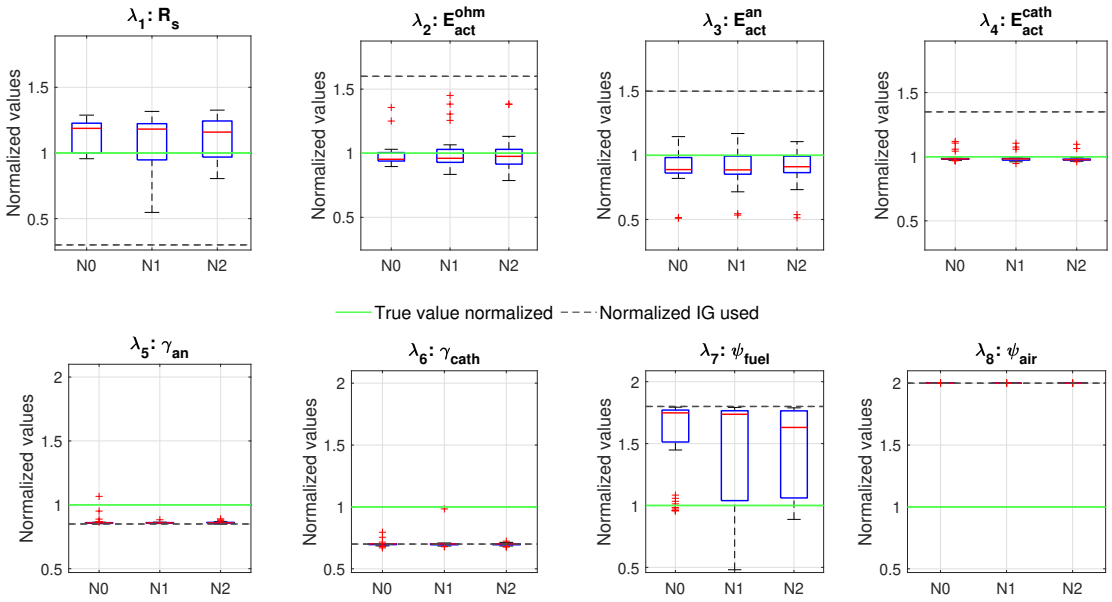

Figure 3.17: Parameter estimation using TLM starting from IG6

Thèse accessible à l'adresse : https://theses.insa-lyon.fr/publication/2026ISAL0017/these.pdf © [Z. Yazbeck], [2026], INSA Lyon, tous droits réservés

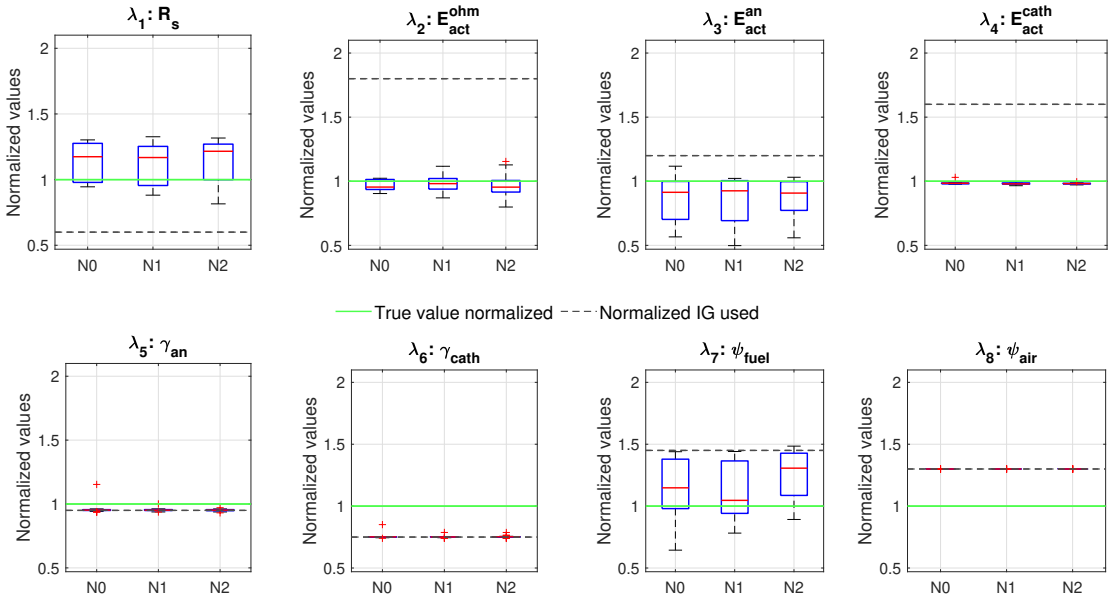

Figure 3.18: Parameter estimation using TLM starting from IG7

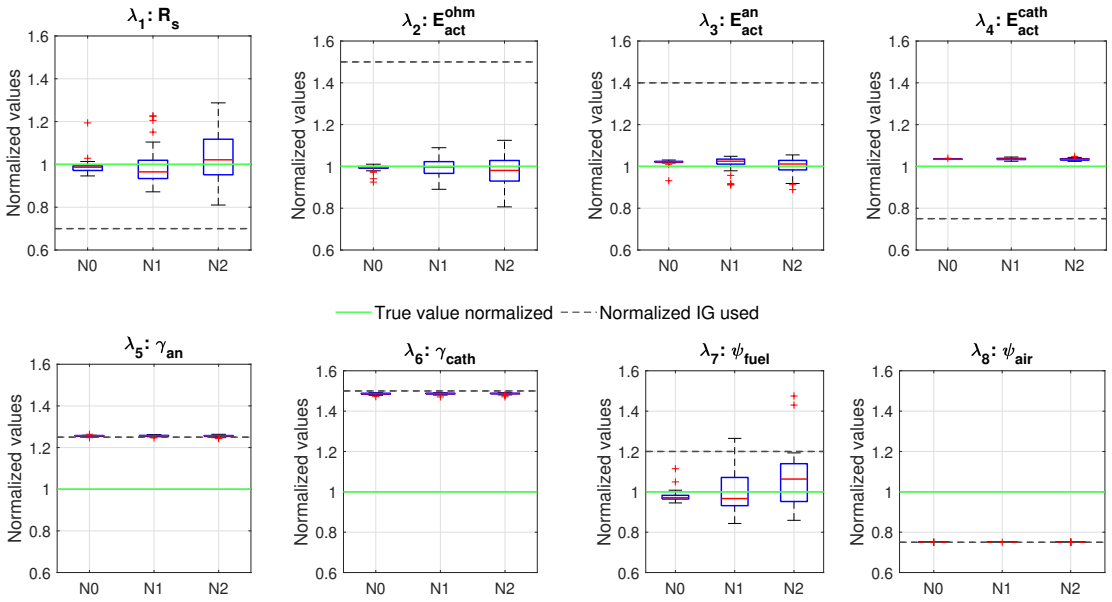

Figure 3.19: Parameter estimation using TLM starting from IG8

Thèse accessible à l'adresse : https://theses.insa-lyon.fr/publication/2026ISAL0017/these.pdf © [Z. Yazbeck], [2026], INSA Lyon, tous droits réservés

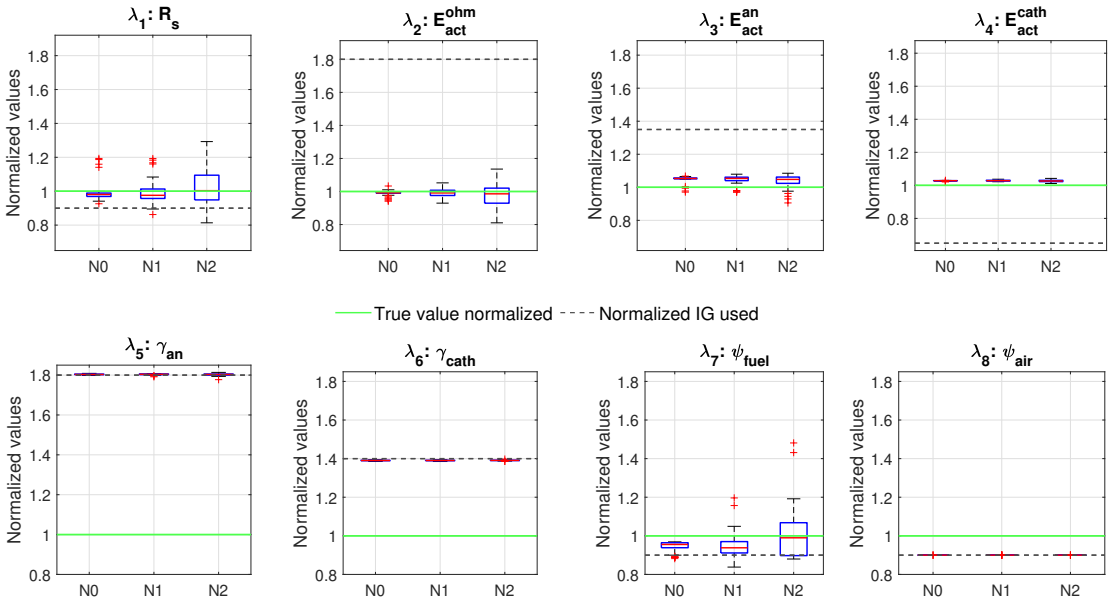

Figure 3.20: Parameter estimation using TLM starting from IG9

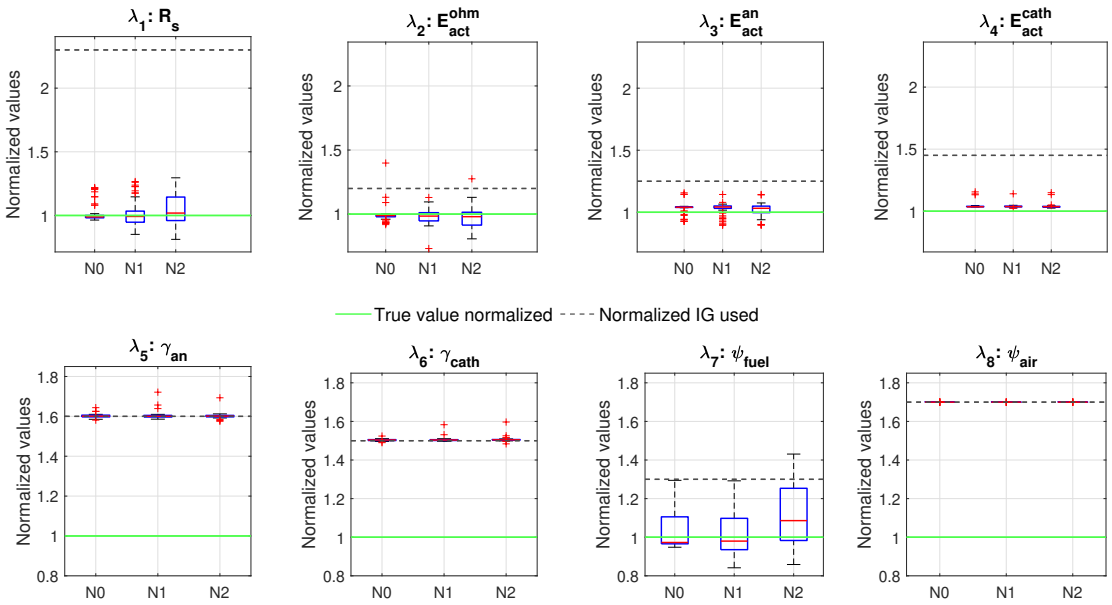

Figure 3.21: Parameter estimation using TLM starting from IG10

Thèse accessible à l'adresse : https://theses.insa-lyon.fr/publication/2026ISAL0017/these.pdf © [Z. Yazbeck], [2026], INSA Lyon, tous droits réservés

3.6 Confidence interval

Considering that the measured output is affected by additive white noise:

$$y_k^{measured} = y_k(\lambda) + e_k, \quad e_k \sim \mathcal{N}(0, C_y) \tag{3.27}$$

where C_y is the measurement noise covariance. Thus, the Fisher Information Matrix (FIM) which presents the information content of the excitation can be approximated by:

$$FIM(\hat{\lambda}) = S(\hat{\lambda})^\top C_y^{-1} S(\hat{\lambda}), \tag{3.28}$$

where S is the sensitivity matrix defined in Equation (3.7). Thus, $\hat{\lambda}$ can be approximated as $\hat{\lambda} \sim \mathcal{N}(\lambda^*, C_\lambda)$, where $C_\lambda \in R^{n_\lambda \times n_\lambda}$ is the parameter covariance matrix.

When the estimate is close to the optimum and under a local linearization, the parameter covariance can be approximated by the inverse of the Fisher Information Matrix, according to the Cramér-Rao bound [130]:

$$C_\lambda \approx FIM(\hat{\lambda})^{-1}. \tag{3.29}$$

We consider thus that the standard parameter error is:

$$\sigma_\lambda(\hat{\lambda}) = \sqrt{diag\left(FIM(\hat{\lambda})^{-1}\right)} \tag{3.30}$$

Using t-distribution assumption [123, 130], the 95% confidence intervals for the estimates are calculated as follows:

$$\hat{\lambda} - t_{(1-0.05,\ N-n_\lambda)}\sigma_\lambda \leq \lambda^* \leq \hat{\lambda} + t_{(1-0.05,\ N-n_\lambda)}\sigma_\lambda, \tag{3.31}$$

where N is the number of observations, and t is the upper critical value for the t-distribution with $N - n_\lambda$ degrees of freedom.

It is important to clarify that this estimated confidence interval does not necessarily reflect the true confidence interval, it is mainly used here to quantify the robustness of the estimates. Parameters having weak sensitivity directions can take very different values each time the estimation is performed under noisy measured outputs, while having a negligible effect on the output. This leads to larger confidence intervals, and such parameters are truncated from the sensitivity matrix. Consequently, they remain close to their nominal values (initial guesses), as explained in Section 3.4.1. Therefore, for synthetic cases where the true parameter vector is known, the true parameter vector does not necessarily lie within the computed interval for a given noise realization.

Thèse accessible à l'adresse : https://theses.insa-lyon.fr/publication/2026ISAL0017/these.pdf © [Z. Yazbeck], [2026], INSA Lyon, tous droits réservés

3.7 Parameter estimation with experimental data

In this section, we evaluate the four estimation methods on experimental data provided by the CEA. The dataset was collected on the test bench shown in Figure 3.22 using a stack of six planar cathode-supported cells. The measurement used for estimation of the electrochemical parameters is the stack voltage V_s, and the input vector u in Equation (3.2).

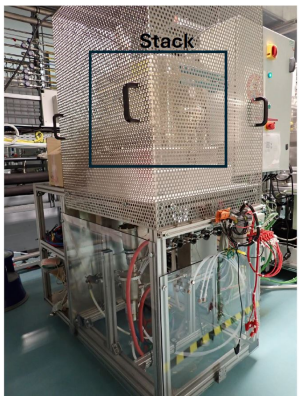

Figure 3.22: Solid Oxide electrolyzer stack test bench with auxiliary components

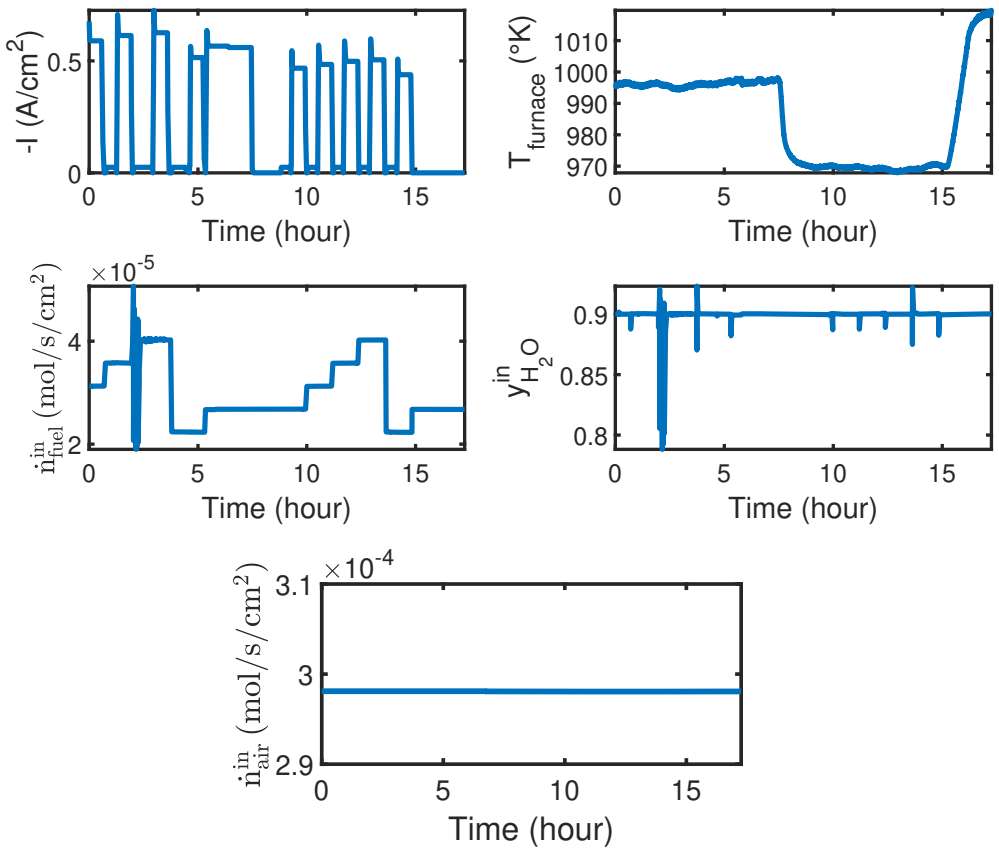

Figure 3.23: Experimental input trajectory.

Thèse accessible à l'adresse : https://theses.insa-lyon.fr/publication/2026ISAL0017/these.pdf © [Z. Yazbeck], [2026], INSA Lyon, tous droits réservés

Table 3.8: Estimation with experimental data

λ	λ_0	$\hat{\lambda}_{fmincon}$	$\hat{\lambda}_{TGN}$	$\hat{\lambda}_{LM}$	$\hat{\lambda}_{TLM}$	$\frac{C.I.}{\hat{\lambda}_{TLM}} \times 100$
R_s	0.154	$\mathbf{0.063}$	0.38	0.35	0.34	1.01
E_{act}^{ohm}	$180e3$	$179e3$	$74.31e3$	$79.7e3$	$82.2e3$	0.96
E_{act}^{an}	$140e3$	$118.4e3$	$95.3e3$	$49.22e3$	$84.73e3$	38.34
E_{act}^{cath}	$75e3$	$74.76e3$	$128.11e3$	$108e3$	$95.9e3$	0.08
γ_{an}	$1.25e5$	$1.26e5$	$5.32e5$	$1.26e5$	$1.26e5$	**426.45**
γ_{cath}	$3.37e5$	$3.37e5$	$3.74e5$	$1.22e6$	$3.36e5$	1.05
ψ_{fuel}	0.21	$\mathbf{0.051}$	$\mathbf{1.6}$	$\mathbf{4.03}$	0.2	0.15
ψ_{air}	0.15	$\mathbf{1.6e4}$	0.157	0.21	0.15	$\mathbf{151.35}$

The experimental input trajectory used is presented in Figure 3.23, showing less excitation for the air flow rate $\dot{n}_{air}^{in}$ and steam molar fraction $y_{H_2O}^{in}$, with a sampling time of 2 seconds.

The parameter estimates obtained with the four methods are summarized in Table 3.8. Since the true parameter values are unknown for the experimental dataset, we do not report normalized estimation errors with respect to a reference value like in Sections 3.3-3.4. Those obtained with LM and TLM are in close agreement for the most influential parameters, and both methods provide physically reasonable values for R_s and the activation energies except for E_{act}^{and}, which shows a relative small estimate with LM. However, several parameters have nonphysical estimates with `fmincon`, most notably R_s and ψ_{fuel}, and it also leads to an unrealistically large value of ψ_{air}. The TGN method also yields a large value of ψ_{fuel}.

From an output data fitting point of view, `fmincon` performs the worst (RMSE = 0.0163), while LM and TLM achieve the smallest errors, with similar root mean square error values (RMSE) of 0.0083 for both methods, and TGN gives a slightly larger RMSE of 0.0091. This is consistent with Figure 3.24, where LM and TLM keep the absolute error lower compared with other methods over the full window, and the cross-validation results in Figure 3.25 confirm that LM and TLM exhibit the same degree of predictive accuracy in a different time window, while `fmincon` and TGN provide poorer generalization. TLM keeps γ_{an} and ψ_{air} parameters close to their nominal (or initial) values, indicating a lack of practical identifiability for these directions, the output is weakly sensitive to these directions over the considered experiment. This is further supported by the confidence-interval estimation reported in the last column of Table 3.8, which shows large uncertainty for γ_{an},and a lesser extent for ψ_{air}.

Thèse accessible à l'adresse : https://theses.insa-lyon.fr/publication/2026ISAL0017/these.pdf © [Z. Yazbeck], [2026], INSA Lyon, tous droits réservés

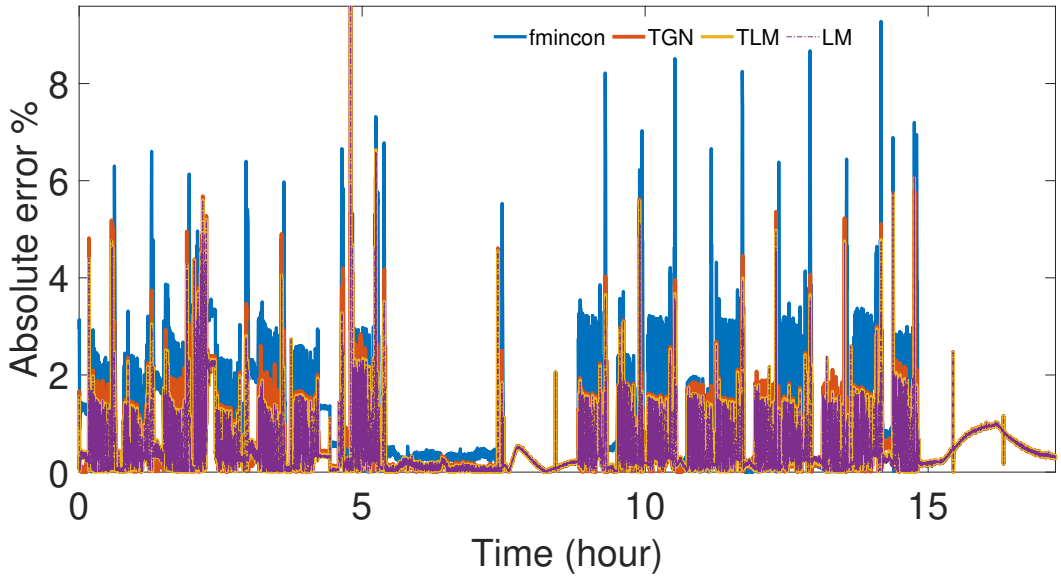

Figure 3.24: Absolute voltage error between experimental and output model for different optimizers

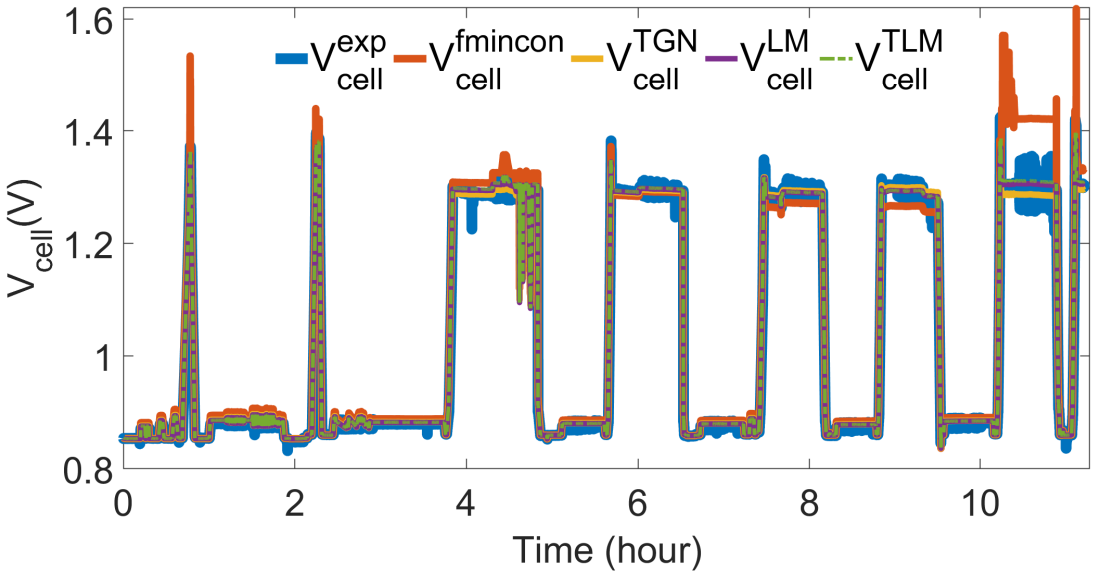

Figure 3.25: Cross-validation on experimental data

3.8 Design of optimal experimental data

The goal of optimal experimental design is to choose excitation profiles and a measurement schedule that are maximally informative about the unknown parameter vector λ. In the model-based experimental design framework, where a physical model is used to predict the expected

Thèse accessible à l'adresse : https://theses.insa-lyon.fr/publication/2026ISAL0017/these.pdf © [Z. Yazbeck], [2026], INSA Lyon, tous droits réservés

information content of candidate excitations, an optimization problem can be formulated to generate the most persistently exciting input trajectories by maximizing the FIM. However, the true parameter vector λ^* is unknown, thus, the FIM obtained from sensitivity differential Equations 3.5 is quantified at the nominal parameter vector λ_0, resulting in a so-called local optimal design. According to the Cramer-Rao inequality, maximizing the FIM is equivalent to minimizing a lower bound on the uncertainty of the estimated parameters [123, 127, 128].

We assume that the measured output for each excitation profile is affected by Gaussian noise σ_y^2, thus the measurement noise covariance presented in (3.6) is $C_y = \sigma_y^2 I_N$, and I_N is the identity matrix of order N. In this work, we assume for all OED methods considered $\sigma_y = 5\ mV$. Thus, under this assumption, the Fisher information matrix associated with sampled data can be written as:

$$FIM(\lambda) = \sum_{k=0}^{N} S_y(t_k)^\top C_y^{-1} S_y(t_k),$$

where $S_y(t_k)$ is the output sensitivity evaluated at the nominal parameter vector λ, N is the number of sampling intervals.

To maximize the amount of information, the FIM is reduced to a scalar measure, and several commonly metrics can be considered for this problem and are known as alphabetic optimality criteria [127, 128]:

- D-optimality: $\log\det\left(\text{FIM}^{-1}\right)$,
- A-optimality: $\text{trace}\left(\text{FIM}^{-1}\right)$,
- E-optimality: $\lambda_{\max}\left(\text{FIM}^{-1}\right)$.

These optimality criteria have different geometrical interpretations in terms of the confidence ellipsoid in parameter space. Figure 3.26 illustrates the uncertainty associated with the estimates of a two-parameter case, representing the confidence region, which is typically 90% or 95%. D-optimality minimizes the volume of the confidence region which is proportional to the $(\det(\text{FIM}))^{-1/2}$, equivalent to maximizing $\det(\text{FIM})$ (or equivalently, minimizing $-\det(\text{FIM})$). In practice, the logarithm function is used to have a concave function, leading to the objective function: $-\log\det(\text{FIM})$, which is convex [146]. E-optimality maximizes the minimum eigenvalue of the information matrix, thus changing the size of the major axis of the confidence interval, and A-optimality minimizes the variance of the parameter estimates, thereby reducing the dimensions of the enclosing box around the confidence region.

Thèse accessible à l'adresse : https://theses.insa-lyon.fr/publication/2026ISAL0017/these.pdf © [Z. Yazbeck], [2026], INSA Lyon, tous droits réservés

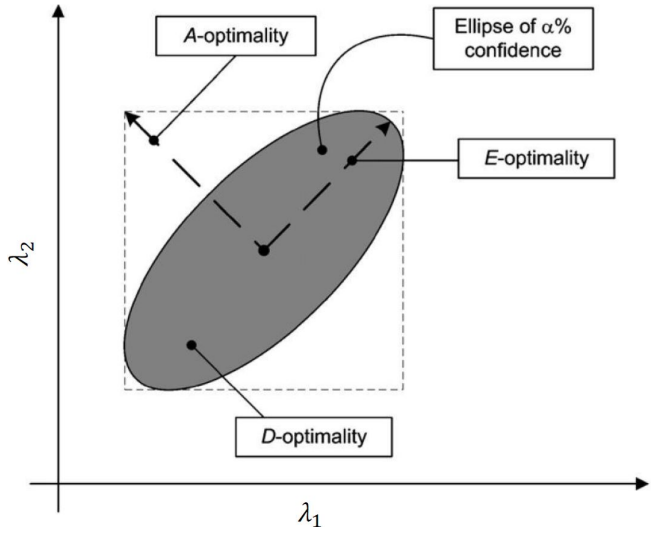

Figure 3.26: Geometric interpretation of optimality criterion in the (λ_1, λ_2) parameter plane [127].

We consider here a D-optimal experimental design problem, where the design vector is:

$$\varphi = (x(t_k),\, u(t_k),\, t_{sp}, \tau)\,, \qquad k \in \{1, .., N+1\}$$

where $x(t)$, $u(t)$, and t_{sp} are the state vector, the input vector, and the is the vector of sampling times in which the control variable remains constant, and τ is the experiment duration. N is the number of sampling points fixed to 10000. And the optimal experimental design problem can be formulated as the following nonlinear programming problem (NLP):

$$\min_{\varphi}\ \log\det\left(\sum_{k=0}^{N} S_y(t_k,\lambda_0)^\top C_y^{-1} S_y(t_k,\lambda_0)\right)^{-1} \tag{3.32}$$

subject to constraints in Equations (3.21)- (3.26), and

$$x_{k+1} = x_k + \Delta t_k\, f(x_{k+1}, u_k, \lambda), \qquad k = 0, \ldots, N-1. \tag{3.33}$$

$$0\ \leq p_i^{ch} \leq 1\ atm \tag{3.34}$$

$$0\ \leq T \leq 1050\ ^\circ K \tag{3.35}$$

$$0.1\ s\ \leq t_s \leq 10\ s \tag{3.36}$$

$$\tau = \sum_{0}^{N} t_s(k)\ \leq 1 \text{ hour} \tag{3.37}$$

Thèse accessible à l'adresse : https://theses.insa-lyon.fr/publication/2026ISAL0017/these.pdf © [Z. Yazbeck], [2026], INSA Lyon, tous droits réservés

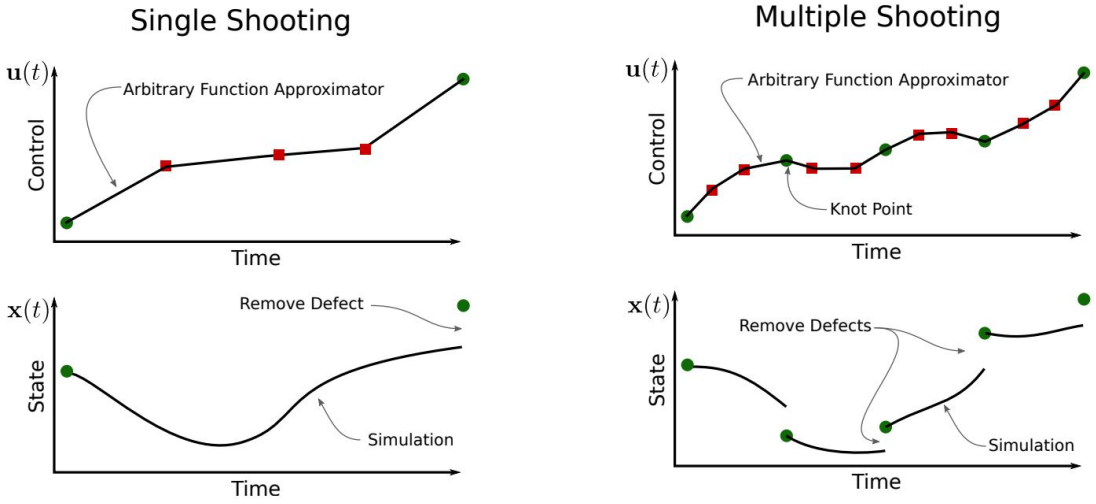

Figure 3.27: Single Shooting vs Multiple Shooting [147].

The constraints used guarantee the feasibility of the solution and its applicability to a real system taking into account its physical limitations. They include the minimum and maximum bounds of the variables, the ramp rate of the furnace temperature, the steam conversion to ensure safe operating conditions, the sampling time, which is here related to the variation of the decision variables specifically the control input, and the total experiment duration which is here limited to one hour. The resulting NLP problem is non-convex due to the nonlinearity of SOEC model and the dependence of the FIM on the sensitivities, and is solved here using an interior-point algorithm (Ipopt) within CasADi. Since the integrators embedded in CasADI do not support symbolic sampling time, an implicit Euler scheme is used to integrate the system in discrete time, as represented in Equation (3.33). Additionally, a scaling procedure is performed a priori in order to improve solver efficiency to consider the difference in orders of magnitude of the parameters [140].

In a standard single-shooting method, the decision variables are typically limited to the control inputs over time, and the state trajectory is implicitly determined by integrating the system dynamics from the initial conditions using these controls resulting from the optimization. However, using this approach for complex problems can lead to numerical instabilities, slow convergence, and higher sensitivity to the initial guess. Instead, multiple shooting works by breaking up the trajectory into several segments and using both the states and control inputs as decision variables at each shooting node, or the so-called knot point which is the boundary between consecutive segments, as shown in Figure 3.27. The control input in practice is often parametrized as a piecewise-constant function over each segment (zero-order hold), and its value is optimized at the knot points and kept constant between them. The end of one segment will not necessarily match the start of the next node, which leads to so-called defects. Therefore, the dynamics of the system are enforced through the equality constraint as in Equations (3.33) [147].

Thèse accessible à l'adresse : https://theses.insa-lyon.fr/publication/2026ISAL0017/these.pdf © [Z. Yazbeck], [2026], INSA Lyon, tous droits réservés

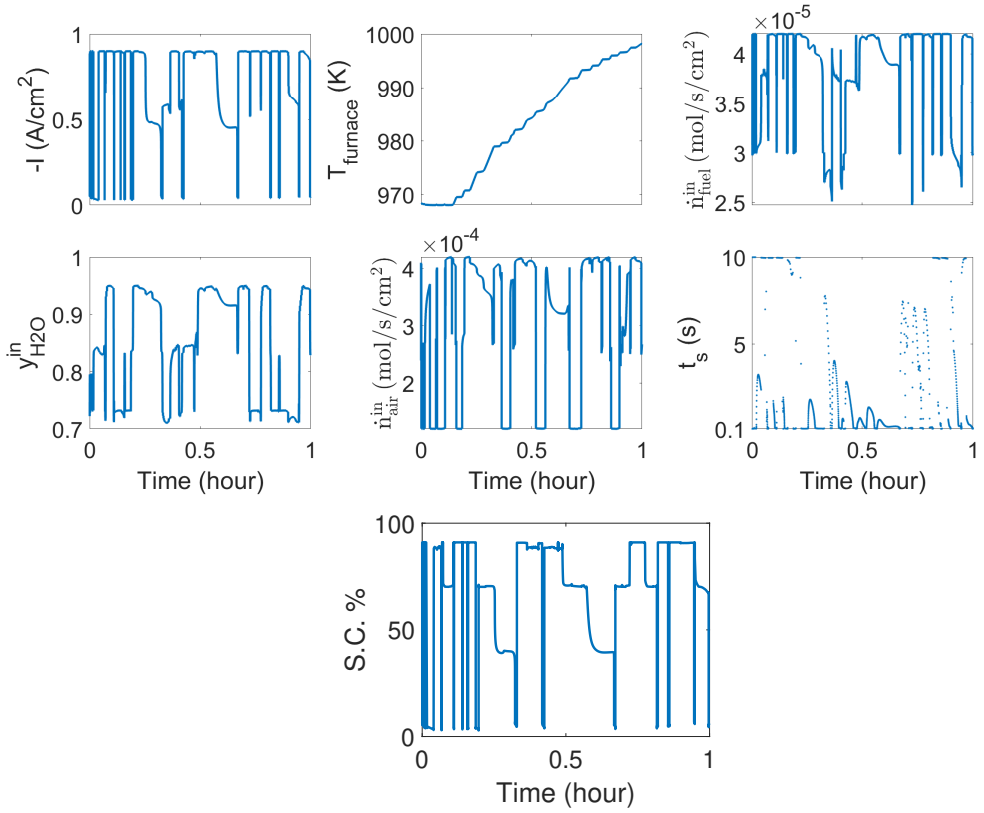

Figure 3.28: OED data

Table 3.9: Normalized OED parameter estimates and confidence intervals.

λ	$\frac{\hat{\lambda}_{OED}}{\lambda^*}$	$\frac{C.I.}{\hat{\lambda}_{OED}}$ (%)
R_s	1.004	0.61
E^{ohm}_{act}	0.99	0.92
E^{an}_{act}	1.01	6.31
E^{cath}_{act}	1.02	2.95
γ_{an}	1.26	79.05
γ_{cath}	1.43	37.06
ψ_{fuel}	0.99	0.136
ψ_{air}	0.74	158.25

The result of the optimization problem in Equations (3.32)-(3.36) is illustrated in Figure 3.28. A constant input profile is used as an initial guess, and the solver converges to a final value of the cost function Equation (3.32) equal to 120.45 after 3.65 hours of computation. An enhancement of the sensitivity magnitudes for several parameters is obtained with the optimized input profile,

Thèse accessible à l'adresse : https://theses.insa-lyon.fr/publication/2026ISAL0017/these.pdf © [Z. Yazbeck], [2026], INSA Lyon, tous droits réservés

compared to the synthetic input profile shown in Figure 3.1, and this improvement is clearly visible in Figure 3.29.

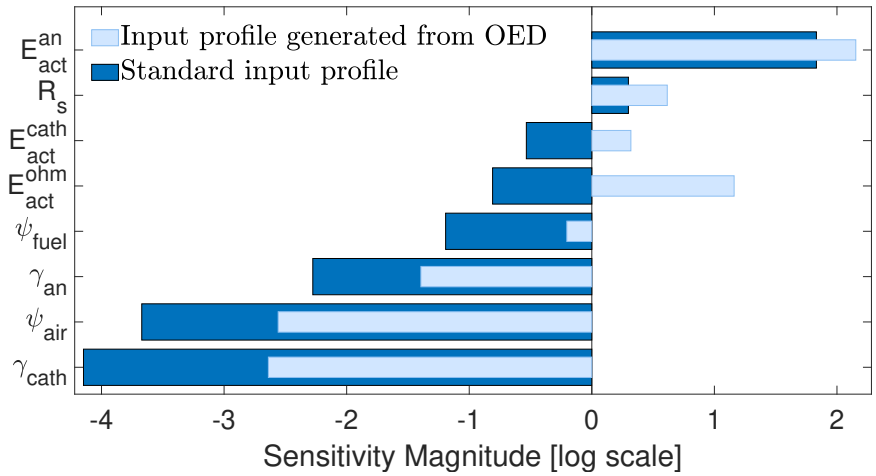

Figure 3.29: Orthogonalized sensitivity magnitudes for the input profile in Figure 3.1 and for the profile generated from OED using the initial guess λ_0.

After the generation of the input profile, parameter estimation is performed using the TLM algorithm. The values of the estimates $\hat{\lambda}_{OED}$ and their confidence intervals are reported in Table 3.9. An improvement of estimation is observed for R_s, E_{act}^{ohm}, and ψ_{fuel} with respect to the noise-free synthetic-data case (N_0) reported in Table 3.4, even though the OED validation includes measurement noise. A minor improvement is also observed for E_{act}^{an} and E_{act}^{cath}. In contrast, the parameters γ_{an}, γ_{cath}, and ψ_{air} remain nearly unchanged. These parameters correspond to the smallest sensitivity magnitude directions under the standard input profile, which is reflected by their larger confidence intervals in Table 3.9.

3.9 Sequential OED

The optimal problem defined in Equation (3.32) is evaluated locally at a nominal parameter vector λ_0. Thus, the generated input may lose informativeness when the true parameters differ significantly from λ_0. This motivates the use of a sequential optimal experimental design strategy, in which the identification procedure is organized as a succession of short experiments, each with a duration of 500 seconds, with N = 1500 sampling points considered here.

As shown in Figure 3.30, at each iteration, an input profile is generated by solving an OED problem based on the current estimate of the parameters $\hat{\lambda}$, then the experiment is performed to incorporate the new measurements in the estimation step, and the parameter vector is updated before designing the next experiment. This workflow allows the excitation to progressively adapt to the parameter estimate evolving in each iteration, leading to a gradual reduction of uncertainty and better estimation, as shown in Figure 3.32. The algorithm is stopped when the difference

Thèse accessible à l'adresse : https://theses.insa-lyon.fr/publication/2026ISAL0017/these.pdf © [Z. Yazbeck], [2026], INSA Lyon, tous droits réservés

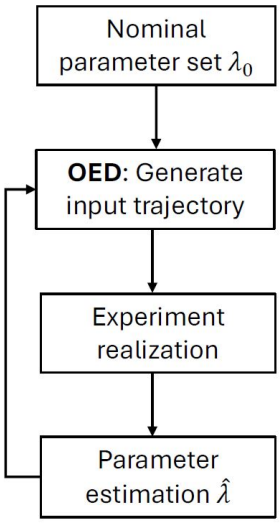

Figure 3.30: Sequential OED scheme.

between two consecutive parameter estimates is less than 10^{-6}. This general principle is adopted here and is inspired by the sequential procedure reported by Pozzi et al. in [126].

$$\min_{\varphi_i} \ \log\det\left(\sum_{k=0}^{N} S_y(t_k,\hat{\lambda}_i)^\top C_y^{-1} S_y(t_k,\hat{\lambda}_i)\right)^{-1} \tag{3.38}$$

$$\text{Equations (3.21)} - \text{(3.26)}, \text{(3.33)}, \text{(3.36)}$$

$$\text{Maximum number of tests = 8}$$

$$\tau_i = \sum_{0}^{N} t_{s_i}(k) \ \leq 500 \text{ seconds}$$

The result of the sequential OED procedure is summarized in Figures 3.31 and 3.32. Three consecutive tests are generated, each of length 500 s, as shown in Figure 3.31, to have an overall input trajectory of 1500 s, and the corresponding parameter evolution is reported in Figure 3.32.

The complete sequential OED procedure required 0.54 hours of computation time. After three iterations, the estimates of R_s, the activation energies, and ψ_{fuel} converge towards the true values. However, γ_{an}, γ_{cath} and ψ_{air} remain close to their initial guesses, indicating that these directions are still weakly informed by the designed trajectory and therefore remain practically unidentifiable under the considered sequential OED setting.

The normalized values of the estimated parameters are presented in Table 3.10 with their confidence intervals. The estimated confidence intervals shown in Table 3.10 are higher than those calculated with the NLP OED in Table 3.9, which is expected because the number of measurements is lower in sequential OED than in the NLP OED. Nevertheless, they still show tighter intervals for the well-estimated parameter directions and wider intervals for the poorly

Thèse accessible à l'adresse : https://theses.insa-lyon.fr/publication/2026ISAL0017/these.pdf © [Z. Yazbeck], [2026], INSA Lyon, tous droits réservés

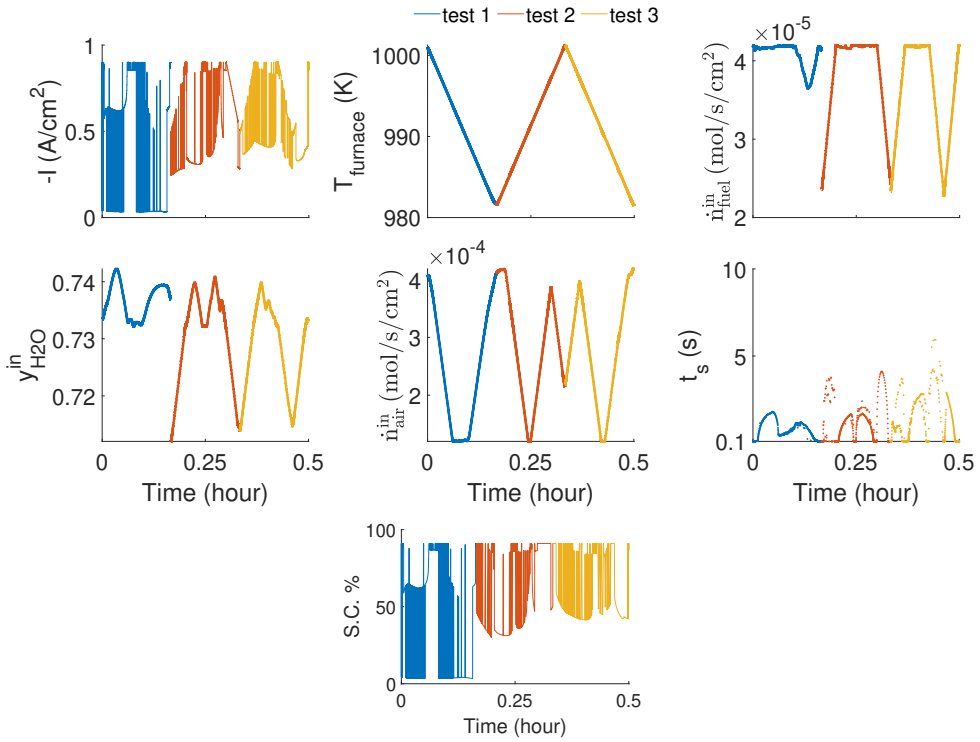

Figure 3.31: Input profile generated using sequential OED.

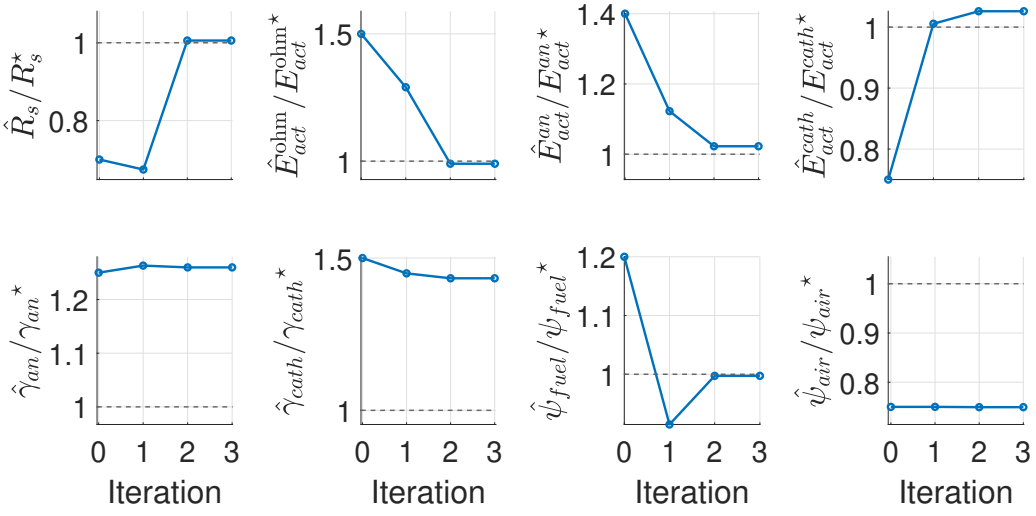

Figure 3.32: Evolution of the normalized parameter estimates in sequential OED

Thèse accessible à l'adresse : https://theses.insa-lyon.fr/publication/2026ISAL0017/these.pdf © [Z. Yazbeck], [2026], INSA Lyon, tous droits réservés

estimated ones.

Table 3.10: Normalized sequential OED parameter estimates ($\hat{\lambda}_{seq,OED}$) and confidence intervals.

λ	$\frac{\hat{\lambda}_{seq,OED}}{\lambda^*}$	$\frac{C.I.}{\hat{\lambda}_{seq,OED}}$ (%)
R_s	1.005	4.9
E_{act}^{ohm}	0.99	10.7
E_{act}^{an}	1.02	57.09
E_{act}^{cath}	1.02	19.09
γ_{an}	1.25	710.68
γ_{cath}	1.43	237.4
ψ_{fuel}	0.99	1.26
ψ_{air}	0.74	$1.23e3$

3.10 OED based on a predefined library

Since the complexity of the optimization problem defined in Equation (3.32) grows with the dimension of the system and the number of parameters to estimate, it becomes computationally intractable for large-scale models. Therefore, alternative method based on a predefined library of input profiles can be used to address the OED problem.

We build a library of L experimental inputs $u_i(t)$, $i = 1, 2, \ldots, L$. For each input profile $u_i(t)$, we obtain the corresponding sensitivity $S_y(t)$ by solving Equations (3.1), (3.3) and (3.6) simultaneously. We then select M inputs among these L inputs $u_i(t)$, $i = 1, 2, \ldots, L$, that are maximally informative as measured by the Fisher information matrix F, where $M < L$. Then, the total number of experiments is given by:

$$m_1 + m_2 + \cdots + m_L = M. \tag{3.39}$$

Where $m_i \in \{0, 1\}$ is a binary value indicating if experiment i is executed from the input library. Thus, the Fisher information matrix is:

$$F = \sum_{i=1}^{L} m_i S_{y,i}^{\top} C_y^{-1} S_{y,i}. \tag{3.40}$$

Thèse accessible à l'adresse : https://theses.insa-lyon.fr/publication/2026ISAL0017/these.pdf © [Z. Yazbeck], [2026], INSA Lyon, tous droits réservés

And the optimization problem to maximize the D-optimality criterion of F is:

$$\min_{m_i} \ \log\det\left(\sum_{i=1}^{L} m_i S_{y,i}^{\top} C_y^{-1} S_{y,i}\right)^{-1}, \tag{3.41}$$

subject to

$$\begin{aligned} m_i &\in \{0,1\}, \\ m_1 + \cdots + m_L &= M, \\ \sum_{i=1}^{M} t_{m_i} &\leq \tau. \end{aligned} \tag{3.42}$$

where t_{m_i} is the duration of the test m_i, $\tau = 3600$ seconds, and $M = 10$.

Input library

An input library of a finite set of tests was constructed to address the OED problem. Thus, sequential tests are executed one after another, so their duration can be adapted to the dominant time scales of the system. Nine durations were considered: 0.1, 0.5, 1, 5, 10, 50, 100, 500, and 1000 seconds, covering the different excitation frequencies of current density from approximately 0.05 to 3000 Hz. Each test was discretized using 2000 time steps, so that the sampling time t_s depends on the chosen duration.

For each duration, we attribute a specific design of: air inlet flow rates $\dot{n}_{air}^{in}$, inlet composition $y_{H_2}^{in}$ and furnace temperature $T_{furnace}$, which we refer to as a "secondary" input profile, while respecting the ramp-rate and operating constraints introduced in Equations (3.21)-(3.26). The inlet fuel flow rate $\dot{n}_{fuel}^{in}$ is kept constant to ensure that the steam conversion does not exceed the safe limit in Equation (3.25). However, the family of current density signals $I(t)$ is more diverse for each duration, it includes frequency sweeps, ramps and PRBS sequences. For these signals, the amplitudes, offsets and frequencies were chosen to take values within the admissible operating window and to have both slow and fast dynamics.

In total, 387 candidate tests were generated, with 43 current-density profiles for each duration, where each current-density profile was paired with the corresponding secondary-input pattern (defined for that duration), to have a complete set of input trajectories. After that, sensitivities $S_{y,i}(t)$ were computed based on the nonlinear SOES model, and the associated FIM were evaluated and subsequently used in the optimization step, where a combination of tests that maximizes the richness of the input trajectory is selected under constraints on total test time, τ and number of tests M taken as 1 hour maximally and 10 here respectively.

Thèse accessible à l'adresse : https://theses.insa-lyon.fr/publication/2026ISAL0017/these.pdf © [Z. Yazbeck], [2026], INSA Lyon, tous droits réservés

D-Optimality Results

The computation of this combinatorial optimization problem is demanding and becomes too complex to handle for a library containing a lot of inputs. In this case, selecting an optimal set of input profiles to maximize parameter sensitivity (measured by the D-optimality score) is a combinatorial problem, where the number of possible combinations grows exponentially with the number of candidate inputs. Some studies address this problem by relaxing the binary constraint and allowing tests to be partly selected as in [123].

To address the limitations of combinatorial optimization, Genetic Algorithms (GAs), as a computational analogue of natural evolution [148], can be a useful tool, and are investigated in this work. GAs apply principles such as selection, crossover, and mutation to evolve solutions to complex problems, and are well-suited for this kind of problems because they effectively search large, discrete, and complex problem spaces without evaluating every possible combination, even if they do not guarantee optimality.

GAs work by mimicking natural selection, instead of exhaustively testing all combinations, where an initial population of possible input sets is generated, each representing a different combination of input profiles. These populations are then evaluated based on a fitness function which in this case can be the D-optimality score. A population was first initialized to formulate this problem for a Genetic Algorithm (GA), consisting of many possible solutions known as "individuals". Each individual is a binary array of ones and zeros, where a 1 indicates that a specific input is included, and a 0 means it is not. Each individual is the same length as the number of inputs in the library and represents a specific selection of tests. To speed up convergence, the initial population is initialized in an efficient way, where each individual was built by adding one random test at a time until the total test duration reached the constraint limit. This ensured that all individuals in the initial population were feasible solutions from the outset, which improves significantly the convergence speed compared to a random initialization, as shown in Figure 3.33, where it can be noticed that until the 83th generation that the randomly initialized population produces a solution within the constraints. The algorithm then runs through several iterations, also known as generations, during which the population evolves using the following steps [149]:

- **Selection:** Individuals with better fitness (lower D-optimality scores) are more likely to be chosen for the next generation.
- **Crossover:** Two selected individuals are combined to form new offspring by exchanging parts of their binary strings.
- **Mutation:** Random changes are introduced to some individuals to maintain diversity and avoid local minima.

The population gradually converges towards better input combinations after successive generations, and constraints such as the total test duration and maximum number of tests were added to the optimization problem.

Thèse accessible à l'adresse : https://theses.insa-lyon.fr/publication/2026ISAL0017/these.pdf © [Z. Yazbeck], [2026], INSA Lyon, tous droits réservés

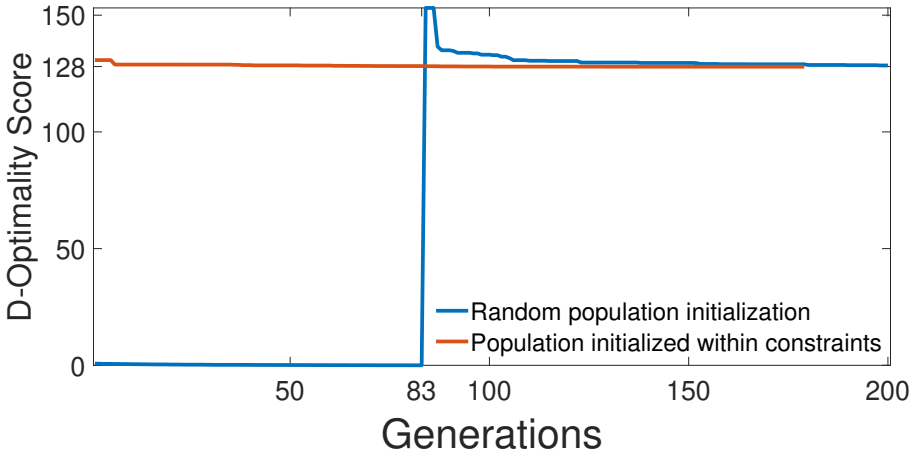

Figure 3.33: Effect of initially constraining Genetic Algorithm (GA) population within duration and test number constraints.

The result of GA algorithm to enhance the D-optimality criterion is shown in Figure 3.34. Each color in this figure corresponds to a different test selected from the predefined library. The full trajectory is composed of several tests with different durations, frequencies, and amplitudes. It combines short and long tests with different current density frequencies, under different operating conditions (furnace temperature, inlet composition and flow rates) respecting the constraint of total duration less than 3600 s and 10 as maximum number of tests.

After this step, parameter estimation was performed using the TLM algorithm presented in Section 3.4.1. In this case the estimates and their corresponding confidence intervals are denoted as $\hat{\lambda}_{OED,lib}$, and $CI_{\hat{\lambda}_{OED,lib}}$, respectively. The normalized values of the estimates are presented in the Table 3.11 and compared in Figure 3.35 with those obtained from solving the NLP OED problem in Equation (3.32). The estimates $\hat{\lambda}_{OED,lib}$ are very close to those obtained from generating input profile from Equation (3.32), with a better estimate of ψ_{fuel} and a slightly better one for R_s in the NLP OED case. This is expected, because for the NLP OED problem defined in Equation (3.32) the solution reaches a lower D-optimality score (120.45) than the library-based OED design (128 as shown in Figure 3.33). Additionally, the confidence intervals in the case of library-based OED are generally larger than those of the NLP OED, while the parameters associated with the weakest sensitivity directions, namely γ_{an}, γ_{cath}, and ψ_{air}, exhibit large confidence intervals in both cases.

Thèse accessible à l'adresse : https://theses.insa-lyon.fr/publication/2026ISAL0017/these.pdf © [Z. Yazbeck], [2026], INSA Lyon, tous droits réservés

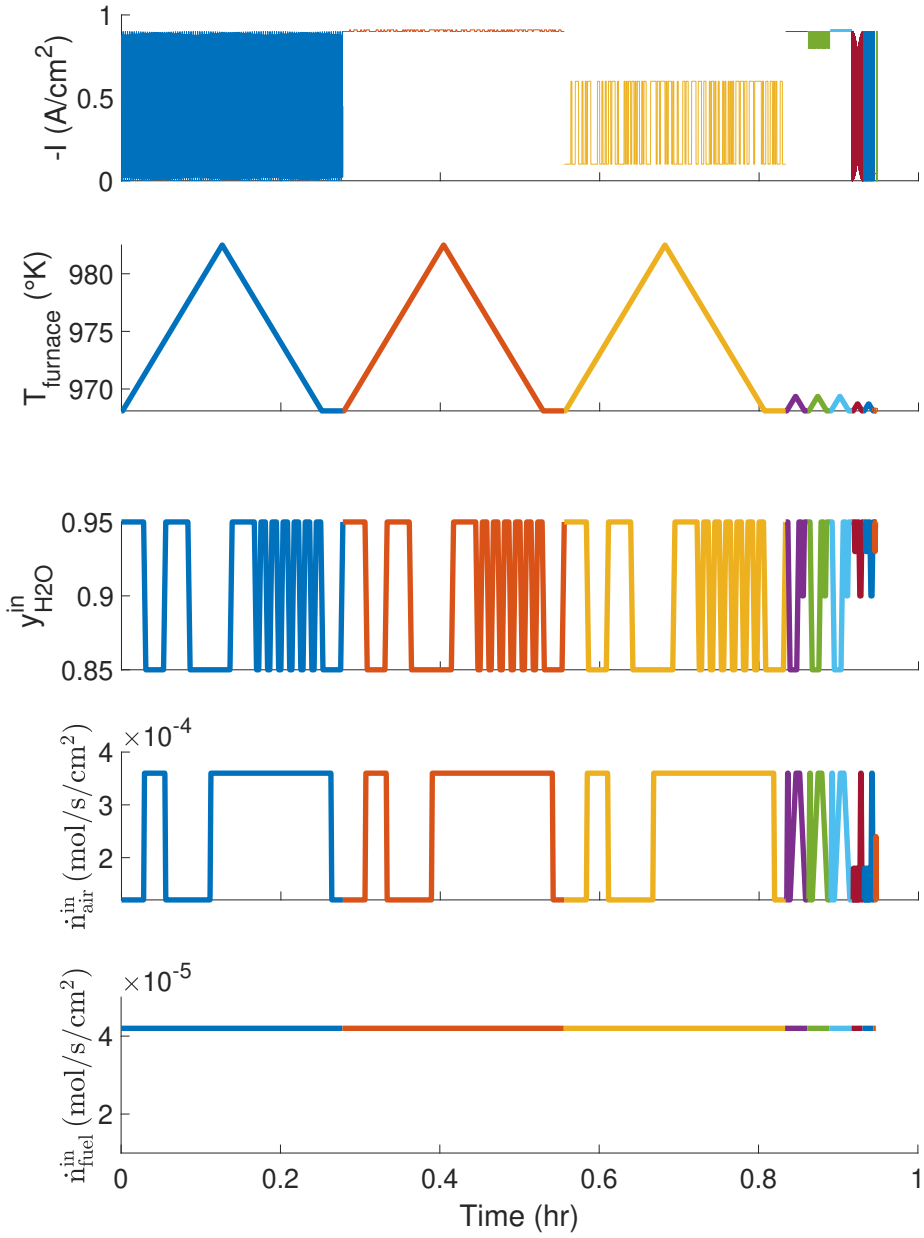

Figure 3.34: Genetic Algorithm (GA) optimization result for constraints of 3600 seconds, and maximum 12 tests.

Thèse accessible à l'adresse : https://theses.insa-lyon.fr/publication/2026ISAL0017/these.pdf © [Z. Yazbeck], [2026], INSA Lyon, tous droits réservés

Table 3.11: Normalized parameter estimates and 95% confidence intervals for the library-based OED input.

λ	$\frac{\hat{\lambda}_{OED,lib}}{\lambda^*}$	$\frac{C.I._{\hat{\lambda}_{OED,lib}}}{\hat{\lambda}_{OED,lib}}$ (%)
R_s	0.985	1.3
E_{act}^{ohm}	1.005	1.7
E_{act}^{an}	1.024	8.42
E_{act}^{cath}	1.026	6.7
γ_{an}	1.254	106.84
γ_{cath}	1.403	85.2
ψ_{fuel}	0.953	0.96
ψ_{air}	0.748	75.8

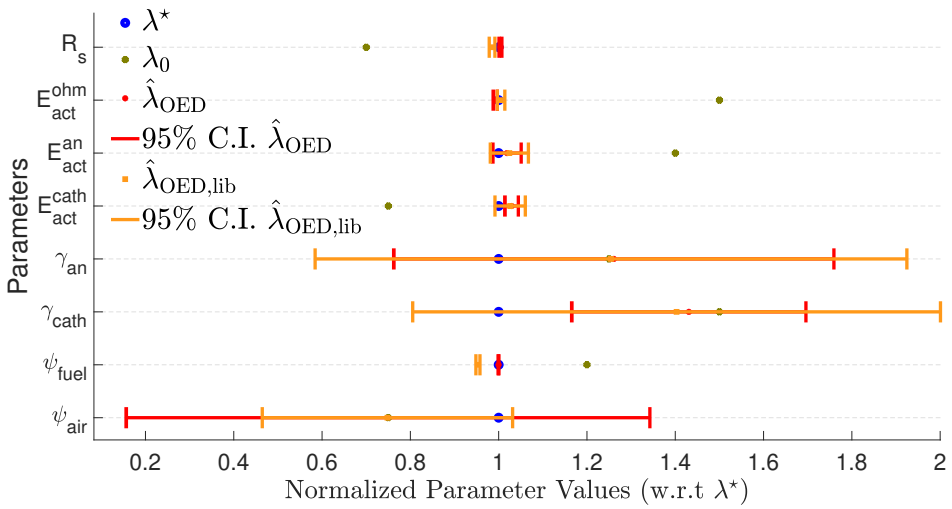

Figure 3.35: Parameter estimates and 95% confidence intervals obtained using a standard input profile and an input profile generated from OED.

3.11 Conclusion

In this chapter, we studied the problem of calibrating a nonlinear electrochemical model of a SOEC stack. Starting from typical input profiles based on IV curves at different operating conditions, a local sensitivity analysis followed by a QR-based orthogonalization of the sensitivity matrix is performed. This allows us to quantify the practical identifiability of the parameters and to cluster them manually into groups according to their influence on the stack voltage. Subse-

Thèse accessible à l'adresse : https://theses.insa-lyon.fr/publication/2026ISAL0017/these.pdf © [Z. Yazbeck], [2026], INSA Lyon, tous droits réservés

quently, a sequential estimation strategy is adopted as proposed in the literature [123], to mitigate compensation effects between dependent parameters. At each step, the most sensitive parameter group is estimated first, while the other less sensitive parameters are kept fixed and only updated in the subsequent stages of the sequence. Although this approach reduces compensation, parameters with collinear sensitivities, in particular ψ_{air}, may still converge to non-physical values, even when the voltage fit is good. However, assessing the sensitivity and linear dependence between parameters is local, depends on the parameter values, and can change when the parameter vector changes due to the nonlinearity of the system.

To better handle these limitations, we proposed a truncated Levenberg-Marquardt (TLM) algorithm that explicitly exploits the sensitivity differential equations at each iteration. The sensitivities are first normalized, then decomposed via SVD and truncated so that only well-informed, well-conditioned directions are updated, while collinear sensitivity directions are strongly damped, instead of manually clustering the parameters into groups. Using synthetic data, a comparison with standard LM, truncated Gauss-Newton and the interior-point algorithm using MATLAB's built-in function (`fmincon`) shows that the TLM recovers the most informative electrochemical parameters (R_s, E_{act}^{ohm}, E_{act}^{an}, E_{act}^{cath}) with good accuracy, avoids non-physical estimate of ψ_{air}, and keeps a reasonable computational cost. To provide a broader view of the proposed method performance with respect to the data, the initial guess, and measurement noise, we conducted a study with 50 different IV input scenarios, ten initial guesses, and two Gaussian noises $N1$ and N_2, in addition to free-noise case N_0. The estimates show some dependence on the initial guess because of the non-convexity of nonlinear least squares problem, which is more noticeable for weakly sensitive parameters. For the most informative parameters the estimates converge close to the true values for almost all scenarios and initializations, while their accuracy depends on the richness of the input scenario. When adding measurement noise, the dispersion of the estimates slightly increases, but its impact remains moderate for the informative parameters and is less influential than initialization for the weakly sensitive parameters.

On this basis, we then investigated optimal experimental design as a way to enrich the information content of the experiments and reduce the linear dependence between parameters. A first formulation relies on a nonlinear programming problem that maximizes a D-optimality criterion built from the discrete FIM, under constraints on current density, furnace temperature, inlet composition, steam conversion and ramp rates. The corresponding optimal input profiles improve the conditioning of the sensitivity matrix and the estimation of the well-informed directions. Since this design is local and depends on the nominal parameter vector, we also introduced a sequential OED strategy based on a succession of short experiments, where the excitation is updated iteratively using the current parameter estimate. In the presented results, after only two iterations with short experiment durations, the well-informed directions converge toward their true values, while the remaining weakly informed directions stay close to their initial guesses. In addition, because solving the resulting NLP can be computationally demanding, we also presented a library-based design inspired by [123], where a finite set of signals (steps, ramps, frequency

Thèse accessible à l'adresse : https://theses.insa-lyon.fr/publication/2026ISAL0017/these.pdf © [Z. Yazbeck], [2026], INSA Lyon, tous droits réservés

sweeps, PRBS or multisine profiles) is defined, and a genetic algorithm is used to select the sequence of tests that maximize the information content of the total input profile taking into account the total experimental time and maximum number of tests. The library-based sequence achieves a D-optimality score close to that of the NLP-based design, and the two strategies lead to very close estimates. However, R_s is slightly better identified and ψ_{fuel} is better estimated with the input excitation obtained by solving the NLP OED problem than with the library-based input. However, weakly informed directions γ_{an}, γ_{cath}, and ψ_{air} did not improve with the proposed OED methods. Thus, working to enhance estimation of these parameters is a perspective of this work.

Therefore, this chapter proposes a complete and practically oriented calibration framework that combines sensitivity analysis with a truncated Levenberg-Marquardt algorithm, and optimal experimental design implemented through NLP-based, sequential, and library-based strategies.

Thèse accessible à l'adresse : https://theses.insa-lyon.fr/publication/2026ISAL0017/these.pdf © [Z. Yazbeck], [2026], INSA Lyon, tous droits réservés

Thèse accessible à l'adresse : https://theses.insa-lyon.fr/publication/2026ISAL0017/these.pdf © [Z. Yazbeck], [2026], INSA Lyon, tous droits réservés

Chapter 4

Fault detection

Contents

4.1 Introduction 99

4.2 Fault description 100

4.3 State of the art 100

4.4 Fault detection methodology 104

4.4.1 Square-Root Unscented Kalman Filter 106

4.4.2 Adaptive Threshold for Fault Detection 110

4.4.3 Experimental Studies 111

4.5 Aging-aware monitoring 117

4.5.1 Proposed Approach 118

4.5.2 Application to experimental data 120

4.5.3 Results 122

4.6 Conclusion 123

Sections 4.1 to 4.4, as well as part of 4.6 of this chapter are based on our paper [79]: Zaman Yazbeck, Federico Bribiesca-Argomedo, Minh Tu Pham, Bertrand Morel, and Vincent Dimitriou. *System-level monitoring and diagnosis of starvation faults in solid oxide electrolyzers*. International Journal of Hydrogen Energy, 198:152808, 2026. DOI: 10.1016/j.ijhydene.2025.152808[1]

Adaptations were made for homogeneity in notations, formatting, and integration into the rest of the manuscript.

[1]Open access article under the CC BY license: https://creativecommons.org/licenses/by/4.0/

Thèse accessible à l'adresse : https://theses.insa-lyon.fr/publication/2026ISAL0017/these.pdf © [Z. Yazbeck], [2026], INSA Lyon, tous droits réservés

4.1 Introduction

This Chapter presents the fault detection methodology based on the lumped 0D model of the stack developed in Chapter 2.3 and calibrated using the truncated Levenberg-Marquardt algorithm presented in Chapter 3.4.1. Thus, after estimating the parameters (see Table 3.8, Section 3.7) using experimental data, the model is assumed to represent the nominal and healthy behavior of the system and is therefore used as a reference for monitoring and diagnosis using an observer-based method.

The objective is to detect faults related to starvation by reconstructing the internal states that are not directly measurable, and to quantify the fault from the deviations from nominal behavior. However, over long operating periods, such deviations do not necessarily result from a fault, but can also occur due to system aging. In this chapter, we first present the intended experimental starvation cases and evaluate the observer performance over relatively short periods, using the identified parameter set in Table 3.8, which is assumed not to vary over the considered trajectory. To improve robustness over long-term operation, the last part of this chapter introduces an aging-aware monitoring extension, in which slowly varying state-of-health parameters are intermittently updated to preserve model fidelity.

The proposed strategy follows a classical model-based diagnosis framework, in which a state observer is used to estimate the system states from available measurements, and the fault magnitude is inferred from the inconsistencies between measured and estimated outputs.

The proposed methodology specifically addresses starvation-related faults in solid oxide electrolyzers operating in electrolysis mode. Two fault scenarios are considered: steam starvation and hydrogen starvation, which directly affect the internal gas partial pressures (which appear in the state vector of the state-space formulation in Equation (3.1)) and thus the measured outputs. Therefore, starvation constitutes a critical operating condition that must be detected at an early stage to avoid or reduce the severity of irreversible degradation.

Failing to detect starvation-related faults can lead to severe performance degradation. In electrolysis mode, steam starvation, which can be caused by pump malfunctions, leakages, and other system-related failures, can induce thermal stresses and irreversible electrolyte reduction [150]. While in fuel cell mode, hydrogen starvation causes nickel reoxidation of the hydrogen electrode, and air starvation can lead to undesired morphological changes [37, 151]. Therefore, real-time monitoring and diagnosis of faults are crucial for ensuring the reliability and longevity of solid oxide cells. Accurate fault detection enables timely intervention, preventing irreversible damage to the stack. By minimizing the occurrence and severity of faults through precise diagnosis and effective control, serious degradation can be avoided, ultimately enhancing the durability and performance of the SOC stack [152].

To this end, a nonlinear observer based on a square-root Unscented Kalman Filter (SR-UKF) is used. Relying on a set of standard measurements, the SR-UKF reconstructs the partial pressures of hydrogen, steam, and oxygen, the stack temperature, as well as deviations between

Thèse accessible à l'adresse : https://theses.insa-lyon.fr/publication/2026ISAL0017/these.pdf © [Z. Yazbeck], [2026], INSA Lyon, tous droits réservés

the real inlet fuel flow rates and their nominal setpoints. Then, Fault detection and isolation are achieved by analyzing these reconstructed quantities using adaptive thresholds derived from the nominal model under nominal input conditions. Finally, to extend the approach to long-term operation, an aging-aware monitoring strategy is introduced, in which a subset of slowly varying state-of-health parameters is intermittently updated so that the observer remains consistent as the system degrades.

4.2 Fault description

As mentioned in Chapter 1.6, in electrolysis mode, steam starvation and hydrogen starvation, defined as an interruption in hydrogen supply, can lead to irreversible damage to the cell material. Thus, we address the problem of detecting these faults by employing the partial pressures of the gases directly affected by starvation as key indicators of these faults.

Using available experimental data, we investigate both fault scenarios. Hydrogen starvation is induced by setting the hydrogen flow to zero, resulting in a hydrogen molar fraction of zero. Steam starvation is implemented by reducing the overall fuel flow rate, thus having high steam conversion by lowering both the hydrogen and steam inlet flow rates, while maintaining the same molar fractions. Under normal operating conditions, the fuel supply to the stack remains constant. The observer, utilizing stack voltage, air outlet temperature, and outlet hydrogen flow rate measurements, reconstructs the actual fuel flows (inlet hydrogen and steam flow rates) and gas partial pressures. When an anomaly occurs, deviations from nominal conditions indicate a fault. To isolate and quantify the detected fault in the hydrogen and steam starvation case, the deviation of flow rates from their nominal setpoint values is reconstructed by the observer. Finally, the total resistance is calculated to show how the low-frequency resistance responds to these faults during impedance measurements. A significant variation in resistance indicates steam starvation, while hydrogen starvation has little to no effect on the total resistance.

4.3 State of the art

Existing fault detection approaches for SOFC and SOEC systems can be categorized into three main types: model-based, data-driven, and hybrid methods that integrate both strategies [153]. Although data-driven methods have shown promising results, they often require extensive datasets, typically generated through simulations due to the difficulty of obtaining failure data from operating SOC systems in electrolysis or fuel cell mode without risking irreversible damage.

Data-driven approaches based on experimental data have been explored, though they remain challenging due to limited access to real faulty conditions. Zheng et al. [154] proposed a Principal Component Analysis (PCA) for dimensionality reduction with a Support Vector Machine (SVM) classifier, applied to the detection of air leakage and fuel starvation from SOFC experiments.

Thèse accessible à l'adresse : https://theses.insa-lyon.fr/publication/2026ISAL0017/these.pdf © [Z. Yazbeck], [2026], INSA Lyon, tous droits réservés

Similarly, Zhang et al. [155] developed a deep neural network outperforming SVM and PCA-SVM models to classify power stack degradation faults, validated using actual system data.

To address limitations in data availability, simulation-generated data have been also employed in various studies. For instance, a higher-order pseudo-2D model of SOFC was utilized to train an Artificial Neural Network (ANN) and k-nearest neighbors (KNN) models for detecting hydrogen starvation faults, with an additional ANN regressor estimating the affected area of Nickel electrode [156]. Similarly, a COMSOL-based physics model simulated SOFC failures for EIS diagnostics, enabling a SVM model to classify failure types under diverse operating conditions [157]. Signal-based methods, such as wavelet transforms, have also been used to decompose SOFC voltage signals, enhancing fault detection through extracted features [158]. Techniques like total harmonic distortion provide further non-physical model alternatives [151].

Despite the advancements in non model-based and data-driven methods, their application in real-time monitoring remains limited due to the need for large datasets and substantial computational resources, making real-time implementation challenging for SOEC systems.

In contrast, model-based methods rely on a physical model derived from first principles or system identification techniques to explicitly describe system behavior and the interactions between the variables [159]. Fault detection is achieved by monitoring the coherence between estimated and measured process variables, making this approach more interpretable, computationally efficient, and suitable for real-time SOFC fault diagnosis.

A model-based diagnosis approach typically involves developing a nominal system model, which reconstructs expected signal values during operation. By analyzing residuals, any significant deviation between the predictions of the model and measured signals serves as an indicator of faults, allowing for early diagnosis and preventive actions [153, 159].

Several model-based techniques have been explored in the literature. Polverino et al. [160] developed a dynamic SOFC system model combined with Fault Tree Analysis to identify fault-symptom relationships. They simulated five faults, generated residuals, and used thresholds to build a refined version of Fault Signature Matrix in [161] for fault detection in both the stack and balance-of-plant components.

Gallo et al. [162] developed a fault mitigation strategy that integrates the health state of the stack in fuel cell mode through electrochemical impedance spectroscopy (EIS) for real-time fault detection and isolation. Their approach utilizes a proportional-integral derivative (PID) controller-based estimator to evaluate fault severity, demonstrated through a hydrogen leakage scenario in SOFC mode, and enables adaptive mitigation strategies using PID controller.

For degradation assessment, Dolenc et al. [54] introduced an integrated method based on area-specific resistance (ASR). Their approach combines a lumped stack model with two Kalman filters: an Unscented Kalman Filter (UKF) for estimating total resistance and temperature as states and a standard Kalman Filter (KF), assumed to be linear, operating at a slower time scale to track the gradual variation of total resistance. The identified ASR drift is then used with a

Thèse accessible à l'adresse : https://theses.insa-lyon.fr/publication/2026ISAL0017/these.pdf © [Z. Yazbeck], [2026], INSA Lyon, tous droits réservés

Monte Carlo simulation to predict the remaining useful life of the stack. Observer-based ap-

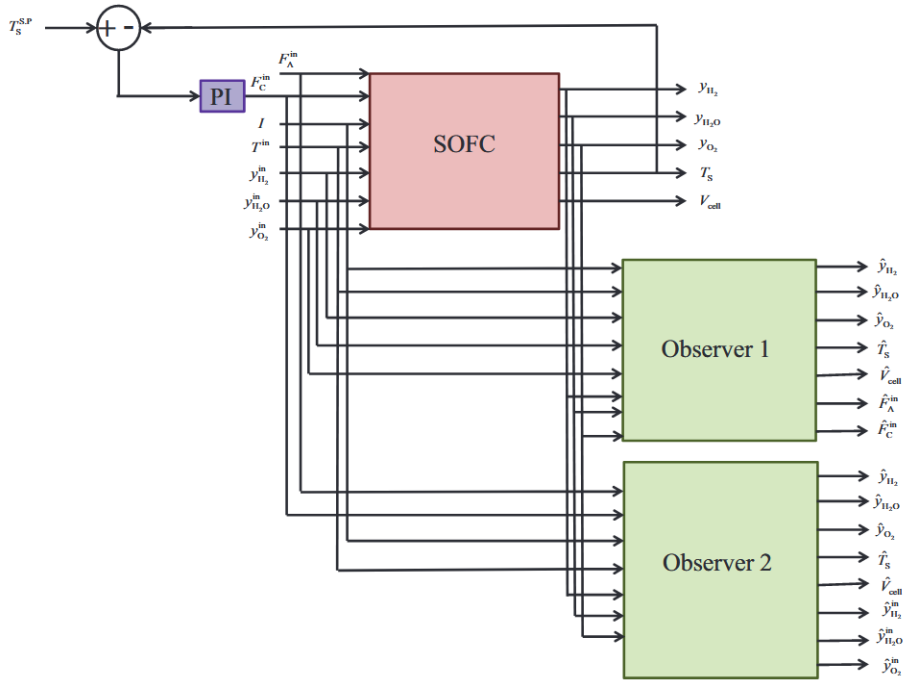

Figure 4.1: Fault diagnosis approach proposed in [163].

proaches have also been used for SOFC fault detection, leveraging state observers to estimate system states and detect discrepancies indicative of faults. Vijay et al. [163] proposed a nonlinear observer-based strategy that employs two adaptive observers as shown in Figure 4.1, relying on the voltage, the temperature and the outlet molar fractions of hydrogen, steam, and oxygen as measured outputs with the input vector that presents the nominal operating conditions to detect and classify five different SOFC faults. The methodology was validated through simulations, demonstrating its effectiveness in fault detection and classification. Wu et al. [164] developed a state observer-based method for SOFC fuel input fault detection, utilizing outlet air temperature measurements instead of internal sensors. Their approach tracks stack chamber temperature variations, effectively identifying input flow sensor faults and fuel supply issues, while filtering disturbances for real-time diagnosis. Xu et al. [159] introduced a real-time fault diagnosis scheme for gas leakage detection in SOFC, integrating a UKF with adaptive covariance matching and an adaptive threshold generator, as shown in Figure 4.2. By reconstructing air and fuel leakage states from outlet fuel and air temperatures as output measurements, their approach improves fault diagnosis robustness through dynamically adjusting thresholds. In this chapter, a real-time fault diagnosis scheme based on a square-root Unscented Kalman Filter (SR-UKF) is proposed to monitor and detect starvation related faults in SOCs that can operate in electrolysis or fuel cell mode. Unlike the standard UKF, which directly propagates covariance matrices, the SR-UKF propagates their Cholesky factors, thereby improving numerical stability and ensuring positive semi-definiteness throughout the filtering process [165]. To validate the proposed approach, an

Thèse accessible à l'adresse : https://theses.insa-lyon.fr/publication/2026ISAL0017/these.pdf © [Z. Yazbeck], [2026], INSA Lyon, tous droits réservés

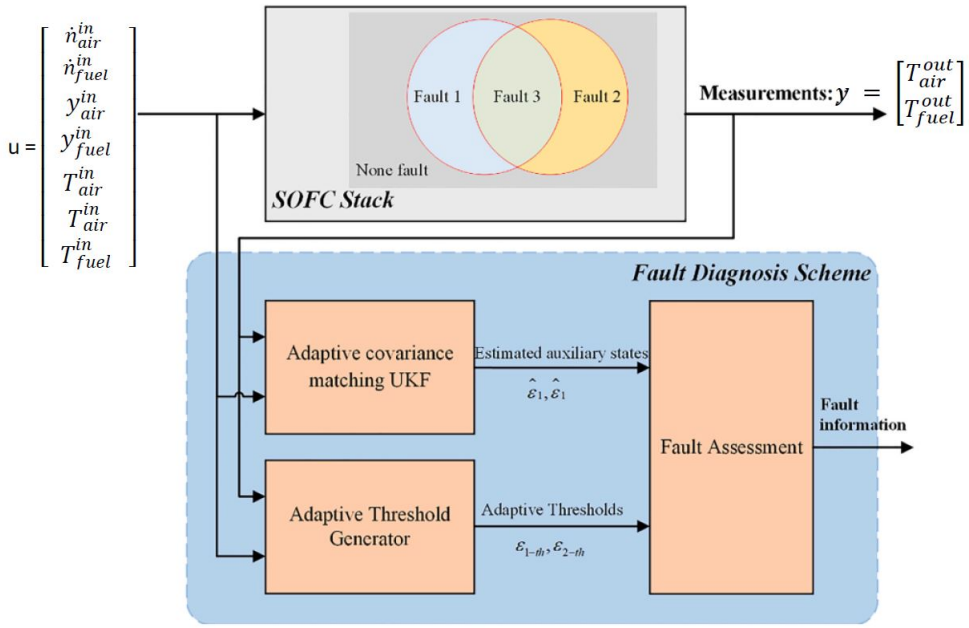

Figure 4.2: Fault diagnosis approach proposed in [159].

experimental SOEC system operating in electrolysis mode is considered, with outlet air temperature, voltage, and outlet hydrogen flow rate used as the measured outputs. Based on these signals, the SR-UKF estimates and reconstructs the partial pressures of hydrogen, steam, and oxygen, the stack temperature, and the fuel input flow rate to the system.
The contributions of this work are as follow:

- Minimal reliance on sensor instrumentation is used: voltage, outlet air temperature, and hydrogen flow rate while additional or different measurements are used in previous approaches [159, 163] requiring more intrusive measurements.
- Direct estimation of key internal states including partial pressures and fuel input rate, enabling fault detection through deviation relative to a nominal model.
- Design of an adaptive thresholds using moving window filter to reduce false alarms.
- Use of an SR-UKF formulation, which improves numerical stability compared to the standard UKF used in other model-based SOFC fault diagnosis schemes [159].
- Studying hydrogen starvation or hydrogen inlet molar fraction fault in electrolysis mode.

In this work, two fault scenarios are analyzed in electrolysis mode:

1. Steam starvation: caused by a sudden reduction in steam inlet flow rate leading to high steam conversion.

Thèse accessible à l'adresse : https://theses.insa-lyon.fr/publication/2026ISAL0017/these.pdf © [Z. Yazbeck], [2026], INSA Lyon, tous droits réservés

2. Hydrogen starvation: a small amount of hydrogen is added alongside steam to prevent nickel reoxidation at the stack inlet during electrolysis operation, a decrease in this hydrogen supply is considered as a fault.

This methodology is also applicable to fuel cell operation, enabling the detection of air starvation in addition to hydrogen starvation, where the consumption rate of hydrogen to produce electricity exceeds its supply. By accurately reconstructing key internal states and fuel flow conditions, the proposed SR-UKF framework enhances fault diagnosis reliability, ensuring early intervention and preventing irreversible degradation.

4.4 Fault detection methodology

The SOEC mathematical model formulated in state space model in Chapter 3.2 is considered, but in addition to the voltage of the stack, the temperature is also considered as measurement, since starvation affects both outputs. Thus, the measured output considered is $y = [V_s\ T]^T$ under the nominal input vector
$u = [I\ \dot{n}_{fuel}^{in,nom}\ \dot{n}_{air}^{in,nom}\ y_{H_2O}^{in,nom}\ T_{furnace} T_{fuel}^{in}\ T_{air}^{in}]^T$ as in Equation (3.2).

These measurements are sufficient to reconstruct the partial pressures of hydrogen, steam, and oxygen, as well as the stack temperature even in faulty conditions. They also enable the detection of faults on either the fuel or oxygen side. In the case of a fault on the fuel side, the partial pressures of hydrogen and steam will be both affected. Consequently, these partial pressures can be reconstructed, and the fault can be detected.

To distinguish whether the fault corresponds to hydrogen or steam starvation in the fuel side, the variation of the total resistance is analyzed. A significant increase in total resistance indicates steam starvation, whereas a negligible change suggests hydrogen starvation. However, to quantify this fault, an additional measurement is required, in this case we use the outlet hydrogen flow rate.

Since this measurement is available in the test bench used, the considered measured output becomes:

$$y = [V_s\ T\ \dot{n}_{H_2}^{out}]^T$$

To specifically address starvation, which is directly related to the real inlet fuel flow rate fed to the stack, two additional state variables, ϵ_1 and ϵ_2, are introduced in the state vector of the observer. These variables represent the deviation of the real inlet steam and hydrogen flow rate respectively from their nominal setpoint value, where:

$$\begin{aligned} \dot{n}_{H_2O}^{in,real} &= \dot{n}_{H_2O}^{in,nom} \cdot (1 - \epsilon_1) \\ \dot{n}_{H_2}^{in,real} &= \dot{n}_{H_2}^{in,nom} \cdot (1 - \epsilon_2) \end{aligned} \tag{4.1}$$

where $\dot{n}_{H_2O}^{in,nom}$ and $\dot{n}_{H_2}^{in,nom}$ are the nominal inlet steam and hydrogen molar flow rates respectively,

Thèse accessible à l'adresse : https://theses.insa-lyon.fr/publication/2026ISAL0017/these.pdf © [Z. Yazbeck], [2026], INSA Lyon, tous droits réservés

and $\epsilon_{1/2}$ quantifies the deviation from nominal values due to faults. By incorporating these states, we gain insight into the actual fuel supply during a faulty condition, which is crucial for distinguishing starvation-related issues. Additionally, this information is essential for fault-tolerant control, a key aspect of the overall health management strategy.

Thus, the model used by the observer is now:

$$\begin{aligned} \dot{x} &= f_2(x, \lambda, u) \\ y &= h_2(x, \lambda, u) \end{aligned} \tag{4.2}$$

where $f_2 = \begin{bmatrix} f \\ 0 \\ 0 \end{bmatrix}$ and $h_2 = \begin{bmatrix} h \\ T \end{bmatrix}$.

$f(\cdot)$ and $h(\cdot)$ refer to the nonlinear functions in Equation (3.1),(3.4). The new state vector is $x = [p^{ch}_{H_2}\ p^{ch}_{H_2O}\ p^{ch}_{O_2}\ T\ \epsilon_1\ \epsilon_2]^T$, the output is $y = [V_s\ T\ \dot{n}^{out}_{H_2}]^T$, and the input vector u as defined in Equation (3.2).

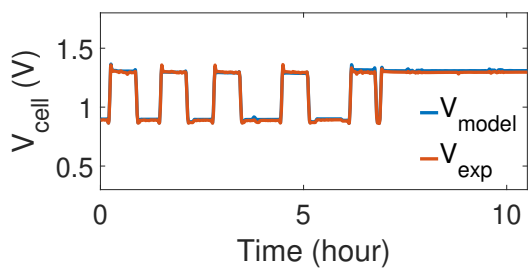

(a) Mean voltage vs Time

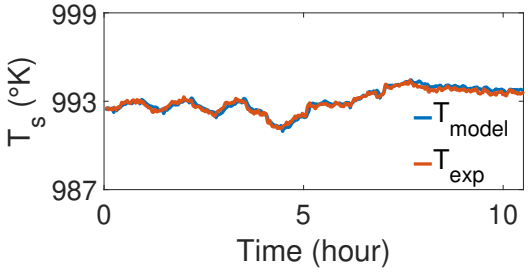

(b) Stack Temperature vs Time

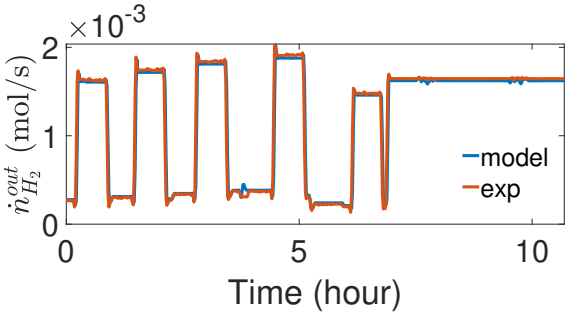

(c) Outlet Hydrogen molar flow rate vs Time

Figure 4.3: Validation of the model outputs against measured data from the experimental test bench.

The model parameters used in the observer were previously identified from experimental data using the calibration procedure presented in Section 3.4.1, with the resulting parameter values reported in Table 3.8. Before employing this calibrated model as the nominal reference for state estimation and fault detection, its outputs are compared with measurements from the experimental test bench. As shown in Figure 4.3, the model satisfactorily reproduces the measured stack

Thèse accessible à l'adresse : https://theses.insa-lyon.fr/publication/2026ISAL0017/these.pdf © [Z. Yazbeck], [2026], INSA Lyon, tous droits réservés

voltage, stack temperature, and outlet hydrogen molar flow rate.

To verify fault occurrence, the estimated state vector is compared to a reference that represents the nominal behavior of the system, as shown in Figure 4.4 and introduced to a decision block to automatically detect the type of fault using an adaptive threshold. The reference states are computed using the SOEC model under nominal operating conditions. By doing so, deviations in $\epsilon_{1/2}$ indicate fuel flow discrepancies (steam, hydrogen, or both inlet flow rates), while the reconstructed partial pressures provide additional insights into starvation conditions.

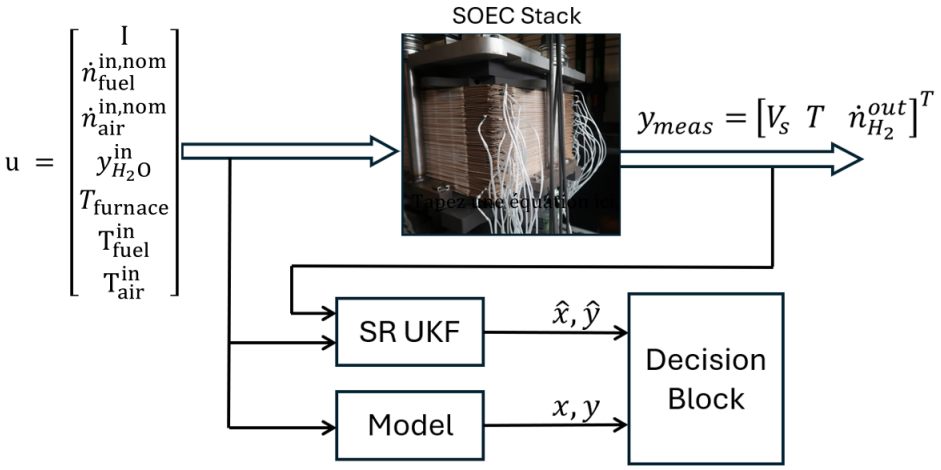

Figure 4.4: Starvation detection scheme.

4.4.1 Square-Root Unscented Kalman Filter

The primary objective of Kalman filters is to iteratively estimate x_k based on the history of measurements, represented as $Y_k = (y_1, y_2, \ldots, y_k)$, by characterizing the posterior density $p(x_k|Y_k)$. Under the assumption that both the process noise and the measurement noise are Gaussian, and that the system dynamics are linear, the Kalman filter represents the posterior density $p(x_k|Y_k)$ by its mean and covariance, enabling recursive state estimation. However, for nonlinear systems, direct parametrization becomes impractical, requiring approximation techniques. A common approach is the Extended Kalman Filter (EKF), which applies local linearization around the predicted mean as shown in Figure 4.5. Despite its utility, the EKF struggles with highly nonlinear systems, potentially degrading estimation performance [165].

To overcome the limitations of local linearization, the Unscented Kalman Filter (UKF) and square-root Unscented Kalman Filter (SR-UKF) approximate $p(x_k|Y_k)$ using a set of deterministically chosen weighted sample points, as shown in Figure 4.5, denoted as χ in the Algorithm in [165]. The weights of these sample points, $W_i^{(m)}$ and $W_i^{(c)}$ for $i \in \{0, \ldots, 2n\}$, are presented in Equation (4.3) and determined using the scaling parameters $\lambda = n(\alpha^2 - 1)$, and $\gamma = \sqrt{n + \lambda}$, where n represents the state-space dimension. The parameter α controls the dispersion of sam-

Thèse accessible à l'adresse : https://theses.insa-lyon.fr/publication/2026ISAL0017/these.pdf © [Z. Yazbeck], [2026], INSA Lyon, tous droits réservés

ple points around the estimated mean $\hat{x}$ and is typically chosen within $10^{-4} \leq \alpha \leq 1$ [165]. The parameter β is a positive scalar used to incorporate prior knowledge of the distribution of x [165]. When the weighted sample points undergo a nonlinear transformation, the mean and covariance of the transformed distribution can be estimated [165]. Compared to the UKF, the SR-UKF enhances numerical stability by avoiding repeated Cholesky factorizations of the full covariance matrix. Instead, it propagates and updates square-root covariance factors through the Kalman recursion, typically using orthogonal transformations (QR factorization) together with Cholesky updates to maintain these factors.

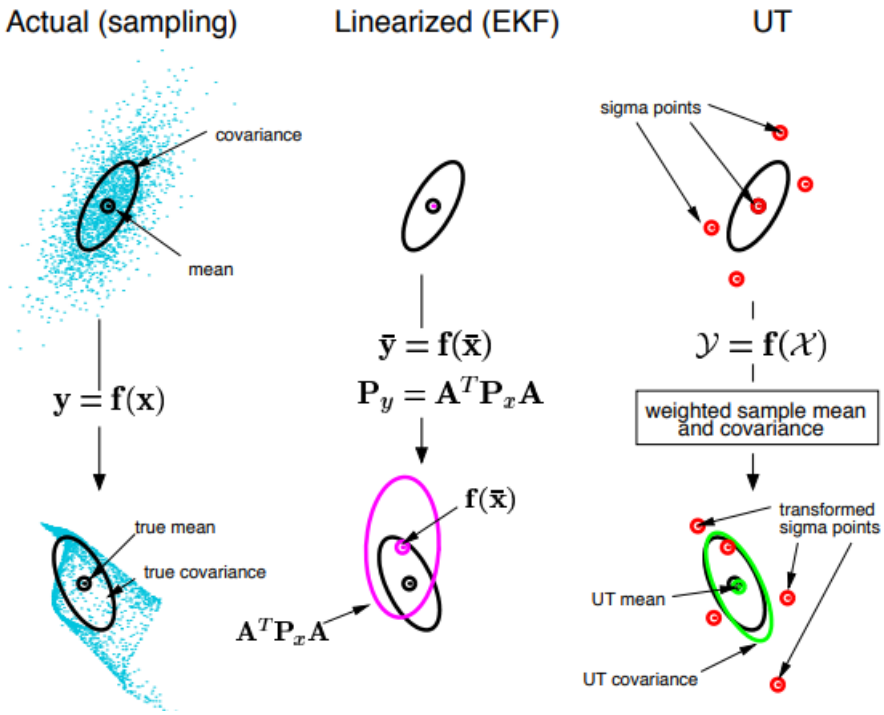

Figure 4.5: Example of the Unscented Transform (UT) for mean and covariance propagation. a) actual, b) first-order linearization used by EKF, c) Unscented Transform (UT) [165].

Algorithm

Select the sigma point set weights $W_i^{(m)}$ and $W_i^{(c)}$, the weight coefficients for mean and error covariance respectively, according to the following equations:

$$\begin{aligned} W_0^{(m)} &= \frac{\lambda}{n+\lambda} \quad \text{for } i = 0; \\ W_0^{(c)} &= W_0^{(m)} + \left(1 - \alpha^2 + \beta\right) \quad \text{for } i = 0; \\ W_i^{(c)} &= W_i^{(m)} = \frac{1}{2(n+\lambda)} \quad \text{for } i \neq 0; \end{aligned} \tag{4.3}$$

where we set $\alpha = 0.1$, and $\beta = 2$ [165].

Thèse accessible à l'adresse : https://theses.insa-lyon.fr/publication/2026ISAL0017/these.pdf © [Z. Yazbeck], [2026], INSA Lyon, tous droits réservés

Initialization:

$$\hat{x}_0 = E[x_0], \quad S_0 = chol\left\{E[(x_0 - \hat{x}_0)(x_0 - \hat{x}_0)^T\right\} \tag{4.4}$$

The initial condition of the partial pressure states are set to be equal to the inlet gas composition, and the initial values of $\epsilon_{1/2}$ are set to zero, indicating that the fuel flow rate used is initially equal to its nominal setpoint value:
$\hat{x}_0 = [y^{in}_{H_2,t=0}\ y^{in}_{H_2O t=0}\ y^{in}_{O_2,t=0}\ T_{,t=0}\ 0\ 0]^T$.
The covariance matrices used in this chapter are as follows :

- S_0 - Cholesky factor of the covariance matrix of the initial state estimate:

$$S_0 = \text{diag}(2e-2,\ 2e-2,\ 2.5e-3,\ 5e-1,\ 1e-4,\ 1e-3)$$

- Q - Process noise covariance matrix:

$$Q = \text{diag}(2e-4,\ 3e-4,\ 1e-4,\ 1e-1,\ 5e-5,\ 5e-2)$$

- R - Measurement noise covariance matrix:

$$R = \text{diag}(1e-3,\ 5e-7,\ 1e-8)$$

The covariance matrices were selected empirically through a trial-and-error tuning procedure rather than a systematic optimization method. Larger diagonal values were assigned to states, model dynamics, or measurements associated with greater uncertainty. However, since the states and measurements involved span markedly different orders of magnitude and physical units, the relative rather than the absolute magnitude of each diagonal entry must be considered when interpreting these weights. The final values were retained based on the stability of the filter, the consistency of the estimated states, and the agreement between the estimated and measured outputs.

Step 1: Time update

- Calculate the sigma points:

$$\chi^-_{k-1} = \begin{bmatrix}\hat{x}_{k-1} & \hat{x}_{k-1} + \gamma S^i_{k-1} & \hat{x}_{k-1} - \gamma S^i_{k-1}\end{bmatrix} \tag{4.5}$$

  Where S^i_{k-1} is the ith column of S_{k-1}.

- Propagate sigma points:

$$\chi^*_{k|k-1} = F_2\left(\chi^-_{k-1}, u_{k-1}\right) \tag{4.6}$$

  Where F_2 is the discrete-time version of the function of f_2 in Equation (4.4)

Thèse accessible à l'adresse : https://theses.insa-lyon.fr/publication/2026ISAL0017/these.pdf © [Z. Yazbeck], [2026], INSA Lyon, tous droits réservés

- Compute predicted mean:

$$\hat{x}_k^- = \sum_{i=0}^{2n} W_i^{(m)} \chi_{i,k|k-1}^* \tag{4.7}$$

- Compute predicted covariance:

$$\begin{aligned} S_{x_k} &= qr\left\{\left[\sqrt{W_1^{(c)}}\left(\chi_{1:2n,k|k-1}^* - \hat{x}_k^-\right), \sqrt{Q}\right]\right\} \\ S_{x_k} &= cholupdate\left\{S_{x_k}, \left(\chi_{0,k}^* - \hat{x}_k^-\right), W_0^{(c)}\right\} \end{aligned} \tag{4.8}$$

  Where $\sqrt{Q}$ is the square root of the diagonal matrix Q.

- Resampling of the sigma point:

$$\chi_{k|k-1} = \begin{bmatrix} \hat{x}_k^- & \hat{x}_k^- + \gamma S_{x_k}^i & \hat{x}_k^- - \gamma S_{x_k}^i \end{bmatrix} \tag{4.9}$$

Step 2: Measurement Update

- Compute predicted measurement:

$$\begin{aligned} \mathcal{Y}_{k|k-1} &= h_2\left(\chi_{k|k-1}\right) \\ \hat{y}_k^- &= \sum_{i=0}^{2n} W_i^{(m)} \mathcal{Y}_{i,k|k-1} \end{aligned} \tag{4.10}$$

- Compute innovation covariance:

$$\begin{aligned} S_{\tilde{y}_k} &= qr\left\{\left[\sqrt{W_1^{(c)}}\left(\mathcal{Y}_{1:2n,k} - \hat{y}_k^-\right), \sqrt{R}\right]\right\} \\ S_{\tilde{y}_k} &= cholupdate\left\{S_{\tilde{y}_k}, \mathcal{Y}_{0,k} - \hat{y}_k^-, W_0^{(c)}\right\} \end{aligned} \tag{4.11}$$

  Where $\sqrt{R}$ is the square root of the diagonal matrix R.

- Compute cross covariance:

$$P_{x_k y_k} = \sum_{i=0}^{2n} W_c^i \left(\chi_{i,k|k-1} - \hat{x}_k^-\right)\left(\mathcal{Y}_{i,k|k-1} - \hat{y}_k^-\right)^T \tag{4.12}$$

- Compute Kalman gain:

$$\mathcal{K}_k = P_{x_k y_k}\left(S_{y_k} S_{\tilde{y}_k}^T\right)^{-1} \tag{4.13}$$

- Update state:

$$\hat{x}_k = \hat{x}_k^- + \mathcal{K}_k\left(y_k - \hat{y}_k^-\right) \tag{4.14}$$

Thèse accessible à l'adresse : https://theses.insa-lyon.fr/publication/2026ISAL0017/these.pdf © [Z. Yazbeck], [2026], INSA Lyon, tous droits réservés

- Update covariance:

$$S_k = cholupdate\left\{S_{x_k}, \mathcal{K}_k S_{\tilde{y}_k}, -1\right\} \tag{4.15}$$

4.4.2 Adaptive Threshold for Fault Detection

Fault detection in electrochemical systems requires dynamic thresholding to distinguish between normal variations and faulty behavior while mitigating false alarms. A fixed threshold is often inadequate due to varying operating conditions, system uncertainties, process noise, and aging effects. To address this, we employ an adaptive threshold computed using a moving window filter approach.

Instead of directly monitoring the residuals between the measured and estimated outputs, the proposed method compares the states estimated by the observer with those computed by the model under nominal operating conditions. The partial pressures of hydrogen, steam, and oxygen are key parameters for detecting starvation, as starvation directly affects the local gas composition. Consequently, these partial pressures serve as reliable indicators of fault conditions. The nominal states calculated using the model under nominal operating conditions represent the expected behavior in a fault-free scenario. Comparing the estimated states by the observer with these nominal values enables accurate fault detection, ensuring effective system monitoring.

A moving window filter is then applied to compute a threshold that adjusts dynamically based on statistical properties of the nominal state evolution. The filtered state vector of the nominal system based on the moving window m, which is set to 120 samples in this study, is:

$$\bar{x}_k = \frac{1}{m} \sum_{i=k-m+1}^{k} x_{nom_i} \tag{4.16}$$

The variance of the state within the same moving window at the kth sample point is given by:

$$\sigma_k^2 = \frac{1}{m-1} \sum_{i=k-m+1}^{k} (x_{nom_i} - \bar{x}_k)^2 \tag{4.17}$$

According to statistical theory, the confidence interval for the mean is given by:

$$P\{\bar{x} - z\sigma < \bar{x} < \bar{x} + z\sigma\} = 1 - \mu \tag{4.18}$$

where μ represents the confidence level, and z is the confidence coefficient [166]. The term $(1 - \mu)$ defines a confidence interval, which is typically selected within the range of 90% to 99%. In this study, the coefficient z is set to 3 to account for noise perturbations. Based on this formulation, the adaptive threshold is determined as:

$$Th_k = \bar{x}_k \pm 3\sigma_k \tag{4.19}$$

Thèse accessible à l'adresse : https://theses.insa-lyon.fr/publication/2026ISAL0017/these.pdf © [Z. Yazbeck], [2026], INSA Lyon, tous droits réservés

where Th_k represents the upper and lower limits of fault-free conditions and adapts dynamically to reflect changes in the actual operating conditions.

The choice of the moving window m directly influences the adaptability of the threshold:

- A small m results in a faster response, increasing the sensitivity to small changes but also making the system more susceptible to noise.
- A large m smooths variations and prevents excessive reactivity, but may reduce the responsiveness of fault detection.

To balance these effects, a weighted sum of past and present residual statistics is used to prevent excessive variations in threshold values [167]:

$$Th_k = \bar{\bar{x}}_k \pm 3\bar{\sigma}_k, \tag{4.20}$$

where the weighted mean and variance are computed as:

$$\begin{aligned} \bar{\sigma}_k &= \rho\sigma_k + (1-\rho)\sigma_{k-1}, \\ \bar{\bar{x}}(k) &= \rho\bar{x}_k + (1-\rho)\bar{x}_{k-1}. \end{aligned} \tag{4.21}$$

Here, $\rho \in (0,1)$ is a momentum parameter that controls the influence of past values on the threshold adaptation that is set to 0.9 in this study.

Thus, a fault is detected when the estimated state $\hat{x}(t)$ deviates from the nominal state $x_{nom}(t)$ by more than the adaptive threshold.

4.4.3 Experimental Studies

As mentioned before, to replicate steam starvation fault experimentally, we gradually reduced the total inlet fuel flow rate $\dot{n}^{\text{in}}_{\text{fuel}}$ from its nominal value $\dot{n}^{\text{in, nom}}_{\text{fuel}}$ to have high steam conversion(S.C.), where S.C.= $\dfrac{I}{2F\dot{n}^{in}_{H_2O}}$. The fuel consisted primarily of steam with a small fraction of hydrogen, and both flows were decreased simultaneously while maintaining roughly a constant molar fraction, as shown in Figure 4.6. At the same time, the current was adjusted to maintain the thermoneutral voltage as shown in Figure 4.7, ensuring high efficiency and preventing irreversible degradation [168].

Hydrogen starvation, defined as an insufficient inlet hydrogen fraction, poses a risk of nickel reoxidation, in particular at the inlet hydrogen electrode. To present this scenario in experiment, the hydrogen fraction was reduced from its nominal value of 0.1 to zero over a defined time window (highlighted in Figure 4.9), while the current was held constant. Under these conditions, the voltage remains largely unaffected, whereas the outlet hydrogen flow rate, directly impacted by this fault, was included among the measured signals.

Thèse accessible à l'adresse : https://theses.insa-lyon.fr/publication/2026ISAL0017/these.pdf © [Z. Yazbeck], [2026], INSA Lyon, tous droits réservés

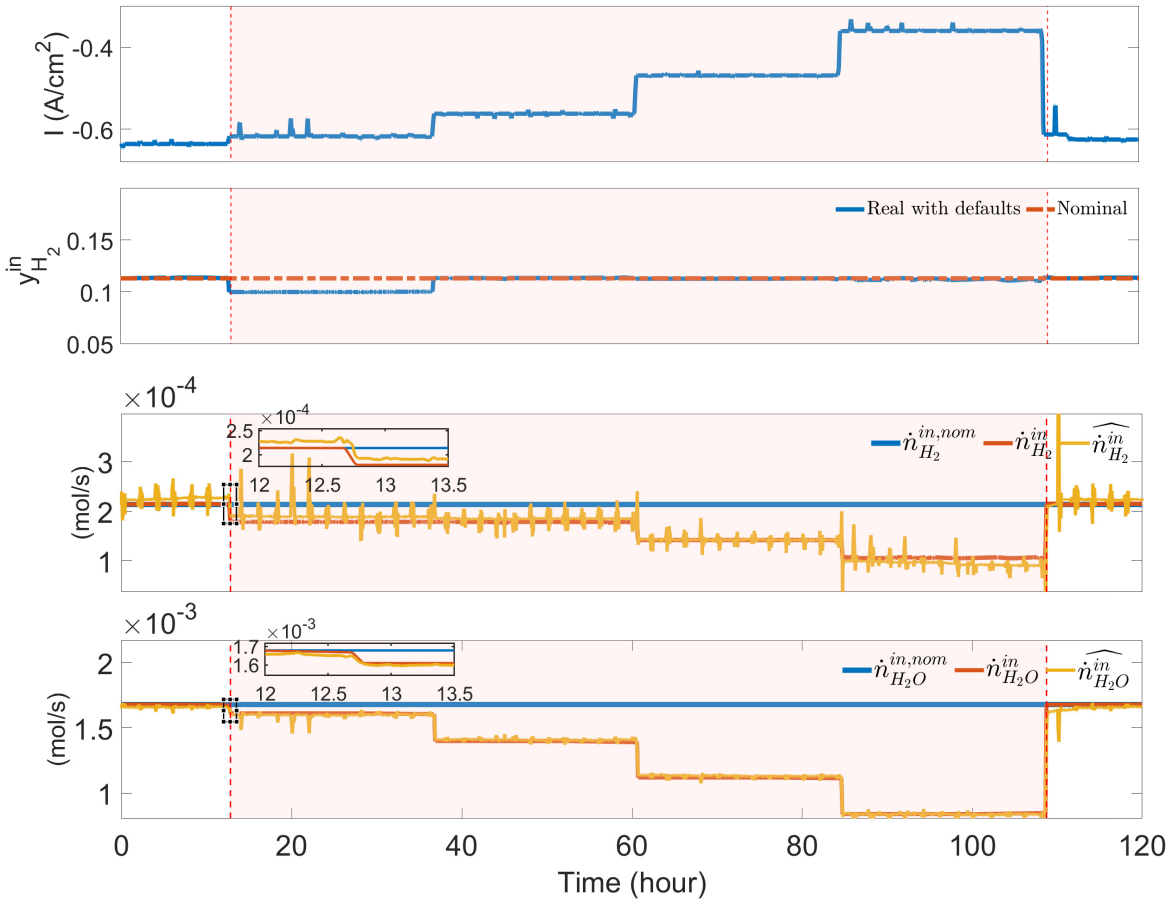

Figure 4.6: Operating conditions showing both estimated and nominal inlet total flow rates during the steam starvation scenario for comparison. The colored regions indicate the time windows where the fault is injected.

Thèse accessible à l'adresse : https://theses.insa-lyon.fr/publication/2026ISAL0017/these.pdf © [Z. Yazbeck], [2026], INSA Lyon, tous droits réservés

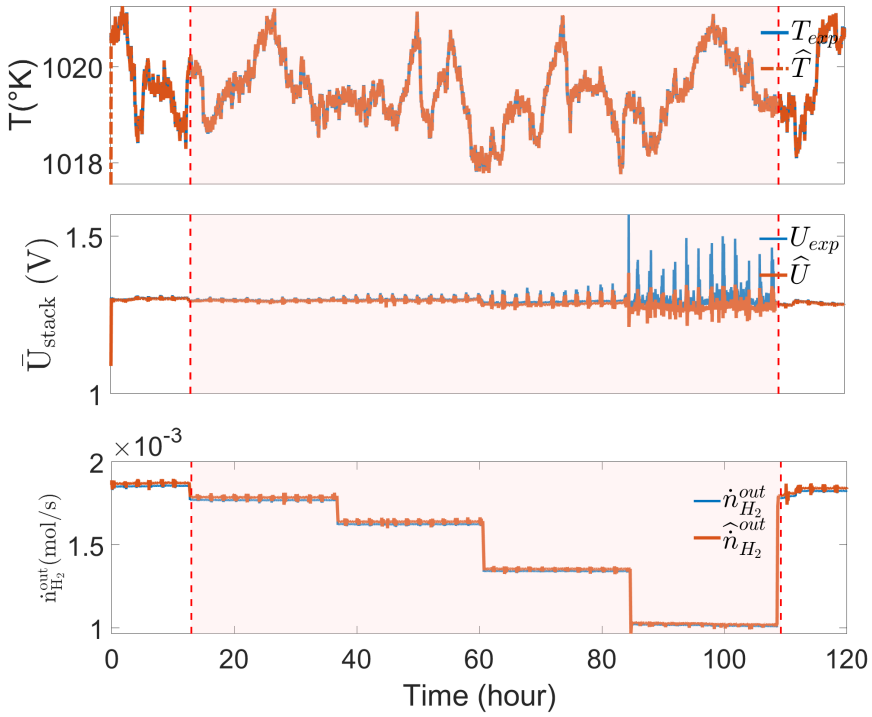

Figure 4.7: Outputs in steam starvation case.

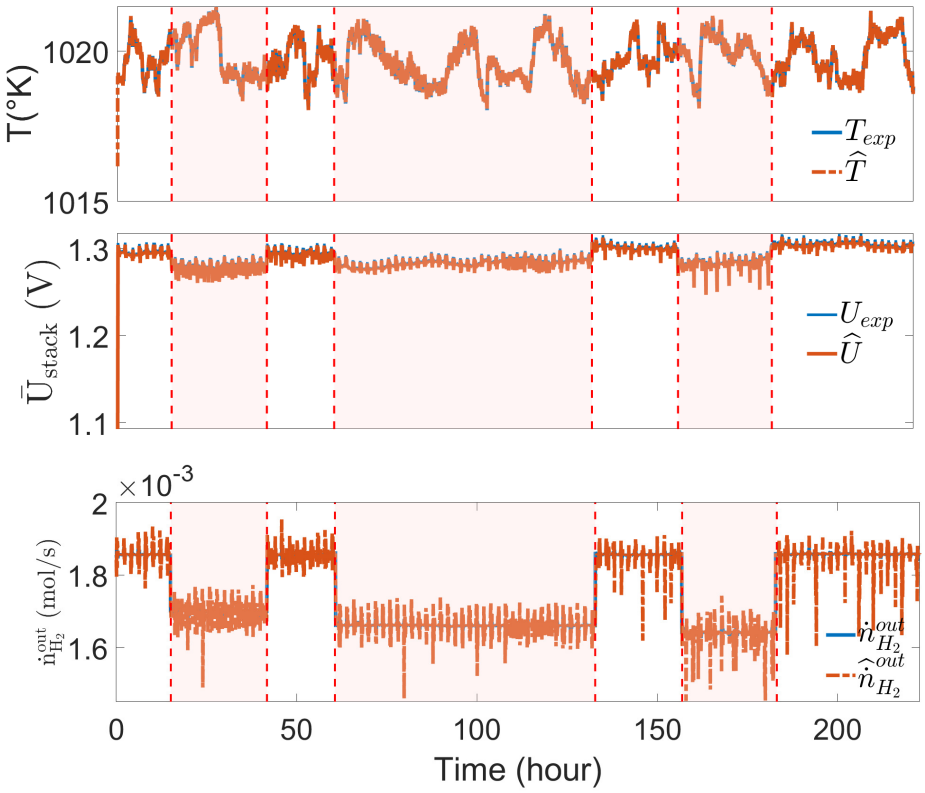

Figure 4.8: Outputs in hydrogen starvation case.

Thèse accessible à l'adresse : https://theses.insa-lyon.fr/publication/2026ISAL0017/these.pdf © [Z. Yazbeck], [2026], INSA Lyon, tous droits réservés

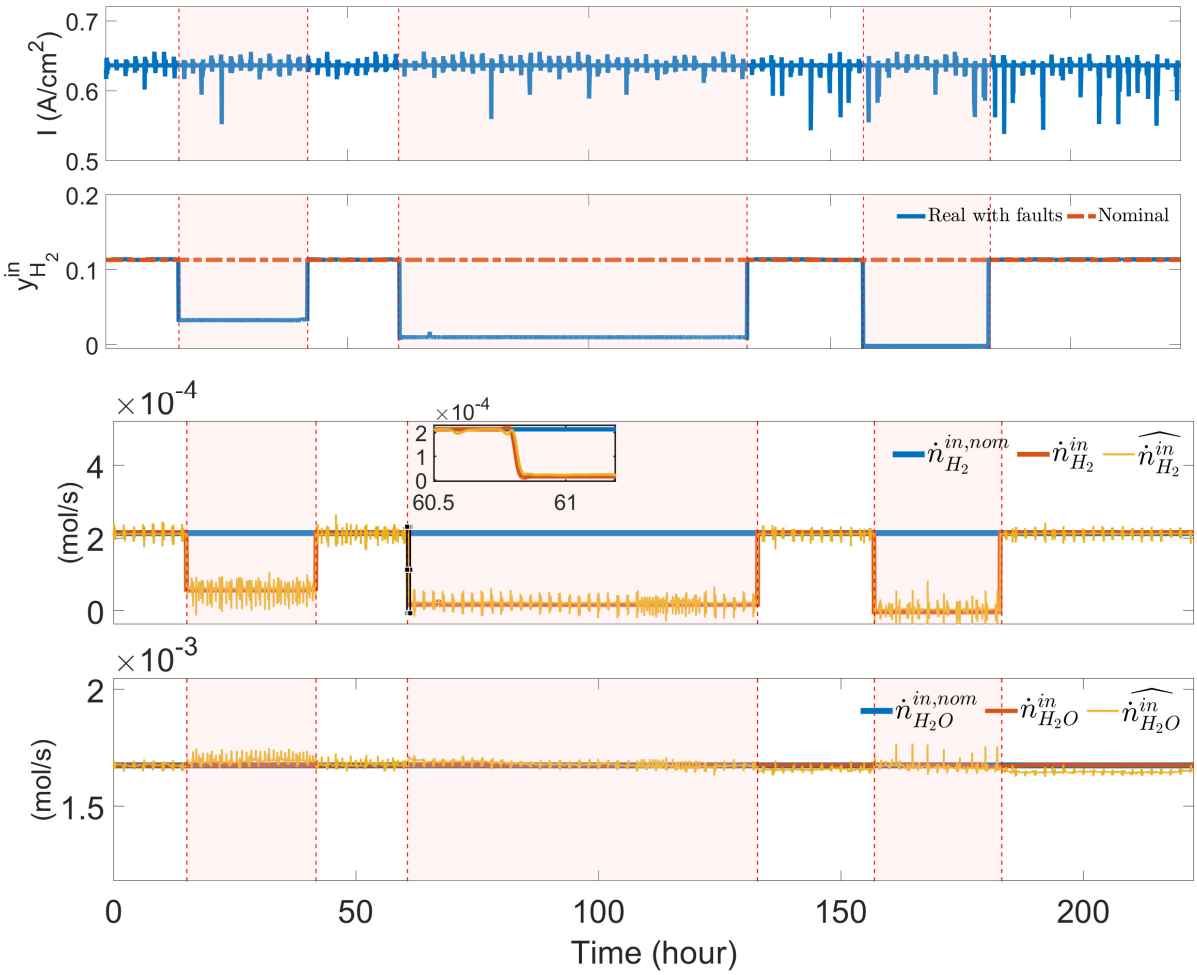

Figure 4.9: Operating conditions showing both estimated and nominal inlet total flow rates during the Hydrogen Starvation scenario for comparison.
The colored regions indicate the time windows where the fault is injected.

The fault detection algorithm was applied using measured stack voltage, temperature (see Figures 4.7, 4.8), and outlet hydrogen flow rate with inputs in nominal operating conditions. When a fault occurred, the reconstructed partial pressures exceeded their adaptive thresholds, confirming the onset of starvation. Additionally, the reconstructed inlet hydrogen and steam flow rates accurately reflected the actual inputs, which is valuable for health management strategies. Initially, estimated fault indicators remained within normal limits but began to diverge clearly as starvation progressed, as shown in the highlighted windows in Figures 4.10 and 4.11, demonstrating the ability of the diagnostic scheme for early detection.

The experimental results validate the proposed fault detection methodology. The SR-UKF observer effectively identified deviations in fuel supply conditions, while the adaptive threshold minimizes false alarms. If implemented in a real SOC system, this approach could enable early intervention strategies, reduce degradation risks, and improve system reliability.

Adaptive thresholding is adjusted dynamically to process variations while maintaining sen-

Thèse accessible à l'adresse : https://theses.insa-lyon.fr/publication/2026ISAL0017/these.pdf © [Z. Yazbeck], [2026], INSA Lyon, tous droits réservés

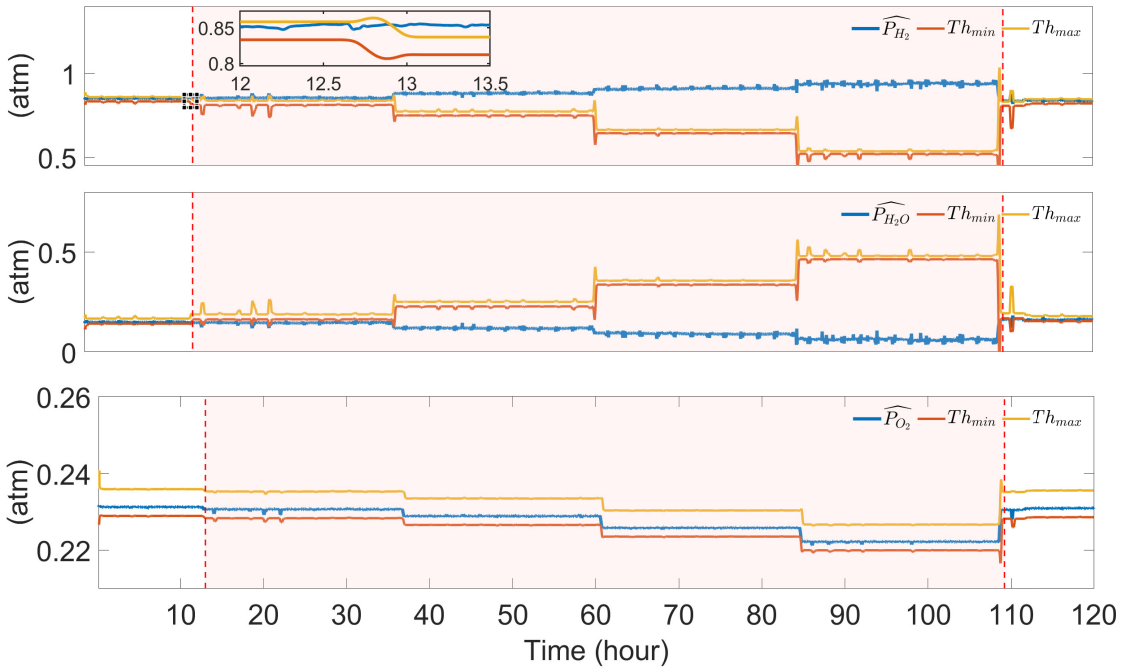

Figure 4.10: States estimation in steam starvation scenario and fault detection thresholds ($Th_{min/max}$) for each variable.

sitivity to faults. Unlike static thresholds, this method responds to evolving system conditions, making it particularly effective for detecting starvation faults in SOCs.

Figures 4.10 and 4.11 illustrate the adaptive threshold applied in electrolysis mode, where partial pressures and inlet fuel flow rates are monitored. The methodology is also applicable to fuel cell mode, where hydrogen starvation can be detrimental for cells due to nickel reoxidation. In addition, air starvation can also be detected by monitoring oxygen partial pressure. A fault is identified when the reconstructed oxygen pressure drops outside the adaptive thresholds, indicating an air starvation event.

Nonetheless, the total resistance was also computed from estimated states as complementary information. This resistance, corresponding to the low-frequency resistance in electrochemical impedance spectra, is given by:

$$R_{\text{total}} = \frac{\partial V_{cell}}{\partial I} \tag{4.22}$$

Although not used for fault identification, this resistance reflects the impact of partial pressure variations on electrochemical performance. In particular, steam starvation causes noticeable changes in overpotentials and a significant increase in total resistance. Figure 4.12 illustrates this evolution, consistent with trends reported in the literature [157]. However, relying only on impedance-derived resistance may not be sufficient to detect hydrogen starvation or deviations in small inlet molar fractions in electrolysis mode, since voltage responses can remain nearly unchanged. This highlights the importance of state estimation-based diagnostics, which enable more precise differentiation and fault interpretation.

Thèse accessible à l'adresse : https://theses.insa-lyon.fr/publication/2026ISAL0017/these.pdf © [Z. Yazbeck], [2026], INSA Lyon, tous droits réservés

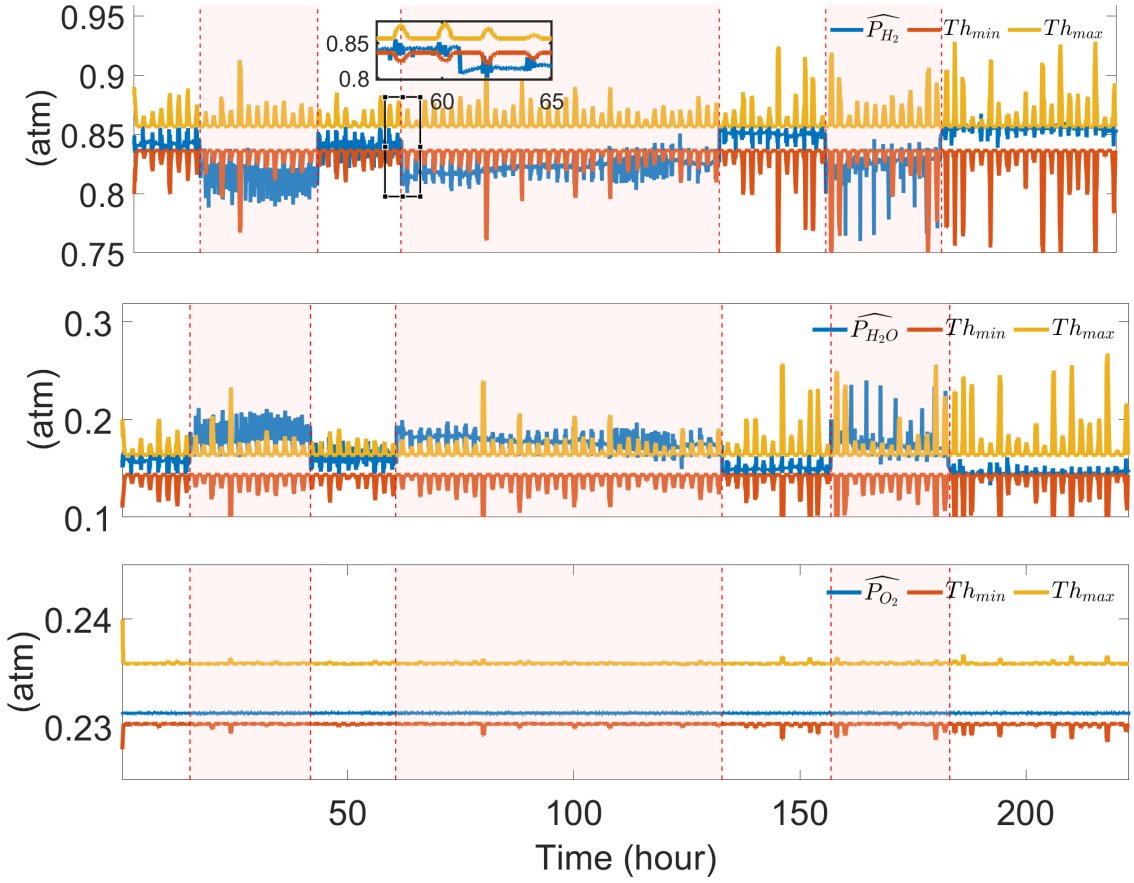

Figure 4.11: States estimation in hydrogen starvation scenario and fault detection thresholds ($Th_{min/max}$) for each variable.

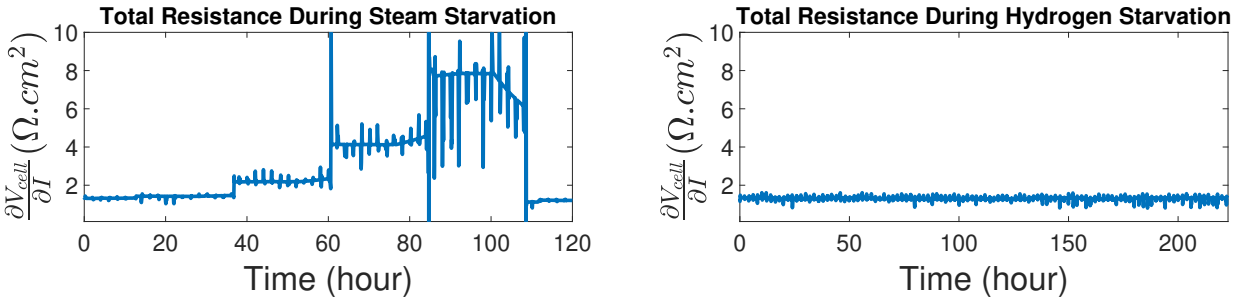

(a) Total resistance in steam starvation scenario

(b) Total resistance in hydrogen starvation scenario

Figure 4.12: Total resistance behavior in steam and hydrogen starvation scenarios, respectively.

Thèse accessible à l'adresse : https://theses.insa-lyon.fr/publication/2026ISAL0017/these.pdf © [Z. Yazbeck], [2026], INSA Lyon, tous droits réservés

4.5 Aging-aware monitoring

As discussed in Chapter 1.6, the electrochemical and thermal behavior of SOECs changes progressively over time due to multiple degradation mechanisms. Compared with the fast dynamics associated with mass transport and thermal transients, these degradation phenomena change the electrode microstructure, the contact resistance, and cause interfacial degradation and material aging on slow time scales. When neglecting this slow evolution, the model gradually loses fidelity and, consequently, leads to unreliable state estimation, fault detection, and health assessment. Therefore, the parameters of a physical SOEC model cannot be assumed constant over long operating periods, even when the system remains free of faults.

The SOEC stack lumped model developed in Chapter 2.3 and calibrated in Chapter 3.7, provides the nominal system behavior over short time horizons. It was used to develop an SR-UKF used to reconstruct fast internal states for starvation fault detection purposes. In this context, the parameter vector λ defined in Table 3.1 was assumed constant and representative of a healthy system, which is a reasonable assumption for short-duration experiments where aging effects remain negligible.

However, this assumption no longer holds when extending the monitoring framework to long operating periods. A slow drift of key electrochemical parameters is expected, such as exchange current densities, ohmic resistances, or effective transport properties, which directly affect the voltage response and temperature of the stack [169]. However, for the SR-UKF, every discrepancy between the model and the measured outputs will be explained as changes in the internal states. In the absence of a dedicated aging representation, this risks being interpreted as a fault, and will degrade fault isolation performance while increasing the risk of false alarms.

This aging tracking has been widely recognized in the literature as state-of-health (SoH) estimation. The work of Dolenc et al. [54] proposed a two-time scale estimation framework for SOFC stacks, in which the total area-specific resistance (ASR), assumed to represent the total resistance of the stack, is introduced as a slowly varying health indicator. In their approach, the stack temperature is modeled as a fast dynamic state, while the drift model of ASR, is considered as a parameter evolving on a much slower time scale and estimated using Kalman filtering. The mismatch between the measured and predicted voltage is compensated by the ASR effectively, capturing the cumulative effect of aging phenomena. ASR represents the SoH of the system enabling online tracking and remaining useful life estimation.

Bressel et al. [170] adopted a similar philosophy for the remaining useful lifetime estimation of PEMFC. An Extended Kalman Filter, based on a very simplified static voltage model, was used, only considering the dynamics of aging to compensate the drift in the voltage measurement. The varying parameters considered are the open circuit voltage (OCV), exchange current density, global resistance, and limiting current density. The methodology is validated using both steady-state and dynamic experimental data for prognostic purposes, to estimate the remaining useful lifetime of the studied system.

Thèse accessible à l'adresse : https://theses.insa-lyon.fr/publication/2026ISAL0017/these.pdf © [Z. Yazbeck], [2026], INSA Lyon, tous droits réservés

However, this assumption becomes problematic, especially in the presence of operational faults or abnormal conditions. To illustrate this with an extreme condition for SOEC system, if steam starvation occurs, which is a common problem in real systems, it will lead to voltage deviations that are not related to irreversible degradation [65, 171]. As a result, the estimated state-of-health parameters may drift rapidly.

This limitation highlights the need for a timescale separation approach for the estimation of fast dynamics associated with operating conditions, and slow dynamics associated with aging. In other words, a multi-time-scale framework is required to have a reliable health management in which fast state estimation are not compensating, as much as possible, slow varying parameters related to degradation.

The SR-UKF design used in Section 4.4 provides an accurate solution for reconstructing fast internal states (partial pressures of reactants and temperature). However, to make this framework more robust in long-term monitoring and prognostics, it is necessary to update aging-sensitive parameters.

4.5.1 Proposed Approach

In this thesis, we propose an aging-aware monitoring approach that combines the SR-UKF framework in Section 4.4 with a scheduled and triggered parameter estimation strategy. The fast states governed by the dynamic equations presented in Equation (4.4) are estimated using the SR-UKF, while the underlying model is updated by the varying SoH parameters (λ_{SoH}). In parallel, these parameters varying slowly are updated intermittently using the parameter estimation approach presented in Section 3.4.1. The proposed aging-aware monitoring scheme is illustrated in Figure 4.13.

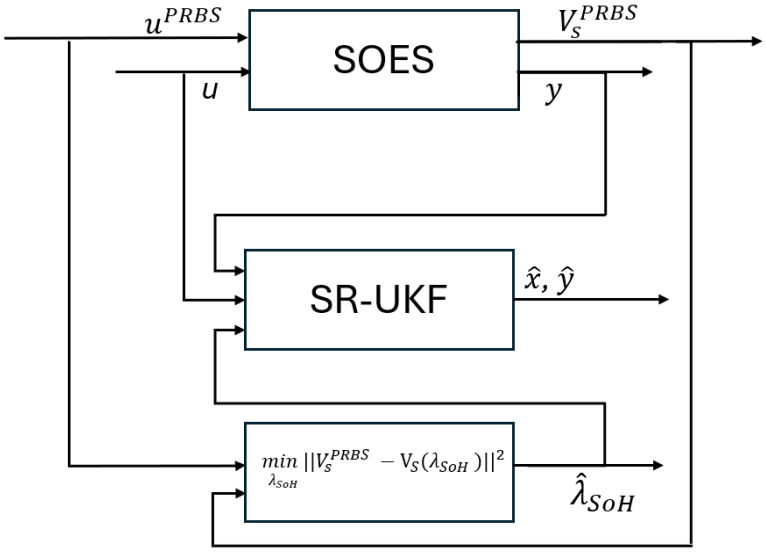

Figure 4.13: Aging-aware monitoring approach scheme

Thèse accessible à l'adresse : https://theses.insa-lyon.fr/publication/2026ISAL0017/these.pdf © [Z. Yazbeck], [2026], INSA Lyon, tous droits réservés

This approach is not only important to prevent deviations induced by faults from being misrepresented as aging parameters. It also makes the estimation of fast state dynamics more robust in the presence of aging, by limiting the risk that slow degradation effects being compensated by the fast dynamic states. As a result, this approach preserves the interpretability of both fault indicators and health indicators.

Choice of slowly-varying SoH parameters

Only a subset of parameters is expected to change slowly over long operating periods to track aging. In this work, the SoH parameters considered are:

$$\lambda_{SoH} = \begin{bmatrix} R_s & \gamma^{an} & \gamma^{cat} & \psi_{fuel} & \psi_{\text{air}} \end{bmatrix}^\top. \tag{4.23}$$

The ohmic resistance R_s is chosen to estimate the long-term changes in ohmic contributions, which directly affect the stack voltage response. Additionally, the exchange current densities prefactors, γ^{an} and γ^{cat}, are selected as lumped kinetic indicators to capture aging in the electrodes. Finally, electrode microstructure parameters, ψ_{fuel} and ψ_{air}, are also selected to represent the slow evolution of effective time-varying diffusion coefficient terms presented in Equations (2.8)-(2.9) with operation and aging [37, 65, 66]. In contrast, activation energies (E_{act}^{ohm}, E_{act}^{an}, E_{act}^{cath}) are kept constant using the values estimated with TLM in Table 3.8.

SR-UKF and parameter estimation coupling

The scheduling of the SoH parameter updates is motivated by the qualitative "bathtub" degradation behavior, presented in Figure 4.14, commonly used to describe degradation rates over time: an initially higher apparent drift (early-life changes), followed by a long quasi-stationary period with slower evolution, and potentially a late-life acceleration [172]. Based on this idea, the proposed approach uses a more frequent update policy at the beginning of operation and relaxes it afterward.

Accordingly, we trigger parameter estimation every 12 hours for the first the first 7 days (first 168 hours) of operation. After this period, updates are scheduled every 40 hours. The estimation is performed according to these intervals and only when an excitation window is available (the onset of a PRBS sequence, see Section 4.5.2). Each new update is initialized using the SoH parameter values obtained from the previous estimation. In addition to the scheduled parameter estimate, another triggered update is activated whenever the estimated SoH parameter estimates lie outside predefined bounds:

$$\begin{aligned} \lambda_{SoH,min} &= \begin{bmatrix} 0.1 & 1e4 & 2.5e4 & 0.1 & 0.1 \end{bmatrix}^\top, \\ \lambda_{SoH,max} &= \begin{bmatrix} 0.5 & 1e6 & 2e6 & 0.45 & 0.45 \end{bmatrix}^\top. \end{aligned} \tag{4.24}$$

Thèse accessible à l'adresse : https://theses.insa-lyon.fr/publication/2026ISAL0017/these.pdf © [Z. Yazbeck], [2026], INSA Lyon, tous droits réservés

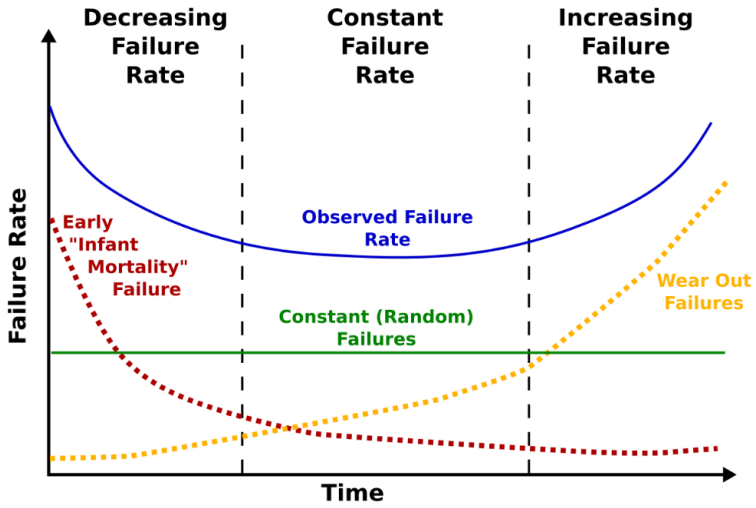

Figure 4.14: Bathtub curve. Adapted from [173]

4.5.2 Application to experimental data

In the experimental dataset used in this chapter, Pseudo Random Binary Sequences (PRBS) of current density excitation with different frequency contents were applied approximately every 2 hours for a total test duration of 650 hours. The sampling time of the measurements of operating conditions presented in Figure 4.15 and outputs $y = [V_s \; T \; \dot{n}_{H_2}^{out}]^T$ in Equation (4.4) is 2 seconds.

The system is operates under fixed conditions (inlet flow rates, inlet temperatures, furnace temperature, and pressures are held constant) during each PRBS measurement, thus we define $u^{PRBS} = [I^{PRBS} \; \dot{n}_{fuel}^{in} \; \dot{n}_{air}^{in} \; y_{H_2O}^{in} \; T_{furnace} T_{fuel}^{in} \; T_{air}^{in}]^T$. The current density is the only input perturbed according to the PRBS profile, which is why the PRBS excitation appears as noise in the current density shown in Figure 4.15. Only the voltage response, denoted V_s^{PRBS}, is then recorded using a much finer time resolution than the monitoring sampling time, where its values and the corresponding PRBS frequency are presented in Table 4.1.

PRBS bandwidth	Excitation time (s)	$t_{s,PRBS}$ (s)
1 Hz	40.0	4×10^{-4}
10 Hz	25.0	4×10^{-5}
100 Hz	0.35	2×10^{-5}
1000 Hz	0.10	2×10^{-6}
10 kHz	0.05	2×10^{-6}

Table 4.1: PRBS bandwidth, excitation duration, and associated acquisition sampling time.

The application of the proposed approach is restricted to a simplified scenario where the system is assumed free of starvation faults, in order to illustrate the proposed aging-aware monitor-

Thèse accessible à l'adresse : https://theses.insa-lyon.fr/publication/2026ISAL0017/these.pdf © [Z. Yazbeck], [2026], INSA Lyon, tous droits réservés

ing concept under controlled conditions. However, in practice, if starvation faults occur, additional logic should be introduced to preserve the separation between fast fault dynamics and slow aging drift. For instance, the parameter estimation step could be postponed during detected fault intervals, since voltage deviations could otherwise bias the identified parameters.

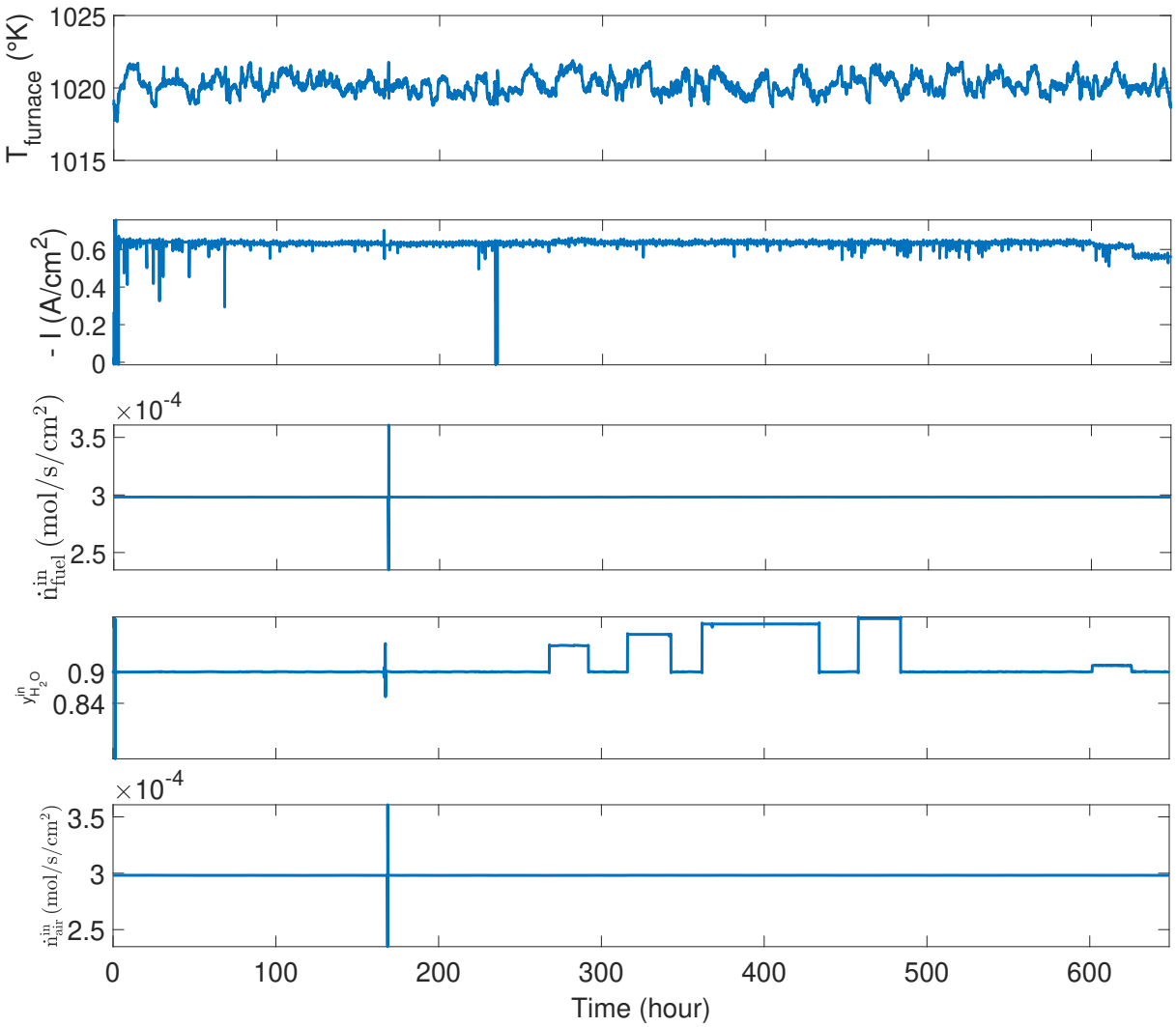

Figure 4.15: Operating condition window.

Thèse accessible à l'adresse : https://theses.insa-lyon.fr/publication/2026ISAL0017/these.pdf © [Z. Yazbeck], [2026], INSA Lyon, tous droits réservés

4.5.3 Results

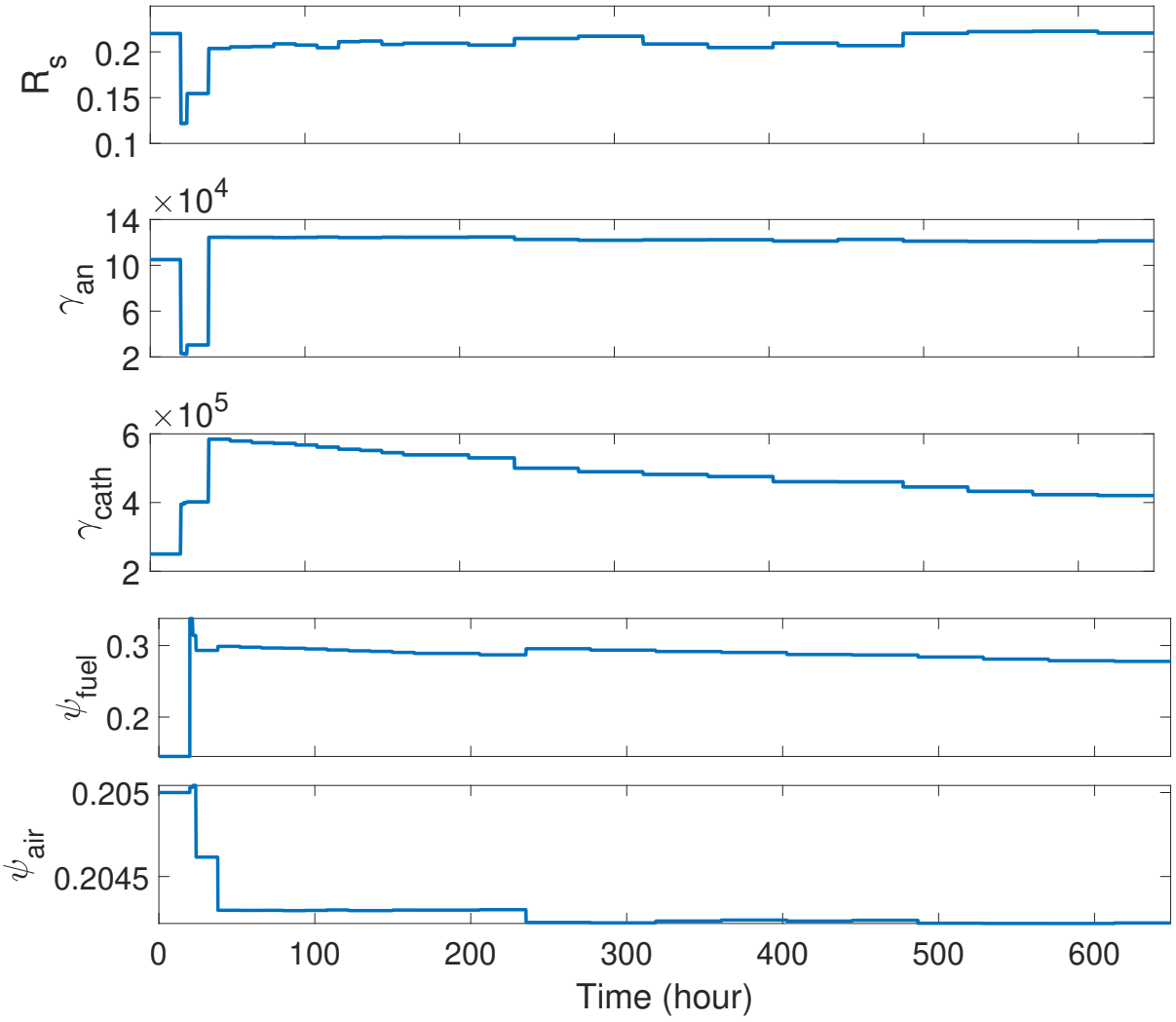

Figure 4.16: SoH estimation for whole measurement data.

The evolution of the estimated SoH parameters over the full 650-hour dataset is reported in Figure 4.16. Larger variations are observed during the first estimation windows, after which the estimates become more stable and follow clearer long-term trends. This initial behavior is mainly attributed to the limited frequency content of the PRBS excitations available at the beginning of the dataset. Indeed, the first estimation windows do not contain the full range of excitation frequencies used later in the experiment and therefore provide less information for distinguishing the effects of the different, and potentially correlated, parameters. As PRBS sequences covering a broader range of frequencies become available, the richness of the identification data increases, leading to more stable parameter estimates. Consequently, the initial variations should not be interpreted as rapid physical degradation of the stack.

R_s, representing the ohmic contributions due to contact loss, electrolyte degradation, and

Thèse accessible à l'adresse : https://theses.insa-lyon.fr/publication/2026ISAL0017/these.pdf © [Z. Yazbeck], [2026], INSA Lyon, tous droits réservés

interconnect is very slightly varied. γ_{an}, the anode exchange-current prefactor remains more or less stabilized over the operating window, whereas γ_{cath} shows a gradual decrease consistent with a progressive loss of apparent kinetics due to aging in the hydrogen electrode [37, 66]. The microstructure parameter ψ_{fuel} decreases very slowly with time, yielding a reduction of the effective diffusion coefficient at the hydrogen electrode. Therefore the mass-transport limitations increase with time, which is consistent with the literature [66]. In contrast, ψ_{air} shows only a negligible decrease over the full test duration.

No fast degradation of the SoH parameters is observed at the beginning of the presented time window because it is not the beginning of life of the stack. In fact, the considered stack was previously used in fuel cell mode for studies at CEA before starting this operating window in SOEC mode.

The test duration is not long enough to observe significant irreversible degradation, which typically evolves over thousand-hour time scales [65, 169, 171]. As a result, the measured voltage and temperature are weakly affected by aging, and the impact on the estimation of fast dynamics remains limited. However, the PRBS excitation of the current density with a broad frequency range increases the information content of the measurements.

4.6 Conclusion

This chapter presents a real-time fault detection approach for SOECs using a pre-calibrated model for the observer approach. A square-root Unscented Kalman Filter (SR-UKF) estimates key states, including the partial pressures of hydrogen, steam, and oxygen, as well as the deviation of the actual fuel flow rate from its nominal setpoint value. The outlet hydrogen flow rate, directly affected by hydrogen starvation, is used as one of the measured outputs with stack voltage and air outlet temperature. Using these measurements with nominal inputs, the observer detects starvation faults by comparing estimated states with their nominal counterparts and is able to reconstruct the actual inlet flow rates. An adaptive threshold, computed using a moving window filter of the nominal states, helps in automatic fault detection. In addition, the total resistance is calculated and increases in the case of steam starvation, while remaining nearly unchanged during hydrogen starvation in electrolysis mode, providing further insight into the nature of the fault.

The effectiveness of the proposed method is validated on experimental data, demonstrating that fuel starvation can be detected with minimal measurements, making it suitable for implementation. The approach also extends to SOFCs operating in fuel cell mode, where air starvation can be identified by monitoring deviations in oxygen partial pressure from its thresholds.

Finally, an aging-aware monitoring approach is proposed to ensure a time-scale separation between the fast dynamics associated with operating conditions and faults, and the slow dynamics representing the state of health of the system associated with aging. The nominal model

Thèse accessible à l'adresse : https://theses.insa-lyon.fr/publication/2026ISAL0017/these.pdf © [Z. Yazbeck], [2026], INSA Lyon, tous droits réservés

used by the SR-UKF is updated whenever the state-of-health (SoH) parameters are re-estimated. These SoH parameters include the ohmic resistance, exchange current density prefactors, and microstructure-related transport parameters. Over the 650 hours dataset, the variations of R_s, γ_{an}, and ψ_{air} remain moderate, while γ_{cath} and ψ_{fuel} exhibit a clearer drift, consistent with progressive aging effects in the hydrogen electrode. Since the observation window remains limited compared with degradation time scales of thousands of hours, no significant degradation is expected to occur, and its effect on the measured outputs, and thus on the estimated internal states, remains very limited.

Thèse accessible à l'adresse : https://theses.insa-lyon.fr/publication/2026ISAL0017/these.pdf © [Z. Yazbeck], [2026], INSA Lyon, tous droits réservés

Thèse accessible à l'adresse : https://theses.insa-lyon.fr/publication/2026ISAL0017/these.pdf © [Z. Yazbeck], [2026], INSA Lyon, tous droits réservés

Conclusion and perspectives

In this thesis, the problem of developing a model-based health management approach for Solid Oxide Electrolysis Cell (SOEC) stacks has been addressed. The focus has been placed on parameter estimation and fault detection, more specifically for fuel-side starvation faults that can lead to irreversible damage if they are not detected and mitigated early.

In this context, a central difficulty lies in the strong coupling between the different submodels of the stack: electrochemistry, mass transport, and thermal dynamics, combined with the fact that the quantities that are the most informative for diagnosis, like the internal partial pressures of reactants, are not directly measurable. Additionally, the model has to be compatible with real-time application, and take into account system aging over time. This motivates developing a framework where the model is used for state estimation and for continuously updating the parameters affected by aging.

In Chapter 2, we present the SOEC technology as well as its modeling at different levels. Beyond providing the physical background and the different existing models, this chapter is essential because it details the construction of a control-oriented model for monitoring that must strike a balance between generating physically meaningful internal variables and sufficient tractability to be embedded in estimation and fault detection algorithms, while remaining fast enough for real-time implementation.

The parameter estimation and identifiability for model calibration, a key prerequisite for any model-based monitoring strategy, are developed in Chapter 3. The practical identifiability is assessed with the sensitivity differential equations based on the state-space formulation of the nonlinear model. The analysis showed that, under the considered operating conditions and measurement, not all parameters can be reliably inferred from data. In particular, some parameter groups (including microstructure-related parameters and pre-exponential factors of the exchange current densities) were poorly informed by the chosen excitation, exhibiting negligible sensitivity on the output or strong linear dependence, while other parameters could be recovered with good accuracy. To address ill-conditioning and collinearity in the estimation, a truncation of the sensitivity matrix was proposed based on SVD decomposition, coupled with gradient-based optimization (Gauss-Newton and Levenberg-Marquardt) with robustness checks against noise and initial guess dispersion.

However, parameter practical identifiability is affected by the experimental data used, as

Thèse accessible à l'adresse : https://theses.insa-lyon.fr/publication/2026ISAL0017/these.pdf © [Z. Yazbeck], [2026], INSA Lyon, tous droits réservés

demonstrated through Monte-Carlo simulations across 50 different scenarios. For this reason, Chapter 3 also investigated optimal experimental design (OED) to generate informative inputs, and proposed different approaches: an NLP-based OED formulation, sequential OED due to the local property of the sensitivities, and a predefined library with genetic selection to handle the computational time. The results of these different OED approaches showed an improvement in the quality of the estimates only for the well-informed sensitivity directions, whereas the estimates of weakly sensitive parameters were not improved. This highlights that a perspective of this work is to further investigate the practical identifiability of these parameters.

After calibrating the model, the problem of online monitoring and fault diagnosis is addressed in Chapter 4. A Square-Root Unscented Kalman Filter (SR-UKF), which is a more numerically stable version of the Unscented Kalman filter (UKF), based on sigma-points, is designed to reconstruct internal partial pressures of reactants, stack temperature, and the deviation from the nominal setpoint in steam and hydrogen flow rates, added as states. This information is reconstructed based on temperature, voltage, and outlet hydrogen flow rate measurements. The state estimation is combined with adaptive-thresholds derived from the nominal states and applied to the estimated partial pressures in order to detect fuel-side starvation and discriminate steam starvation from hydrogen starvation in electrolysis mode. Additionally, the total resistance can also be used as discriminant between steam and hydrogen starvation, when the outlet hydrogen flow rate measurement is not available and the two additional states related to the deviation of flow rates can not be considered. A significant variation of the total resistance indicates steam starvation, whereas negligible variation happens in hydrogen starvation case.

The work in Chapter 4 is extended to combine fast observer dynamics with a slow parameter update mechanism, adapting the estimation framework of Chapter 3 to track health indicators and degradation related parameters online, while preserving real-time capability. This integration is a critical step toward an operational PHM framework, to have a robust state estimation, and as a possible path to work on the prognosis of the the stack. A validation of the methodology with 650 hours of experimental data and PRBS current density excitation shows a variation of SoH estimates in the expected direction while the effect on the model output and on the estimated states remains negligible, since the considered window is not long enough for significant degradation to develop.

The main contributions of this thesis can be summarized as follows. First, a complete calibration workflow was developed for a control-orient electrochemical model, based on combining sensitivity analysis with parameter estimation. Weak and linearly dependent sensitivity directions are truncated using SVD. This method provides both numerical stability, by limiting the condition number of the sensitivity matrix, and interpretability in terms of the richness of information about the parameters. Second, three OED strategies were formulated to improve practical identifiability under physical constraints, including a computationally cheaper library-based alternative, thereby improving the deployability of informative test campaigns. Third, an SR-UKF based monitoring and diagnosis approach was proposed and validated using experimental data, capable of re-

Thèse accessible à l'adresse : https://theses.insa-lyon.fr/publication/2026ISAL0017/these.pdf © [Z. Yazbeck], [2026], INSA Lyon, tous droits réservés

constructing internal variables and detecting starvation faults using adaptive thresholds, with an explicit discrimination mechanism between steam and hydrogen starvation based on total resistance behavior. Finally, the overall architecture was integrated to provide a more practical and robust PHM approach, where the fast varying dynamics are updated using SR-UKF, with the update of parameters that are slowly varying in time due to aging.

Several remaining challenges naturally arise from this work and define clear perspectives. A first challenge concerns the limitations of the simplified control-oriented model structure. While it was designed to remain computationally efficient, its reduced-order nature limits the details that can be represented. Future work could enhance the model while preserving real-time capability by incorporating additional thermal balance equations and a more detailed description of heat exchange within the stack and balance of plant. In addition, investigating extensions of the model dimension to capture more spatial information could improve the description of internal gradients. Such developments would enhance the model accuracy and broaden its applicability for monitoring and diagnosis. In parallel, exploring Bayesian approaches for parameter estimation and optimal experiment design could be valuable, since they provide a framework to integrate prior knowledge and quantify uncertainty, and can formulate OED objectives in terms of expected information gain rather than relying only on local identifiability metrics.

A second challenge is the generalization of the diagnosis algorithm so that it is not limited to fuel-starvation faults alone. In real operation, starvation may coexist with other anomalies, and a reliable PHM framework must explicitly manage fault interactions and uncertainty. Thus, additional sources of information can be integrated, like electrochemical impedance spectroscopy (EIS) for instance. Indeed, EIS measurements, combined with expertise in attributing impedance features to different frequency ranges, can support the classification and characterization of different anomalies and faults. In this broader framework, the SR-UKF developed in this thesis can serve as a dedicated module to quantify the fault once fuel starvation is classified as the root cause. In addition, extending the observer from a mean stack behavior representation to a worst-case supervision using segmented measurements could be interesting. In practice, a big stack is usually instrumented to measure the voltage corresponding to clusters of cells. Thus, rather than estimating only the average behavior, future work could exploit these cluster-level measurements to design an observer that explicitly tracks the most limiting cluster, and updates the diagnosis based on this worst-case indicator. This would make the monitoring strategy more conservative and better aligned with degradation risk, since irreversible damage is typically initiated locally and may remain hidden in stack-level signals.

A fourth challenge concerns the link to prognostics. While this thesis targets RUL oriented applications, an alternative direction would be to explore hybrid approaches that combine the proposed physics-based model with data-driven models. Such hybrid models could combine the reconstructed internal variables and estimated health parameters as informative features, while learning residual degradation dynamics directly from operational data, potentially improving long-horizon prediction and robustness under varying conditions, and requiring less data compared to

Thèse accessible à l'adresse : https://theses.insa-lyon.fr/publication/2026ISAL0017/these.pdf © [Z. Yazbeck], [2026], INSA Lyon, tous droits réservés

pure data-driven models.

Thèse accessible à l'adresse : https://theses.insa-lyon.fr/publication/2026ISAL0017/these.pdf © [Z. Yazbeck], [2026], INSA Lyon, tous droits réservés

Thèse accessible à l'adresse : https://theses.insa-lyon.fr/publication/2026ISAL0017/these.pdf © [Z. Yazbeck], [2026], INSA Lyon, tous droits réservés

Bibliography

[1] United Nations, Department of Economic and Social Affairs, Population Division. World population prospects 2024: Summary of results. https://population.un.org/wpp/assets/Files/WPP2024_Summary-of-Results.pdf, 2024.

[2] International Energy Agency. Growth in global energy demand surged in 2024 to almost twice its recent average. https://www.iea.org/news/growth-in-global-energy-demand-surged-in-2024-to-almost-twice-its-recent-average, 2025.

[3] Richard Gray. The Biggest Energy Challenges Facing Humanity. https://www.bbc.com/future/article/20170313-the-biggest-energy-challenges-facing-humanity, 2017.

[4] Shonali Pachauri. Demography, urbanisation and energy demand. In Energy for development: Resources, technologies, environment, pages 81–94. Springer, 2012. URL https://doi.org/10.1007/978-94-007-4162-1_7.

[5] Leendert A Verhoef, Bart W Budde, Cindhuja Chockalingam, Brais García Nodar, and Ad JM van Wijk. The effect of additive manufacturing on global energy demand: An assessment using a bottom-up approach. Energy Policy, 112:349–360, 2018. URL https://doi.org/10.1016/j.enpol.2017.10.034.

[6] Muhammad Shahbaz, Malin Song, Shabbir Ahmad, and Xuan Vinh Vo. Does economic growth stimulate energy consumption? the role of human capital and r&d expenditures in china. Energy Economics, 105:105662, 2022. URL https://doi.org/10.1016/j.eneco.2021.105662.

[7] Energy Institute and Vaclav Smil. Primary energy from other renewables [dataset]. https://ourworldindata.org/grapher/global-energy-substitution, 2025. Based on data from Energy Institute, Statistical Review of World Energy (2025), and Vaclav Smil, Energy Transitions: Global and National Perspectives (2017); processed by Our World in Data.

[8] Joel Mokyr and Robert H Strotz. The second industrial revolution, 1870-1914. Storia dell'economia Mondiale, 21945(1):219–245, 1998.

Thèse accessible à l'adresse : https://theses.insa-lyon.fr/publication/2026ISAL0017/these.pdf © [Z. Yazbeck], [2026], INSA Lyon, tous droits réservés

[9] David I Stern and Astrid Kander. The role of energy in the industrial revolution and modern economic growth. The Energy Journal, 33(3):125–152, 2012.

[10] Robert A. Berner. The long-term carbon cycle, fossil fuels and atmospheric composition. Nature, 426(6964):323–326, 2003. URL https://doi.org/10.1038/nature02131.

[11] Mohan Kelkar. Demise of fossil fuels part i: Supply and demand. Heliyon, 10(20), 2024. URL https://doi.org/10.1016/j.heliyon.2024.e39200.

[12] Yongjun Lv. Transitioning to sustainable energy: opportunities, challenges, and the potential of blockchain technology. Frontiers in Energy Research, 11:1258044, 2023. URL https://doi.org/10.3389/fenrg.2023.1258044.

[13] Simon R Sinsel, Rhea L Riemke, and Volker H Hoffmann. Challenges and solution technologies for the integration of variable renewable energy sources—a review. renewable energy, 145:2271–2285, 2020. URL https://doi.org/10.1016/j.renene.2019.06.147.

[14] Bassma Reda, Amr A Elzamar, Shehab AlFazzani, and Shahira M Ezzat. Green hydrogen as a source of renewable energy: a step towards sustainability, an overview. Environment, Development and Sustainability, pages 1–21, 2024. URL https://doi.org/10.1007/s10668-024-04892-z.

[15] Hannah Ritchie and Max Roser. Co emissions. Our World in Data, 2020. URL https://ourworldindata.org/co2-emissions.

[16] Daniel J. Soeder. Greenhouse gas sources and mitigation strategies from a geosciences perspective. Advances in Geo-Energy Research, 5(3):274–285, 2021. URL https://doi.org/10.46690/ager.2021.03.04.

[17] Leonardo Vidas and Rui Castro. Recent developments on hydrogen production technologies: state-of-the-art review with a focus on green-electrolysis. Applied Sciences, 11(23):11363, 2021. URL https://doi.org/10.3390/app112311363.

[18] United Nations. Adoption of the paris agreement. In United Nations Framework Convention on Climate Change, Paris, page 31, 2015.

[19] The european hydrogen market landscape. Technical report, Clean Hydrogen Joint Undertaking, November 2024. URL https://observatory.clean-hydrogen.europa.eu/sites/default/files/2024-11/The%20European%20hydrogen%20market%20landscape_November%202024.pdf.

[20] Sonal Singh, Shikha Jain, Avanish K Tiwari, Mansa R Nouni, Jitendra K Pandey, Sanket Goel, et al. Hydrogen: A sustainable fuel for future of the transport sector. Renewable

Thèse accessible à l'adresse : https://theses.insa-lyon.fr/publication/2026ISAL0017/these.pdf © [Z. Yazbeck], [2026], INSA Lyon, tous droits réservés

and sustainable energy reviews, 51:623–633, 2015. URL https://doi.org/10.1016/j.rser.2015.06.040.

[21] Kasper T Møller, Torben R Jensen, Etsuo Akiba, and Hai-wen Li. Hydrogen-a sustainable energy carrier. Progress in natural science: Materials International, 27(1):34–40, 2017. URL https://doi.org/10.1016/j.pnsc.2016.12.014.

[22] Huaguang Yan, Wenda Zhang, Jiandong Kang, and Tiejiang Yuan. The necessity and feasibility of hydrogen storage for large-scale, long-term energy storage in the new power system in china. Energies, 16(13):4837, 2023. URL https://doi.org/10.3390/en16134837.

[23] Jiang Hu, Yunhe Zou, and Yao Zhao. Robust operation of hydrogen-fueled power-to-gas system within feasible operating zone considering carbon-dioxide recycling process. International Journal of Hydrogen Energy, 58:1429–1442, 2024. URL https://doi.org/10.1016/j.ijhydene.2024.01.337.

[24] Linchao Ma, Jingkui Mao, and Mohammad Marefati. Assessment of a new coal-fired power plant integrated with solid oxide fuel cell and parabolic trough solar collector. Process Safety and Environmental Protection, 163:340–352, 2022. URL https://doi.org/10.1016/j.psep.2022.05.053.

[25] Mohsen Rostami, Mojtaba Dehghan Manshadi, Amir Hamzeh Farajollahi, and Mohammad Marefati. Introducing and evaluation of a new propulsion system composed of solid oxide fuel cell and downstream cycles; usage in unmanned aerial vehicles. International Journal of Hydrogen Energy, 47(28):13693–13709, 2022. URL https://doi.org/10.1016/j.ijhydene.2022.02.104.

[26] Shuaibing Wang, Xianhua Wu, Samad Jafarmadar, Pradeep Kumar Singh, Saleh Khorasani, Mohamad Marefati, and As' ad Alizadeh. Numerical assessment of a hybrid energy system based on solid oxide electrolyzer, solar energy and molten carbonate fuel cell for the generation of electrical energy and hydrogen fuel with electricity storage option. Journal of Energy Storage, 54:105274, 2022. URL https://doi.org/10.1016/j.est.2022.105274.

[27] Hongliang Wang, Zhanguo Su, Azher M Abed, Kaushik Nag, Ahmed Deifalla, Mohammad Marefati, Ibrahim Mahariq, and Yanming Wei. Multi-criteria evaluation and optimization of a new multigeneration cycle based on solid oxide fuel cell and biomass fuel integrated with a thermoelectric generator, gas turbine, and methanation cycle. Process Safety and Environmental Protection, 170:139–156, 2023. URL https://doi.org/10.1016/j.psep.2022.11.087.

Thèse accessible à l'adresse : https://theses.insa-lyon.fr/publication/2026ISAL0017/these.pdf © [Z. Yazbeck], [2026], INSA Lyon, tous droits réservés

[28] Waqad Ul Mulk, A Rashid A Aziz, Mhadi A Ismael, Asghar Ali Ghoto, Syed Awais Ali, Mohammad Younas, and Fausto Gallucci. Electrochemical hydrogen production through anion exchange membrane water electrolysis (AEMWE): Recent progress and associated challenges in hydrogen production. International Journal of Hydrogen Energy, 94:1174–1211, 2024. URL https://doi.org/10.1016/j.ijhydene.2024.11.143.

[29] Kai Zeng and Dongke Zhang. Recent progress in alkaline water electrolysis for hydrogen production and applications. Progress in energy and combustion science, 36(3):307–326, 2010. URL https://doi.org/10.1016/j.pecs.2009.11.002.

[30] Immanuel Vincent and Dmitri Bessarabov. Low cost hydrogen production by anion exchange membrane electrolysis: A review. Renewable and Sustainable Energy Reviews, 81:1690–1704, 2018. URL https://doi.org/10.1016/j.rser.2017.05.258.

[31] Kewei Hu, Jiakun Fang, Xiaomeng Ai, Danji Huang, Zhiyao Zhong, Xiaobo Yang, and Lei Wang. Comparative study of alkaline water electrolysis, proton exchange membrane water electrolysis and solid oxide electrolysis through multiphysics modeling. Applied Energy, 312:118788, 2022. URL https://doi.org/10.1016/j.apenergy.2022.118788.

[32] Yuhao Xu, Shanshan Cai, Bo Chi, and Zhengkai Tu. Technological limitations and recent developments in a solid oxide electrolyzer cell: A review. International Journal of Hydrogen Energy, 50:548–591, 2024. URL https://doi.org/10.1016/j.ijhydene.2023.08.314.

[33] Jerome Aicart, Lionel Tallobre, Alexander Surrey, Bastien Gervasoni, Christian Geipel, Hervé Fontaine, Sonia Desousanobre, and Julie Mougin. Lifespan evaluation of two 30-cell electrolyte-supported stacks for hydrogen production by high temperature electrolysis. International Journal of Hydrogen Energy, 60:531–539, 2024. URL https://doi.org/10.1016/j.ijhydene.2024.02.239.

[34] Rajangam Vinodh, Shankara Sharanappa Kalanur, Sadesh Kumar Natarajan, and Bruno G Pollet. Recent advancements of polymeric membranes in anion exchange membrane water electrolyzer (AEMWE): A critical review. Polymers, 15(9):2144, 2023. URL https://doi.org/10.3390/polym15092144.

[35] W Nernst. On the electrolytic conduction of solid bodies at high temperatures. Z. Electrochem, 6(2):41–43, 1899.

[36] Emil Baur and Hans Preis. Über brennstoff-ketten mit festleitern. Zeitschrift für Elektrochemie und angewandte physikalische Chemie, 43(9):727–732, 1937.

[37] Stephen J McPhail, Stefano Frangini, Jérôme Laurencin, Elisa Effori, Amira Abaza, Aiswarya Krishnakumar Padinjarethil, Anke Hagen, Aline Léon, Annabelle Brisse, Daria

Thèse accessible à l'adresse : https://theses.insa-lyon.fr/publication/2026ISAL0017/these.pdf © [Z. Yazbeck], [2026], INSA Lyon, tous droits réservés

Vladikova, et al. Addressing planar solid oxide cell degradation mechanisms: A critical review of selected components. Electrochemical Science Advances, 2(5):e2100024, 2022. URL https://doi.org/10.1002/elsa.202100024.

[38] Henry S Spacil and CS Tedmon. Electrochemical dissociation of water vapor in solid oxide electrolyte cells: I. thermodynamics and cell characteristics. Journal of the Electrochemical Society, 116(12):1618, 1969. URL https://doi.org/10.1149/1.2411642.

[39] W Doenitz, R Schmidberger, E Steinheil, and R Streicher. Hydrogen production by high temperature electrolysis of water vapour. International Journal of Hydrogen Energy, 5(1): 55–63, 1980. URL https://doi.org/10.1016/0360-3199(80)90114-7.

[40] Cameron M Priest, Joshua Y Gomez, Nicholas J Kane, Jeremy L Hartvigsen, Lucun Wang, Dong Ding, Micah J Casteel, Frederick F Stewart, and Gang Wu. Challenges in practical button cell testing for hydrogen production from high temperature electrolysis of water. Frontiers in Energy Research, 11:1278203, 2023. URL https://doi.org/10.3389/fenrg.2023.1278203.

[41] Kitco. Base metals prices, 2025. URL https://www.kitco.com/price/base-metals/. Accessed: 2025-08-14.

[42] Chapter 9 - electrochemical hydrogen generation. In Francesco Calise, Massimo Dentice D'Accadia, Massimo Santarelli, Andrea Lanzini, and Domenico Ferrero, editors, Solar Hydrogen Production, pages 299–317. Academic Press, 2019. ISBN 978-0-12-814853-2. doi: https://doi.org/10.1016/B978-0-12-814853-2.00009-6. URL https://www.sciencedirect.com/science/article/pii/B9780128148532000096.

[43] National hydrogen strategy: Harnessing the hydrogen sector's full potential in pursuit of france's decarbonization and reindustrialization, 2023. URL https://www.france-hydrogene.org/app/uploads/sites/4/2023/10/France-Hydrogene_National-Hydrogen-Strategy_EN.pdf.

[44] I Sreedhar, Bhawana Agarwal, Priyanka Goyal, and Satyapaul A Singh. Recent advances in material and performance aspects of solid oxide fuel cells. Journal of Electroanalytical Chemistry, 848:113315, 2019. URL https://doi.org/10.1016/j.jelechem.2019.113315.

[45] Hon Huin Chin, Petar Sabev Varbanov, Jiři Jaromír Klemeš, Michael Francis D Benjamin, and Raymond R Tan. Asset maintenance optimisation approaches in the chemical and process industries–a review. Chemical Engineering Research and Design, 164:162–194, 2020. URL https://doi.org/10.1016/j.cherd.2020.09.034.

Thèse accessible à l'adresse : https://theses.insa-lyon.fr/publication/2026ISAL0017/these.pdf © [Z. Yazbeck], [2026], INSA Lyon, tous droits réservés

[46] M Hanasaki, C Uryu, T Daio, T Kawabata, Yuya Tachikawa, Stephen Matthew Lyth, Yusuke Shiratori, Shunsuke Taniguchi, and Kazunari Sasaki. SOFC durability against standby and shutdown cycling. Journal of The Electrochemical Society, 161(9):F850, 2014. URL https://doi.org/10.1149/2.0421409jes.

[47] Carleton University Prognostics and Health Management (PHM) Laboratory. What is phm? URL https://carleton.ca/phm/what-is-phm/.

[48] M. Lebold, K. Reichard, C. S. Byington, and R. Orsagh. OSA-CBM architecture development with emphasis on XML implementations. In Proceedings of the Maintenance and Reliability Conference (MARCON), pages 6–8, 2002.

[49] Mehdi Brahimi, Kamal Medjaher, Mohammed Leouatni, and Noureddine Zerhouni. Development of a prognostics and health management system for the railway infrastructure—review and methodology. In 2016 Prognostics and System Health Management Conference (PHM-Chengdu), pages 1–8. IEEE, 2016. URL https://doi.org/10.1109/PHM.2016.7819783.

[50] Thamo Sutharssan, Stoyan Stoyanov, Chris Bailey, and Chunyan Yin. Prognostic and health management for engineering systems: a review of the data-driven approach and algorithms. The Journal of engineering, 2015(7):215–222, 2015. URL https://doi.org/10.1049/joe.2014.0303.

[51] A Datta, C Mavroidis, and M Hosek. A role of unsupervised clustering for intelligent fault diagnosis. In ASME International Mechanical Engineering Congress and Exposition, volume 43033, pages 687–695, 2007. URL https://doi.org/10.1115/IMECE2007-43492.

[52] Marine Jouin, Rafael Gouriveau, Daniel Hissel, Marie-Cécile Péra, and Noureddine Zerhouni. Prognostics and health management of PEMFC–state of the art and remaining challenges. International Journal of Hydrogen Energy, 38(35):15307–15317, 2013. URL https://doi.org/10.1016/j.ijhydene.2013.09.051.

[53] Léa Rorato, Yijing Shang, Shenglan Yang, Maxime Hubert, Karine Couturier, Lijun Zhang, Julien Vulliet, Ming Chen, and Jérôme Laurencin. Understanding the ni migration in solid oxide cell: a coupled experimental and modeling approach. Journal of The Electrochemical Society, 170(3):034504, 2023. URL https://doi.org/10.1149/1945-7111/acc1a3.

[54] Bostjan Dolenc, Pavle Boškoski, Martin Stepančič, Antti Pohjoranta, and Đani Juričić. State of health estimation and remaining useful life prediction of solid oxide fuel cell stack. Energy Conversion and Management, 148:993–1002, 2017. URL https://doi.org/10.1016/j.enconman.2017.06.041.

Thèse accessible à l'adresse : https://theses.insa-lyon.fr/publication/2026ISAL0017/these.pdf © [Z. Yazbeck], [2026], INSA Lyon, tous droits réservés

[55] Johanna Bartlechner, Martin Vrlić, Christoph Hametner, and Stefan Jakubek. State-of-health observer for PEM fuel cells—a novel approach for real-time online analysis. International Journal of Hydrogen Energy, 95:1112–1125, 2024. URL https://doi.org/10.1016/j.ijhydene.2024.03.061.

[56] Alireza Beigi, Wesley Romey, and Krishna Vijayaraghavan. Extended Kalman filter for quantifying hydrogen leaks in PEM fuel cells by estimating oxygen concentration. International Journal of Hydrogen Energy, 78:907–917, 2024. URL https://doi.org/10.1016/j.ijhydene.2024.06.094.

[57] Yuanwu Xu, Chang Jiang, Jingxuan Peng, Xiao-Long Wu, Li Xiao, and Xi Li. Fault prognosis method for solid oxide fuel cells based on mechanism degradation process model and particle filtering. IEEE Transactions on Power Electronics, 38(6):6831–6840, 2023. URL https://doi.org/10.1109/TPEL.2023.3246068.

[58] Chiara Pettorossi, Raphaël Morvillier, Vincent Heiries, Sébastien Rosini, and Mathias Gerard. Physics-guided fault diagnosis method for proton exchange membrane fuel cells based on LSTM neural network. Journal of Power Sources, 626:235696, 2025. ISSN 0378-7753. URL https://doi.org/10.1016/j.jpowsour.2024.235696.

[59] Steven X Ding. Model-based fault diagnosis techniques: design schemes, algorithms, and tools. Springer, 2008.

[60] Agata Godula-Jopek. Hydrogen production: by electrolysis. John Wiley & Sons, 2015.

[61] Zezhi Zeng, Yuping Qian, Yangjun Zhang, Changkun Hao, Dan Dan, and Weilin Zhuge. A review of heat transfer and thermal management methods for temperature gradient reduction in solid oxide fuel cell (SOFC) stacks. Applied Energy, 280:115899, 2020. URL https://doi.org/10.1016/j.apenergy.2020.115899.

[62] Maxime Piffard, Ramon Naiff da Fonseca, Paolo Massioni, Eric Bideaux, and Mathias Gerard. Fuel cell management system: PEMFC lifetime optimization by model based approach. ECS Transactions, 86(13):25, 2018. URL https://doi.org/10.1149/08613.0025ecst.

[63] Javid Beyrami, Rafael Nogueira Nakashima, Arash Nemati, and Henrik Lund Frandsen. Degradation modeling in solid oxide electrolysis systems: a comparative analysis of operation modes. Energy Conversion and Management: X, 23:100653, 2024. URL https://doi.org/10.1016/j.ecmx.2024.100653.

[64] Giuseppe Sassone, Ozden Celikbilek, Maxime Hubert, Katherine Develos-Bagarinao, Thomas David, Laure Guetaz, Isabelle Martin, Julie Villanova, Anass Benayad, Léa Rorato, et al. Effect of the operating temperature on the degradation of solid oxide electrolysis

Thèse accessible à l'adresse : https://theses.insa-lyon.fr/publication/2026ISAL0017/these.pdf © [Z. Yazbeck], [2026], INSA Lyon, tous droits réservés

cells. Journal of Power Sources, 605:234541, 2024. URL https://doi.org/10.1016/j.jpowsour.2024.234541.

[65] Federico Monaco. Analysis of the degradation in solid oxide cells operated in fuel cell and electrolysis modes : microstructural evolution and stability of the electrodes materials. PhD Thesis, Universite Grenoble Alpes.

[66] Giuseppe Sassone. Degradation Mechanisms of the Lanthanum Strontium Cobalt Ferrite Used as Oxygen Electrode in Solid Oxide Cells. PhD thesis, Université Grenoble Alpes [2020-....], 2024.

[67] Giuseppe Sassone, Ozden Celikbilek, Maxime Hubert, Katherine Develos-Bagarinao, Anass Benayad, Bertrand Morel, Aline Léon, and Jérôme Laurencin. Impact of air moisture and operating mode on the degradation of solid oxide cells. Journal of The Electrochemical Society, 171(12):124507, 2024. URL https://doi.org/10.1149/1945-7111/ada0ec.

[68] Kongfa Chen et al. Materials degradation of solid oxide electrolysis cells. Journal of The Electrochemical Society, 163(11):F3070, 2016. URL https://doi.org/10.1149/2.0101611jes.

[69] Jens Foldager Bregnballe Rasmussen, Peter Vang Hendriksen, and Anke Hagen. Study of internal and external leaks in tests of anode-supported SOFCs. Fuel Cells, 8(6):385–393, 2008. URL https://doi.org/10.1002/fuce.200800019.

[70] Laurent Peigat, Magali Reytier, F Ledrappier, and Jacques Besson. A leakage model to design seals for solid oxide fuel and electrolyser cell stacks. international journal of hydrogen energy, 39(13):7109–7119, 2014. URL https://doi.org/10.1016/j.ijhydene.2014.02.097.

[71] EV Tsipis, AV Samoilov, DV Matveev, Yu S Fedotov, MS Dyakina, DV Zhigacheva, DA Agarkov, SI Bredikhin, and VV Kharton. Performance of industrial-scale solid oxide electrolysis cells: An assessment of leakage effects. International Journal of Hydrogen Energy, 97:614–621, 2025. URL https://doi.org/10.1016/j.ijhydene.2024.11.480.

[72] J Schefold, A Brisse, and M Zahid. Electronic conduction of yttria-stabilized zirconia electrolyte in solid oxide cells operated in high temperature water electrolysis. Journal of The Electrochemical Society, 156(8):B897, 2009. URL https://doi.org/10.1149/1.3138701.

[73] Marco Gallo. Design, development and on-field testing of advanced solutions for monitoring, diagnosis and fault mitigation of SOFCs. 2020.

Thèse accessible à l'adresse : https://theses.insa-lyon.fr/publication/2026ISAL0017/these.pdf © [Z. Yazbeck], [2026], INSA Lyon, tous droits réservés

[74] Vanja Subotić and Christoph Hochenauer. Analysis of solid oxide fuel and electrolysis cells operated in a real-system environment: State-of-the-health diagnostic, failure modes, degradation mitigation and performance regeneration. Progress in Energy and Combustion Science, 93:101011, 2022. URL https://doi.org/10.1016/j.pecs.2022.101011.

[75] Jiawen Pan, Jiajun Yang, Dong Yan, Jian Pu, Bo Chi, and Jian Li. Effect of thermal cycling on durability of a solid oxide fuel cell stack with external manifold structure. International Journal of Hydrogen Energy, 45(35):17927–17934, 2020. URL https://doi.org/10.1016/j.ijhydene.2020.04.260.

[76] Fangzheng Liu, Liusheng Xiao, Ruidong Zhou, Qi Liu, and Jinliang Yuan. Evaluation of thermal stress and performance for solid oxide electrolysis cells employing graded fuel electrodes. Energies, 18(11):2790, 2025. URL https://doi.org/10.3390/en18112790.

[77] Huan Cheng, Xi Li, Jianhua Jiang, Zhonghua Deng, Jie Yang, and Jian Li. A nonlinear sliding mode observer for the estimation of temperature distribution in a planar solid oxide fuel cell. International Journal of Hydrogen Energy, 40(1):593–606, 2015. URL https://doi.org/10.1016/j.ijhydene.2014.10.117.

[78] Yu Chen, Xiaogang Wu, Kai Zhou, and Haoran Hu. Local temperature difference control of high temperature solid oxide electrolytic cell based on temperature observer. International Journal of Hydrogen Energy, 93:715–725, 2024. URL https://doi.org/10.1016/j.ijhydene.2024.11.001.

[79] Zaman Yazbeck, Federico Bribiesca-Argomedo, Minh Tu Pham, Bertrand Morel, and Vincent Dimitriou. System-level monitoring and diagnosis of starvation faults in solid oxide electrolyzers. International Journal of Hydrogen Energy, 198:152808, 2026. URL https://doi.org/10.1016/j.ijhydene.2025.152808.

[80] Zaman Yazbeck, Federico Bribiesca Argomedo, Minh Tu Pham, Bertrand Morel, Ronit-Kumar Panda, and Vincent Dimitriou. Sensitivity function-based identification of solid oxide electrolyzer parameters. In IEEE Conference on Decision and Control, 2024. URL https://doi.org/10.1109/CDC56724.2024.10886047.

[81] Mohsen Fallah Vostakola and Bahman Amini Horri. Progress in material development for low-temperature solid oxide fuel cells: A review. Energies, 14(5):1280, 2021. URL https://doi.org/10.3390/en14051280.

[82] Martin Andersson, Jinliang Yuan, and Bengt Sundén. Review on modeling development for multiscale chemical reactions coupled transport phenomena in solid oxide fuel cells. Applied Energy, 87(5):1461–1476, 2010. URL https://doi.org/10.1016/j.apenergy.2009.11.013.

Thèse accessible à l'adresse : https://theses.insa-lyon.fr/publication/2026ISAL0017/these.pdf © [Z. Yazbeck], [2026], INSA Lyon, tous droits réservés

[83] Shambhu Singh Rathore, Saheli Biswas, Daniel Fini, Aniruddha P Kulkarni, and Sarbjit Giddey. Direct ammonia solid-oxide fuel cells: A review of progress and prospects. International Journal of Hydrogen Energy, 46(71):35365–35384, 2021. URL https://doi.org/10.1016/j.ijhydene.2021.08.092.

[84] Jérôme Aicart. Modeling and experimental validation of high temperature steam and carbon dioxide co-electrolysis. PhD thesis, Université de Grenoble, 2014.

[85] Arunkumar Pandiyan, Aarthi Uthayakumar, Rengaraj Subrayan, Suk Won Cha, and Suresh Babu Krishna Moorthy. Review of solid oxide electrolysis cells: a clean energy strategy for hydrogen generation. Nanomaterials and energy, 8(1):2–22, 2019. URL https://doi.org/10.1680/jnaen.18.00009.

[86] M Mamlouk and M Manolova. Electrochemical methods for hydrogen production. Energy and Environment Series, pages 180–252, 2019.

[87] Jérôme Laurencin, D Kane, Gerard Delette, Jonathan Deseure, and Florence Lefebvre-Joud. Modelling of solid oxide steam electrolyser: Impact of the operating conditions on hydrogen production. Journal of Power Sources, 196(4):2080–2093, 2011. URL https://doi.org/10.1016/j.jpowsour.2010.09.054.

[88] Zubair Masaud, Muhammad Zubair Khan, Amjad Hussain, Hafiz Ahmad Ishfaq, RH Song, Seung-Bok Lee, Dong Woo Joh, and Tak-Hyoung Lim. Recent activities of solid oxide fuel cell research in the 3D printing processes. Trans. Korean Hydrog. New Energy Soc, 32(1): 11–40, 2021. URL https://doi.org/10.7316/KHNES.2021.32.1.11.

[89] Tomas Tronstad, Hanne Høgmoen Åstrand, Gerd-Petra Haugom, and Lars Langfeldt. Study on the use of fuel cells in shipping. 2017.

[90] Jie Ma, Suning Ma, Xinyi Zhang, Daifen Chen, and Juan He. Development of large-scale and quasi multi-physics model for whole structure of the typical solid oxide fuel cell stacks. Sustainability, 10(9):3094, 2018. URL https://doi.org/10.3390/su10093094.

[91] European Commission, CORDIS. Multimegawatt high-temperature electrolyser to generate green hydrogen for production of high-quality biofuels. https://cordis.europa.eu/project/id/875123, 2020–2025.

[92] Elcogen. Elcogen's new production facility to expand manufacturing capacity to 360 mw. Elcogen website, May 3 2024, 2024. URL https://elcogen.com/elcogens-new-production-facility-to-expand-manufacturing-capacity-to-360-mw/.

[93] Genvia. Hydrogène bas carbone et acier : une alliance stratégique pour réduire les émissions de CO2 — vers une industrie décarbonée : le projet pilote SOEL200 Genvia. Dossier

Thèse accessible à l'adresse : https://theses.insa-lyon.fr/publication/2026ISAL0017/these.pdf © [Z. Yazbeck], [2026], INSA Lyon, tous droits réservés

de presse, 4 novembre 2024, 2024. URL https://www.genvia.com/wp-content/uploads/2024/11/ArcelorMittal-x-Genvia-DossierDePresse-Nov2024.pdf.

[94] Aiswarya Krishnakumar Padinjarethil, Fiammetta Rita Bianchi, Barbara Bosio, and Anke Hagen. Electrochemical characterization and modelling of anode and electrolyte supported solid oxide fuel cells. Frontiers in Energy Research, 9:668964, 2021. doi: 10.3389/fenrg.2021.668964. URL https://doi.org/10.3389/fenrg.2021.668964.

[95] Catarina Mendonça, António Ferreira, and Diogo M. F. Santos. Towards the commercialization of solid oxide fuel cells: Recent advances in materials and integration strategies. Fuels, 2(4):393–419, 2021. URL https://doi.org/10.3390/fuels2040023.

[96] Kun Wang, Daniel Hissel, Marie-Cecile Péra, Nadia Steiner, Dario Marra, Marco Sorrentino, Cesare Pianese, Michela Monteverde, Pietro Cardone, and Jaakko Saarinen. A review on solid oxide fuel cell models. International journal of hydrogen energy, 36(12):7212–7228, 2011. URL https://doi.org/10.1016/j.ijhydene.2011.03.051.

[97] Jan Pawel Stempien, Qiang Sun, and Siew Hwa Chan. Solid oxide electrolyzer cell modeling: A review. Journal of Power Technologies, 93(4), 2013.

[98] Zhen Wu, Pengfei Zhu, Yakun Huang, Jing Yao, Fusheng Yang, Zaoxiao Zhang, and Meng Ni. A comprehensive review of modeling of solid oxide fuel cells: from large systems to fine electrodes. Chemical reviews, 125(4):2184–2268, 2025. URL https://pubs.acs.org/doi/10.1021/acs.chemrev.4c00614.

[99] Xiaojuan Wu, Danan Yang, Junhao Wang, and Xi Li. Temperature gradient control of a solid oxide fuel cell stack. Journal of Power Sources, 414:345–353, 2019. URL https://doi.org/10.1016/j.jpowsour.2018.12.058.

[100] Biao Zhang, Nor Farida Harun, Nana Zhou, Jose J Colon-Rodriguez, Danylo Oryshchyn, Lawrence Shadle, David Tucker, and Samuel Bayham. A real-time multiphysics model of a pressurized solid oxide electrolysis cell (SOEC) for cyber-physical simulation. Energy Conversion and Management, 298:117778, 2023. URL https://doi.org/10.1016/j.enconman.2023.117778.

[101] Marco Gallo, Dario Marra, Marco Sorrentino, Cesare Pianese, and Siu Fai Au. A versatile computational tool for model-based design, control and diagnosis of a generic solid oxide fuel cell integrated stack module. Energy conversion and management, 171:1514–1528, 2018. URL https://doi.org/10.1016/j.enconman.2018.06.062.

[102] Marco Gallo, Pierpaolo Polverino, Julie Mougin, Bertrand Morel, and Cesare Pianese. Coupling electrochemical impedance spectroscopy and model-based aging estimation for

Thèse accessible à l'adresse : https://theses.insa-lyon.fr/publication/2026ISAL0017/these.pdf © [Z. Yazbeck], [2026], INSA Lyon, tous droits réservés

solid oxide fuel cell stacks lifetime prediction. Applied Energy, 279:115718, 2020. URL https://doi.org/10.1016/j.apenergy.2020.115718.

[103] Yashan Xing, Ramon Costa-Castelló, Jing Na, and Hugues Renaudineau. Control-oriented modelling and analysis of a solid oxide fuel cell system. International Journal of Hydrogen Energy, 45(40):20659–20672, 2020. URL https://doi.org/10.1016/j.ijhydene.2020.02.061.

[104] L van Biert, P Segovia Castillo, A Haseltalab, and RR Negenborn. A reduced-order model of a solid oxide fuel cell stack for model predictive control. In Proceedings of the International Ship Control Systems Symposium, volume 16, page 26. Institute of Marine Engineering Science and Technology, 2022.

[105] Guoqiang Liu, Wei Zhao, Zexin Li, Zhiping Xia, Chang Jiang, Jakub Kupecki, Shui Pang, Zhonghua Deng, and Xi Li. Modeling and control-oriented thermal safety analysis for mode switching process of reversible solid oxide cell system. Energy Conversion and Management, 255:115318, 2022. URL https://doi.org/10.1016/j.enconman.2022.115318.

[106] Yigeng Huangfu, Fei Gao, Abdeljalil Abbas-Turki, David Bouquain, and Abdellatif Miraoui. Transient dynamic and modeling parameter sensitivity analysis of 1D solid oxide fuel cell model. Energy Conversion and Management, 71:172–185, 2013. URL https://doi.org/10.1016/j.enconman.2013.03.029.

[107] Young Jin Kim, Woo Nam Jung, Ji Haeng Yu, Hyeon Jin Kim, Kyong Sik Yun, Dong Gu Kang, and Min Chul Lee. Design and analysis of SOFC stack with different types of external manifolds. International Journal of Hydrogen Energy, 45(53):29143–29154, 2020. URL https://doi.org/10.1016/j.ijhydene.2020.07.145.

[108] Grant Hawkes, James O'Brien, Carl Stoots, and Brian Hawkes. 3D CFD model of a multi-cell high-temperature electrolysis stack. International journal of Hydrogen energy, 34(9):4189–4197, 2009. URL https://doi.org/10.1016/j.ijhydene.2008.11.068.

[109] Eduardo Da Rosa Silva, Maxime Hubert, Bertrand Morel, Hamza Moussaoui, Johan Debayle, and Jérôme Laurencin. A dynamic multi-scale model for solid oxide cells validated on local current measurements: impact of global cell operation on the electrodes reaction mechanisms. ECS Transactions, 103(1):893, 2021.

[110] Alireza Saeedmanesh. Solid Oxide Electrolysis Cell (SOEC) and System Technology for Widespread Use with Renewable Energy. PhD thesis, University of California, Irvine, 2021.

Thèse accessible à l'adresse : https://theses.insa-lyon.fr/publication/2026ISAL0017/these.pdf © [Z. Yazbeck], [2026], INSA Lyon, tous droits réservés

[111] A. K. M. Monjur Murshed. Modeling, Control and Fault Detection of Solid Oxide Fuel Cell System. PhD thesis, University of Alberta, Department of Chemical and Materials Engineering, Edmonton, Alberta, Canada, 2007.

[112] Marco Sorrentino, Cesare Pianese, and Yann G Guezennec. A hierarchical modeling approach to the simulation and control of planar solid oxide fuel cells. Journal of Power Sources, 180(1):380–392, 2008. URL https://doi.org/10.1016/j.jpowsour.2008.02.021.

[113] Dario Marra. Development of Solid Oxide Fuel Cell stack models for monitoring, diagnosis and control applications. PhD thesis, University of Salerno, 2013.

[114] R Suwanwarangkul, E Croiset, MW Fowler, PL Douglas, E Entchev, and MA Douglas. Performance comparison of fick's, dusty-gas and stefan–maxwell models to predict the concentration overpotential of a SOFC anode. Journal of Power Sources, 122(1):9–18, 2003. URL https://doi.org/10.1016/S0378-7753(02)00724-3.

[115] Andre Leonide, Yannick Apel, and Ellen Ivers-Tiffee. SOFC modeling and parameter identification by means of impedance spectroscopy. ECS Transactions, 19(20):81, 2009. URL https://doi.org/10.1149/1.3247567.

[116] Ana Gallet Segarra. Robust control of a solid oxide fuel cell for combined heat and power applications. PhD thesis, Universitätsbibliothek der Universität Stuttgart, 2017.

[117] B Todd and JB Young. Thermodynamic and transport properties of gases for use in solid oxide fuel cell modelling. Journal of power Sources, 110(1):186–200, 2002. URL https://doi.org/10.1016/S0378-7753(02)00277-X.

[118] Caisheng Wang and M Hashem Nehrir. A physically based dynamic model for solid oxide fuel cells. IEEE Transactions on Energy conversion, 22(4):887–897, 2007. URL https://doi.org/10.1109/TEC.2007.895468.

[119] Allen J Bard, Larry R Faulkner, and Henry S White. Electrochemical methods: fundamentals and applications. John Wiley & Sons, 2022.

[120] NIST. NIST chemistry WebBook, standard reference database 69, 2023. URL https://doi.org/10.18434/T4D303. National Institute of Standards and Technology.

[121] Federico Monaco. Analysis of the degradation in solid oxide cells operated in fuel cell and electrolysis modes: microstructural evolution and stability of the electrodes materials. PhD thesis, Universite Grenoble Alpes, 2020.

[122] Gene A Bunin, Zacharie Wuillemin, Grégory François, Arata Nakajo, Leonidas Tsikonis, and Dominique Bonvin. Experimental real-time optimization of a solid oxide fuel cell stack

Thèse accessible à l'adresse : https://theses.insa-lyon.fr/publication/2026ISAL0017/these.pdf © [Z. Yazbeck], [2026], INSA Lyon, tous droits réservés

via constraint adaptation. Energy, 39(1):54–62, 2012. URL https://doi.org/10.1016/j.energy.2011.04.033.

[123] Saehong Park, Dylan Kato, Zach Gima, Reinhardt Klein, and Scott Moura. Optimal experimental design for parameterization of an electrochemical lithium-ion battery model. Journal of The Electrochemical Society, 165(7):A1309, 2018. URL https://doi.org/10.1149/2.0421807jes.

[124] Etki Acilan and Murat Gol. Identifiability analysis for power plant parameter calibration in the presence of collinear parameters. IEEE Transactions on Power Systems, 37(4):2988–2997, 2021. URL https://doi.org/10.1109/TPWRS.2021.3130076.

[125] Alireza Goshtasbi, Jixin Chen, James R Waldecker, Shinichi Hirano, and Tulga Ersal. Effective parameterization of PEM fuel cell models—part i: Sensitivity analysis and parameter identifiability. Journal of The Electrochemical Society, 167(4):044504, 2020. URL https://doi.org/10.1149/1945-7111/ab7091.

[126] Andrea Pozzi, Gabriele Ciaramella, Krishnakumar Gopalakrishnan, Stefan Volkwein, and Davide M Raimondo. Optimal design of experiment for parameter estimation of a single particle model for lithium ion batteries. In 2018 IEEE Conference on Decision and Control (CDC), pages 6482–6487. IEEE, 2018. URL https://doi.org/10.1109/CDC.2018.8619340.

[127] Gaia Franceschini and Sandro Macchietto. Model-based design of experiments for parameter precision: State of the art. Chemical Engineering Science, 63(19):4846–4872, 2008. URL https://doi.org/10.1016/j.ces.2007.11.034.

[128] Margherita Geremia, Sandro Macchietto, and Fabrizio Bezzo. A review on model-based design of experiments for parameter precision–open challenges, trends and future perspectives. Chemical Engineering Science, 319:122347, 2026. URL https://doi.org/10.1016/j.ces.2025.122347.

[129] Nicholas N Lam, Paul D Docherty, and Rua Murray. Practical identifiability of parametrised models: A review of benefits and limitations of various approaches. Mathematics and Computers in Simulation, 199:202–216, 2022. URL https://doi.org/10.1016/j.matcom.2022.03.020.

[130] Thomas M Cover. Elements of information theory. John Wiley & Sons, 1999.

[131] Henri P Gavin. The levenberg-marquardt algorithm for nonlinear least squares curve-fitting problems. Department of Civil and Environmental Engineering Duke University August, 3: 1–23, 2019.

Thèse accessible à l'adresse : https://theses.insa-lyon.fr/publication/2026ISAL0017/these.pdf © [Z. Yazbeck], [2026], INSA Lyon, tous droits réservés

[132] S Srikantha, MP Heddrich, S Gupta, and KA Friedrich. Transient reversible solid oxide cell reactor operation–experimentally validated modeling and analysis. Applied Energy, 232: 473–488, 2018. URL https://doi.org/10.1016/j.apenergy.2018.09.186.

[133] OB Rizvandi and HL Frandsen. Modeling of single-and double-sided high-pressure operation of solid oxide electrolysis stacks. International Journal of Hydrogen Energy, 2023. URL https://doi.org/10.1016/j.ijhydene.2023.04.169.

[134] Chitra Dangwal and Marcello Canova. Parameter identification for electrochemical models of lithium-ion batteries using sensitivity analysis. ASME Letters in Dynamic Systems and Control, 1(4):041014, 2021. URL https://doi.org/10.1115/1.4050794.

[135] Zachary T Gima, Dylan Kato, Reinhardt Klein, and Scott J Moura. Analysis of online parameter estimation for electrochemical li-ion battery models via reduced sensitivity equations. In 2020 American Control Conference (ACC), pages 373–378. IEEE, 2020. URL https://doi.org/10.23919/ACC45564.2020.9147260.

[136] Mohammed I Radaideh and Majdi I Radaideh. Efficient analysis of parametric sensitivity and uncertainty of fuel cell models with application to SOFC. International Journal of Energy Research, 44(4):2517–2534, 2020. URL https://doi.org/10.1002/er.4837.

[137] Barath Ram Jayasankar, Amos Ben-Zvi, and Biao Huang. Identifiability and estimability study for a dynamic solid oxide fuel cell model. Computers & Chemical Engineering, 33(2): 484–492, 2009. URL https://doi.org/10.1016/j.compchemeng.2008.11.005.

[138] Ian A Hiskens. Nonlinear dynamic model evaluation from disturbance measurements. IEEE Transactions on Power Systems, 16(4):702–710, 2001. URL https://doi.org/10.1109/59.962416.

[139] H Khalil. Nonlinear systems. Prentice Hall, 2002.

[140] JA Andersson, J Gillis, G Horn, JB Rawlings, and M Diehl. Casadi: a software framework for nonlinear optimization and optimal control. Mathematical Programming Computation, 11:1–36, 2019.

[141] David J Gardner, Daniel R Reynolds, Carol S Woodward, and Cody J Balos. Enabling new flexibility in the SUNDIALS suite of nonlinear and differential/algebraic equation solvers. ACM Transactions on Mathematical Software (TOMS), 48(3):1–24, 2022. doi: 10.1145/3539801.

[142] Bernd Müller, Bernhard Rolle, and Oliver Sawodny. Sensitivity analysis and fisher-information matrix for a dynamic model of a turntable ladder. IFAC-PapersOnLine, 55(27): 172–177, 2022. URL https://doi.org/10.1016/j.ifacol.2022.10.507.

Thèse accessible à l'adresse : https://theses.insa-lyon.fr/publication/2026ISAL0017/these.pdf © [Z. Yazbeck], [2026], INSA Lyon, tous droits réservés

[143] AKM M Murshed, Biao Huang, and Kumar Nandakumar. Control relevant modeling of planer solid oxide fuel cell system. Journal of Power Sources, 163(2):830–845, 2007. URL https://doi.org/10.1016/j.jpowsour.2006.09.080.

[144] Mark K Transtrum and James P Sethna. Improvements to the levenberg-marquardt algorithm for nonlinear least-squares minimization. arXiv preprint arXiv:1201.5885, 2012. URL https://doi.org/10.48550/arXiv.1201.5885.

[145] Julia Albicker. The gauß-newton method and its implementation in the optimization library oppy. 2022.

[146] Stephen Boyd and Lieven Vandenberghe. Convex optimization. Cambridge university press, 2004.

[147] Matthew P Kelly. Transcription methods for trajectory optimization: a beginners tutorial. arXiv preprint arXiv:1707.00284, 2017.

[148] John H. Holland. Adaptation in Natural and Artificial Systems: An Introductory Analysis with Applications to Biology, Control, and Artificial Intelligence. The MIT Press, 04 1992. ISBN 9780262275552. doi: $10.7551/\mathrm{mitpress}/1090.001.0001$. URL https://doi.org/10.7551/mitpress/1090.001.0001.

[149] Oliver Kramer. Genetic algorithms. In Genetic algorithm essentials, pages 11–19. Springer, 2017.

[150] Benjamin Königshofer, Michael Höber, Gjorgji Nusev, Pavle Boškoski, Christoph Hochenauer, and Vanja Subotić. Accelerated degradation for solid oxide electrolysers: Analysis and prediction of performance for varying operating environments. Journal of Power Sources, 523:230982, 2022. URL https://doi.org/10.1016/j.jpowsour.2022.230982.

[151] Hamza Moussaoui, Gerald Hammerschmid, Vanja Subotić, et al. Fast online diagnosis for solid oxide fuel cells: Optimisation of total harmonic distortion tool for real-system application and reactants starvation identification. Journal of Power Sources, 556:232352, 2023. URL https://doi.org/10.1016/j.jpowsour.2022.232352.

[152] Jingxuan Peng, Jian Huang, Xiao-long Wu, Yuan-wu Xu, Haochun Chen, and Xi Li. Solid oxide fuel cell (SOFC) performance evaluation, fault diagnosis and health control: A review. Journal of Power Sources, 505:230058, 2021. URL https://doi.org/10.1016/j.jpowsour.2021.230058.

Thèse accessible à l'adresse : https://theses.insa-lyon.fr/publication/2026ISAL0017/these.pdf © [Z. Yazbeck], [2026], INSA Lyon, tous droits réservés

[153] Yannick Wilhelm, Peter Reimann, Wolfgang Gauchel, and Bernhard Mitschang. Overview on hybrid approaches to fault detection and diagnosis: Combining data-driven, physics-based and knowledge-based models. Procedia Cirp, 99:278–283, 2021. URL https://doi.org/10.1016/j.procir.2021.03.041.

[154] Yi Zheng, Xiao-long Wu, Dongqi Zhao, Yuan-wu Xu, Beibei Wang, Yanmin Zu, Dong Li, Jianhua Jiang, Chang Jiang, Xiaowei Fu, et al. Data-driven fault diagnosis method for the safe and stable operation of solid oxide fuel cells system. Journal of Power Sources, 490: 229561, 2021. URL https://doi.org/10.1016/j.jpowsour.2021.229561.

[155] Zehan Zhang, Shuanghong Li, and Yupu Yang. A general approach for fault identification in SOFC-based power generation systems. In 2018 Annual American Control Conference (ACC), pages 3816–3821. IEEE, 2018. URL https://doi.org/10.23919/ACC.2018.8430954.

[156] Babak Ghorbani and Krishna Vijayaraghavan. Developing a virtual hydrogen sensor for detecting fuel starvation in solid oxide fuel cells using different machine learning algorithms. International Journal of Hydrogen Energy, 45(51):27730–27744, 2020. URL https://doi.org/10.1016/j.ijhydene.2020.07.154.

[157] Giang Tra Le, Luca Mastropasqua, Jacob Brouwer, and Stuart B Adler. Simulation-informed machine learning diagnostics of solid oxide fuel cell stack with electrochemical impedance spectroscopy. Journal of The Electrochemical Society, 169(3):034530, 2022. URL https://doi.org/10.1149/1945-7111/ac59f4.

[158] Elodie Pahon, Nadia Yousfi Steiner, Samir Jemei, Daniel Hissel, Marie-Cécile Péra, Kun Wang, and Philippe Moçoteguy. Solid oxide fuel cell fault diagnosis and ageing estimation based on wavelet transform approach. International Journal of Hydrogen Energy, 41(31): 13678–13687, 2016. URL https://doi.org/10.1016/j.ijhydene.2016.06.143.

[159] Yuan-wu Xu, Xiao-long Wu, Xiao-bo Zhong, Dong-qi Zhao, Marco Sorrentino, Jianhua Jiang, Chang Jiang, Xiaowei Fu, and Xi Li. Mechanism model-based and data-driven approach for the diagnosis of solid oxide fuel cell stack leakage. Applied Energy, 286: 116508, 2021. URL https://doi.org/10.1016/j.apenergy.2021.116508.

[160] Pierpaolo Polverino, Cesare Pianese, Marco Sorrentino, and Dario Marra. Model-based development of a fault signature matrix to improve solid oxide fuel cell systems on-site diagnosis. Journal of Power Sources, 280:320–338, 2015. URL https://doi.org/10.1016/j.jpowsour.2015.01.037.

[161] Ivan Arsie, Arturo Di Filippi, Dario Marra, Cesare Pianese, and Marco Sorrentino. Fault tree analysis aimed to design and implement on-field fault detection and isolation schemes

Thèse accessible à l'adresse : https://theses.insa-lyon.fr/publication/2026ISAL0017/these.pdf © [Z. Yazbeck], [2026], INSA Lyon, tous droits réservés

for SOFC systems. In International Conference on Fuel Cell Science, Engineering and Technology, volume 44045, pages 389–399, 2010. URL https://doi.org/10.1115/FuelCell2010-33344.

[162] Marco Gallo, Carmine Costabile, Marco Sorrentino, Pierpaolo Polverino, and Cesare Pianese. Development and application of a comprehensive model-based methodology for fault mitigation of fuel cell powered systems. Applied Energy, 279:115698, 2020. URL https://doi.org/10.1016/j.apenergy.2020.115698.

[163] Periasamy Vijay, Moses O Tadé, and Zongping Shao. Adaptive observer based approach for the fault diagnosis in solid oxide fuel cells. Journal of Process Control, 84:101–114, 2019. URL https://doi.org/10.1016/j.jprocont.2019.09.010.

[164] Xiao-long Wu, Yuan-wu Xu, Tao Xue, Junchao Shuai, Jianhua Jiang, Zhonghua Deng, Xiaowei Fu, and Xi Li. Control-oriented fault detection of solid oxide fuel cell system unknown input on fuel supply. Asian Journal of Control, 21(4):1824–1835, 2019. URL https://doi.org/10.1002/asjc.2014.

[165] Rudolph Van Der Merwe and Eric A Wan. The square-root unscented Kalman filter for state and parameter-estimation. In 2001 IEEE international conference on acoustics, speech, and signal processing. Proceedings (Cat. No. 01CH37221), volume 6, pages 3461–3464. IEEE, 2001. URL https://doi.org/10.1109/ICASSP.2001.940586.

[166] Xiaoyu Li, Mohan Lyu, Xiao Gao, Changgui Yuan, and Dong Zhen. An adaptive threshold method for multi-faults diagnosis of lithium-ion batteries based on electro-thermal model. Measurement, 222:113671, 2023. URL https://doi.org/10.1016/j.measurement.2023.113671.

[167] Krzysztof Patan. Artificial neural networks for the modelling and fault diagnosis of technical processes, volume 377. Springer Science & Business Media, 2008. URL https://doi.org/10.1007/978-3-540-79872-9.

[168] Ming Chen, Xiufu Sun, Christodoulos Chatzichristodoulou, Søren Koch, Peter Vang Hendriksen, and Mogens Bjerg Mogensen. Thermoneutral operation of solid oxide electrolysis cells in potentiostatic mode. ECS Transactions, 78(1):3077, 2017. URL https://doi.org/10.1149/MA2017-03/1/287.

[169] Michael Lang, Sebastian Raab, Michelle Sophie Lemcke, Corinna Bohn, and Matthias Pysik. Long-term behavior of a solid oxide electrolyzer (SOEC) stack. Fuel Cells, 20(6):690–700, 2020. URL https://doi.org/10.1002/fuce.201900245.

Thèse accessible à l'adresse : https://theses.insa-lyon.fr/publication/2026ISAL0017/these.pdf © [Z. Yazbeck], [2026], INSA Lyon, tous droits réservés

[170] Mathieu Bressel, Mickael Hilairet, Daniel Hissel, and Belkacem Ould Bouamama. Extended Kalman filter for prognostic of proton exchange membrane fuel cell. Applied Energy, 164:220–227, 2016. URL https://doi.org/10.1016/j.apenergy.2015.11.071.

[171] Josef Schefold, Annabelle Brisse, and Hendrik Poepke. Long-term steam electrolysis with electrolyte-supported solid oxide cells. Electrochimica Acta, 179:161–168, 2015. URL https://doi.org/10.1016/j.electacta.2015.04.141.

[172] David J Smith. Understanding terms and jargon. In Reliability and Maintainability in Perspective: Practical, contractual, commercial and software aspects, pages 16–28. Springer, 1988.

[173] Wikipedia contributors. Bathtub curve. https://en.wikipedia.org/wiki/Bathtub_curve.

Thèse accessible à l'adresse : https://theses.insa-lyon.fr/publication/2026ISAL0017/these.pdf © [Z. Yazbeck], [2026], INSA Lyon, tous droits réservés

Appendix A

Résumé étendu en Français

Contents

A.1 Motivation et contexte 151
A.2 Dégradations des SOEC et diagnostic des défauts basé sur un modèle153
A.3 Technologie SOEC 154
A.3.1 Cellule d'électrolyse à oxyde solide et mécanismes de réaction 154
A.3.2 Régimes thermiques et fonctionnement thermoneutre 155
A.3.3 Niveaux de modélisation 155
A.3.4 Courbe de performance électrochimique et de polarisation 155
A.3.5 Structure globale du modèle 157
A.3.6 Intégration temporelle 157
A.4 Estimation des paramètres 157
A.4.1 Représentation d'état 158
A.4.2 Modèle d'espace d'état et fonctions de sensibilité 158
A.4.3 Méthode de Levenberg-Marquardt tronqué 159
A.4.4 Estimation à partir de données simulées 160
A.4.5 Intervalle de confiance 161
A.4.6 Estimation à partir de données experimentaux 162
A.4.7 Planification optimale d'expériences (OED) 163
A.4.8 Stratégies alternatives de planification expérimentale optimale 164
A.5 Détection des défauts 166
A.5.1 Application aux données expérimentales 170
A.5.2 Résultats 170
A.6 Conclusion et perspectives 172

Thèse accessible à l'adresse : https://theses.insa-lyon.fr/publication/2026ISAL0017/these.pdf © [Z. Yazbeck], [2026], INSA Lyon, tous droits réservés

A.1 Motivation et contexte

La population mondiale devrait continuer de croître au cours des cinq à six prochaines décennies, pour atteindre un pic d'environ 10.3 milliards d'habitants au milieu des années 2080, contre 8.2 milliards en 2024 [1].

Cette croissance démographique, conjuguée à la croissance économique, notamment dans les pays en développement [2], et à l'urbanisation rapide, exerce une pression sans précédent sur les systèmes énergétiques mondiaux [3, 4, 5, 6]. Bien que non renouvelables et lourds de conséquences environnementales, les combustibles fossiles dominent toujours les systèmes énergétiques modernes. Cette dépendance persiste surtout en raison des obstacles majeurs à la transition vers des énergies durables: coûts prohibitifs et infrastructures encore insuffisantes [12, 13]. Pourtant, la combustion des énergies fossiles rejette d'importants volumes de gaz résiduaires dans l'atmosphère, notamment du dioxyde de carbone (CO_2), dont la concentration a commencé à augmenter significativement avec la croissance des activités industrielles [14], atteignant ces dernières années 35 milliards de tonnes de gaz émis annuellement [15]. Or le dioxyde de carbone (CO_2) agit comme un gaz à effet de serre en absorbant le rayonnement infrarouge, piégeant ainsi la chaleur et contribuant au réchauffement climatique [16]. C'est dans ce contexte que l'Accord de Paris de 2015, adopté en 2015, fixe un objectif clair : contenir la hausse de la température mondiale bien en dessous de 2°C par rapport aux niveaux préindustriels [18].

Face à ces enjeux, l'hydrogène émerge comme une solution prometteuse pour diversifier le mix énergétique mondial. Ses atouts majeurs sont sa combustion propre, son contenu énergétique élevé et sa polyvalence d'usage. Cependant, sa production industrielle se heurte à un paradoxe. En effet, cette dernière est principalement réalisée à partir de combustibles fossiles annulant de fait une grande partie de ses avantages environnementaux. Pour exploiter pleinement les atouts environnementaux de l'hydrogène, il est donc indispensable de le produire à partir de sources d'énergies renouvelables et durables. Le développement d'une production industrielle à grande échelle pourrait ainsi concilier performance énergétique et respect de l'environnement. Parmi les voies de production bas-carbone disponibles, l'électrolyse de l'eau est considérée comme une méthode prometteuse, permettant la production d'hydrogène de haute pureté avec de l'oxygène comme sous-produit, grâce à une réaction électrochimique alimentée par de l'énergie électrique et thermique.

$$H_2O \xrightarrow{\textit{Electricité + Chaleur}} H_2 + \frac{1}{2}O_2 \tag{A.1}$$

Parmi les technologies d'électrolyse, la cellule d'électrolyse à oxyde solide (SOEC) se distingue par son potentiel de rendement élevé et fait l'objet d'une attention particulière dans les travaux de thèse de ce manuscrit. Fonctionnant à haute température (600-1000°C), les SOEC utilisent à la fois l'électricité et l'énergie thermique (par exemple, la chaleur résiduelle industrielle), réduisant ainsi la demande en énergie électrique et améliorant le rendement global [40].

Thèse accessible à l'adresse : https://theses.insa-lyon.fr/publication/2026ISAL0017/these.pdf © [Z. Yazbeck], [2026], INSA Lyon, tous droits réservés

Cet avantage découle de la thermodynamique de la réaction d'électrolyse de l'eau:

$$\Delta H = \Delta G + T\Delta S \tag{A.2}$$

Où ΔH est la demande énergétique totale, ΔG la variation d'énergie libre de Gibbs ou d'énergie électrique fournie, T la température et ΔS la variation d'entropie. L'utilisation de l'eau à l'état gazeux pour l'électrolyse réduit la demande énergétique ΔH nécessaire à la dissociation des molécules d'eau en hydrogène et en oxygène, comme illustré dans la figure A.1. Cette différence d'énergie correspond à la chaleur latente de vaporisation de l'eau. Lorsque la température augmente, une partie de l'énergie électrique peut être remplacée par de l'énergie thermique, tandis que la demande énergétique totale reste quasiment constante. Outre cette substitution d'énergie électrique par de l'énergie thermique, l'électrolyse à haute température offre également une cinétique de réaction améliorée et des pertes aux électrodes réduites [42].

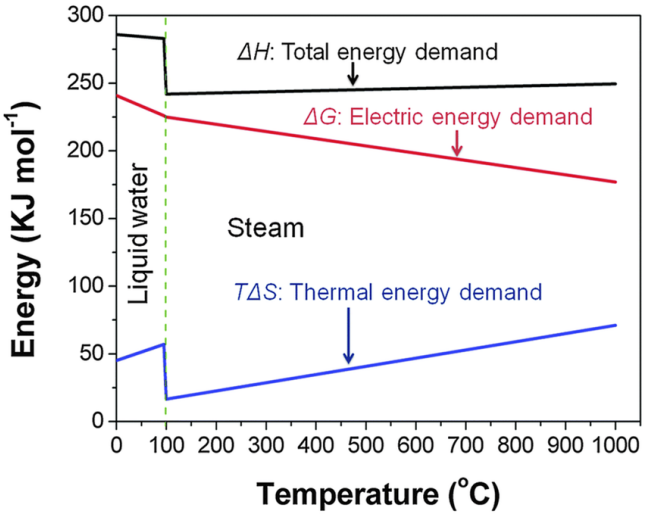

Figure A.1: Besoins énergétiques pour l'électrolyse de l'eau en fonction de la température [40].

Malgré leurs avantages, le déploiement à grande échelle des piles à oxyde solide (SOC) reste limité par leurs coûts de fabrication élevés et les problèmes de durabilité. Bien que les progrès réalisés en matière de propriétés des matériaux aient amélioré les performances des SOEC [44], ils ne suffisent pas à eux seuls, et travailler uniquement sur ces propriétés ne permet pas de garantir leur fiabilité à long terme. Il est tout aussi important de mettre en œuvre des stratégies efficaces de gestion de la santé (PHM), impliquant une surveillance continue des états internes, la détection précoce des défauts et le pronostic, afin de prédire la durée de vie restante (RUL), ainsi que des actions de commande optimale permettant de prévenir la dégradation irréversible des cellules d'électrolyse à oxyde solide et d'assurer un fonctionnement sûr et efficace dans des conditions variables.

Thèse accessible à l'adresse : https://theses.insa-lyon.fr/publication/2026ISAL0017/these.pdf © [Z. Yazbeck], [2026], INSA Lyon, tous droits réservés

A.2 Dégradations des SOEC et diagnostic des défauts basé sur un modèle

En pratique, la dégradation de SOEC résulte des effets de l'utilisation (vieillissement électrochimique), du temps (vieillissement calendaire) et de diverses contraintes permanentes et/ou accidentelles [63]. D'après différentes études [37, 60, 64], il est pertinent de regrouper les facteurs de dégradation en deux catégories: la dégradation intrinsèque des matériaux (due au vieillissement des matériaux avec le temps et l'utilisation) et la dégradation extrinsèque (due à des dysfonctionnements ou à des défauts au niveau du système). Parmi les problèmes intrinsèques représentatifs, on peut citer les modifications microstructurales des électrodes, la dégradation de l'interface de l'électrode à oxygène, l'augmentation de la résistance d'interconnexion/de contact, le vieillissement des joints et la perte de conductivité de l'électrolyte ainsi que son interdiffusion avec l'électrode à oxygène [37, 60, 65, 68]. Les dégradations extrinsèques sont dues à des conditions de fonctionnement difficiles, elles-mêmes induites par des défauts au niveau du système, tels que les fuites, le manque de vapeur, la contamination/l'empoisonnement, les contraintes thermomécaniques lors des cycles thermiques et les transitoires de charge électrique [37, 60, 74, 73]. De nombreux défauts induits par l'exploitation sont initialement récupérables, mais sans intervention rapide, ils peuvent évoluer vers des dommages irréversibles.

Pour passer des approches théoriques à leur application concrète, les méthodes de diagnostic de défauts basées sur des modèles s'appuient généralement sur le schéma de principe présenté à la figure A.2. Ce processus repose sur la comparaison entre les sorties mesurées et les prédictions du modèle, permettant de générer des résidus. Ceux-ci sont ensuite analysés pour en extraire des caractéristiques significatives, puis interprétés via une logique de décision. L'objectif est d'évaluer l'état de santé du système, identifier les indicateurs clés et isoler la nature des défauts. Cette méthodologie est celle adoptée dans le cadre de cette thèse.

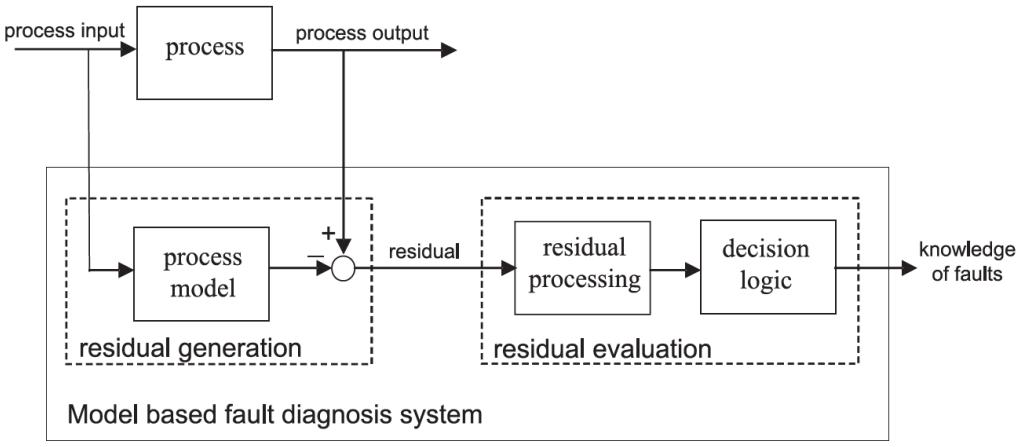

Figure A.2: Description schématique d'une méthode de diagnostic de défauts basée sur un modèle [59].

Thèse accessible à l'adresse : https://theses.insa-lyon.fr/publication/2026ISAL0017/these.pdf © [Z. Yazbeck], [2026], INSA Lyon, tous droits réservés

A.3 Technologie SOEC

A.3.1 Cellule d'électrolyse à oxyde solide et mécanismes de réaction

Les piles à oxyde solide (SOC) sont des dispositifs de conversion d'énergie électrochimique à haute température. Une pile est constituée d'un électrolyte céramique dense pris en sandwich entre deux électrodes poreuses. Fonctionnant à des températures élevées, entre 600 et 1000°C, l'électrolyte céramique devient conducteur d'ions oxygène avec une très faible conductivité électronique [81, 82]. Cette température de fonctionnement offre plusieurs avantages: (i) un rendement élevé, (ii) la réversibilité, permettant à la pile de fonctionner en mode électrolyse ou pile à combustible, (iii) la flexibilité en matière de combustible, (iv) l'utilisation de catalyseurs peu coûteux et (v) la possibilité de récupérer de la chaleur utile pouvant être réutilisée dans des systèmes de cogénération ou des systèmes énergétiques hybrides [60, 83, 84]. La figure A.3 illustre la structure du SOC en mode d'électrolyse de la vapeur, montrant les électrodes individuelles avec leurs demi-réactions respectives, ainsi que la cellule unique complète.

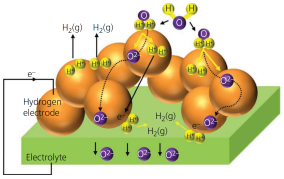

(a) Électrode à hydrogène (cathode).

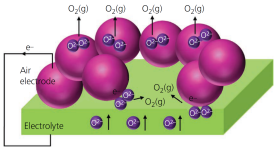

(b) Électrode à air (anode).

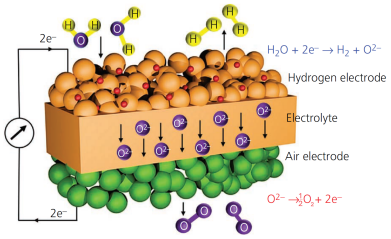

(c) Cellule SOEC et ses compartiments.

Figure A.3: Électrodes individuelles SOEC et cellule complète [85].

Dans l'électrolyse à oxyde solide, la réaction électrochimique est amorcée par de la vapeur d'eau surchauffée circulant sur la cathode, une différence de potentiels suffisante étant appliquée entre les électrodes pour forcer la réaction à se produire. À la cathode, les molécules d'eau en phase gazeuse sont réduites à l'interface cathode/électrolyte, produisant de l'hydrogène gazeux et des ions oxygène (Figure A.3). Les ions oxygène migrent à travers l'électrolyte dense et sont oxydés à l'interface anode/électrolyte pour former du dioxygène gazeux. Parallèlement, l'hydrogène produit à la cathode reste mélangé à la vapeur d'eau résiduelle [60, 86].

Thèse accessible à l'adresse : https://theses.insa-lyon.fr/publication/2026ISAL0017/these.pdf © [Z. Yazbeck], [2026], INSA Lyon, tous droits réservés

A.3.2 Régimes thermiques et fonctionnement thermoneutre

En mode électrolyse, selon l'équilibre entre les contributions électrique et thermique, on distingue trois régimes thermiques pour les électrolyseurs haute température: endothermique, thermoneutre et exothermique [87]. En mode thermoneutre, la cellule reste thermiquement stable et la chaleur générée par les irréversibilités internes est utilisée pour fournir l'énergie nécessaire à l'électrolyse de l'eau; la chaleur dégagée est donc intégralement utilisée par le système. Ce mode de fonctionnement est particulièrement important pour les SOEC, car il évite le recours à des sources de chaleur externes ou à des échangeurs de chaleur.

A.3.3 Niveaux de modélisation

Les modèles SOEC peuvent être classés selon leur dimensionnalité géométrique, allant des formulations localisées (0D) aux formulations distribuées (1D/2D) et basées sur la CFD (3D) [54, 87, 103, 104, 107]. Les modèles de dimension supérieure permettent de résoudre les gradients spatiaux de température, de composition et de densité de courant, mais leur coût de calcul limite leur utilisation directe pour la surveillance en temps réel et les applications de gestion de l'état de santé de l'electrolyseur. Dans cette optique, le présent travail adopte un modèle dynamique 0D intégrant des bilans massiques et thermiques couplés ainsi qu'une loi de tension électrochimique. Ce modèle, conçu pour une exécution en temps réel, est également optimisé pour une intégration au niveau système.

A.3.4 Courbe de performance électrochimique et de polarisation

Les performances électrochimiques de SOEC sont caractérisées par la courbe de polarisation, c'est-à-dire la courbe courant-tension (IV), qui montre l'évolution de la tension de la cellule en fonction de la densité de courant, telle que présentée dans la figure A.4. Cette loi de tension électrochimique combine deux contributions essentielles :

- la tension réversible, U_{rev}, représentant le potentiel thermodynamique minimal requis pour amorcer la réaction d'électrolyse,
- la polarisation de la cellule qui apparaît sous courant avec les surtensions.

La tension de la pile, V_s, est donnée par la tension de la cellule, U_{cell}, multipliée par le nombre de cellules dans la pile, N_{cell}, comme suit:

$$V_s = N_{cell}U_{cell} = N_{cell}\left(U_{rev} - \eta_{ohmic} - (\eta_{act}^{cathode} - \eta_{act}^{anode}) - (\eta_{conc}^{cathode} - \eta_{conc}^{anode})\right) \tag{A.3}$$

La surtension peut être décomposé en différentes contributions, chacune étant attribuée à un processus spécifique limitant le rendement de la cellule et donc le taux de production

Thèse accessible à l'adresse : https://theses.insa-lyon.fr/publication/2026ISAL0017/these.pdf © [Z. Yazbeck], [2026], INSA Lyon, tous droits réservés

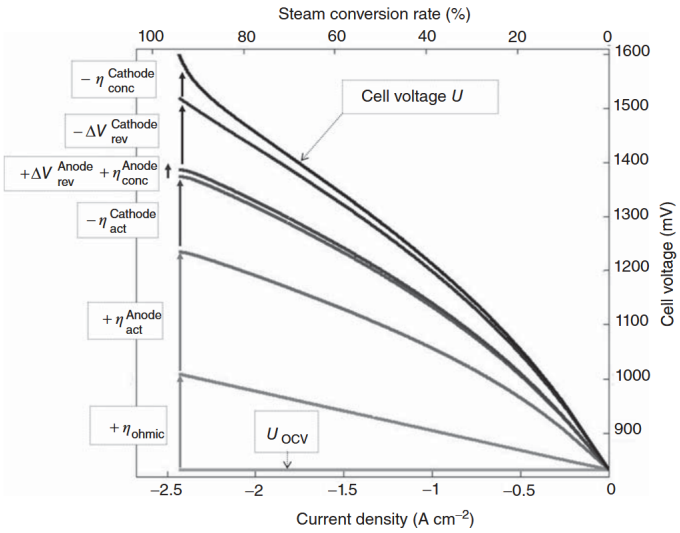

Figure A.4: Décomposition d'une courbe de polarisation typique. Courbe issue de [60].

d'hydrogène. η_{ohmic} correspond à la surtension ohmique, associée aux pertes résistives dans les différentes couches de la cellule; il regroupe notamment la résistance ionique de l'électrolyte R_{elec} ainsi que les résistances électroniques des deux électrodes, R_{an} et R_{cath}. Outre la contribution de tension réversible et surtension ohmique, le potentiel à l'électrode est influencé par plusieurs autre processus irréversibles qui s'y produisent. Ces irréversibilités modifient le potentiel par le biais des surtensions d'activation et de concentration, notées respectivement η_{act} et η_{conc}. Plus précisément, la surtension de concentration η_{conc} augmente à un taux de conversion de vapeur élevé en raison des limitations de transport de masse à travers l'électrode poreuse, tandis que la surtension d'activation η_{act} résulte de la cinétique intrinsèque de la réaction électrochimique.

À faible densité de courant, la polarisation de la cellule est principalement due à la surtension d'activation résultant du transfert de charge vers et depuis la surface de l'électrode, nécessaire aux réactions électrochimiques, car la barrière d'activation doit être franchie. Les surtensions de concentration deviennent significatives à forte densité de courant, car ces conditions de fonctionnement induisent des flux de gaz importants à travers les électrodes. Ainsi, à forte densité de courant, la polarisation de la cellule est principalement due à la surtension de concentration. Dans la plage de densité de courant intermédiaire, la contribution ohmique est généralement prédominante.

Le modèle selectionné et developé dans la thèse est général et s'applique aussi bien aux piles à combustible qu'aux électrolyseurs. En mode pile à combustible, un courant positif est utilisé, tandis qu'en mode électrolyseur, le courant est négatif afin de refléter la réaction électrochimique inverse.

Thèse accessible à l'adresse : https://theses.insa-lyon.fr/publication/2026ISAL0017/these.pdf © [Z. Yazbeck], [2026], INSA Lyon, tous droits réservés

A.3.5 Structure globale du modèle

Afin de mettre en évidence les interactions des trois sous-modèles - thermique, fluide (associé au bilan massique) et électrochimique - la figure A.5 présente l'architecture globale du modèle.

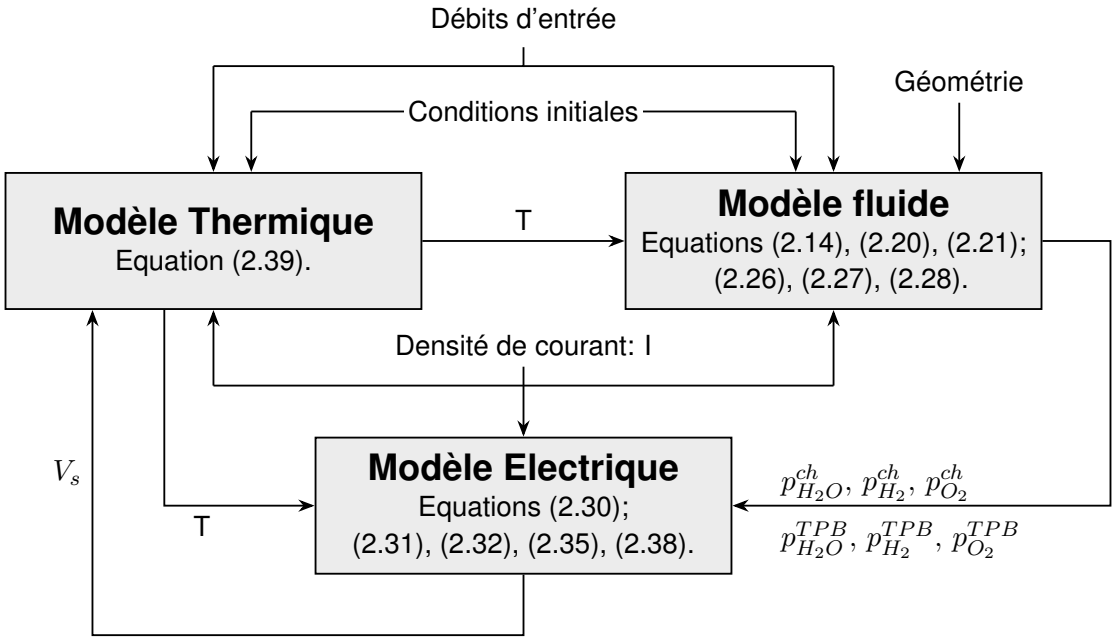

Figure A.5: Schéma de modélisation d'une pile d'électrolyse à oxyde solide (SOES).

A.3.6 Intégration temporelle

Les équations couplées thermo-fluidiques-électrochimiques forment un système raide d'équations ordinaires, différentielles et algébriques. L'intégration temporelle est donc réalisée à l'aide d'un schéma implicite, qui garantit une bonne stabilité numérique pour les transitoires électrochimiques rapides et permet l'utilisation de grands pas de temps compatibles avec les simulations de longs scénarios. Ce choix est également bien adapté aux applications de commande envisagées, à l'estimation d'état et à la conception optimale des entrées.

A.4 Estimation des paramètres

Les modèles SOEC basés sur la physique décrivent le transport de masse, la thermodynamique et les phénomènes électrochimiques, mais ils incluent des paramètres non directement mesurables qui doivent être identifiés à partir de données expérimentales. La principale difficulté pratique réside dans le fait que de nombreux paramètres peuvent être faiblement excités ou corrélés dans des conditions de fonctionnement standard, ce qui engendre des problèmes d'identification mal conditionnés et des estimations peu fiables.

Thèse accessible à l'adresse : https://theses.insa-lyon.fr/publication/2026ISAL0017/these.pdf © [Z. Yazbeck], [2026], INSA Lyon, tous droits réservés

A.4.1 Représentation d'état

Toutes les équations du modèle sont écrites sous la forme d'espace d'état non linéaire

$$\begin{aligned} \dot{x} &= f(x, \lambda, u), \\ Y &= h(x, \lambda, u), \end{aligned} \tag{A.4}$$

avec le vecteur d'état

$$x = \begin{bmatrix} p_{H_2}^{ch} & p_{H_2O}^{ch} & p_{O_2}^{ch} & T \end{bmatrix}^\top, \quad \text{avec } x \in R^{n_x} \tag{A.5}$$

le vecteur d'entré

$$u = [I \ \dot{n}_{fuel}^{in} \ \dot{n}_{air}^{in} \ y_{H_2O}^{in} \ T_{furnace} \ T_{fuel}^{in} \ T_{air}^{in}]^T \quad \text{avec } u \in R^{n_u} \tag{A.6}$$

et la sortie mesurée

$$Y = V_s(x, u, \lambda), \quad \text{avec } Y \in R^{n_Y} \tag{A.7}$$

L'objectif est d'estimer le vecteur de paramètres $\lambda \in R^{n_\lambda}$ à partir de la tension du stack mesurée et de la trajectoire d'entrée appliquée, avec

$$\lambda = \begin{bmatrix} R_s, & E_{act}^{ohm}, & E_{act}^{an}, & E_{act}^{cath}, & \gamma_{an}, & \gamma_{cath}, & \psi_{fuel}, & \psi_{air} \end{bmatrix}^\top. \tag{A.8}$$

A.4.2 Modèle d'espace d'état et fonctions de sensibilité

Les sensibilités locales sont calculées en augmentant le modèle avec des équations différentielles de sensibilité:

$$\dot{S}_x = \frac{\partial f}{\partial x} S_x + \frac{\partial f}{\partial \lambda}, \tag{A.9}$$

$$S_y = \frac{\partial h}{\partial x} S_x + \frac{\partial h}{\partial \lambda}, \tag{A.10}$$

where $S_x = \partial x / \partial \lambda$ and $S_y = \partial Y / \partial \lambda$. Sur une trajectoire échantillonnée, la matrice de sensibilité discrète est construite par concaténation :

$$S(\lambda) = \begin{bmatrix} S_y(t_1, \lambda) \\ \vdots \\ S_y(t_N, \lambda) \end{bmatrix} \in R^{N n_Y \times n_\lambda}. \tag{A.11}$$

avec $S_{y,t_k} = \dfrac{\partial Y}{\partial \lambda}(\lambda, t_k)$.

Thèse accessible à l'adresse : https://theses.insa-lyon.fr/publication/2026ISAL0017/these.pdf © [Z. Yazbeck], [2026], INSA Lyon, tous droits réservés

A.4.3 Méthode de Levenberg-Marquardt tronqué

Le problème d'estimation des paramètres est formulé comme un problème de moindres carrés non linéaires :

$$\min_{\lambda} \|\epsilon(\lambda)\|_2^2, \qquad \epsilon_k(\lambda) = V_s(\lambda, t_k) - V_s^{exp}(t_k). \tag{A.12}$$

où $V_s^{exp}(t_k)$ est la tension de pile mesurée au temps d'échantillonnage t_k.

Par définition on a $S(\lambda) = \dfrac{\partial \epsilon}{\partial \lambda}$. Pour résoudre le problème d'optimisation de l'équation (A.12), les méthodes de Gauss-Newton (GN) et de Levenberg-Marquardt (LM) sont envisagées et comparées :

$$\text{GN:} \quad \lambda_{k+1} = \lambda_k - \mu_k \left(S^\top S\right)^{-1} S^\top \epsilon, \tag{A.13}$$

$$\text{LM:} \quad \lambda_{k+1} = \lambda_k - \left(S^\top S + \beta_k I\right)^{-1} S^\top \epsilon. \tag{A.14}$$

où β_k et μ_k sont typiquement ajustés afin d'assurer une diminution de la fonction de coût, et $I \in R^{n_\lambda \times n_\lambda}$ est la matrice identité.

Pour améliorer la robustesse face au mauvais conditionnement et au bruit, une itération de Levenberg-Marquardt tronquée (TLM) est utilisée. À chaque itération, deux précautions sont prises :

1. Normalisation : la matrice de sensibilité est mise à l'échelle afin de rendre comparables des paramètres de différents ordres de grandeur,

$$S_{\text{nrm}} = S\,\Gamma, \tag{A.15}$$

où $\Gamma = \operatorname{diag}\left(\dfrac{|\lambda_k|}{\|y\|}\right)$ est une matrice diagonale de normalisation.

2. Troncature (SVD) : S_{nrm} est décomposée et seules les directions suffisamment riches en informations sont conservées :

$$S_{\text{nrm}} = U\,\Sigma\,V^\top, \qquad \mathcal{I} = \{i : \sigma_i \geq \sigma_{\text{thr}}\}, \tag{A.16}$$

$$S_{\text{nrm}}^{\text{trc}} = U_{(:,\mathcal{I})}\,\operatorname{diag}(\sigma_{\mathcal{I}})\,V_{(:,\mathcal{I})}^\top. \tag{A.17}$$

La mise à jour des algorithmes Truncated Levenberg-Marquardt (TLM) et Gauss-Newton tronquée (TGN) est donnée par :

$$\begin{aligned} \text{TLM:} \quad & \lambda_{k+1} = \lambda_k - \Gamma \left(\left(S_{nrm}^{trc}\right)^\top S_{nrm}^{trc} + \beta_k I\right)^{-1} \left(S_{nrm}^{trc}\right)^\top \epsilon, \\ \text{TGN:} \quad & \lambda_{k+1} = \lambda_k - \mu_k \Gamma \left(\left(S_{nrm}^{trc}\right)^\top S_{nrm}^{trc}\right)^{-1} \left(S_{nrm}^{trc}\right)^\top \epsilon, \end{aligned} \tag{A.18}$$

Thèse accessible à l'adresse : https://theses.insa-lyon.fr/publication/2026ISAL0017/these.pdf © [Z. Yazbeck], [2026], INSA Lyon, tous droits réservés

A.4.4 Estimation à partir de données simulées

La méthodologie est validée sur des jeux de données simulées générés avec des paramètres connus λ^*. Le tableau A.1 présente les estimations normalisées pour le cas sans bruit (N_0) et compare les méthodes TGN, LM, TLM et `fmincon`. Dans ce cas, en utilisant `fmincon`, une optimisation sous contraintes avec uniquement une contrainte de positivité ici, les estimations de ψ_{air} et ψ_{fuel} divergent vers des valeurs non physiques, et montrent la même tendance pour le cas sans bruit et le cas avec bruit. Les méthodes TLM et LM fournissent des estimations précises pour la plupart des paramètres: R_s, les énergies d'activation (E_{act}^{ohm}, E_{act}^{an}, E_{act}^{cath}) et ψ_{fuel} convergent vers λ^*, tandis que γ_{an}, γ_{cath} et ψ_{air} restent proches de leur estimation initiale, ce qui indique une identifiabilité pratique limitée pour ces paramètres sous l'excitation considérée. En revanche, le modèle TGN sous-estime fortement R_s et E_{act}^{cath} , que ce soit pour les sorties sans bruit ou pour les sorties mesurées bruitées par un bruit gaussien additif.

Le tableau A.2 présente les résultats correspondants lorsque la sortie est perturbée par un bruit gaussien additif (écart-type de 6%, cas N_1). En présence de bruit, TLM conserve des performances proches de celles obtenues sans bruit, maintenant R_s, E_{act}^{ohm}, E_{act}^{an}, E_{act}^{cath} et ψ_{fuel} proches de λ^*, et laissant γ_{an}, γ_{cath} et ψ_{air} proche de sa valeur initiale. LM devient plus sensible au bruit, avec une dégradation visible de R_s, E_{act}^{ohm} et surtout E_{act}^{an}, ainsi qu'un valeur plus importants sur γ_{cath}. Globalement, la comparaison entre les quatres méthodes montre que TLM fournit les estimations les plus robustes, LM est précis en l'absence de bruit mais moins performant lorsque du bruit est ajouté, TGN ne parvient pas à récupérer les paramètres clés dans les deux cas, et `fmincon` diverge dans les directions de faible sensibilité.

Table A.1: Estimation de la sortie sans bruit(N_0)

λ^*	$\frac{\lambda_0}{\lambda^*}$	$\frac{\hat{\lambda}_{fmincon}}{\lambda^*}$	$\frac{\hat{\lambda}_{TGN}}{\lambda^*}$	$\frac{\hat{\lambda}_{LM}}{\lambda^*}$	$\frac{\hat{\lambda}_{TLM}}{\lambda^*}$
R_s^*	0.7	1.28	**0.048**	0.95	1.08
E_{act}^{ohm*}	1.5	1.5	1.16	0.97	1.15
E_{act}^{an*}	1.4	1.06	1.16	1.02	0.96
E_{act}^{cath*}	0.75	0.74	**0.61**	1.03	1.04
${\gamma_{an}}^*$	1.25	1.27	1.2	1.25	1.26
${\gamma_{cath}}^*$	1.5	1.5	1.52	1.4	1.49
${\psi_{fuel}}^*$	1.2	**8.04e4**	**0.375**	0.94	1.19
${\psi_{air}}^*$	0.75	**8.03e5**	0.75	0.75	0.76

Thèse accessible à l'adresse : https://theses.insa-lyon.fr/publication/2026ISAL0017/these.pdf © [Z. Yazbeck], [2026], INSA Lyon, tous droits réservés

Table A.2: Estimation avec bruit de sortie (6%) (N_1)

λ^*	$\frac{\lambda_0}{\lambda^*}$	$\frac{\hat{\lambda}_{fmincon}}{\lambda^*}$	$\frac{\hat{\lambda}_{TGN}}{\lambda^*}$	$\frac{\hat{\lambda}_{LM}}{\lambda^*}$	$\frac{\hat{\lambda}_{TLM}}{\lambda^*}$
R_s^*	0.7	1.56	**0.01**	1.32	1.10
E_{act}^{ohm*}	1.5	1.5	1.14	0.87	1.16
E_{act}^{an*}	1.4	0.93	1.22	**0.33**	0.95
E_{act}^{cath*}	0.75	0.74	**0.61**	1.04	1.03
${\gamma_{an}}^*$	1.25	1.28	1.19	1.27	1.26
${\gamma_{cath}}^*$	1.5	1.50	1.51	1.82	1.49
${\psi_{fuel}}^*$	1.2	**1.09e5**	**0.018**	0.86	1.19
${\psi_{air}}^*$	0.75	**1.09e5**	0.74	0.75	0.75

A.4.5 Intervalle de confiance

En supposant un bruit de mesure blanc additif:

$$y_k^{measured} = y_k(\lambda) + e_k, \quad e_k \sim \mathcal{N}(0, C_y), \tag{A.19}$$

où C_y est la matrice de covariance du bruit de mesure e_k. La matrice d'informations de Fisher (FIM) peut être approximée par:

$$FIM(\hat{\lambda}) = S(\hat{\lambda})^\top C_y^{-1} S(\hat{\lambda}), \tag{A.20}$$

où S est la matrice de sensibilité définie dans l'équation (A.11). Au voisinage de l'optimum et sous l'hypothèse d'une linéarisation locale, la matrice de covariance des estimations peut être approximée par l'inverse de la matrice d'information de Fisher, conformément à la borne de Cramér–Rao [130] :

$$C_\lambda \approx FIM(\hat{\lambda})^{-1}. \tag{A.21}$$

En conséquence, l'erreur de paramètre standard est

$$\sigma_\lambda(\hat{\lambda}) = \sqrt{diag\left(FIM(\hat{\lambda})^{-1}\right)}, \tag{A.22}$$

et l'intervalle de confiance à 95% est approximativement égal à

$$\hat{\lambda} \pm t_{(1-0.05,\ N-n_\lambda)} \frac{\sigma_\lambda}{\sqrt{N}}. \tag{A.23}$$

où N est le nombre d'observations et t est la valeur critique supérieure pour la distribution t avec $N - n_\lambda$ degrés de liberté.

Thèse accessible à l'adresse : https://theses.insa-lyon.fr/publication/2026ISAL0017/these.pdf © [Z. Yazbeck], [2026], INSA Lyon, tous droits réservés

Cet intervalle de confiance est utilisé ici comme indicateur quantitatif de la robustesse des estimations plutôt que comme un véritable intervalle statistique. Les paramètres associés à des directions de faible sensibilité ont un effet négligeable sur le résultat, ce qui conduit à de grands intervalles de confiance, ils sont donc tronqués dans la matrice de sensibilité, ce qui les maintient proches de leurs valeurs nominales.

A.4.6 Estimation à partir de données experimentaux

Après avoir évalué l'approche à partir de données simulées, nous évaluons les quatre méthodes d'estimation sur des données expérimentales fournies par le CEA. Ces données ont été collectées d'un banc d'essai avec un stack de six cellules planaires à cathode supportée. La mesure utilisée est la tension du stack V_s, et le vecteur d'entrée u dans l'équation (A.6).

La trajectoire d'entrée expérimentale utilisée est présentée sur la figure A.6, montrant une excitation moindre pour le débit d'air $\dot{n}_{air}^{in}$ et la fraction molaire de vapeur d'eau $y_{H_2O}^{in}$, avec un temps d'échantillonnage de 2 secondes.

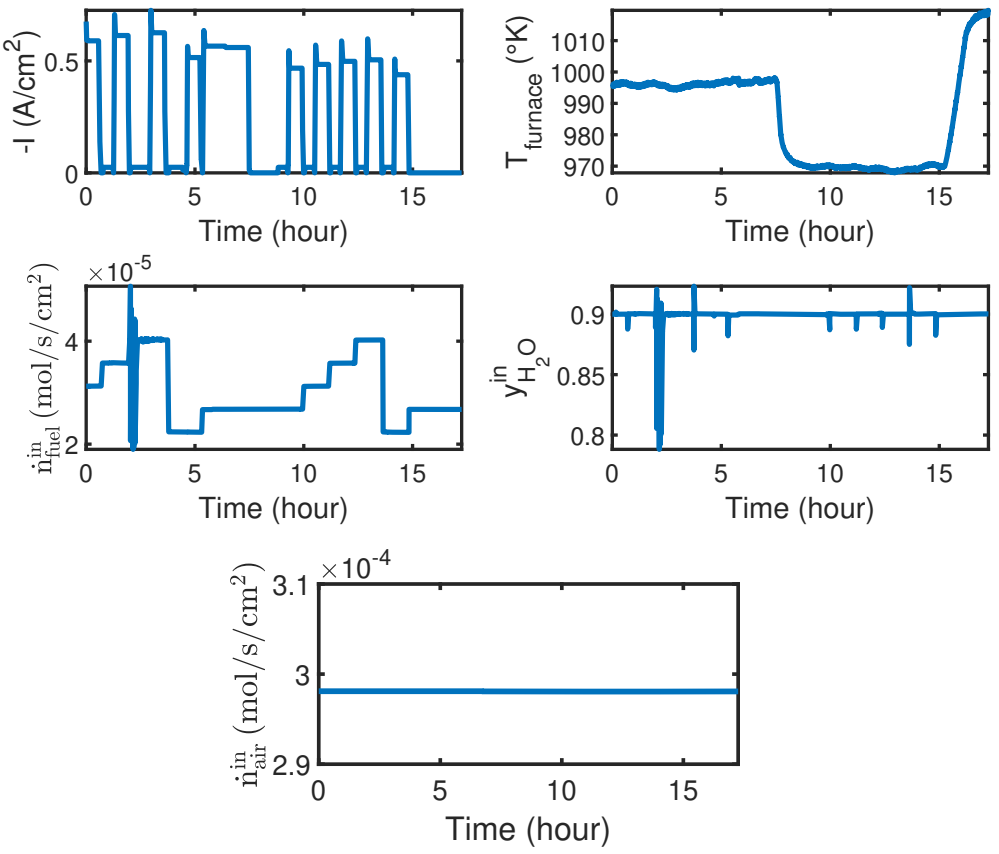

Figure A.6: Trajectoire d'entrée expérimentale.

Thèse accessible à l'adresse : https://theses.insa-lyon.fr/publication/2026ISAL0017/these.pdf © [Z. Yazbeck], [2026], INSA Lyon, tous droits réservés

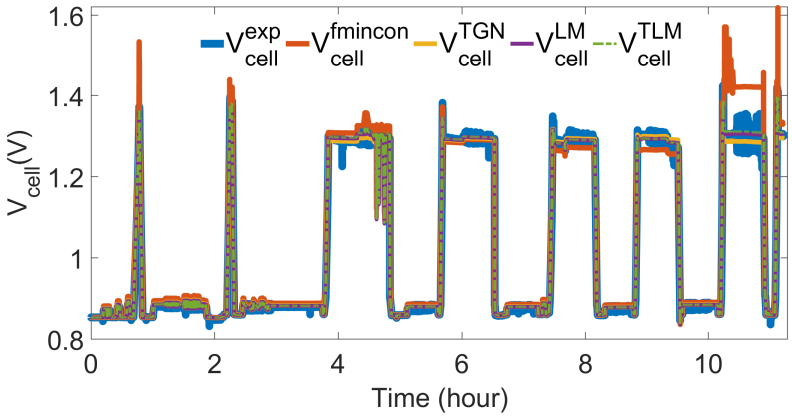

Figure A.7: Validation croisée sur des données expérimentales

Les estimations des paramètres obtenues avec les quatre méthodes sont résumées dans le tableau A.3. Celles obtenues avec LM et TLM concordent bien pour les paramètres les plus influents, et les deux méthodes fournissent des valeurs physiquement raisonnables pour R_s et les énergies d'activation, à l'exception de E_{act}^{an}, qui présente une estimation relativement faible avec LM. Cependant, plusieurs paramètres donnent des estimations non physiques avec `fmincon`, notamment R_s et ψ_{fuel}, et cette méthode conduit également à une valeur non physique de ψ_{air}. La méthode TGN donne également une valeur élevée de ψ_{fuel}. Du point de vue de l'ajustement des données de sortie, la méthode `fmincon` présente les performances les moins bonnes (RMSE = 0.0163), tandis que LM et TLM affichent les erreurs les plus faibles, avec des valeurs de RMSE similaires (0.0083). La méthode TGN présente une RMSE légèrement supérieure (0.0091). Les résultats de validation croisée dans la figure A.7 confirment que LM et TLM présentent le même degré de précision prédictive dans différentes fenêtres temporelles, tandis que `fmincon` et TGN offrent une généralisation moins performante. La méthode TLM maintient les paramètres γ_{an} et ψ_{air} proches de leurs valeurs nominales (ou initiales), ce qui indique un manque d'identifiabilité pratique pour ces directions. La sortie est peu sensible à ces directions au cours de l'expérience considérée. Ceci est également confirmé par l'estimation de l'intervalle de confiance rapportée dans la dernière colonne du tableau A.3, qui montre une grande incertitude pour γ_{an} et une moindre incertitude pour ψ_{air}.

A.4.7 Planification optimale d'expériences (OED)

Pour améliorer la pertinence des paramètres, un problème de planification optimale d'expériences basé sur un modèle est formulé à l'aide d'un critère d'optimalité D construit à partir de la matrice d'information discrète de Fisher. Le vecteur de conception (décision) est défini comme suit:

$$\varphi = (x(t_k),, u(t_k),, t_{sp},, \tau)\,, \qquad k \in 1, \ldots, N+1,$$

Thèse accessible à l'adresse : https://theses.insa-lyon.fr/publication/2026ISAL0017/these.pdf © [Z. Yazbeck], [2026], INSA Lyon, tous droits réservés

Table A.3: Estimation with experimental data

λ	λ_0	$\hat{\lambda}_{fmincon}$	$\hat{\lambda}_{TGN}$	$\hat{\lambda}_{LM}$	$\hat{\lambda}_{TLM}$	$\frac{C.I.}{\hat{\lambda}_{TLM}} \times 100$
R_s	0.154	0.063	0.38	0.35	0.34	1.01
E_{act}^{ohm}	$180e3$	$179e3$	$74.31e3$	$79.7e3$	$82.2e3$	0.96
E_{act}^{an}	$140e3$	$118.4e3$	$95.3e3$	$49.22e3$	$84.73e3$	38.34
E_{act}^{cath}	$75e3$	$74.76e3$	$128.11e3$	$108e3$	$95.9e3$	0.08
γ_{an}	$1.25e5$	$1.26e5$	$5.32e5$	$1.26e5$	$1.26e5$	426.45
γ_{cath}	$3.37e5$	$3.37e5$	$3.74e5$	$1.22e6$	$3.36e5$	1.05
ψ_{fuel}	0.21	0.051	1.6	4.03	0.2	0.15
ψ_{air}	0.15	$1.6e4$	0.157	0.21	0.15	151.35

où $x(t_k)$ est le vecteur d'état aux instants d'échantillonnage, $u(t_k)$ est le vecteur d'entrée, t_{sp} est le vecteur des temps d'échantillonnage associés à la paramétrisation par morceaux des entrées, et τ est la durée totale de l'expérience. Le vecteur de paramètres réel λ^* étant inconnu, les sensibilités sont évaluées au vecteur de paramètres nominal λ_0, ce qui conduit à une solution optimale locale. Le problème OED s'écrit alors:

$$\min_{\varphi} \ \log\det\left(\sum_{k=0}^{N} S_y(t_k,\lambda_0)^\top C_y^{-1} S_y(t_k,\lambda_0)\right)^{-1}. \tag{A.24}$$

où C_y est la matrice de covariance du bruit de mesure. Le problème est formulé à l'aide d'un modèle de tir multiple, où l'horizon est divisé en plusieurs segments et où les états $x(t_k)$ et les entrées $u(t_k)$ aux nœuds de tir sont considérés comme des variables de décision. Les entrées sont paramétrées comme constantes sur chaque segment, et la dynamique du système est assurée par des contraintes de continuité entre les segments consécutifs. La génération de la trajectoire d'entrée optimale est présentée à la Figure A.8.

A.4.8 Stratégies alternatives de planification expérimentale optimale

Outre la résolution du problème OED comme un programme non linéaire, deux stratégies alternatives sont également étudiées. Premièrement, une procédure OED séquentielle est envisagée, dans laquelle l'identification est organisée en une succession d'expériences courtes: à chaque itération, un problème OED est résolu à l'aide de l'estimation courante $\hat{\lambda}$, l'expérience est réalisée et les paramètres sont mis à jour avant la planification d'expériences suivante [126]. Deuxièmement, une planification basée sur une bibliothèque de fonction d'excitation est étudiée, où un ensemble fini de fonctions tests candidates admissibles (échelons, rampes, balayages de

Thèse accessible à l'adresse : https://theses.insa-lyon.fr/publication/2026ISAL0017/these.pdf © [Z. Yazbeck], [2026], INSA Lyon, tous droits réservés

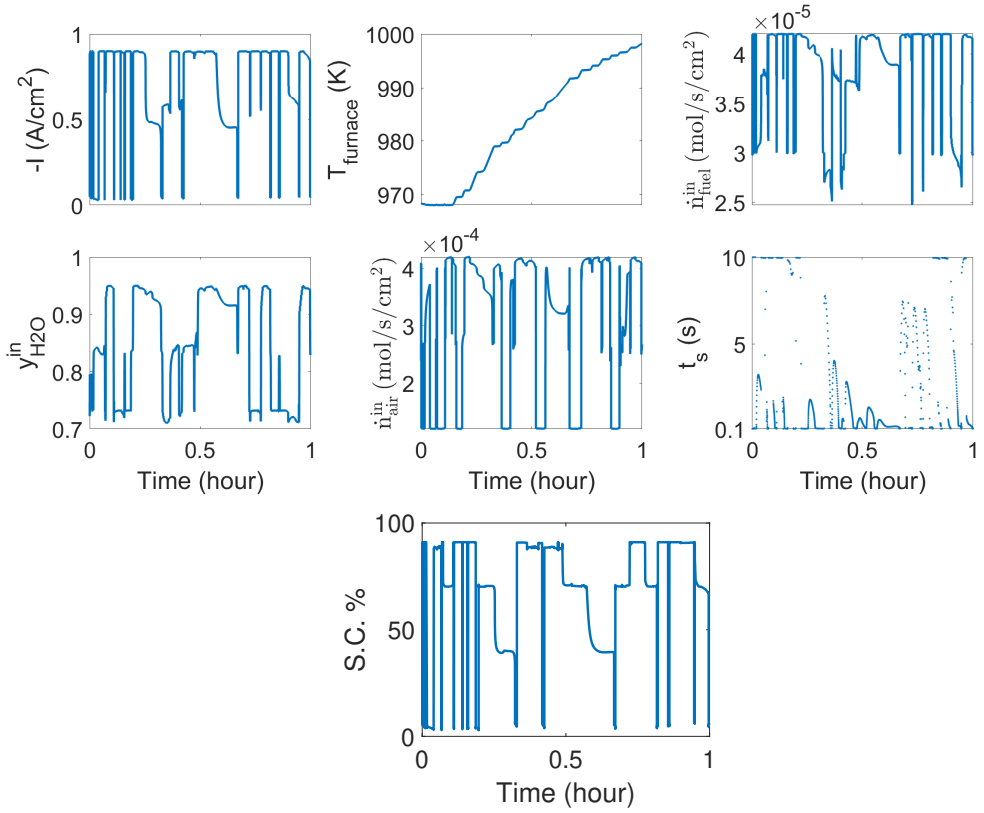

Figure A.8: Trajectoire d'entrée générée à partir de l'OED et conversion de vapeur correspondante.

Thèse accessible à l'adresse : https://theses.insa-lyon.fr/publication/2026ISAL0017/these.pdf © [Z. Yazbeck], [2026], INSA Lyon, tous droits réservés

fréquence, PRBS ou profils multisinusoïdaux) est généré. Les sensibilités sont évaluées pour chaque fonction test et un sous-ensemble de fonctions tests est sélectionné afin de maximiser le contenu informationnel de la trajectoire d'excitation combinée résultante, sous contraintes de durée totale et de nombre de tests [123].

A.5 Détection des défauts

La méthodologie proposée traite spécifiquement des défauts liés à la sous-alimentation dans les électrolyseurs à oxyde solide fonctionnant en mode électrolyse. Deux scénarios de défauts sont considérés: "steam starvation" (manque de vapeur), obtenu en réduisant le débit global de combustible, ce qui diminue les débits d'entrée d'hydrogène et de vapeur tout en maintenant les mêmes fractions molaires, et "hydrogen starvation" (manque d'hydrogène), induit par l'arrêt du débit d'hydrogène, ce qui entraîne une fraction molaire d'hydrogène nulle. Ces défauts affectent directement les pressions partielles internes des gaz (qui apparaissent dans le vecteur d'état de la formulation d'espace d'état du système) et donc les sorties mesurées. Par conséquent, la sous-alimentation (starvation) constitue une condition de fonctionnement critique qui doit être détectée précocement afin d'éviter ou de réduire une dégradation irréversible du système.

À cette fin, un observateur non linéaire basé sur un filtre de Kalman sans parfum à racine carrée (square-root unscentend kalman filter: SR-UKF) est utilisé. En s'appuyant sur un ensemble de mesures standard, le SR-UKF reconstruit les pressions partielles d'hydrogène, de vapeur et d'oxygène, ainsi que la température de l'empilement, et compense les écarts entre le valeur réel et le valeur de consigne nominal des débits de combustible d'entrée en augmentant le vecteur d'état. Comparé au filtre de Kalman classique (UKF), le SR-UKF améliore la stabilité numérique en évitant une décomposition de Cholesky à chaque itération. Il propage les facteurs de racine carrée à travers l'itération de Kalman et utilise une transformation orthogonale pour calculer les matrices de covariance [165]. L'UKF/SR-UKF utilise un ensemble de points d'échantillonnage pondérés (points sigma) choisis de manière déterministe pour traiter les non-linéarités du modèle [165].

Schéma de détection des défauts et modèle d'observateur

Le modèle mathématique SOEC formulé dans l'espace d'état de l'équation (A.4) est considéré, mais outre la tension de l'empilement, la température est également mesurée. Ainsi, la sortie mesurée considérée est $y = [V_s \ T]^T$ sous le vecteur d'entrée nominal u^{nom} comme dans l'équation (A.6). De plus, la mesure du débit molaire d'hydrogène en sortie $\dot{n}_{H_2}^{out}$, disponible sur le banc d'essai etudié, est ajoutée à la sortie mesurée afin de permettre la compensation via l'état $\epsilon_1/2$.

Pour traiter spécifiquement le problème de starvation, directement lié au débit réel de combustible alimentant l'empilement, deux variables d'état supplémentaires, ϵ_1 et ϵ_2, sont introduites

Thèse accessible à l'adresse : https://theses.insa-lyon.fr/publication/2026ISAL0017/these.pdf © [Z. Yazbeck], [2026], INSA Lyon, tous droits réservés

dans le vecteur d'état de l'observateur. Ces variables représentent respectivement l'écart des débits réels de vapeur et d'hydrogène à l'entrée par rapport à leur valeur de consigne nominale.

$$\begin{aligned} \dot{n}_{H_2O}^{in,real} &= \dot{n}_{H_2O}^{in,nom} \cdot (1 - \epsilon_1) \\ \dot{n}_{H_2}^{in,real} &= \dot{n}_{H_2}^{in,nom} \cdot (1 - \epsilon_2) \end{aligned} \tag{A.25}$$

Ainsi, le nouveau vecteur d'état est: $x = [p_{H_2}^{ch}\ p_{H_2O}^{ch}\ p_{O_2}^{ch}\ T\ \epsilon_1\ \epsilon_2]^T$, la sortie est $y = [V_s\ T\ \dot{n}_{H_2}^{out}]^T$, et le vecteur d'entrée u est défini par l'équation (A.6). Les états de référence sont calculés à l'aide du modèle SOEC dans des conditions de fonctionnement nominales, et le vecteur d'état estimé est comparé à cette référence pour la détection des défauts, comme illustré dans la figure A.9.

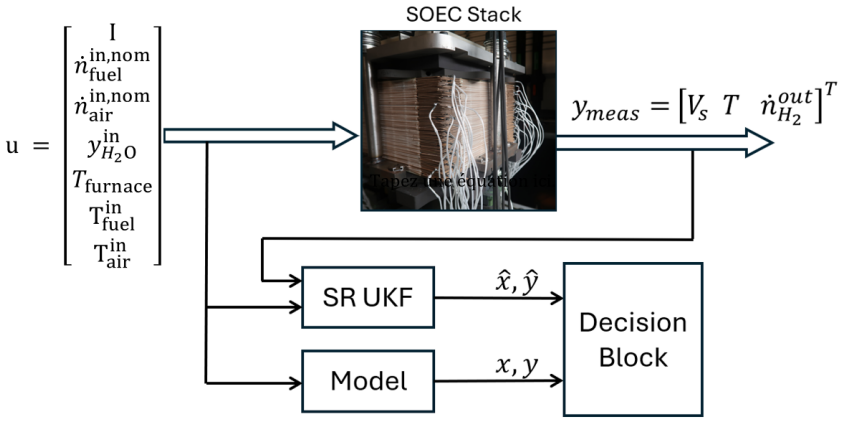

Figure A.9: Schéma de détection de la famine.

Seuil adaptatif

La détection de défauts dans les systèmes électrochimiques nécessite un seuillage dynamique pour distinguer les variations normales des comportements anormaux tout en limitant les fausses alarmes. Pour ce faire, un seuil adaptatif calculé à l'aide d'un filtre à fenêtre glissante est utilisé. Le vecteur d'état nominal filtré dans une fenêtre glissante de taille m (fixée à 120 échantillons) est:

$$\bar{x}_k = \frac{1}{m} \sum_{i=k-m+1}^{k} x_{nom_i}, \tag{A.26}$$

et la variance correspondante est:

$$\sigma_k^2 = \frac{1}{m-1} \sum_{i=k-m+1}^{k} (x_{nom_i} - \bar{x}_k)^2. \tag{A.27}$$

Dans cette étude, pour tenir compte des perturbations du bruit, les bornes adaptatives sont:

$$Th_k = \bar{x}_k \pm 3\sigma_k. \tag{A.28}$$

Thèse accessible à l'adresse : https://theses.insa-lyon.fr/publication/2026ISAL0017/these.pdf © [Z. Yazbeck], [2026], INSA Lyon, tous droits réservés

Une panne est détectée lorsque l'état estimé $\hat{x}(t)$ s'écarte de l'état nominal $x_{nom}(t)$ au-delà du seuil adaptatif.

Scénario expérimental de starvation de vapeur

Pour reproduire expérimentalement un défaut de starvation de vapeur, le débit total de combustible à l'entrée, $\dot{n}^{in}_{fuel}$, a été progressivement réduit par rapport à sa valeur nominale, $\dot{n}^{in,nom}_{fuel}$.

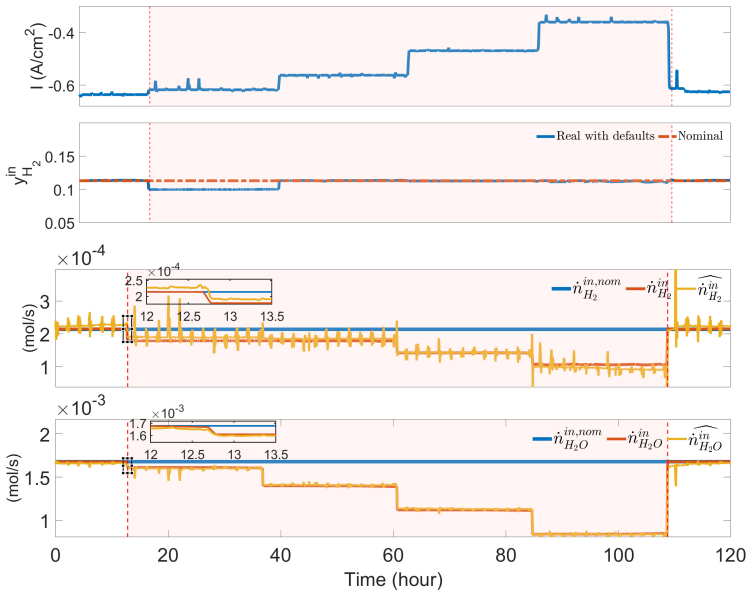

Figure A.10: Les conditions de fonctionnement, illustrées par les débits totaux d'entrée estimés et nominaux lors du scénario de starvation de vapeur, sont comparées. Les zones colorées indiquent les intervalles de temps durant lesquels le défaut est injecté.

Le combustible était principalement composé de vapeur d'eau et d'une faible proportion d'hydrogène. Les deux débits ont été diminués simultanément tout en maintenant une fraction molaire approximativement constante, comme illustré sur la figure A.10. Simultanément, le courant a été ajusté pour maintenir la tension thermoneutre [168]. Dans ces conditions, SR-UKF reconstruit les débits de combustible à l'entrée et les pressions partielles internes comme montré dans les figures A.10 A.11. Le défaut de starvation est détecté lorsque les pressions partielles reconstruites dépassent leurs seuils d'adaptation.

Thèse accessible à l'adresse : https://theses.insa-lyon.fr/publication/2026ISAL0017/these.pdf © [Z. Yazbeck], [2026], INSA Lyon, tous droits réservés

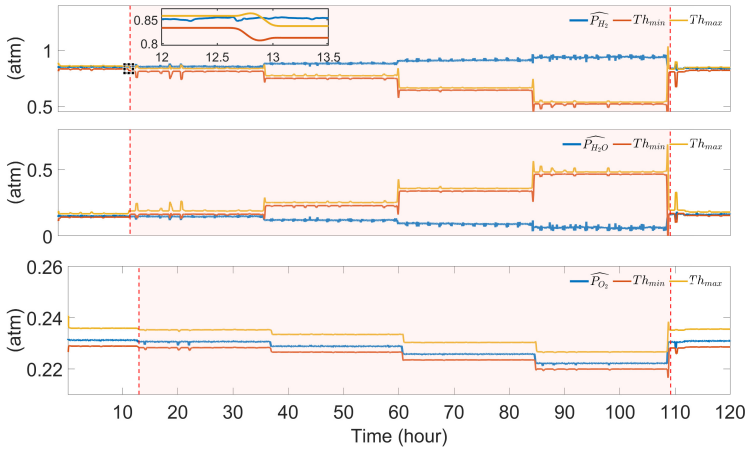

Figure A.11: Estimation des états dans un scénario de starvation de vapeur et seuils de détection des défauts ($Th_{min/max}$) pour chaque variable.

Surveillance tenant compte du vieillissement: Aging-aware monitoring

Le comportement électrochimique et thermique des SOEC évolue au fil du temps en raison de mécanismes de dégradation agissant sur des échelles de temps lentes. Cette lente dérive affecte des propriétés clés telles que la microstructure des électrodes et la résistance de contact. Si cette évolution est négligée, le modèle perd progressivement en précision, ce qui conduit à une estimation d'état, une détection de défauts et une évaluation de santé peu fiables. Par conséquent, les paramètres du modèle ne peuvent être considérés comme constants sur de longues périodes de fonctionnement.

Pour de longues périodes de fonctionnement, l'hypothèse d'un vecteur de paramètres constant n'est plus valable. Une lente dérive des paramètres électrochimiques clés est attendue, tels que les densités de courant d'échange, les résistances ohmiques ou les propriétés de transport effectives, qui affectent directement la réponse en tension et la température de la pile [169]. Cependant, pour le SR-UKF, tout écart entre le modèle et les sorties mesurées sera expliqué par des changements dans les états internes. En l'absence d'une représentation dédiée au vieillissement, cette dérive risque d'être interprétée comme un défaut, ce qui peut dégrader les performances d'isolation des défauts tout en augmentant le risque de fausses alarmes.

Approche proposée

Dans cette thèse, nous proposons une approche de surveillance prenant en compte le vieillissement, combinant le cadre SR-UKF avec une stratégie d'estimation de paramètres planifiée et déclenchée. Les états rapides, régis par les équations dynamiques, sont estimés à l'aide du SR-UKF, tandis que le modèle sous-jacent est mis à jour par les paramètres d'état de santé (λ_{SoH}) variables. En parallèle, ces paramètres, variant lentement, sont mis à jour de manière intermittente grâce à l'approche d'estimation de paramètres. Le schéma de surveillance proposé,

Thèse accessible à l'adresse : https://theses.insa-lyon.fr/publication/2026ISAL0017/these.pdf © [Z. Yazbeck], [2026], INSA Lyon, tous droits réservés

prenant en compte le vieillissement, est illustré dans la figure A.12.

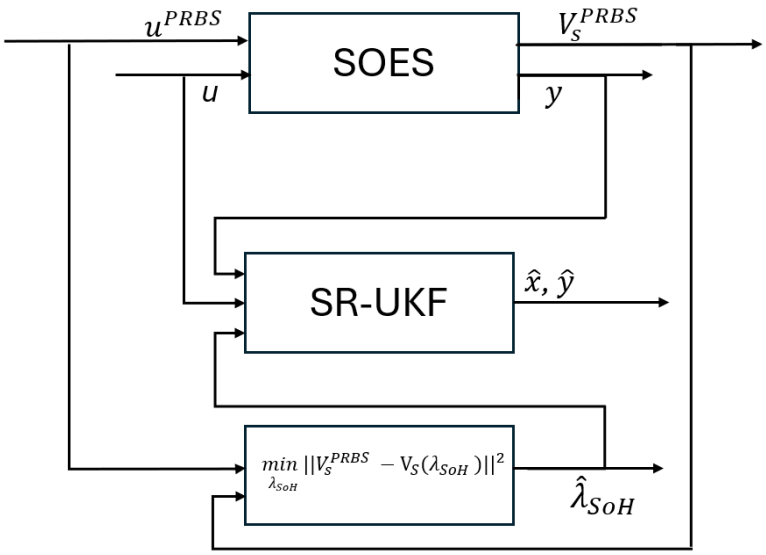

Figure A.12: Aging-aware monitoring approach scheme

Cette approche est essentielle non seulement pour éviter que les écarts induits par des défauts ne soient interprétés à tort comme des paramètres de vieillissement, mais aussi pour renforcer la robustesse de l'estimation de la dynamique des états rapides face au vieillissement, en limitant le risque que les effets de la dégradation lente soient compensés par les états dynamiques rapides. De ce fait, cette approche préserve l'interprétabilité des indicateurs de défauts et des indicateurs de santé.

A.5.1 Application aux données expérimentales

Dans l'ensemble de données expérimentales utilisé dans ce chapitre, des excitations de densité de courant PRBS avec différentes fréquences ont été appliquées de manière répétée chaque 2 heures sur une durée totale de test de 650 heures. Seule la réponse en tension a été enregistrée avec une résolution temporelle beaucoup plus fine que la période d'échantillonnage de la surveillance, permettant ainsi l'extraction d'informations supplémentaires pour l'estimation des paramètres de l'état de santé (SoH).

A.5.2 Résultats

L'évolution de l'état de santé (SoH) estimé sur l'ensemble des 650 heures de données est présentée dans la figure A.13. Les tendances observées sont cohérentes avec la dégradation à long terme attendue et rapportée dans la littérature [65, 66]. Une variation plus rapide est constatée au début de la période d'observation, après quoi les paramètres se stabilisent et suivent une tendance à long terme plus marquée.

Thèse accessible à l'adresse : https://theses.insa-lyon.fr/publication/2026ISAL0017/these.pdf © [Z. Yazbeck], [2026], INSA Lyon, tous droits réservés

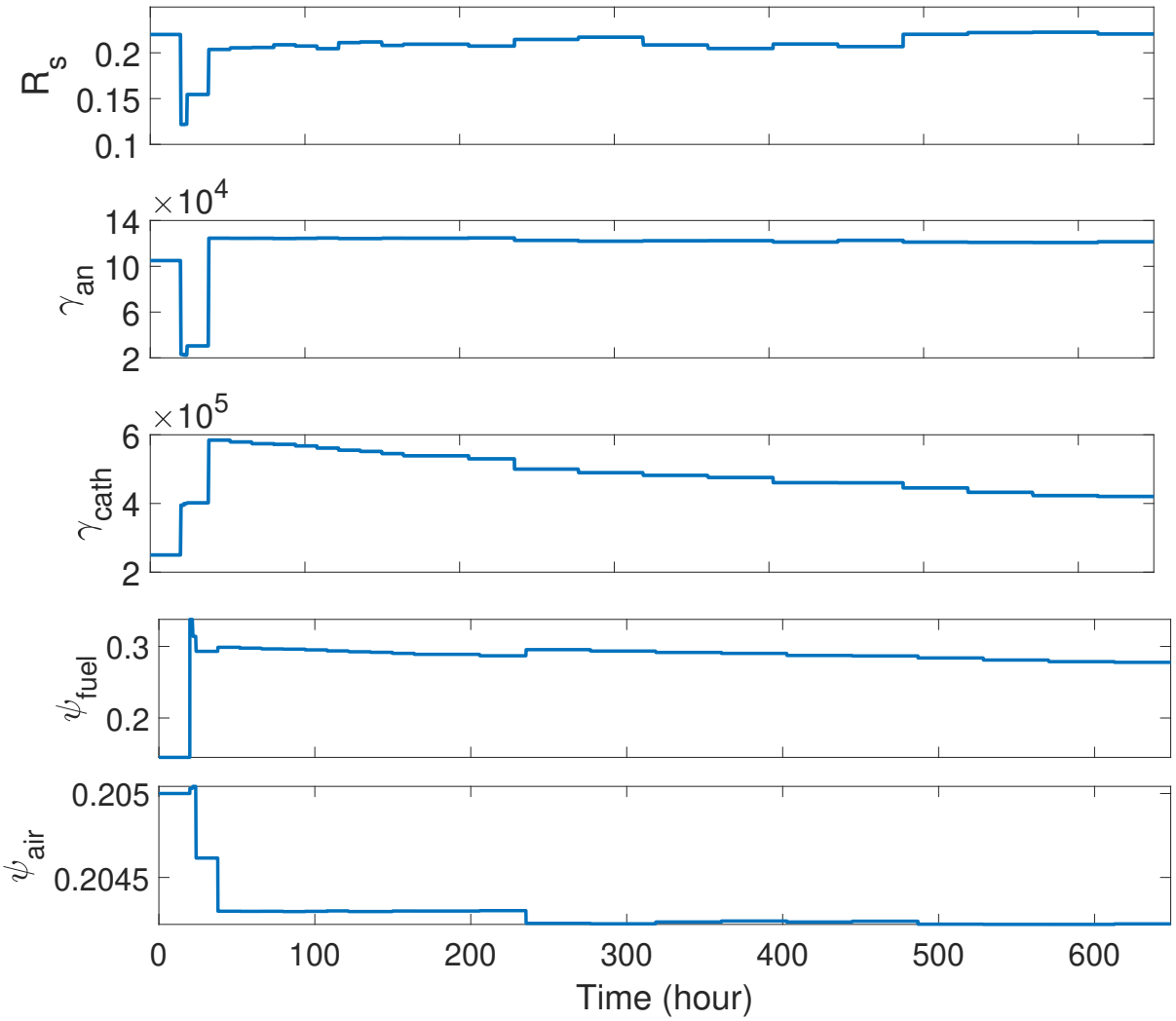

Figure A.13: Estimation de l'état de santé (SoH) pour l'ensemble des données de mesure.

La résistance ohmique R_s, représentant les contributions dues aux pertes de contact, à la dégradation de l'électrolyte et à l'interconnexion, varie très légèrement. Le facteur pré-exponentiel du courant d'échange anodique γ_{an} reste plus ou moins stabilisé sur toute la plage de fonctionnement, tandis que γ_{cath} diminue progressivement, ce qui est cohérent avec une perte progressive de cinétique apparente due au vieillissement de l'électrode à hydrogène [37, 66]. Le paramètre de microstructure ψ_{fuel} diminue très lentement avec le temps, entraînant une réduction du coefficient de diffusion effectif à l'électrode à hydrogène. Par conséquent, les limitations de transport de masse augmentent avec le temps, ce qui est conforme à la littérature [66]. En revanche, ψ_{air} ne présente qu'une diminution négligeable sur toute la durée du test.

La durée du test est insuffisante pour observer une dégradation irréversible significative, qui se développe généralement sur des échelles de temps de l'ordre de 1000 heures [65, 169, 171]. Par conséquent, la tension et la température mesurée est peu affectée par le vieillissement, et l'impact sur l'estimation de la dynamique rapide reste limité. Cependant, l'excitation PRBS de

Thèse accessible à l'adresse : https://theses.insa-lyon.fr/publication/2026ISAL0017/these.pdf © [Z. Yazbeck], [2026], INSA Lyon, tous droits réservés

la densité de courant sur une large bande de fréquences accroît la richesse des informations fournies par les mesures.

A.6 Conclusion et perspectives

Dans cette thèse, le problème du développement d'une approche de gestion de l'état de santé d'empilements (stacks) de cellules d'électrolyse à oxyde solide (SOEC) à partir d'un modèle dynamique a été abordé. L'accent a été mis sur l'estimation des paramètres et la détection de défauts, plus spécifiquement pour les défauts de manquement de vapeur et d'hydrogène (steam starvation et hydrogène starvation), qui peuvent entraîner des dommages irréversibles s'ils ne sont pas détectés et atténués à temps. Dans ce contexte, une difficulté centrale réside dans le fort couplage entre les différents sous-modèles de l'empilement : l'électrochimie, le transport de masse et la dynamique thermique, combiné au fait que les quantités les plus informatives pour le diagnostic, comme les pressions partielles internes des réactifs, ne sont pas directement mesurables. De plus, le modèle doit être compatible avec une application en temps réel et prendre en compte le vieillissement du système au fil du temps. Ce constat motive le développement d'un cadre où le modèle est utilisé pour l'estimation d'état et pour la mise à jour continue des paramètres affectés par le vieillissement du système. Dans le Chapitre 2, nous avons présenté la technologie SOEC ainsi que sa modélisation à différents niveaux. Au-delà du tour d'horizon sur les principes physiques et les différents modèles existants, ce chapitre est essentiel car il détaille la construction d'un modèle orienté commande pour la surveillance, qui doit trouver un équilibre entre un choix judicieux de variables internes physiquement significatives et une tractabilité suffisante pour être intégré dans des algorithmes d'estimation et de détection de défauts, tout en restant assez rapide pour une implémentation en temps réel. L'estimation des paramètres et l'identifiabilité pour le calibrage du modèle, une condition préalable clé pour toute stratégie de surveillance basée sur un modèle, sont développées dans le Chapitre 3. L'identifiabilité pratique est évaluée à l'aide des équations différentielles de sensibilité basées sur la formulation dans l'espace d'état d'un modèle non linéaire. L'analyse a montré que, dans les conditions de fonctionnement et de mesure considérées, tous les paramètres ne peuvent pas être déduits de manière fiable à partir des données. En particulier, certains groupes de paramètres (y compris les paramètres liés à la microstructure et les préfacteurs des densités de courant d'échange) étaient mal identifiés par l'excitation choisie, présentant une sensibilité négligeable sur la sortie ou une forte dépendance linéaire, tandis que d'autres paramètres pouvaient être estimés avec une bonne précision. Pour remédier aux problèmes de mauvais conditionnement et de colinéarité dans l'estimation, une troncature de la matrice de sensibilité a été proposée sur la base de la décomposition SVD du matrice de sensibilité normalisée, couplée à une optimisation basée sur le gradient (Gauss-Newton et Levenberg-Marquardt) avec des vérifications de robustesse contre le bruit et la dispersion des hypothèses initiales. Cependant, l'identifiabilité des paramètres

Thèse accessible à l'adresse : https://theses.insa-lyon.fr/publication/2026ISAL0017/these.pdf © [Z. Yazbeck], [2026], INSA Lyon, tous droits réservés

est affectée par les données expérimentales utilisées, comme le démontrent les simulations de Monte-Carlo sur 50 scénarios différents. Pour cette raison, le Chapitre 3 examine également la planification expérimentale optimale (OED) pour générer des entrées persistantes, et propose différentes approches : une formulation OED basée sur la programmation non linéaire (NLP), une OED séquentielle en raison de la propriété locale des sensibilités, et une bibliothèque de fonctions prédéfinies. Les résultats ont montré une amélioration de la qualité des estimations pour les différentes approches. Après le calibrage du modèle, le problème de la surveillance en ligne et du diagnostic de défauts est abordé dans le Chapitre 4. Un filtre de Kalman Unscented à racine carrée (SR-UKF), qui est une version numériquement plus stable du filtre de Kalman Unscented (UKF) basé sur des points sigma, est conçu pour reconstruire les pressions partielles internes des réactifs, la température de l'empilement et l'écart par rapport à la consigne des débits de vapeur et d'hydrogène, ajoutés en tant qu'états. Ces informations sont reconstruites uniquement à partir des mesures de température, de tension et de débit d'hydrogène en sortie. L'estimation d'état est combinée à des seuils adaptatifs dérivés des états nominaux et appliqués aux pressions partielles estimées afin de détecter les privations côté alimentation et de discriminer la privation de vapeur de celle d'hydrogène en mode électrolyse. De plus, la résistance totale peut également être utilisée comme discriminant entre la privation de vapeur et celle d'hydrogène, lorsque la mesure du débit d'hydrogène en sortie n'est pas disponible et que les deux états supplémentaires liés à l'écart des débits ne peuvent pas être considérés. Une variation significative de la résistance totale indique une privation de vapeur, tandis qu'une variation négligeable se produit dans le cas d'une privation d'hydrogène. Les travaux du Chapitre 4 s'intéressent aussi à la combinaison entre une dynamique d'observateur rapide avec un mécanisme de mise à jour lente des paramètres. La méthode proposée adapte le cadre d'estimation du Chapitre 3 pour suivre les indicateurs de santé et les paramètres liés à la dégradation en ligne. Cette intégration est une étape cruciale vers un cadre PHM (Prognostics and Health Management) opérationnel, permettant une estimation d'état robuste et ouvrant une voie possible pour travailler sur le pronostic de l'empilement. Une validation de la méthodologie avec 650 heures de données expérimentales et une excitation de densité de courant PRBS montre une variation des estimations de l'état de santé (SoH) dans la bonne direction et un meilleur ajustement de la sortie du modèle.

Les principales contributions de cette thèse peuvent être résumées comme suit. Tout d'abord, une méthodologie complète d'estimation paramétrique a été développée pour un modèle électrochimique orienté commande. La technique proposée repose sur la combinaison de l'analyse de sensibilité avec l'estimation des paramètres, en tronquant les directions de sensibilité faibles et linéairement dépendantes à l'aide d'une décomposition SVD. Cette méthode offre à la fois une stabilité numérique, en limitant le conditionnement de la matrice de sensibilité, et une interprétabilité en termes de richesse d'informations sur les paramètres. Ensuite, trois stratégies de planification expérimentale optimale ont été formulées pour améliorer l'identifiabilité pratique sous contraintes physiques, y compris une alternative basée sur une bibliothèque moins coûteuse en

Thèse accessible à l'adresse : https://theses.insa-lyon.fr/publication/2026ISAL0017/these.pdf © [Z. Yazbeck], [2026], INSA Lyon, tous droits réservés

calcul, améliorant ainsi la faisabilité des campagnes de tests. Troisièmement, une approche de surveillance et de diagnostic basée sur le SR-UKF a été proposée et validée à l'aide de données expérimentales, capable de reconstruire les variables internes et de détecter les défauts de privation avec un mécanisme explicite de discrimination entre la privation de vapeur et celle d'hydrogène basé sur le comportement de la résistance. Enfin, l'architecture globale a été intégrée pour fournir une approche PHM plus pratique et robuste, où les dynamiques à variation rapide sont mises à jour à l'aide du SR-UKF, avec la mise à jour des paramètres qui varient lentement dans le temps en raison du vieillissement.

Plusieurs défis subsistent naturellement à la suite de ces travaux et définissent des perspectives claires. Un premier défi concerne les limites de la structure simplifiée du modèle orienté commande. Bien qu'il ait été conçu pour rester efficace en terme de temps de calculs, sa nature d'ordre réduit limite les détails qui peuvent être représentés. Des travaux futurs pourraient améliorer le modèle tout en préservant sa capacité de simulation en temps réel en incorporant des équations supplémentaires de bilan thermique et une description plus détaillée des échanges de chaleur au sein de l'empilement et du système de régulation. De plus, l'exploration d'extensions de la dimension du modèle pour capturer davantage d'informations spatiales pourrait améliorer la description des gradients internes. De tels développements amélioreraient la précision du modèle et élargiraient son applicabilité pour la surveillance et le diagnostic. En parallèle, l'exploration d'approches bayésiennes pour l'estimation des paramètres et la planification optimale d'expériences pourrait être précieuse, car elles offrent un cadre pour intégrer des connaissances a priori et quantifier l'incertitude, et peuvent formuler des objectifs OED en termes de gain d'information attendu plutôt qu'en s'appuyant uniquement sur des métriques d'identifiabilité locales. Un deuxième défi est la généralisation de l'algorithme de diagnostic afin qu'il ne soit pas limité aux défauts de privation de l'alimentation uniquement. En fonctionnement réel, la privation peut coexister avec d'autres anomalies, et un cadre PHM fiable doit gérer explicitement les interactions entre défauts et l'incertitude. Ainsi, des sources d'information supplémentaires peuvent être intégrées, comme la spectroscopie d'impédance électrochimique (EIS). En effet, les mesures EIS, combinées à une expertise dans l'attribution des caractéristiques d'impédance à différentes gammes de fréquences, peuvent soutenir la classification et la caractérisation de différentes anomalies et défauts. Dans ce cadre plus large, le SR-UKF développé dans cette thèse peut servir de module dédié pour quantifier le défaut une fois que la privation de l'alimentation est identifiée comme la cause initiale. De plus, l'extension de l'observateur d'une représentation du comportement moyen de l'empilement à une supervision du pire cas en utilisant des mesures segmentées pourrait être intéressante. En pratique, un grand empilement est généralement instrumenté pour mesurer la tension correspondant à des groupes de cellules. Ainsi, plutôt que d'estimer uniquement le comportement moyen, des travaux futurs pourraient exploiter ces mesures au niveau des groupes pour concevoir un observateur qui suit explicitement le groupe le plus limitant et met à jour le diagnostic en fonction de cet indicateur du pire cas. Cela rendrait la stratégie de surveillance plus conservative et mieux alignée avec le risque de dégrada-

Thèse accessible à l'adresse : https://theses.insa-lyon.fr/publication/2026ISAL0017/these.pdf © [Z. Yazbeck], [2026], INSA Lyon, tous droits réservés

tion, puisque les dommages irréversibles sont généralement initiés localement et peuvent rester cachés dans les signaux au niveau de l'empilement. Un quatrième défi concerne le lien avec la prognostic. Bien que cette thèse cible des applications orientées vers la durée de vie utile résiduelle (RUL), une direction alternative pourrait être d'explorer des approches hybrides combinant le modèle basé sur la physique proposé avec des modèles basés sur les données. De tels modèles hybrides pourraient combiner les variables internes reconstruites et les paramètres de l'état de santé estimés comme caractéristiques informatives, tout en apprenant directement les dynamiques résiduelles de dégradation à partir des données opérationnelles, améliorant potentiellement la prédiction à long terme et la robustesse dans des conditions variables, et nécessitant moins de données par rapport aux modèles purement basés sur les données.

Thèse accessible à l'adresse : https://theses.insa-lyon.fr/publication/2026ISAL0017/these.pdf © [Z. Yazbeck], [2026], INSA Lyon, tous droits réservés

FOLIO ADMINISTRATIF

THESE DE L'INSA LYON, MEMBRE DE L'UNIVERSITE DE LYON

NOM : **Yazbeck** DATE de SOUTENANCE : **19/03/2026**

Prénoms : **Zaman**

TITRE : **Production efficace et rentable d'hydrogène pour la décarbonation : Modélisation, mise en œuvre et validation de solutions de pronostic et de gestion de l'état de santé pour l'électrolyse à oxyde solide**

NATURE : **Doctorat** Numéro d'ordre : **2026ISAL0017**

École Doctorale : **Électronique, Électrotechnique et Automatique (ED 160)**

Spécialité : **Automatique**

RÉSUMÉ :

Les cellules d'électrolyse à oxyde solide (SOEC) offrent une production d'hydrogène à haut rendement et faible empreinte carbone, mais leur déploiement industriel reste limité par la complexité multi-physique, les enjeux de durabilité et la difficulté d'observer les états internes avec peu de capteurs. Cette thèse propose un cadre méthodologique de PHM basé sur la modélisation, combinant modélisation dynamique, identification de paramètres, planification optimale d'expériences et diagnostic de défauts.

Un modèle global (à paramètres localisés) 0D d'un empilement de cellules ("stack") est développé, couplant électrochimie, bilans de masse gazeuse et une description thermique réduite cohérente avec les mesures. L'identifiabilité pratique est évaluée via des équations de sensibilité et la matrice d'information de Fisher. Des algorithmes Levenberg-Marquardt tronqué et Gauss-Newton sont ensuite utilisés pour identifier les paramètres, en s'appuyant sur la SVD d'une matrice de sensibilité normalisée pour sélectionner les directions les plus identifiables et estimer les intervalles de confiance. La méthode est validée sur des données simulées puis expérimentales.

À partir de ce modèle identifié, un filtre de Kalman non linéaire de type « square-root Unscented Kalman Filter » est conçu pour reconstruire les pressions partielles internes des gaz, la température du stack et les écarts de débit d'alimentation en combustible à partir d'un nombre limité de mesures (tension de stack, température de sortie de l'air et débit de sortie d'hydrogène). Des seuils adaptatifs, sont ensuite utilisés pour détecter et distinguer la raréfaction de vapeur et d'hydrogène au niveau du stack, avec validation sur des données experimentales de SOEC. Enfin, les dynamiques rapides liées sont mises en regard des dynamiques lentes associées au vieillissement afin d'analyser leur interaction et de préparer un cadre unifié de diagnostic en conditions de dégradation.

Dans l'ensemble, cette thèse propose une méthodologie cohérente orientée PHM, améliorant la fiabilité, la sécurité et la capacité de diagnostic d'électrolyseurs SOEC pour la production industrielle d'hydrogène à haute température.

MOTS-CLÉS : **Solid oxide electrolyzer (SOEC), diagnostic, modélisation, estimation de paramètres, analyse de sensibilité, filtre de Kalman non linéaire.**

Laboratoire(s) de recherche : **Ampère**
Directeur de thèse : **Minh Tu Pham**
Président du Jury : **Marie-Cécile Péra**
Composition du Jury :

Marie-Cécile Péra, Thierry Poinot, Dani Juricic, Bertrand Morel, Minh Tu Pham, Federico Bribiesca-Argomedo

Thèse accessible à l'adresse : https://theses.insa-lyon.fr/publication/2026ISAL0017/these.pdf © [Z. Yazbeck], [2026], INSA Lyon, tous droits réservés

Thèse accessible à l'adresse : https://theses.insa-lyon.fr/publication/2026ISAL0017/these.pdf © [Z. Yazbeck], [2026], INSA Lyon, tous droits réservés